ALMA MATER STUDIORUM – UNIVERSITÀ DI BOLOGNA

DOTTORATO DI RICERCA IN GEOFISICA

Ciclo XXVI

Settore concorsulale: 04/A4 Geofisica

Settore Scientifico disciplinare: GEO/10 Geofisica della Terra Solida

GLOBAL AND REGIONAL SEA LEVEL VARIATIONS IN THE RECENT PAST AND FUTURE:
INSIGHT FROM OBSERVATIONS AND MODELING

Presentata da: Gaia GALASSI

Coordinatore Dottorato	**Relatore**
Ch.mo Prof. Michele DRAGONI	Prof. Giorgio SPADA

ESAME FINALE ANNO 2015

Contents

List of Figures

List of acronyms and abbreviations

AIS	Antarctic Ice Sheet
AMO	Atlantic Multidecadal Oscillation
ANN	Artificial Neural Network
AR4	Fourth Assessment Report (IPCC)
AR5	Fifth Assessment Report (IPCC)
AS	Adriatic stack
ASL	Absolute Sea Level
ENSO	El Niño Southern Oscillation
ESL	Equivalent Sea Level
EW	Early Warning
GIA	Glacial Isostatic Adjustment
GIC	Glaciers and Ice Cap
GIS	Greenland Ice Sheet
GMSLR	Global Mean Sea Level Rise
GSLA	Global Sea Level Acceleration
IMF	Image Function
IPCC	Intergovernamental Panel on Climate Change
MEI	Multivariate ENSO Index
MSL	Mean Sea Level
NAO	North Atlantic Oscillation
NEP	North Est Pacific
NG	Nuuk/Godthab (Greenland)
NOAA	National Oceanic and Atmospheric Administration (USA)
NPGO	North Pacific Gyre Oscillation
OR	Ocean Response
PDO	Pacific Decadal Oscillation
PSMSL	Permanent Service for Mean Sea Level
RLR	Revised Local Reference
RSL	Relative Sea Level
SH	Spherical Harmonic
SHE	Spherical Harmonic Espansion
SLE	Sea Level Equation
TG	Tide Gauge
TIM	Terrestrial Ice Melting
TME	Terrestrial Mass Exchange
T/P	Topex/Poseidon

Chapter 1

Overview

This work is focused on recent sea–level change, *i.e.* on a time period over which data from modern instruments (tide gauges and altimetry) are available (last century). During this period, individual components of sea–level change have been investigated, both at global and at regional scale, and the geophysical processes involved have been analyzed through models. Sea–level observations, especially those from tide gauges, have been used to infer information on sea–level trends and periodicity. The understanding of mechanisms driving sea–level change gained analyzing the past, has been utilized to project sea–level to the future.

The Thesis is organized into six chapters. The first chapter contains an overview on sea–level, with the illustration of sea–level observations and models used for interpretation. In addition, the contribution of geophysical processes (namely, glacial isostatic adjustment and elastic rebound consequent to current ice melting) to present and future sea–level is shown here. In chapter 2, the tide gauge data are analyzed to assess a global value of sea–level rise for the last century. The glacial isostatic adjustment contribution is taken in to account and it is used to reach a proper selection of tide gauges. Then, the sea–level spatial variability at low wavelength is investigated to obtain information on mass balance of glaciers and ice sheets for the last century (chapter 3). In chapter 4 some non linear components of sea–level variability are analyzed: staring from single tide gauge records, different approaches are used to understand regime change and the connection with the oceanic modes. In chapter 5, two distinct approaches for sea–level projections are presented. Finally, the conclusions are drawn in chapter 6.

1.1 Sea level change

Sea–level variations have ever occurred, at global and regional scales. Over geologic epochs, sea–level has changed drastically many times, primarily following the glacial cycles. During the Last Glacial Maximum (about $21,000$ years ago) sea–level was in average about 130 m lower that today, because of the large amount of water held by glaciers and ice sheets (Peltier, 2004). Going back to remote epochs, there is evidence of similar changes associated to glacial and interglacial cycles.

During the last three millennia (i.e. since the end of last deglaciation), sea–level has remained almost stable (Lambeck et al., 2004b).

After the beginning of the industrial era, our knowledge of sea–level comes from tide gauges measurements taken along continental coasts and islands. Tide gauges measurements show significant sea–level rise during the twentieth century (Douglas, 2001). From about 1993, the introduction of satellite altimetry supplies measures of sea–level over the whole oceanic domain (Nerem and Mitchum, 2001).

Sea–level is defined as the level of the free surface of the sea. When this level is referred to the Earth's center of mass, it is referred to as "absolute sea–level" (ASL) whereas when it is referred to a benchmark on the solid Earth, it represent the "relative sea–level" (RSL). Mean sea–level (MSL) is a datum representing the average height of the ocean surface (such as the halfway point between the mean high tide and the mean low tide). Sea–level change (S) is defined as the variation of sea–level relative to a previous time in a given place.

1.2 Observations

1.2.1 Tide gauge observation

Tide gauges (hereinafter TGs) are the oldest instruments for measuring sea–level changes. The first instrumental records of sea–level date back at the beginning of 18^{th} century, when TGs were set up in Amsterdam, Stockholm, Kronstadt and Liverpool. In its basic form, a TG is a graduated staff in which the sea–level can be visually observed. At present, staffs have been replaced with more elaborate instruments that allow to eliminate the wave effects and to obtain a continuous recording of sea–level. However, the idea behind remains the same: a tide gauge is an instrument capable to detect the height (and its variations) of the free surface of the ocean relative to the solid Earth. As a consequence, TGs measure the relative sea–level (RSL).

For TG measurements, we employ observations obtained from the Permanent Service for the Mean Sea Level (PSMSL, see *http://www.psmsl.org/*) that collects sea–level data from individual national authorities since 1933 (Holgate et al., 2012). Currently, PSMSL distributes both Metric and Revised Local Reference (RLR) data, which correspond to different quality standards. Metric data are monthly and annual observations directly received from the national authorities. The RLR dataset, on the other hand, contains revised data, with monthly and annual records reduced to a common benchmark based on the history of the TG datum in order to construct time series of sea–level measurements. In this Thesis, we mainly use RLR annual and monthly mean data, which constitute the most appropriate record for analyses of long–term sea–level rise (Spencer and Woodworth, 1991).

At present, the PSMSL RLR database contains data from $\sim$ 2000 TGs for which monthly and annual mean sea–level information is available. However, many stations have historically only been measured for some months or years. If we look to the TG RLR measurements available each year, we see that in 1980 approximately 670 stations were available (400 more than in 1940), but now this number is declining (in 2010 data from about 600 station were available). The records

are also inhomogeneous in terms of data length and quality. Only few TGs were functioning in the beginning of 20^{th} century, thus series usable for long–term studies represents about the 10% of the whole dataset (Cazenave and Llovel, 2010).

In addition to the not homogeneous availability of data during time, tide gauges with RLR data are not uniformly distributed across the oceans. Obviously, they are only along the coasts, so that big portions of oceans are not covered by data. Furthermore, TGs are mostly located in the northern hemisphere, especially in northern Europe and USA (it is estimated that only a 10% of TGs are located in the southern hemisphere). The distribution of TGs with at least three years of measurements in their record is shown in Fig. 1.1.

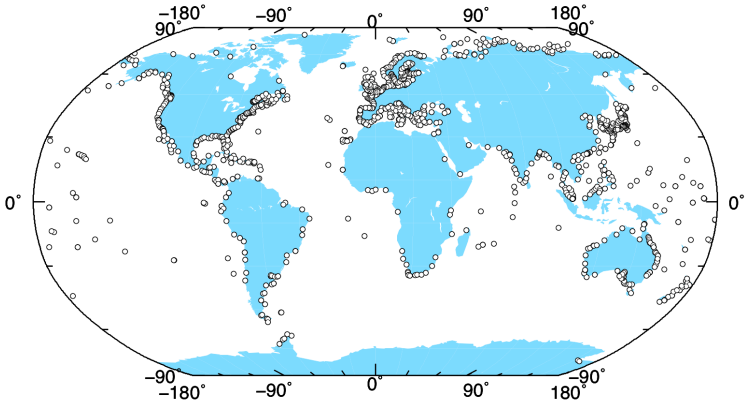

Figure 1.1: Location of the PSMSL TGs with at least three yearly RLR observations.

1.2.2 Altimetric observations

Satellite altimetry represents a tool for precisely and continuously measuring of sea–level, with a quasi–global and uniform coverage. Data of sea–level height measured by satellite altimetry are available since early 1990s, when the TOPEX/Poseidon (T/P) radar altimeter satellite was launched (1992–2005). Together with the missions Jason-1 (2001–present) and Jason-2 (launched in June 2008), the altimeter satellites have provided a continuous time series of sea–surface height with 10–day intervals and covering the area between 66°N and 66°S (Nerem and Mitchum, 2001). Altimeters RS-1, ERS-2, Envisat, Geosat follow–on, are less accurate then those from T/P and Jason satellites, but they allowed for measurements up to $\pm 82°$ latitude and at different temporal sampling (3 to 35 days) (Rhein et al., 2013).

The data are obtained with a radar altimeter mounted on satellite that transmits microwave radiation toward the sea surface, partially reflected back to the satellite itself. Measurement of the round-trip travel time provides the height of the satellite above the instantaneous sea surface (Cazenave and Llovel, 2010). Since altimetry satellites, unlike tide gauges, measure the ASL, *i.e.*

the sea surface height with respect to a geodetic reference frame (*e. g.* a reference ellipsoid) they are not affected by vertical land movement; nevertheless, it is necessary to apply a small correction for the change in location of the ocean bottom due to Glacial Isostatic Adjustment relative to the reference frame (Rhein et al., 2013; Nerem and Mitchum, 2001).

In this Thesis, different sources of Altimeter data have been used but we mainly employ T/P data from AVISO (*http://www.aviso.oceanobs.com*). The rate of sea–level change from 1992 to 2005 observed by T/P is shown in Fig. 1.2.

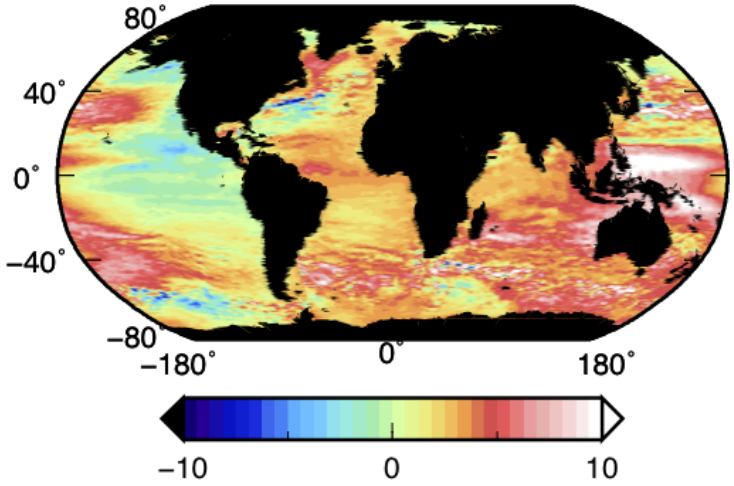

Figure 1.2: Rate of sea–level from 1992 to 2005, based on TOPEX/Poseidon altimetry data from AVISO (*http://www.aviso.oceanobs.com*).

1.3 Causes of sea–level change

Global sea–level variations result from a combination of various factors. On decadal and longer time scales, global mean sea–level change results from two major processes, namely the thermal expansion and the exchange of water between oceans and other reservoirs (as glaciers and ice caps, ice sheets, the atmosphere and land water reservoirs, see Bindoff et al., 2007). In addition, glacial isostatic adjustment (GIA) and other local factors may influence sea–level variations.

For the subsequent discussion, it is convenient to model the sea–level variations relative to the solid Earth, S, as the combination of the different contributions:

$$S^{TOT}(\theta,\lambda,t) = S^{GIA} + S^{MAS} + S^{STE} + S^{OTH}, \tag{1.1}$$

where θ and λ are longitude and co–latitude, respectively, t is time, S^{GIA} is the glacial isostatic adjustment component of sea–level , S^{MAS} is the contribution associated with mass exchange, S^{STE}

is the steric component (this includes thermo–steric and halo–steric effects), and S^{OTH} represents the contribution of other factors (including, for instance, sediments compaction and anthropogenic effects).

The rate of sea–level change is obtained by

$$r_k^{TOT} = \frac{dS^{TOT}}{dt}(\omega_k, t_p), \tag{1.2}$$

where $\omega_k = (\theta_k, \lambda_k)$ represent a specific place (*e. g.* a tide gauge at co–latitude θ_k and longitude λ_k) and t_p is present time. Similarly, the rate of change in relative sea–level can be written as sum of the various contribution

$$r_k^{TOT} = r_k^{GIA} + r_k^{MAS} + r_k^{STE} + r_k^{OTH}, \tag{1.3}$$

where r_k^{TOT} is defined by Equation 1.2 and in the right hand side of the equation are considered the time derivates of the same terms described in Equation 1.3.

1.3.1 Steric component

The term S^{STE} and its derivative r_k^{STE} in Eqs. 1.1 and 1.3 represents the steric component, *i.e.* the variation induced by change in temperature and salinity of oceans in response to climate change. The term "steric" includes the thermo–steric and the halo–steric component of sea–level, associated with changes in temperature and salinity, respectively. Both these components contribute to global change and are responsible of local sea–level variations.

Thermo–steric sea–level is defined as the variation in sea surface height caused by expansion or contraction of the ocean volume due to temperature and salinity changes (Antonov et al., 2005). In the 20th century, the largest contribution to sea–level variations derives from the thermo–steric contributions. Temperature observations during the last half century indicate that the ocean has warmed in all basins (Bindoff et al., 2007). The average rate of thermo–steric sea–level rise caused by heating of the global ocean is estimated to be 0.40 ± 0.09 mm yr^{-1} over 1955 to 1995 (Antonov et al., 2005). For the 0 to 700 m depth ocean layer and the 1955 to 2003 period, the averaged thermo–steric trend is 0.33 ± 0.07 mm yr^{-1} (Bindoff et al., 2007). For the same period and depth range, the mean thermo–steric rate based on monthly ocean temperature data from Ishii et al. (2006) is 0.36 ± 0.12 mm yr^{-1}.

Changes in salinity are often linked to changes in the amount of salt or in the amount of water, and often result in a net mass change that must be considered in the overall sea–level budget (Jordà and Gomis, 2013). At a global level, changes in the steric component are mainly attributed to thermal component and the impact of salinity changes (the halo–steric sea–level) is considered less important (Antonov et al., 2002). At the regional scale, however, salinity can play an important role in determining steric sea–level (Jordà and Gomis, 2013).

In this Thesis, different sources for thermo–steric data have been used. The thermo–steric trend was calculated using the Ishii and Kimoto (2009) dataset and the EN3 dataset (Ingleby and

Huddleston, 2007). The Ishii and Kimoto dataset has been evaluated to a reference depth of 1500 m on a uniform 1 degree grid, for the period 1945–2010 (IS45 in the following). The EN3 dataset has been evaluated to the sea floor on a uniform 1–degree grid, for the period 1966–2010 (EN66 in the following).

The halo–steric component has been considered together with the thermo–steric, as total steric sea–level. Data have been extracted from the National Oceanographic Data Center (NODC) of the NOAA (*http://www.nodc.noaa.gov*). The trend has been computed for pendadal average from 1955–1959 to 2007–2011, at two different depths (0–2000 m and 0–700 m respectively).

In Fig. 1.3 the steric data used in the following chapters are presented. Maps on the top show the thermo–steric sea–level trend according with the Ishii and Kimoto and the EN3 datasets; maps on the bottom show the thermo–steric, the halo–steric and the (total) steric sea–level trend at the 0–700 depth layer.

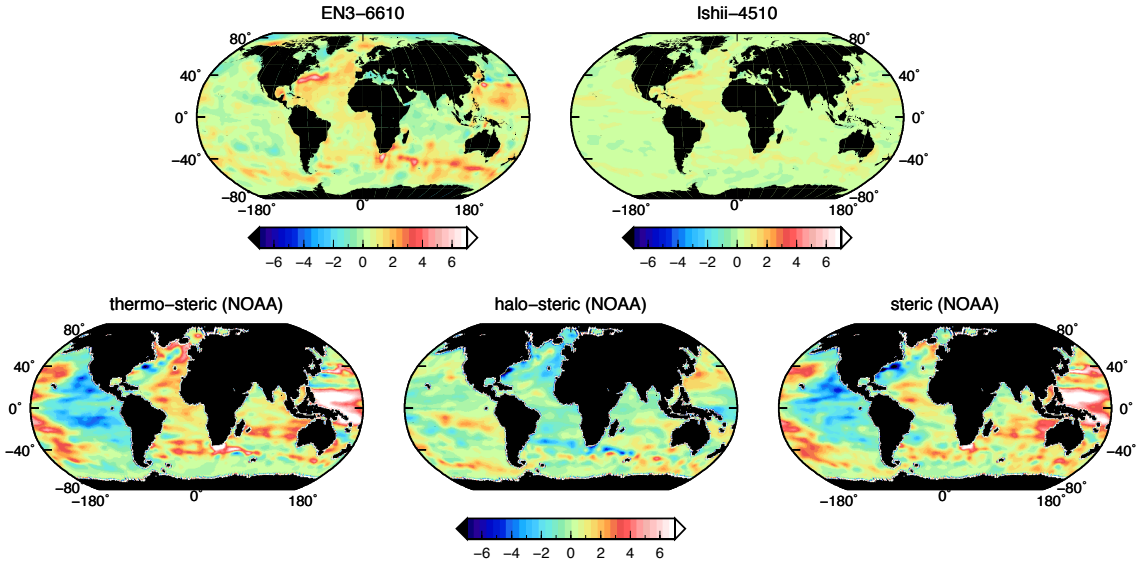

Figure 1.3: Steric sea–level trends (mm yr^{-1}). Top: thermo–steric sea–level trends from 1966 to 2010 (reference depth 1500 m) for the EN3 dataset Ingleby and Huddleston (2007) and from 1945 to 2010 for the Ishii and Kimoto (2009) dataset; bottom: thermo–steric, halo–steric and (total) steric sea–level trend computed on pentadal data from National Oceanographic Data Center (NODC) of the NOAA (*http://www.nodc.noaa.gov*) at 0–700 m depth.

1.3.2 Mass exchange

An other important contribution to sea–level change is given by the land–ice melting (hereinafter Terrestrial Ice Melting, TIM) which implies mass variations of the oceans. This is the term S^{MAS}

in Equation 1.1, that can be in turn expressed as the sum of the contribution of the three major ice sources:

$$S^{MAS} = S^{AIS} + S^{GIS} + S^{GIC}, \tag{1.4}$$

where the three terms on the right–hand side represent the contributions to sea–level change from Antarctic Ice Sheets (AIS) and Greenland Ice Sheets (GIS) and Glaciers and Ice Cap (GIC), respectively.

When a land–based mass of ice melts, we can observe several effects. First, melt water represents an input of mass for the oceans. This input is not uniformly distributed on the oceans, and it causes a change in surface load, changing the ocean bathymetry with mantle material being forced under land masses (Fleming et al., 2012), and leading to deformations in Earth's gravity fields and in solid Earth (Farrell and Clark, 1976; Milne and Mitrovica, 1998). In addition, the gravitational effect (*i.e.* land ice attracts ocean water) implies that RSL drops near the melting ice masses and rises at a larger distance (Slangen et al., 2012).

Currently, only two ice sheets are present on the Earth surface: the Greenland and the Antarctica ice sheets. Together, they hold enough ice to raise sea–level about 64 m if fully melted (Lythe et al., 2001). Consistently with the forth IPCC assessment report (IPCC AR4, Lemke et al., 2007), we will refer to all perennial ice masses other than the Greenland and the Antarctic ice sheet as Glaciers and Ice Caps (GIC).

For the AIS, the contribution to global sea–level trend from 1961 to 2003 is about $+0.19$ mm yr^{-1} (Lenaerts et al., 2012; Rignot et al., 2011), corresponding to a negative mass balance (ice loss) of -68.4 Gt yr^{-1}. This is in the range established by the IPCC AR4 report (Lemke et al., 2007) which assesses that the behavior for the same period falls between ice sheet growth of $+100$ Gt yr^{-1}and shrinkage of -200 Gt yr^{-1}. For the period 1993 to 2003, according with Rignot and Thomas (2002), Zwally et al. (2005) and Rignot et al. (2005), the ice sheet has thinned of about -60 Gt yr^{-1}corresponding to ~ 0.17 mm yr^{-1}. These estimates account for a West Antarctic loss and an East Antarctic gain. The IPCC AR4 report (Lemke et al., 2007) suggests an overall AIS mass balance for 1993–2003 ranging from growth of $+50$ Gt yr^{-1}to shrinkage of -200 Gt yr^{-1}. The fifth IPCC assessment report (IPCC AR5, Church et al., 2013) for AIS gives a global mean sea–level budget for the period 1993–2010 between $+0.16$ and $+0.38$ mm yr^{-1}, corresponding to a mean mass balance of about -97 Gt yr^{-1}.

For the GIS, Ettema et al. (2009) and Rignot et al. (2011) established a positive mass balance (ice accumulation) of $+50.4$ Gt yr^{-1}for the period 1961 to 2003. According to the IPCC AR4 report (Lemke et al., 2007), assessment of the data and techniques suggests a mass balance for the GIS ranging between $+25$ Gt yr^{-1}and -60 Gt yr^{-1}for 1961 to 2003, shrinkage of -50 to -100 Gt yr^{-1}for 1993 to 2003 and shrinkage at even higher rates between 2003 and 2005. The increase in rate of mass loss for recent period is confirmed by the the mass balance assessed by Spada et al. (2012) for the period 2003–2008, equal to -240 Gt yr^{-1}. The IPCC AR5 (Church et al., 2013) for 1993–2010 sets an average mass balance, without considering Greenland glaciers, of about -119 Gt yr^{-1}. This values becomes -155 Gt yr^{-1}considering together the GIS and the Greenland glaciers.

For glaciers and ice caps, Dyurgerov and Meier (2005) provide mass balance estimates of 13 large regions across the world. Excluding peripheral ice bodies in Greenland and Antarctica, they suggest a total contribution to sea–level rise of 0.33 mm yr^{-1} corresponding to -219 Gt $yr^{-1}$for 1961–1990. For 1991–2004 the glacier contribution assessed by Dyurgerov and Meier (2005) is -277 Gt yr^{-1}, corresponding to about 0.77 mm yr^{-1} of sea–level rise. Including the smaller Greenland and Antarctic glaciers, these estimates are -137 Gt $yr^{-1}$for 1961–1990 and -352 Gt $yr^{-1}$for 1991–2004. The IPCC AR4 report (Lemke et al., 2007), mostly based on Dyurgerov and Meier (2005) work, between 1960–1961 and 2003–2004 assesses a mass balance of -182 Gt yr^{-1}(including glaciers and ice caps around the ice sheets). According to the IPCC AR5 (Church et al., 2013), the average contribution of Glaciers (including the Greenland ones) to sea–level rise from 1971–2010 is $+0.60$ mm yr^{-1}, corresponding to a mass balance of -245 Gt yr^{-1}. This value increases to $+0.86$ mm yr^{-1}(-309 Gt yr^{-1}) if referred to 1993–2010.

1.3.3 Glacial Isostatic Adjustment effects

The Glacial Isostatic Adjustment (GIA) is a process influencing sea–level change (the term S^{GIA} in Equation 1.1) that is originated by the ongoing mass redistribution still caused by the melting of the late–Pleistocene ice sheets (Farrell and Clark, 1976). The relaxation of the solid earth in response to changes in the mass loading at the Earth's surface is a viscoelastic process, which is a combination of instantaneous (elastic) and delayed (viscous) behavior. The initial response to loading or unloading (as for the melting of present ice) can be considered purely elastic, and results in a direct uplift or depression of the crust (Spada et al., 2013). On timescales of thousands of years, the viscous effects become dominant: this is the GIA process that represents the ongoing response of the viscoelastic Earth to the loading from the ice age.

The GIA effects on relative sea–level average out to zero across the surface of the oceans, but they will be the source of local and regional sea–level variations, both in the formerly glaciated areas at the Last Glacial Maximum (LGM, $\sim 21,000$ years ago) and in key–areas such as the Mediterranean Sea (Stocchi and Spada, 2009). The GIA induced variability ranges from strongly positive (the rebound of previously ice covered area) to neatly negative values. Large ice sheets forming during an ice age, locally increases the load, depressing the crust and making the mantle material flow away: the consequence is a downward movement below and an upward movement around the ice mass (the so–called peripheral bulges), as illustrated in Fig. 1.4. During the melting phase, the process acts in the opposite direction, causing an uplift at the former location of the ice sheet and a downward movement of the bulges (Slangen, 2012).

1.3.4 Other contributions

There are other factors contributing to sea–level change, represented by the term S^{OTH} in Equation 1.1. One of the most important is that linked to the changes in water stored on continents as snow, lakes, permafrost, groundwater or dams. Here, we will refer to sea–level variation due to this processes as S^{TER} (and the correspondent rate r^{TER}), where TER stems for "Terrestrial mass

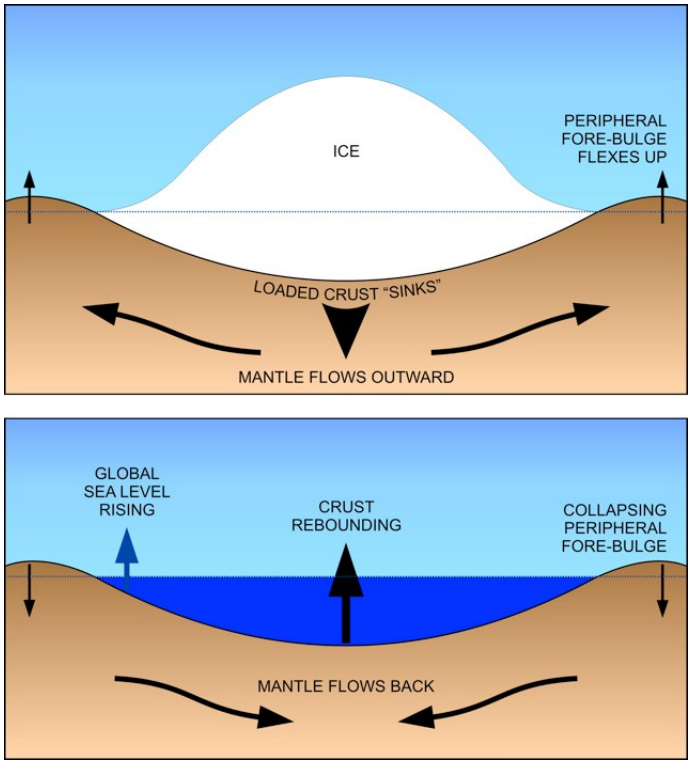

Figure 1.4: Generalized process of glacial isostatic adjustment. The top panel illustrates the effects when the Earth's surface is loaded by a heavy ice sheet. The lower panel shows the rebound effects once the ice sheet is removed. Figure courtesy of the Canadian Geodetic Survey, Natural Resources Canada.

exchange".

The processes contributing to terrestrial mass exchange are related with climate changes (melting of permafrost or snow, increase in lake evaporation) and human activities (mainly building of dams and groundwater extraction). Climate–related changes in water and snow storage on land show inter–annual to decade fluctuations (Nerem et al., 2010), and have not displayed significant trends during recent decades (Church et al., 2013).

Human–driven variations in land water storage can have opposite effects on sea–level. The impoundments of reservoirs has offset some of the sea–level rise that would otherwise have occurred (at a rate of -0.55 mm yr^{-1} between 1950 and 2000 according to Chao et al., 2008). On the other hand, groundwater depletion has exacerbated sea–level rise during the 20$^{\text{th}}$ century, with globally–averaged rates from 0.35 mm yr^{-1} in 1900 to 0.57 mm yr^{-1}in 2000, according to Wada et al. (2012). In the last part of the 20$^{\text{th}}$ century, groundwater depletion has become more important, exceeding the rates of impoundments and contributing to a global sea–level rise (Church et al.,

2013).

Here, we have used the TER global sea–level fingerprint produced by Slangen et al. (2012) combining the groundwater extraction data from Wada et al. (2012) and the reservoir impoundments data from Chao et al. (2008). The global sea–level fingerprint so obtained, mostly shows negative values (see Fig. 1.5), with an average value of -0.20 ± 0.26 mm yr^{-1}.

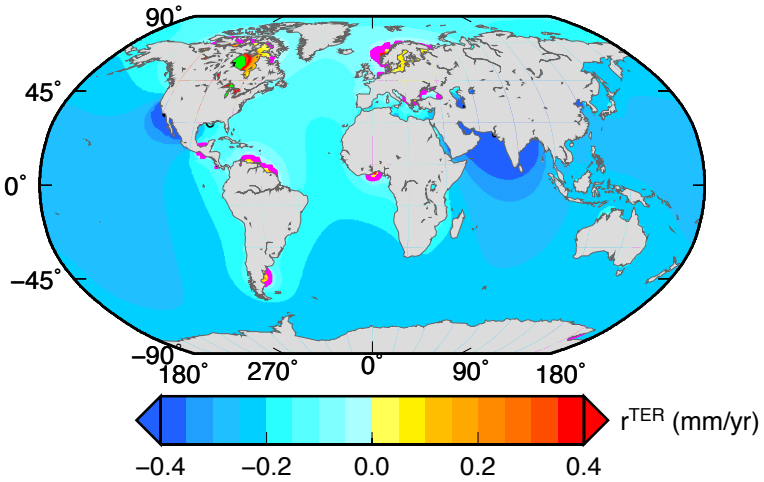

Figure 1.5: Global views of sea–level fingerprint of terrestrial mass exchange (r^{TER}) for the time period 1961–2003. The gridded data for this figure have been provided by Aimee Slangen (personal communication, 2013).

Other important processes that locally could affect sea–level are those of tectonic origin. The possible effects of tectonic vertical deformations on observed sea–level are difficult to assess, since no global predictive model for tectonic deformations can be invoked on a secular or multidecadal time scale, as in the case of other processes. Previous attempts to provide estimates of the contribution of co–seismic and post–seismic deformation to sea–level change at TGs (Melini et al., 2004; Melini and Piersanti, 2006) using data from the Seismic Moment Tensor catalogue (see e.g. Dziewonski and Anderson 1981) have clearly shown that earthquakes have cumulatively the tendency, globally, to produce a positive relative sea–level trend at locations of tide gauges. According to these studies (see, in particular, Melini et al. 2004), estimates of secular sea–level variations that do not account for the effects of global seismicity are likely to be overestimated by ~ 0.2 mm yr^{-1}. Co–seismic and post–seismic effects, however, are only a component of the total tectonic deformation field. While in a non–expanding Earth scenario it is reasonable to assume that tectonic vertical movements average out globally, it is clear that their cumulative effect depends upon the spatial distribution of TGs, which are far from being uniformly spaced (see Fig. 1.1).

1.4 Modeling the mass contribution of sea–level change and Glacial Isostatic Adjustment

1.4.1 The Sea Level Equation

To study the contribution of present and past ice mass variations to sea–level changes we need to model the geophysics processes involved. The physical processes governing sea–level changes of glacio–isostatic and hydro–isostatic origin are described in the so–called "Sea Level Equation" (hence after referred to as SLE), the integral equation first introduced by Farrell and Clark (1976) to model sea–level variations following the melting of late–Pleistocene ice–sheets. GIA and TIM are governed by the same physical process, namely the response to the solid Earth to the change in mass distribution: as the GIA is dominated by visco–elastic process (see subsection 1.3.3) the TIM is governed by purely elastic ones (see subsection 1.3.2). For this reason, the SLE is currently employed also to study the sea–level changes associated with present terrestrial ice melting in response to global warming (*e.g.* Mitrovica et al., 2001).

In its basic form the SLE is

$$S(\omega,t) = N - U, \tag{1.5}$$

where S is the change in relative sea–level (as observed from tide gauges) given by the difference between the sea surface variation N (representing the absolute sea–level variation measured by satellite altimetry) and the vertical displacement U. S, as well N and U depend on the location coordinates ($\omega = (\theta,\lambda)$ where θ is co–latitude and λ is longitude) and on time (t).

According to Farrell and Clark (1976), N can be written as

$$N(\omega,t) = G + c, \tag{1.6}$$

where c is a yet undetermined function of time, and the geoid height variations is

$$G(\omega,t) = \frac{\Phi}{\gamma}, \tag{1.7}$$

in which γ is the reference gravity at the surface of the Earth and $\Phi(\omega,t)$ is the total variation of the gravity potential. Hence, using Equation 1.6 into 1.5 gives the SHE in the form:

$$S(\omega,t) = \frac{\Phi}{\gamma} - U + c. \tag{1.8}$$

Mass conservation of the system (Ice sheets + Oceans) is ensured taking

$$c(t) = -\frac{m_i}{\rho_w A_o} - \overline{\left(\frac{\Phi}{\gamma} - U\right)}, \tag{1.9}$$

where ρ_w is the (constant) density of water, m_i is the mass variation of the ice sheets, A_o is the (constant) area of the present–day oceans and the overbar indicates the average over the surface of the oceans

$$\overline{(\ldots)} = \frac{1}{A_o}\int_o (\ldots)\, dA, \tag{1.10}$$

where $dA = a^2 \sin\theta d\theta d\lambda$ is the area element and a is Earth average radius. From Equation 1.8, the SLE can be therefore written as

$$S(\omega,t) = \left(\frac{\Phi}{\gamma} - U\right) + S^E - \overline{\left(\frac{\Phi}{\gamma} - U\right)}, \tag{1.11}$$

where the "eustatic" sea–level variation

$$S^E(t) = -\frac{m_i}{\rho_w A_o}, \tag{1.12}$$

shows the remarkable property

$$S^E(t) = \overline{S}. \tag{1.13}$$

The SLE has solution $S = S^E$ only in the case of a rigid, non self–gravitating Earth ($U = \Phi = 0$ in Equation 1.11. $S^E(t)$ only depends from the ice mass and density and from the surface of the ocean. It can be expressed in terms of Equivalent Sea Level (ESL), that accounts for the change in global average sea–level that would occur if a given amount of water or ice were added to or removed from the oceans, assuming a rigid, non–gravitationally Earth. At a given time t before present,

$$ESL(t) = (\rho_i/\rho_w)(V_i(t) - V_i(t_p))/A_o), \tag{1.14}$$

where ρ_i and ρ_w are the density of ice and water, respectively, $V_i(t_{bp})$ is the ice volume, $V_i(t)$ is present day volume, and A_o is the current area of the oceans surface. Assuming no ice melting during the last thousand years (*i. e.* $\dot{m}_i = 0$), and considering constant the surface of the ocean (A_0), according to Equation 1.12 the ocean–averaged rate of GIA sea–level change is

$$\dot{\overline{S}} \approx 0. \tag{1.15}$$

Functions $U(\omega,t)$ and $\Phi(\omega,t)$ will depend on the spatiotemporal variations of the *surface load*

$$\mathscr{L}(\omega,t) = \rho_i I + \rho_w S\mathscr{O}, \tag{1.16}$$

where the two terms on the right hand side are associated with the waxing and waning of the ice sheets, and with the redistribution of meltwater in the ocean basins. In Equation 1.16, ρ_i is ice density, $\mathscr{O}$ is the "ocean function" ($\mathscr{O} = 1$ on the oceans, $\mathscr{O} = 0$ on land), and

$$I(\omega,t) = T - T_0, \tag{1.17}$$

is the ice thickness variation, where $T(\omega,t)$ is absolute ice thickness, and $T_0(\omega)$ is a reference thickness at a remote time (e.g. the thickness at the Last Glacial Maximum, LGM, ~ 21 kyrs ago). The mass variation in Equation 1.12 is obtained from Equation 1.17 by integration over the ice–covered regions:

$$m_i(t) = \int_i \rho_i I \, dA. \tag{1.18}$$

According to Equation 1.16, vertical displacement stems from two terms

$$U(\omega,t) = \rho_i G_u \otimes_i I + \rho_w G_u \otimes_o S, \tag{1.19}$$

where G_u is the Green's function for vertical displacement, $\otimes_i$ and $\otimes_o$ are spatiotemporal convolutions over the ice– and ocean–covered regions, respectively. Similarly, the total variation of the gravity potential is

$$\Phi(\omega,t) = \rho_i G_\phi \otimes_i I + \rho_w G_\phi \otimes_o S, \tag{1.20}$$

where G_ϕ is the corresponding Green's function. Explicit expressions for G_u and G_ϕ are given in e.g. Spada and Stocchi (2006) in terms of the load–deformation coefficients (LDCs) $h(t)$ and $k(t)$, respectively.

Introducing the sea–level Green's function G_s as

$$\frac{G_s}{\gamma}(\omega,t) = \frac{G_\phi}{\gamma} - G_u, \tag{1.21}$$

substitution of Eqs. 1.19 and 1.20 into 1.11 gives

$$S(\omega,t) = \frac{\rho_i}{\gamma} G_s \otimes_i I + \frac{\rho_w}{\gamma} G_s \otimes_o S + S^E - \frac{\rho_i}{\gamma}\overline{G_s \otimes_i I} - \frac{\rho_w}{\gamma}\overline{G_s \otimes_o S}, \tag{1.22}$$

which represents the SLE in the "gravitationally self–consistent" form. Since the unknown $S(\omega,t)$ also appears in the spatiotemporal convolutions at the right hand side, the SLE is an integral equation, which cannot be solved explicitly unless some drastic simplifying assumption are made (Spada and Stocchi, 2006). The SLE is a linear equation as long as shorelines are not allowed to migrate horizontally, i.e. if $\mathscr{O}$ (and consequently A_o) are not time dependent. Sea–level variations are sensitive to mantle rheology through G_s, since this is determined by the viscoelastic LDCs h and k (Spada and Stocchi, 2006).

Equation 1.22 is solved numerically by SELEN, an open source program written in Fortran 90, primarily designed to simulate the sea–level and geodetic variations in response to the melting of continental ice sheets (Spada et al., 2012). Though the principal physical ingredients of the SLE are implemented in SELEN, some approximations are adopted. First, SELEN assumes a linear incompressible rheology and a spherically symmetric Earth in the un–deformed state. Therefore, the program takes advantage from the viscoelastic Green's function formalism (see references in Spada et al., 2011a). Consequently, lateral rheological variations are not taken into account. As a second approximation, following Farrell and Clark (1976), SELEN does not take into account for the horizontal migration of shorelines in response to sea–level change. This indeed constitutes a crude approximation especially in areas of shallow bathymetry, which will be relaxed in the future releases of SELEN so to allow for "gravitationally self–consistent" paleogeographical reconstructions (Peltier, 2004). Finally, it is important to remark that SELEN does not account for tectonic contributions to sea–level, for local effects such as subsidence driven by sediment loading, nor any possible anthropic contribution to sea–level change. Furthermore, SELEN does not account for ocean dynamics or possible steric sea–level variations.

The published version of SELEN available on Computational Infrastructure for Geodynamics platform (CIG, *http://geodynamics.org/cig/software/selen/*) does not include rotational feedbacks (Milne and Mitrovica, 1998). Moreover, in this work, an improved version of SELEN has been used, and the sea–level variations associated with rotational feedbacks have been taken in to account.

1.4.2 Glacial Isostatic Adjustment models

To solve the SLE and to find the GIA contribution to sea–level changes it is necessary to use appropriate ice models. This models assume a melting history for the continental ice load existing at LGM. Peltier and Andrews (1976) used a first approximation model, called ICE-1, in which only the Northern hemisphere deglaciation was considered. Currently several models that better asses the whole ice load at the LGM are available.

In this work we will consider three previously published time–histories of the late–Pleistocene ice sheets: ICE–3G (Tushingham and Peltier, 1991), ICE–5G (Peltier, 2004) and the ice model progressively developed at the Research School of Earth Sciences (RSES) of the National Australian University by Kurt Lambeck and co–workers (see Fleming and Lambeck, 2004, and references therein). Since this latter ice model is valid as of 2005, we will refer to it as to KL05 in the following.

In the ICE–3G construction (Tushingham and Peltier, 1991), RSL predictions for a particular location were compared with geological proxy of RSL at the same sites, any adjustments required were made accordingly and the predictions were again compared, in a iterative procedure. A single "standard" model of the Earth interior was selected, and the finite grid element has an approximate 2° x 2° resolution (Tushingham and Peltier, 1991). The total eustatic sea–level since the LGM in ICE–3G is ≈ 110 meters of ESL (see Equation 1.14), with a main contribution deriving from North America (≈ 60 meters), and residual contribution from Antarctica and Europe plus Asia (≈ 25 meters each).

ICE–5G (Peltier, 2004) represents an improvement of previous ice models of the same author, like ICE–3G and ICE–4G. The model data are provided at 10 min spatial resolution for 21ka and 0ka, and at 1 degree spatial resolution for intervals in between these snapshots. According to RSL geological observations, ice thickness and distribution are improved to better fit with RSL data. The main differences compared to the previous model, ICE–4G, concern Northern hemisphere locations that were glaciated at LGM, as northwestern Europe and Eurasia, the British Isles, Greenland, and the North American continent (Justino et al., 2006). For instance, the western flank of the Laurentide ice sheet in the ICE–5G reconstruction is approximately 1500 m thicker whereas the Greenland ice sheet is approximately 500 m thinner in the ICE–5G model as compared to the ICE–4G model. Furthermore, the topographic feature related to the ice sheet on the East Siberian Shelf that was included in the ICE–5G dataset has been entirely eliminated from the ICE–5G dataset (Justino et al., 2006). For the viscoelastic structure of the Earth, VM2 model is used, in which the radial variation of elastic properties is assumed to be fixed to that in the Preliminary Reference Earth Model (PREM) of Dziewonski and Anderson Dziewonski and Anderson (1981). In ICE–5G

Table 1.1: Lithospheric thickness and mantle viscosity for the GIA models employed in this study. ICE-3G data are those presented in Tushingham and Peltier (1991). KL05 data are taken from Fleming and Lambeck (2004), while ICE–5G values have been obtained by volume–averaging the original VM2 viscosity profile of Peltier (2004).

Rheological parameter	Ice model		
	ICE–3G	ICE–5G	KL05
Lithospheric thickness (km)	120	90	65
Upper mantle viscosity ($\times 10^{21}$ Pa·s)	1	0.5	0.3
Lower mantle viscosity ($\times 10^{21}$ Pa·s)	2	2.7	10

the total ESL is approximately 125 m.

The KL05 ice sheets are constructed on the inversion of geological sea–level and shoreline data supplemented by observational evidence of ice margin locations and, in a few instances, by limiting ice thickness estimates. KL05 is based on a combination of field data for ice margins and ice thickness estimates based on rebound data inversions. These inversions are complemented with simple glaciological models when the field data is incomplete. The ice–volume function through time for the sum of the ice sheets is constrained by field data from the far–field sites, where the sea-level signal is predominantly sensitive to the changes in total ice volume. The quality of the single ice sheet models changes for the different regions. For instance, for northern Europe, including the British Isles, the inversions are based on comprehensive datasets, whereas the North American model is not based on complete datasets. The Antarctic model is based on LGM ice margins proposed in Anderson et al. (2002), on an ice volume function that equals the observed global function less the sum of contributions from the other ice sheets, and on the few rebound data points that are available.

The main features of these three models are shown Fig. 1.6. Left frames show the time histories of ESL for the three ice models considered. In Fig. 1.6(a), ESL is shown for the total ice aggregates, while in (b) and (c) we separately consider the major ones: Laurentide and Antarctica, respectively. In all cases, here we assume isostatic equilibrium (constant ice mass) prior to the inception of melting and no ice mass variations during the last 1,000 years. For all models, we employ a time discretization with steps of 1 ka. Right frames show the global distribution of ice complexes for the three models, at the times when the corresponding time histories initiate. The three panels show $T(\theta,\lambda,t) - T(\theta,\lambda,t_p)$, where T is ice thickness. The different spatial distributions and the level of detail of the three ice distributions are apparent. The total ESL for the three models is *broadly* following (to within $\sim \pm 10$m) the same curve until ~ 5 ka (a). This curve is constrained by evidence from coral reefs at Barbados, see *e.g.,* Fairbanks (1989) and subsequent refinements. However, the ice masses are clearly partitioned in different manners and partial ESL curves differ considerably. Thought this detail is barely visible in (c), in KL05 the melting of Antarctica continues essentially until $1,000$ years ago (Nakada and Lambeck, 1987), while in the

other models it terminates between 5 and 4 ka BP. In addition to the distinct viscosity profiles assumed, summarized in Table 1.1, these features have important consequences on the assessment of present day regional sea–level variations. For the motivations and hypotheses behind the three reconstructions, the readers are referred to the original works quoted above.

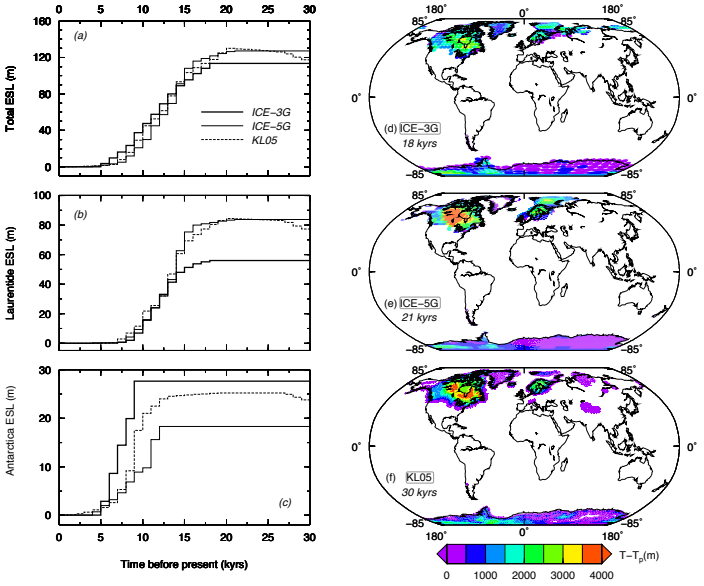

Figure 1.6: Left: equivalent sea–level (ESL) for models ICE–3G, ICE–5G and KL05, relative to the total ice aggregates (a), the Laurentian (b) and the Antarctica (c). Right: spatial distribution of the ice thickness fro the three models, at the times when the corresponding time histories initiate.

For these three GIA models, a radially layered (1–D) Maxwell viscoelastic rheology is assumed for the Earth's mantle, as shown in Table 1.1. Possible effects from 3–D lateral variation in mantle viscosity on final predictions are assessed by Kendall et al. (2006) and Spada et al. (2006). In our reference numerical experiments, we have employed a maximum harmonic degree $\ell_{max} = 128$ on a quasi–regular icosahedral geodesic grid (Tegmark, 1996) with a spacing of ~ 220 km. We remark that details of our numerical implementation of the SLE, described by Spada and Stocchi (2007), may differ from those in the original works where the ice models have been presented. Therefore, the results may deviate somewhat from those obtained by other GIA modelers, although the ice models used are nominally the same. A recent GIA benchmark study has shown that there is a broad consensus in the community on the numerical implementation of some of the major components of the SLE (Spada et al., 2011a).

The fingerprints in Fig. 1.7 represent the rate of sea–level change induced by GIA process obtained computed the derivative of the solution of Equation 1.22. Since for the loads of the size of the major late–Pleistocene ice sheets the Maxwell relaxation time of the mantle is of the order

of a few kilo–years (see *e.g.,* Schubert et al., 2001), the rates of sea–level change shown can be effectively considered as constant through the period of the instrumental sea–level records, at least until the role of transient (*i.e.,* non–Maxwellian) rheological components of deformation will be fully ascertained (Ivins and Sammis, 1996; Spada et al., 2011b).

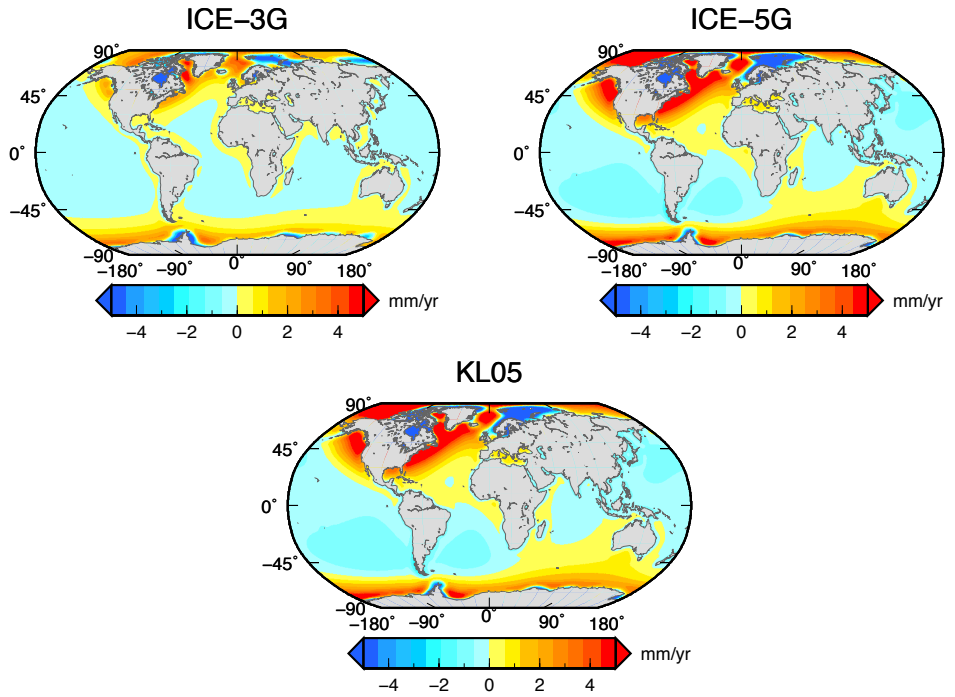

Figure 1.7: GIA sea–level fingerprints obtained solving the SLE with SELEN (including rotational feedback effects) for the three ice models ICE–3G, ICE–5G and KL05, respectively

While in Fig. 1.7 the global features of the GIA component of present–day rate of sea–level change are quite similar for the three ice models considered, it is possible to note remarkable regional and local differences (sometimes at the 0.5 mm yr^{-1} level), reflecting the different chronologies of the ice sheets and the distinct viscosity profiles adopted (see Table 1.1). Some of these differences have a very simple explanation. For instance, it is apparent that the sea–level change patterns suggested by ICE–5G and KL05 across north America and the north Atlantic differ significantly from those of ICE–3G. Inspection of Fig. 1.6 shows that the cause is the larger mass of the Laurentian ice sheet in ICE–5G and KL05, which implies a more vigorous sea–level fall across north America and a much broader peripheral region of sea–level rise compared to ICE–3G. Another major difference between the models considered is the total amount of meltwater from Antarctica (see Fig. 1.6) and the details of the history of melting in this regions, which explains the

different shape of contour lines in the Southern hemisphere.

1.4.3 Terrestrial Ice Melting models

The contribution of recent ice melting to sea–level rise can be found solving the SLE in its "elastic" form. To do this, models describing dynamics and distribution of major present–day ice source are needed. Here we use two kinds of models: the first is referred to the mass balance assessed for the recent period, while the second is based on the modeled ice dynamic for the future. The ice spatial distribution for the three sources used for both present and future estimate of TIM components of sea–level rate, is the same used in Spada et al. (2013) and it is presented in Fig. 1.8, which also shows the time history of their volume variations (in terms of Equivalent sea–level, ESL) to year 2100.

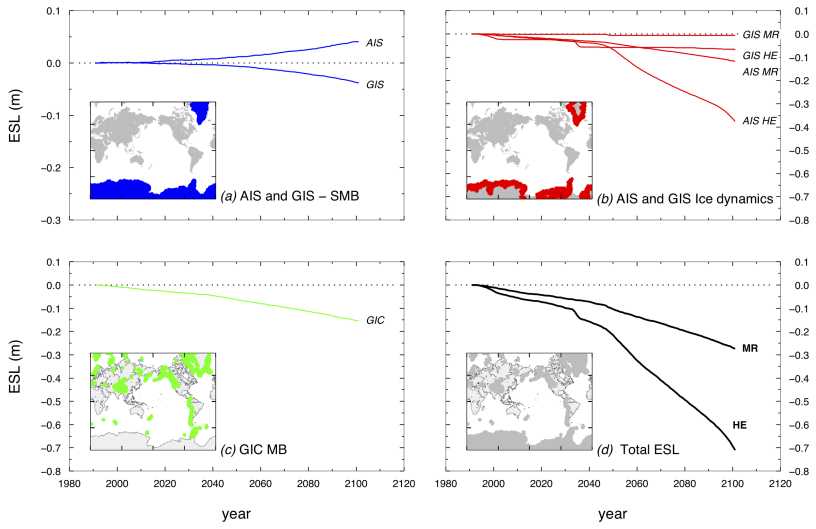

Figure 1.8: TIM ESL and ice sources distributions between 1992 and 2100 according to Spada et al. (2013). (a) SMB for AIS and GIS, (b) GIC mass balance, (c) ice dynamics component for AIS and GIS in the MR and HE scenarios, (d) total TIM.

For the present ice melting, the SLE is solved assuming elastic rheology for the mantle, which is appropriate in view of the short times scales considered here (in the order of decades), compared to those of GIA. For the mass balance a uniform net mass variation, corresponding to 100 Gt yr^{-1}, has been assumed assumed. The modeled sea–level fingerprint for present TIM are presented in Fig. 1.9. Here, the sea–level fingerprint obtained with a uniform ice–loss, is normalized on ocean–average of relative sea–level rate.

The TIM models used for future sea–level projection are based on the work of Spada et al. (2013). For Greenland and Antarctic ice sheets, volume changes are caused by both ice dynamics

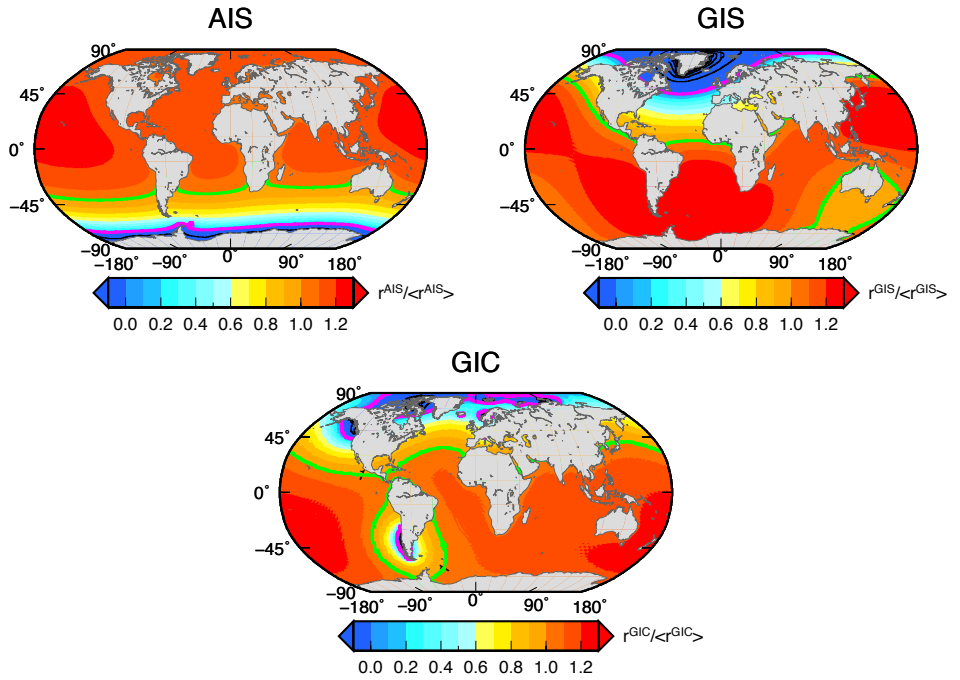

Figure 1.9: Sea–level fingerprints for the AIS (top), GIC (middle) and GIS (bottom), normalized on ocean–average of relative sea–level rate. The values of 0 and 1 are marked in magenta and green, respectively.

(DYN) and surface mass balance (SMB). This latter represents the net mass added or removed from the surface of an ice sheet and it is defined as the sum of mass fluxes towards and away from the ice sheet surface, integrated over the area of the ice sheet (see *e.g.* Dahl-Jensen et al., 2009). The DYN includes dynamic processes, such as basal flow and ice stream dynamics. SMB in Antarctica is driven mainly by surface melting, whereas in Greenland is also driven by accumulation. These fields (DYN and SMB) are considered separately and are obtained by Spada et al. (2013) from two regional climate models (RCMs), namely MAR (Fettweis, 2007) for the GIS and RACMO (Lenaerts et al., 2012) for the AIS, forced by ECHAM5 under scenario A1B (Solomon, 2007). To assess the DYN contribution of the AIS, two scenarios were built from an ensemble of 81 model runs: a "mid range" (MR) scenario contributing ~ 7 cm of mean sea–level rise by 2100, and "high–end" (HE) scenarios contributing ~ 30 cm. For both, only volume variations above flotation are considered. For the GIS, the two scenarios are based on flow–line model simulations to obtain total volume changes due to calving. In the GIS MR scenario, the model was calibrated against present–day observations, while the HE scenario resulted from a lowering the bedrock by its two–sigma error estimate. Note that for both the AIS and the GIS, the HE and MR scenarios only differ in the

DYN components, the SMB contributions being the same. Lastly, for the GIC component of TIM, a regionalized mass balance model is employed, with MR and HE scenarios described by Spada et al. (2013).

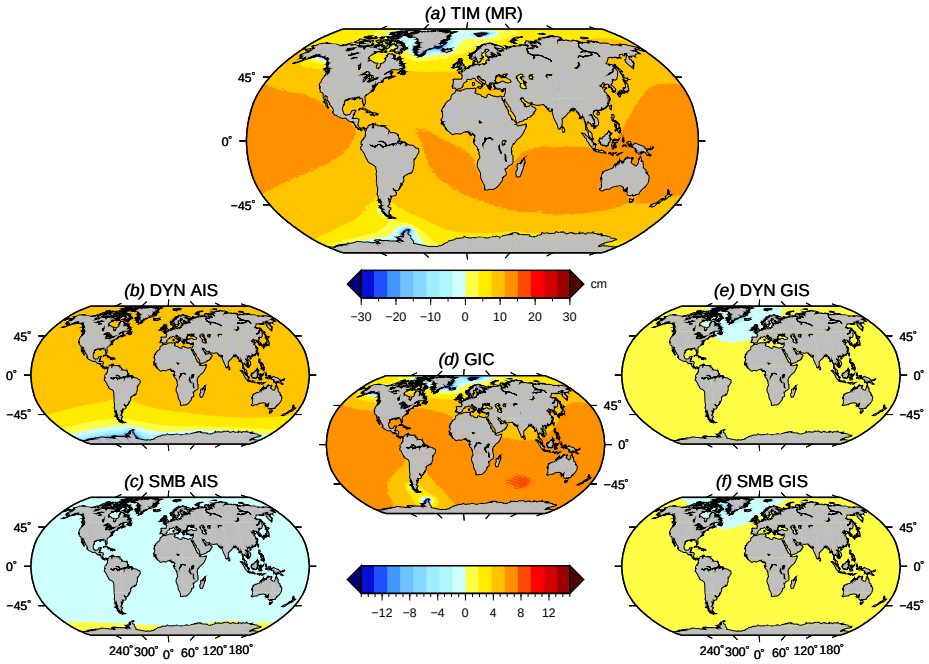

Figure 1.10: Global TIM relative sea–level fingerprints to 2040–2050, according to the MR scenario of Spada et al. (2013). The total component in (a) is split into individual contributions in (b–f).

The estimated global TIM contribution to sea–level change to 2040–2050 relative to 1990–2000 is shown in Figs. 1.10 and 1.11 for the MR and HE scenarios, respectively. The total TIM effect, shown in frames (a) of both figures, is decomposed in the individual contributions in frames b–f. Note that the SMB contribution (frames c and f) is the same for both scenarios. For both the MR and HE scenarios, the TIM component of relative sea–level change departs significantly from eustasy (a spatially uniform response) and is mainly driven by the melt of the GIC and by the dynamic ice loss from Antarctica, shown in frames d and b, respectively. The sea–level variations associated with TIM are significantly influenced by the gravitational interactions between the cryosphere, the oceans and the solid Earth and by long–wavelength rotational variations (Spada et al., 2013). Hence they are characterized by a very smooth global pattern, with their marked zonal symmetry reflecting the dipole pattern of TIM sources.

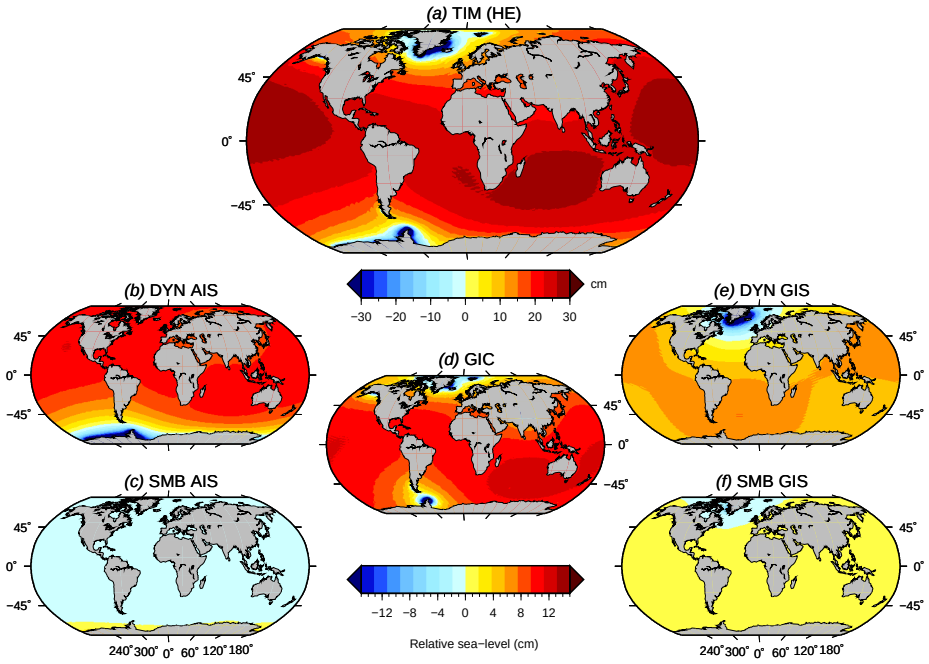

Figure 1.11: Global TIM relative sea–level fingerprints to 2040–2050 relative to 1990–2000, according to the HE scenario in Spada et al. (2013). The total component in (a) is split into individual contributions in (b–f).

Chapter 2

Global mean sea level during the last century

Although the analysis of sea level spatial variability is acquiring a growing role, the assessment of the long–term global mean sea level rise (GMSLR), has been and continues to be of great importance. In fact, ocean–averaged sea level changes directly provide information on the net mass variations of continental ice masses (see *e. g.* Spada et al., 2012) and ocean-water density variations, which cannot be inferred by regional sea level observations.

Tide gauges (TGs) have been historically employed to monitor sea level rise. Although the sparse distribution of TGs and local movements of tectonic and glacio–isostatic origin may hinder a precise evaluation of spatial averages, starting from the first decades of last century considerable attention has been paid to the assessment of long–term GMSLR from instrumental records. of Spada and Galassi (2012).

2.1 Global mean sea level previous studies

Since the seminal work of Gutenberg (1941), various GMSLR estimates have been produced, essentially based on the global TG records now supplied by the Permanent Service for Mean Sea Level (PSMSL). The available estimates obtained from TG observations are presented in Table 2.1, which also shows the period of observation and basic information on the methods employed to estimate the GMSLR (hereafter abbreviated by μ). From Fig. 2.1a, showing the chronological sequence of the estimates, it is apparent that an increased interest into the sea level rise problem took place in the early 1980s, motivated by the awareness of the possible effects of greenhouse gases on the Earth climate (Gröger and Plag, 1993). Figure 2.1b indicates that most of the studies are referred to the period 1900–1990, apparently reflecting a decreased interest in TGs observations after the introduction of satellite altimetry methods in the early 90's.

Traditionally, GMSLR is determined by a mean rate of sea level change, which can be either based on trends at individual TGs extracted from a global database (*e. g.* Gornitz and Lebedeff

1987; Cabanes et al., 2001) or, alternatively, on regional averages (*e. g.* Gutenberg, 1941; Holgate and Woodworth, 2004). Following the work of Barnett (1990), empirical orthogonal functions (EOF) have been widely employed to study the spatial pattern of global sea level change, while the use of spherical harmonics analysis (SHA) appears to be limited to the study of Nakiboglu and Lambeck (1991). As shown in the last column of Table 2.1 , different approaches have been adopted to correct the TG observations from the effects of GIA. Before global GIA models were introduced in this context by Peltier and Tushingham (1989), sea level trends obtained from TG observations were often corrected by GIA trends extrapolated by geological sea level records (Gornitz et al., 1982; Gornitz and Lebedeff, 1987), or not corrected at all. Since the 1990s, due to continuous models refinement, GIA corrections have been routinely applied, usually based on the ICE–3G model of (Tushingham and Peltier, 1991) and subsequent versions. Recently, non-traditional techniques (neural networks) have been employed to determine GMSLR (Wenzel and Schröter, 2010). The application of a GIA correction is, in this case, unnecessary.

Though all estimates in Table 2.1 neatly point to a globally averaged sea level rise and their central values are generally in the range between 1 and 2 mm yr^{-1} (see also Fig. 2.1b), their distribution shows a significant spread. It is remarkable that according to some authors (Pirazzoli, 1986; Stewart, 1989; Emery et al., 1991; Gröger and Plag, 1993) the significance of a global sea level mean is doubtful, mainly because of the large spatial variations of the TG signals, the poor geographic distribution of the stations and various contaminating effects such as crustal deformations associated with GIA. The introduction of GIA corrections, based either on geological observations or on direct modeling, and the adoption of rigorous selection criteria for the TGs (Douglas, 1991) contributed significantly to enlighten the coherence of the TG observations and to better constrain GMSLR. Furthermore, since the early 1990s, all the proposed GMSLR values have been supplied with an uncertainty estimate, though only in some of the works listed in Table 2.1 is it possible to ascertain its statistical significance (this is a major issue when some fundamental problems as the closure of the sea level budget are addressed, see *e. g.* Peltier 2009). The spread of the μ values in Table 2.1 is the consequence of a number of factors that may prevent direct comparisons among the outcomes of these analyses, though all of them are ultimately based on TG data. The most important include: (i) the different criteria adopted to select the TGs which are supposed to be suitable for the determination of μ, (ii) the nature of the data considered (*i. e.* monthly or annual means) and possible quality constraints (*e. g.* the exclusion of data that do not meet the PSMSL Revised Local Reference (RLR) requirements), (iii) possible pre–processing of the TG time–series (*e. g.* the application of moving averages to attenuate the noise level or to smooth decadal fluctuations), (iv) the length of the time period of observation considered (in Table 2.1 it ranges between 16 and 189 years) and the details of averaging procedure employed to obtain μ, and finally (v) the effective application of GIA corrections to the sea level trends and the particular GIA model employed to perform the corrections. All these factors motivate the statement of Pirazzoli (1993), that is, that a simple assessment of GMSLR is not possible, though subsequent studies in Table 2.1 have shown that improvements in the robustness of the assessments are certainly not precluded.

The fundamental issue of the selection of the most appropriate TGs for global sea level analysis has been addressed by virtually all the authors listed in Table 2.1. Though it is clear that the quality

Table 2.1: Review of previous estimates of the rate of GMSLR published since 1941 (data are displayed in Fig. 2.1). Similar summary tables are found in Pirazzoli (1993), Gröger and Plag (1993), Gornitz (1995) and Douglas (2001).

Year and Author(s)	μ^a (mm yr^{-1})	Period^b	Method(s)^c	GIA correction^d
1941 Gutenberg	1.1 ± 0.8	1807–1937	RA	no
1952 Polli	1.1	1871–1940	RA	no
1952 Cailleux	1.3	1885–1951	SA	no
1952 Valentin	1.1	1807–1947	-	no
1958 Lisitzin	1.1	1807–1943	-	no
1962 Fairbridge and Krebs	1.2	1900–1950	SA	no
1974 Lisitzin	1.1 ± 0.4	20th century	SA	no
1978 Kalinin and Klige	1.5	1860–1960	SA	no
1980 Emery	3	1850–1958	SA	no
1982 Gornitz et al.[1]	1.2	1880–1980	RA	no
" "	1.0	1880–1980	RA	geological
1984 Barnett^a	$1.4 \pm 0.1^\dagger$	1881–1980	EOF, RA	no
" "	$2.3 \pm 0.2^\dagger$	1930–1980	EOF, RA	no
1987 Gornitz and Lebedeff	0.6 ± 0.4	1880–1982	SA	geological
" "	1.7 ± 0.3	1880–1982	SA	geological
" "	1.2 ± 0.3	1880–1982	SA	geological
" "	1.0 ± 0.1	1880–1982	RA	geological
1989 Peltier and Tushingham	$2.4 \pm 0.9^*$	1920–1970	EOF	presumably ICE–3G
1986 Pirazzoli	indeterminable	1807–1984	–	–
1989 Stewart	indeterminable	20th century	–	–
1990 Barnett	$1.5 \pm 0.2^*$	1903–1969	EOF	no
1990 Trupin and Wahr	$1.75 \pm 0.13^\dagger$	1900–1979	SA	no
1991 Nakiboglu and Lambeck	1.15 ± 0.38	1820–1990	SHA, RA	ANU models
1991 Douglas	$1.8 \pm 0.1^\dagger$	1880–1980	SA	ICE–3G
1991 Emery et al.	indeterminable	1807–1996	–	–
1992 Shennan and Woodworth	$1.0 \pm 0.15^*$	1901–1988 Eu	SA	geological
1993 Gröger and Plag	indeterminable	1807–1992	–	–
1995 Mitrovica and Davis	1.1–$1.6^\dagger$	1880–1990	SA	ICE–3G
1995 Unal and Ghil	$1.6 \pm 0.4^*$	1807–1990	RA	ICE–3G
1996 Davis and Mitrovica	1.5 ± 0.3	1856–1995 USE	SA	ICE–3G
1996 Peltier	$1.94 \pm 0.56^*$	1920–1970 USE	EOF	ICE–4G
1996 Peltier and Jiang	$1.8 \pm 0.6^*$	1856–1995 USE	SA	ICE–4G
1997 Douglas	1.8 ± 0.1	1880–1980	SA	ICE–3G
2001 Cabanes et al.	1.6 ± 0.15	1955–1996	SA	no
2001 Church et al.	$1.0 - 2.0$	20th century	APE	various models
2001 Peltier	$1.84 \pm 0.35^\dagger$	1880–1980	RA	ICE–4G(VM2)
2001 Mitrovica et al.	$1.5 \pm 0.1^*$	1880–2000	SA	no
" "	$1.8 \pm 0.1^*$	1880–2000	SA	ICE–3G
2004 Church et al.	$1.8 \pm 0.3^*$	1950–2000	EOF	ICE–4G(VM2), L, M
" "	$1.75 \pm 0.10^*$	1950–2000	EOF	ICE–4G(VM2)
" "	$1.89 \pm 0.10^*$	1950–2000	EOF	L
" "	$1.91 \pm 0.10^*$	1950–2000	EOF	M
2004 Holgate and Woodworth	1.7 ± 0.20	1948–2002	RA	ICE–4G
2005 Nakada and Inoue	1.5	20th century	SA	no
2006 Church and White	1.7 ± 0.30	20th century	EOF	ICE–4G(VM2), L, M
" "	1.71 ± 0.40	1870–1935	EOF	ICE–4G(VM2), L, M
" "	1.84 ± 0.19	1936–2001	EOF	ICE–4G(VM2), L, M
2007 Bindoff et al.	1.8 ± 0.5	1961–2003	APE	various models
" "	1.7 ± 0.5	20th century	APE	various models
2007 Hagedoorn et al.	$1.46 \pm 0.20^\dagger$	20th century	RA	ICE–3G
2010 Wenzel and Schröter	1.56 ± 0.25	1900–2006	NN	ICE–5G(VM4)
2011 Church and White	1.7 ± 0.2	1900–2009	EOF	as in Church et al. (2004)
" "	1.9 ± 0.4	1961–2009	EOF	" "
" "	2.8 ± 0.8	1993–2009	EOF	" "

(^{a}) When made explicit by the Authors, a star ($*$) denotes *sdom* (see Equation 2.7), a dag (†) *rms* (Equation 2.6).
(^{b}) Global data are used, unless otherwise stated (Eu=Europe, USE=United States East coast).
(^{c}) RA=Regional Average, SA=Simple average from individual TGs, EOF=Empirical Orthogonal Function, SHA=Spherical Harmonics Analysis, APE=Average of Previous Estimates.
(^{d}) If one is applied, the model is indicated. Geological corrections are based on Holocene RSL curves. L and M denote models developed by K. Lambeck and J. X. Mitrovica (see Church et al. 2004).
(^{1}) The three SA estimates are based on different selections of TGs.

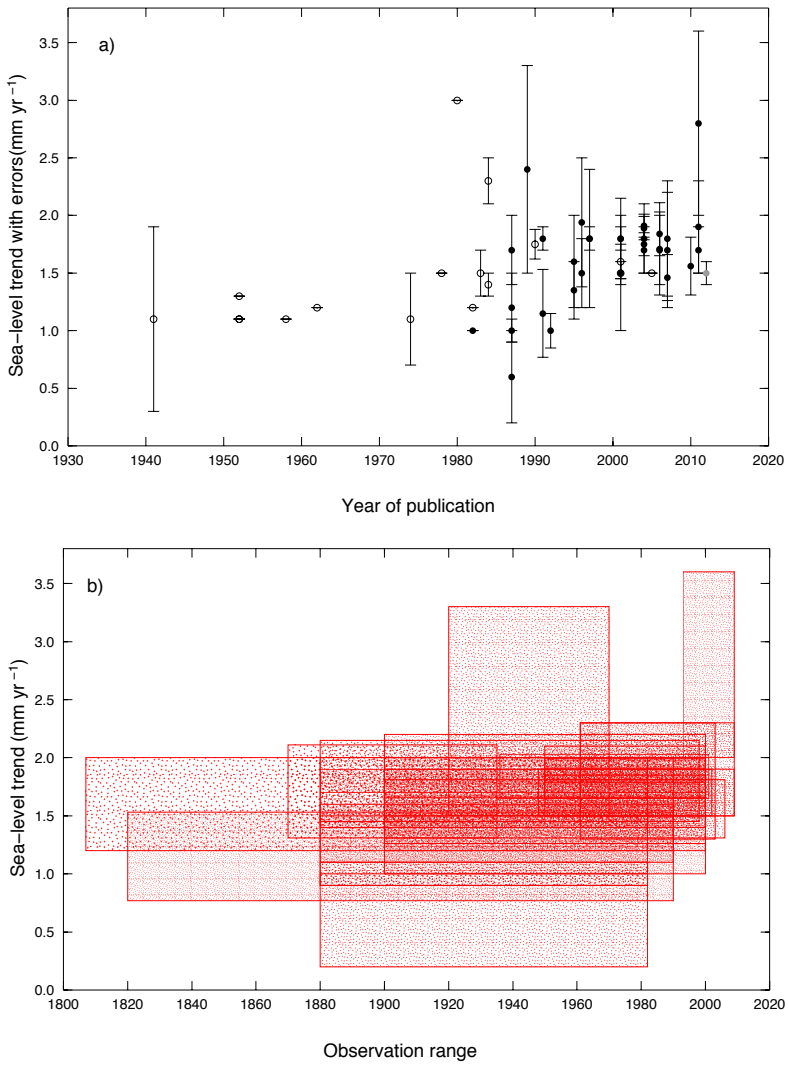

Figure 2.1: (a) GMSLR estimates from TG data according to previous authors (see list in Table 2.1). GIA–corrected and uncorrected estimates are shown by solid and open circles, respectively. (b) GMSLR estimates proposed in the literature based on the analysis of TG observations. The extent of each rectangle shows the time period considered for each estimate, while its width shows its uncertainty. Among the GMSLR estimates considered in (a), only those corrected by GIA are considered in (b).

of the trend estimate will increase with the record length, the minimum length has never been unequivocally determined. As pointed by Douglas (2001), this is certainly one of the fundamental reasons of the disagreement between the various estimates of μ proposed so far. The rule of thumb proposed by Sturges and Hong (2001) suggests that to determine meaningful statistics about sea level trend, the length of the time series should be comparable to ~ 10 times the period of the characteristic decadal oscillation. Since these are of the order of ~ 20 years (Sturges and Hong, 2001), a rigorous application of this rule would reduce the number of appropriate TGs to a few units. It is now accepted that records as short as a few decades are not appropriate for the estimate of GMSLR However, in some of the studies of Table 2.1, short records have been effectively employed. Perhaps not coincidentally, when this is done (see *e. g.* Emery, 1980, who employed records with a span as short as a few decades), the value of GMSLR obtained (3 mm yr^{-1}) clearly represents an outlier in the population of the estimates. Starting from the work of Peltier and Tushingham (1989), it has been realized that a satisfactory trade–off between the length and the number of records can be obtained for records of 50 years or longer. In the two possibly most influential papers published during the last two decades, this minimum number has been set to 60 (Douglas, 1991) and 70 (Douglas, 1997), respectively (in the following this last study will be referred to as D97). The minimum record length is, however, only one of several important criteria useful for estimating GMSLR from TG data. According to Douglas (1991), the time series must *1)* be at least 60 years in length, *2)* be obtained from TGs sufficiently distant from collisional tectonic boundaries, *3)* have a sufficient completeness ($> 80\%$), *4)* be in reasonable agreement with nearby records at low frequencies, and *5)* not belong to previously ice–covered areas during the Last Glacial Maximum (LGM) ~ 21 kyrs ago to avoid GIA contamination. Criterion *5)* has been subsequently extended by D97, to exclude the TG sites from the peripheral bulge adjacent to these areas (the D97 criteria are summarized in the left part of Table 2.3 below). Applying the above criteria, D97 has used trends from 23 PSMSL TGs (listed in Table 2.2 below) for the time period 1880–1980 to determine a GMSLR of $\mu' = 1.8 \pm 0.1$ mm yr^{-1}, where the prime indicates that a GIA correction has been applied (based, in this case, on model ICE–3G of Tushingham and Peltier, 1991) and the uncertainty denotes the standard deviation of the mean.

Although those proposed by D97 probably constitute the "best possible" criteria for the selection of TGs useful to the assessment of GMSLRs, a couple of caveats are apparent. First, the requirement *2)* (distance from collisional tectonic boundaries) is motivated by the possible contamination of the TG signals that could result from vertical movements (and geoid height variations) at subduction zones. However, from forward modeling we know that vertical movements are also possible in transcurrent tectonic environments (*e. g.* Nostro et al., 1999). Since the D97 set contains a significant number of TGs located along the North American West Coast, the assessment of GMSLR could be affected, by an unknown amount, by tectonic deformations. It is unclear whether tectonic contributions in this region have been accurately accounted for (or totally neglected) in previous studies. As pointed by Nakada and Inoue (2005), it is likely that the tectonic trends at the TG of San Francisco (traditionally included in most of previous studies for its considerable record length and completeness), have changed as a consequence of the co–seismic deformation associated with the 1906 M=8.3 earthquake. This issue could be resolved, in principle, by modeling

efforts aimed at estimating the co– and post–seismic displacements associated with the seismic cycle. However, the episodic nature of the earthquake energy release and possible viscoelastic effects could potentially prevent the assessment of a meaningful tectonic sea level trend at TGs (Nakada and Inoue, 2005). The second caveat concerns criterion *5)* of D97, *i. e.* the exclusion of TG stations strongly affected by GIA in the regions previously covered by the ice during the LGM and at their immediate periphery. According to D97, the motivation for the exclusion essentially resides in the difficulties inherent in the calculation of the GIA correction. The main reason to avoid sites on the peripheral bulge was that the response of such sites is strongly dependent on lower mantle viscosity, and that with a change in this viscosity one could reduce the systematic trends in tide gauge rates along the US east coast (Davis and Mitrovica, 1996). Using model ICE–3G, D97 argued that since the correction at some sites can be comparable with the value of GMSLR a–posteriori assessed, even a relatively small error in the evaluation of the correction could impact the assessment. A problem with this approach is that different GIA models will provide different spatial uplift patterns, according to the viscosity profiles assumed and to the spatiotemporal details of ice melting (*e. g.* Nakada and Lambeck, 1987). As we will discuss in the body of the manuscript, since the geometry of the forebulge region is sensitive to the choice of the GIA model, the selection criterion *5)* will be affected accordingly. The *a–priori* exclusion of the TGs located in previously ice–covered areas certainly represents a conservative approach when a unique GIA model is considered, as it is the case for D97. However, this could entail an unmotivated rejection of long and sufficiently complete records, like those located in the northern European regions.

2.2 TG data and uncorrected GMSLR estimates

2.2.1 TG observations

In this work, we employ observations obtained from the PSMSL (see Chapter 1 for details): data have been extracted from database on February 9, 2011. Only data resulting from at least eleven months are considered for the computation of sea level trends.

The distribution of the 1213 sites provided TG time series including at least three yearly records since year 1880, hereafter referred to as the "ALL set", is shown in Fig. 1.1. Figure 2.2 shows the location of the 23 D97 TGs, and the corresponding RLR annual records are shown in Fig. 2.3. For consistency with Douglas (1991) and D97, here we will only employ observations available since year 1880. Furthermore, following the suggestions of PSMLS, for our estimates we will rigorously consider only RLR observations. Apparently, no distinction between RLR and metric data has been made in D97.

In Fig. 2.3, the average sea level is subtracted before plotting and a constant shift of $+150$ mm has been applied for visualization purposes. No smoothing has been performed, nor attempts to cure the gaps in the time series (we note that for some of them the problem of gaps is particularly severe, as for Dunedin II, in New Zeland). Although obviously we do not expect that an extended record, when available, would dramatically modify previous results of D97, the extension is in some case significant – *e. g.* Balboa, Central America – and sometimes characterized by steep

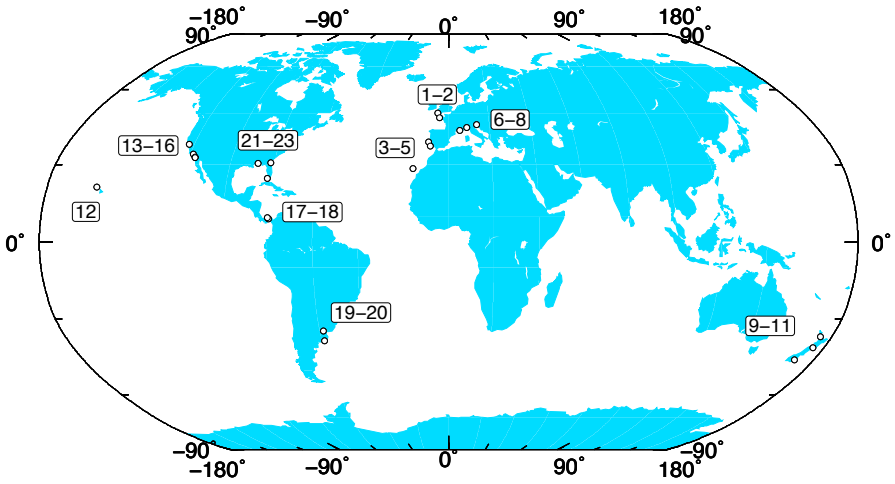

Figure 2.2: Distribution of tide gauges belonging to the D97 set.

slope variations, as in the case of Trieste. Thus, the overall effect of these recent observations upon the long–term sea level trends is, in our opinion, worthy of investigation.

Despite the large annual (Willis et al., 2008), decadal and inter–decadal fluctuations (Sturges and Hong, 2001), the D97 time series shown in Fig. 2.3 coherently denote a long–term sea level rise. The spatial coverage of this specific subset of TGs, shown in Fig. 2.2, strongly suggests that sea level rise is indeed global, though characterized by regional variations that can be partly attributed to the effects of GIA. As noted by Douglas (1991) and D97, separating short–term fluctuations from the low–frequency variations is a difficult task, and even simple visualization of the time series may be problematic without the aid of low–pass filters (*e. g.* moving averages). The fundamental reason is that TG records are characterized by a red spectrum, in which power continues to increase out to the low frequencies (Sturges and Hong, 2001). Hence, establishing the amplitude of long–term sea level variations from time series with periods of a few decades can be particularly problematic. Noise reduction (see *e. g.* Rompelman and Ros, 1986), can be realized by a technique often employed in seismology and known as "stacking" (Gilbert and Dziewonski, 1975). Stacking has been used by Trupin and Wahr (1990) to study the 18.6 year lunar tide and the 14–month pole tide using TG records; here this method is adopted to visualize the low–frequency component of sea level rise.

In Fig. 2.4a, the 23 TG time series shown in Fig. 2.3 have been stacked in an attempt to reduce the signal to noise ratio and to visualize qualitatively the overall coherence of the datum at different epochs. Before stacking, the average has been subtracted by each series, but no smoothing has been applied. The stack shows no apparent sea level rise between 1880 and 1900, when only a few stations were in operation (namely, Genova, Marseille, Brest, Cascais, Fernandina and San Fran-

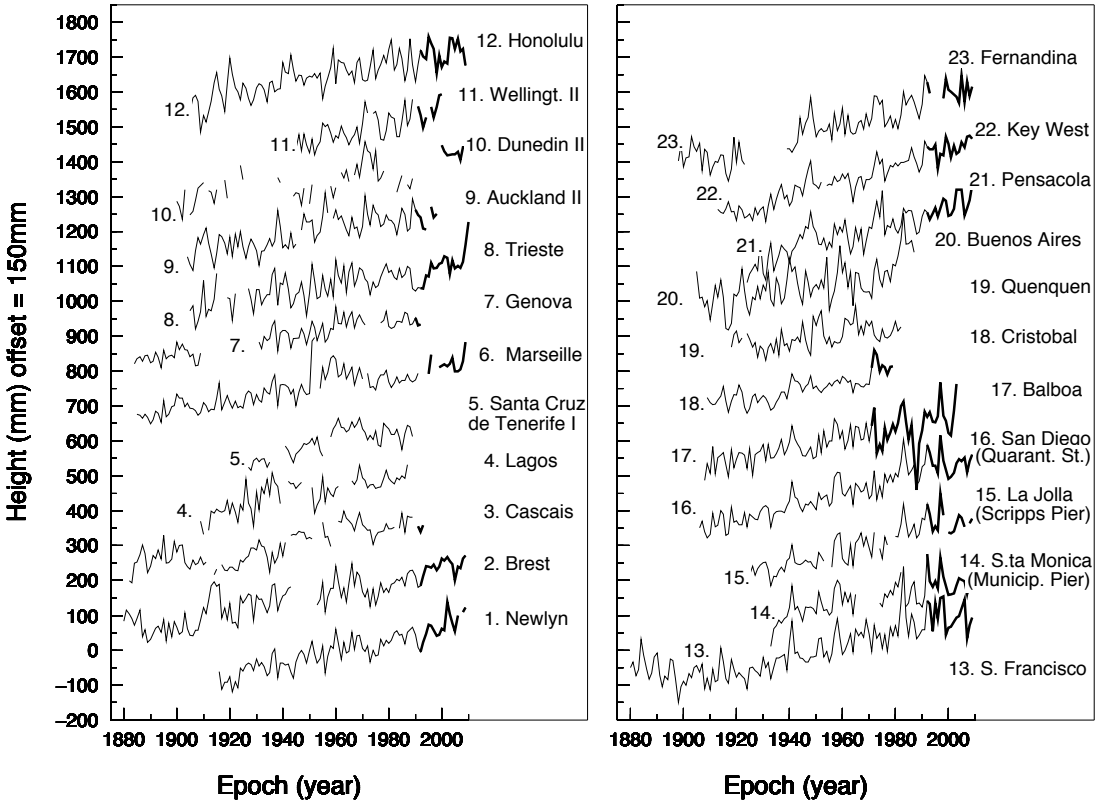

Figure 2.3: RLR annual time series for tide gauges located in the regions of the English Channel (1–2), Atlantic (3–5), Mediterranean Sea (6–8), New Zeland (9–11) and the Pacific (12) (left frame) and for the North American West Coast (13–16), Central America (17–18), South America (19–20), and SE North America (21–23) (right frame), according to the selection of D97. Thick segments at the tip of some of the time series mark yearly observations that were not available when D97 was published.

cisco). This supports previous observations of Nakada and Inoue (2005), indicating that modern sea level rise probably corresponded to the onset of the industrial revolution, approximately 100 years ago. Support of this hypothesis is provided by observations based on TG time–series not belonging to the D97 set (*e. g.* Swinoujscie, along the southern coast of the Baltic Sea), though this datum is not consistent with that of nearby sites. Starting from $\sim$ 1905, RLR records from the sites of Trieste, Honolulu, San Diego and Buenos Aires become available. After a few years, a coherent signal is neatly emerging from the stack of Fig. 2.4a, and is maintained until present time, apparently unaffected by the systematic decrease in the number of operating TGs (and/or the number of available RLR observations) since the early 1980s. Fig. 2.4a suggests that to observe a globally coherent sea level rise, a minimum number of $\sim$ 10 high–quality TG stations is required, providing a sufficient geographical coverage. This is consistent with previous studies (*e. g.* D97), in which sea level trends from the 23 stations have been grouped on a regional basis, practically reducing the number of time series down to nine. We note that a very limited set of TGs (7) has also been considered by Nakada and Inoue (2005), in view of their very long record. Though from their Fig. 1 it is clear that the geographical coverage is poor, their estimate of the 20th GMSLR (1.5 mm yr^{-1}), has been found to be largely consistent with other studies based on the D97 set. The effectiveness of stacking in reducing the signal to noise ratio is apparent when we compare Fig. 2.4a with individual TG series in Fig. 2.3. In the stack, the peak–to–peak amplitude of decadal and inter–decadal oscillations is reduced by a factor of $\sim$ 3, leaving a low–frequency signal that does not seem to indicate, at least visually, any acceleration since the beginning of last century (Woodworth, 1990).

In Fig. 2.4b, all the TGs with a minimum number of three yearly records are considered (ALL set). Clearly, in this case we end up with a more noisy stack as a consequence of the variegate and largely incoherent time series that we are averaging. However, as soon as the number of operating TGs sharply increases to $\sim$ 200 at the beginning of the 30s, a coherent sea level rise can be discerned. The detection of similar "change points" in the time series of sea level change is a particularly challenging problem, which has also been recently addressed by Kemp et al. (2011) on the millennium time scales. On the secular scale, it is known that abrupt variations could be associated with transients that do not imply an effective change of the long–term sea level rise. This is illustrated by Sturges and Hong (2001) for the case of the records at New York and Charleston, which suggest an apparent increase in the rate of rise beginning in the late 20s. As previously pointed by Sturges (1990), it is very difficult to argue for any statistically significant change in sea level trend in the 20s, since the energy in the multi–decadal fluctuations at periods between 40 and 50 years prevents robust assessments. We also note that Church and White (2006) have suggested 1930 as the point in which the slope of sea level trend abruptly changes, implying an acceleration, and that Donnelly et al. (2004) detected an increased sea level rise to modern values in the late 19th century, roughly coincident with the climate warming observed in both instrumental and proxy records. Clearly, the matter of possible change points in the instrumental sea level record is not settled. Beside this, the results of Fig. 2.4 show that an assessment is possible from the analysis of a limited number of coherent and sufficiently long TG time series, also satisfying specific additional requirements. This is consistent with Douglas (2001), who observed that the detection of sea level

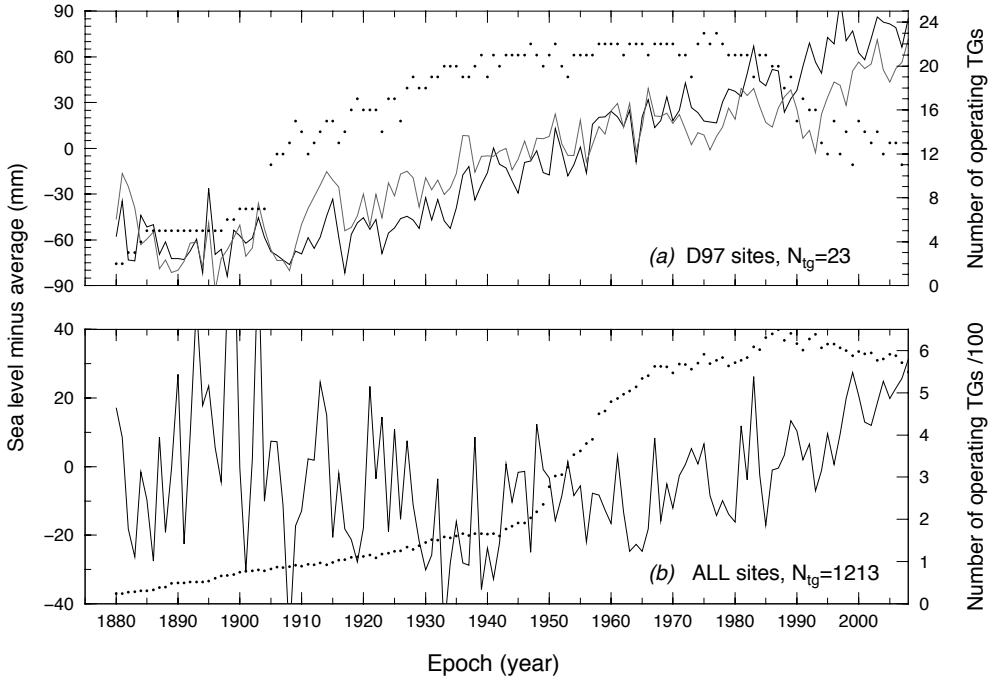

Figure 2.4: (a) Stack of the 23 time series belonging to the D97 set (see Fig. 2.3). The gray shaded curve shows the stack for the 22 time series belonging to the SG01 set, introduced in subsection 2.4.1. (b) Stack for the time series of the ALL set (with at least 3 valid years in the series). Dotted curves show the number of TGs that, at a given epoch, are operating and provide RLR sea level observations according to the PSMSL record (see second *y* axis).

variation by TGs is indeed feasible by means of a few long records, which do not demand the dense coverage of short ones to establish a globally coherent signal. However, contrary to the pessimistic point of view of previous investigators (see *e. g.* Pirazzoli 1986 and Gröger and Plag 1993), Fig. 2.4b shows that it can be also be qualitatively observed from consideration of a sufficiently large number of globally distributed instruments with by a relatively short observation periods.

2.2.2 Sea–level trend at TGs

Previous estimates of GMSLR have relied upon rates of sea level change over a specific time period, computed for individual TGs or groups of TGs (see Table 2.1). Consistent with the guidelines of previous investigations, to extract the background sea level trend from the records, we will use a simple linear regression. Differently from Douglas (1991) and D97, however, we do not start from monthly data and we do not perform any filtering on the time series in order to reduce the

amplitude of decadal cycles. Rather, following Sturges and Hong (2001), we seek a good estimate of long–term trends adopting a "pencil and ruler" approach directly to annual (RLR) observations. This approach is motivated, *a posteriori*, by the consistency of our (GIA–uncorrected) results with D97. Furthermore, since in this Section we are not concerned with possible sea level accelerations (Woodworth, 1990; Douglas, 1992) or decelerations (Houston and Dean, 2011), a constant sea level trend is assumed.

Using basic statistics (see *e. g.* Taylor 1997), the rate of sea level change for the k–th tide gauge is computed by

$$r_k = \frac{N_k^v \sum_j x_j y_j - \left(\sum_j x_j\right)\left(\sum_j y_j\right)}{N_k^v \sum_j x_j^2 - \left(\sum_j x_j\right)^2}, \tag{2.1}$$

where $k = 1,\ldots,N_{tg}$, N_{tg} is the number of TGs considered, y_j is sea level at the year x_j ($j = 1,\ldots,N_k^v$), N_k^v is the number of valid annual records, and $\sum_j$ stands for $\sum_{j=1}^{N_k^v}$. The values of x_j and y_j are directly obtained from the annual RLR PSMSL record. At this stage, no GIA corrections are performed on the annual data nor on the trends computed by Equation 2.1. The formal uncertainty on the computed rate of sea level change is determined building a 95% confidence interval for r_k. This is done by evaluating

$$\sigma_k = \frac{SEE_k}{\sqrt{\sum_j (x_j - \bar{x})^2}}\, t_{0.975,\nu_k}, \tag{2.2}$$

where $\bar{x}$ is the average of the x_j's and $t_{0.975,\nu_k}$ is the 0.975–th quartile of Student's t–distribution with $\nu_k = N_k^v - 2$ degrees of freedom (henceforth, we will only consider TG series with $N_k^v \geq 3$). In Equation 2.2, the standard error of the estimate is defined as the *rms* of the deviations

$$SEE_k = \sqrt{\frac{\sum_j (y_j - y_j^{est})^2}{\nu_k}} \tag{2.3}$$

(Zar, 2010). We note that the uncertainties on the trends evaluated by Douglas (2001) (see his Equation 1) do not define a confidence interval, though they are found to be basically comparable to those obtained by Equation 2.2). Hence after, to properly account for uncertainties on the rates r_k, the rate of sea level change is expressed by

$$\rho_k = r_k \pm \sigma_k, \tag{2.4}$$

with r_k and σ_k given by Eqs. 2.1 and 2.2, respectively. We note that in previous relevant studies (*e. g.* Douglas 1991 and D97), the uncertainties on the computed trends σ_k have not been considered explicitly in the analysis. It is however clear that they have an important role, since they can be used as weighting factors in the assessment of the uncertainties of GMSLR (see *e. g.* Mitrovica et al. 2001 and our Equation 2.8).

The basic statistics of the TG trends are shown in Fig. 2.5. Mainly because here we dispose of a larger number of RLR observations (there are 1213 TGs with with a minimum number of yearly

records $N^v_{min} \geq 3$), details of this figure differ somewhat from similar plots presented in previous studies (see *e. g.*, Figs. 3.1 and 3.11 of Douglas 2001). Their main features, however, are largely reproduced. The distribution of N^v_k, shown in Fig. 2.5a, appears to be bimodal, with the maximum for $N^v_k \approx 15$ and a secondary peak for $N^v_k \approx 45$. This last feature, unnoticed by Douglas 2001, is due to the increased rate of installation of TGs immediately after the end of the Second World War. The cumulative distribution, shown by a stairs–step histogram in Fig. 2.5a, indicates that most of the time series (90%+) are less than ~ 60 years long, which makes the assessment of the secular sea–level trend particularly problematic (the reason is explained by Sturges 1990), also in view of the their uneven spatial coverage (see Douglas, 2001, and Fig. 1.1 above). The rates of sea–level change obtained by least–squares fitting of the time series, shown in Fig. 2.5b, are largely scattered, thought visually it can be appreciated that they are not symmetrically distributed across zero, even for relatively small values of N^v_k. Neatly positive r_k values are shown for most of the longest series ($N^v_k \geq 60$), but the values are scattered significantly. Uncertainties σ_k, shown in Fig. 2.5c, neatly decrease with N^v_k. However, relatively precise r_k values, with error levels $\sigma_k \leq 0.1$ mm yr^{-1} can only be obtained from some of the time series with $N^v_k \geq 85$, as marked by the dotted horizontal line.

For reference, the ρ_k values for the D97 set are listed in Table 2.2. The locations of these sites are shown in Fig. 2.2. Following Mitrovica et al. (2001), the site of Lyttelton (New Zealand), is not considered because its rate is inconsistent with those at nearby sites. Rates are rounded to the first significant digit since it is our opinion that a more precise evaluation is not possible given the noise level of TG observations. It should be remarked, however, that some of the previous estimates of GMSLR are given with two significant digits, see Table 2.1. Rates of sea–level change for the D97, computed since 1880, are all neatly positive and coherently concur to indicate a sea–level rise of about 1.5 mm yr^{-1}, consistently with the stack in Fig. 2.4a. Our computations in Table 2.2, based on Eqs. 2.1 and 2.2, are generally consistent with those of D97. Some of the discrepancies can be attributed to our choice of not pre–processing the observations by a low–pass filter before computing the trends and possibly to different details of the statistical regression adopted to evaluate the trends r_k; some others to the significantly extended RLR record that is currently available for some specific TGs, as shown in Fig. 2.3. In the case of Balboa (Central America), the period of the currently available RLR observations exceed by more than thirty years the one considered by D97, but the two rates do not differ significantly. However, a significant discrepancy with D97 can be observed for the nearby site of Cristobal. Inspection of the annual data for this site, shown in Fig. 2.3, reveals that the cause is a sea–level rise of ~ 10 cm that occurred between 1970 and 1972, which has altered significantly the slope of the best fitting line over the whole time period of observation.

Table 2.2: Computed rates of sea–level change for the D97 set, compared with those determined by D97. The average span of the time series is 95 years (in D97 it was 83 years), while the average number of valid yearly RLR records in each series is 88 years. Note that in D97, uncertainties on the individual trends r_k were not provided. The average completeness c_k of the time series for these TGs (*i. e.*, the average of the ratio N_k^v/span_k) is 92%. According to our computations, for this set of TGs the GMSLR is $\mu = 1.6 \pm 0.1$ mm yr^{-1} (*rms*=*wrms*=0.4 mm yr^{-1}). For reference, GIA corrections corresponding to model ICE–3G are shown in the last column. The sixteen TG sites marked by a star also belong to the D97R set.

Region	Tide gauge site	Period year–year	span_k years	N_k^v years	r_k (D97[a]) mm yr^{-1}	$\rho_k = r_k \pm \sigma_k$ mm yr^{-1}	r_k^{gia} mm yr^{-1}
English Channel	1 Newlyn*	1916–2009	94	93	1.7	1.8 ± 0.1	+0.2
	2 Brest*	1880–2009	130	121	1.4	1.4 ± 0.1	+0.2
Atlantic	3 Cascais*	1882–1993	112	101	1.3	1.3 ± 0.1	−0.2
	4 Lagos*	1909–1987	79	69	1.5	1.4 ± 0.2	−0.2
	5 S. C. Tenerife I*	1927–1989	63	56	1.5	1.6 ± 0.2	−0.0
Mediterranean	6 Marseille*	1885–2009	125	119	1.2	1.2 ± 0.1	−0.1
Sea	7 Genova*	1884–1996	113	85	1.2	1.2 ± 0.1	−0.2
	8 Trieste*	1905–2010	106	100	1.2	1.3 ± 0.1	−0.2
New Zeland	9 Auckland II*	1904–1998	95	92	1.3	1.3 ± 0.1	−0.4
	10 Dunedin II*	1900–2009	110	64	1.4	1.2 ± 0.1	−0.4
	11 Wellington II*	1945–2000	56	53	1.7	2.0 ± 0.3	−0.5
Pacific	12 Honolulu*	1905–2009	105	105	1.5	1.5 ± 0.1	−0.2
North American	13 San Francisco	1880–2009	130	130	1.5	1.6 ± 0.1	−0.1
West Coast	14 Santa Monica[b]	1933–2009	77	67	1.4	1.4 ± 0.2	−0.2
	15 La Jolla[c]	1925–2009	85	78	2.1	2.1 ± 0.1	−0.3
	16 San Diego[d]	1906–2009	104	101	2.1	2.1 ± 0.1	−0.2
Central America	17 Balboa*	1908–2003	96	95	1.6	1.5 ± 0.1	−0.2
	18 Cristobal*	1909–1979	71	71	1.0	1.4 ± 0.1	−0.2
South America	19 Quequen*	1918–1982	65	64	0.8	0.9 ± 0.2	−0.1
	20 Buenos Aires*	1905–1987	83	83	1.5	1.6 ± 0.2	−0.5
South East	21 Pensacola	1924–2009	86	84	2.2	2.2 ± 0.2	−0.1
North America	22 Key West	1913–2009	97	96	2.2	2.3 ± 0.1	−0.1
	23 Fernandina	1898–2009	112	91	1.8	2.0 ± 0.1	−0.0

[a] Reproduced from Table I of Douglas (1997)
[b] Municipal Pier
[c] Scripps Pier
[d] Quarantine Station.

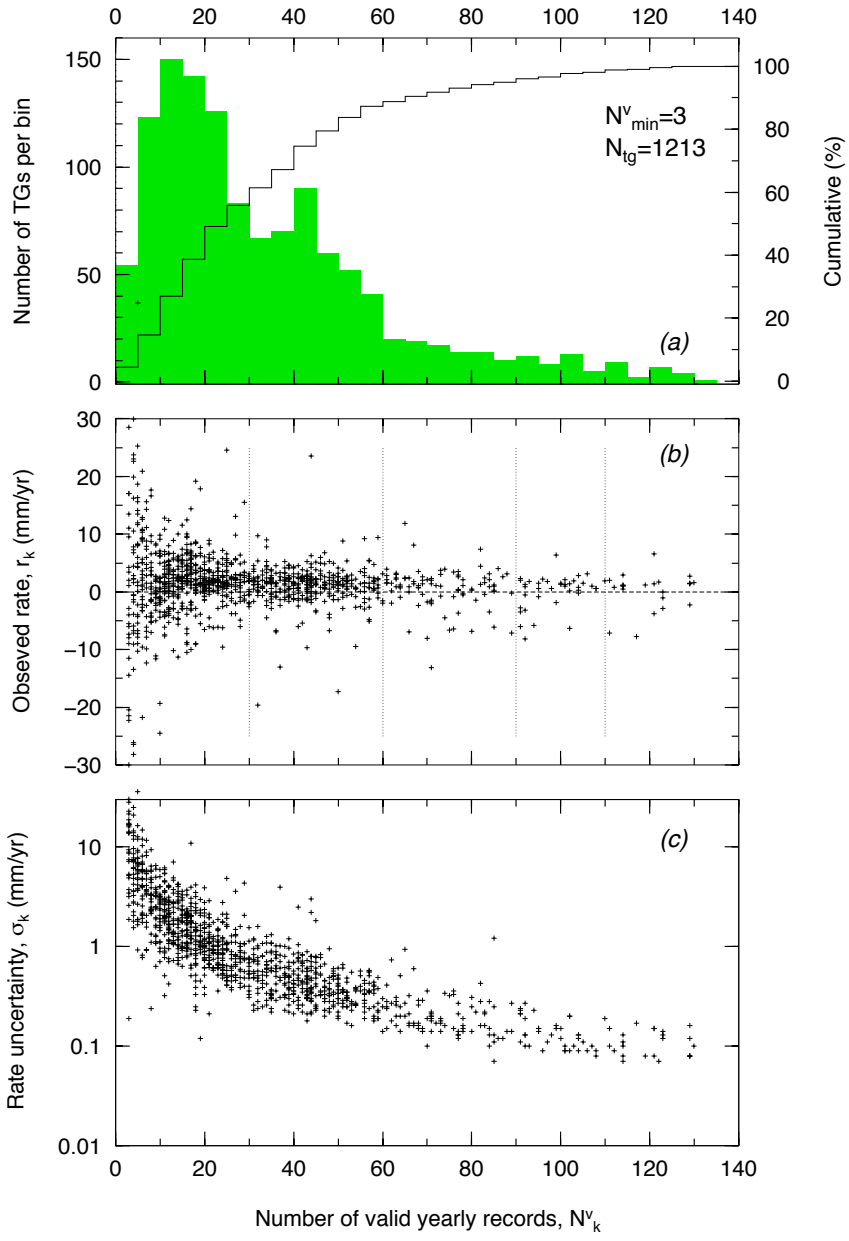

Figure 2.5: Distribution of the number of tide gauges N_{tg} (a), of the observed rates of sea–level change r_k (b) and of their uncertainties σ_k (c) as a function of the number of valid records N_k^v in each time series. Dashed segments in (b) show the ranges of N_{min}^v values considered in Fig. 2.7. Only TGs belonging to the ALL set ($N_{min}^v \geq 3$) are considered.

In the following, we will often consider trends of sea–level change obtained from subsets extracted from the whole set of available RLR time series, containing a minimum number of yearly observations or obeying more articulated criteria, as those adopted by D97. In both circumstances, to characterize the rate of GMSLR obtained from a subset composed by a number N_{tg} of TGs, each providing a rate of sea–level change $\rho_k = r_k \pm \sigma_k$, the "best estimate" of GMSLR will be computed by the arithmetic mean

$$g = \frac{1}{N_{tg}} \sum_k r_k, \tag{2.5}$$

where r_k is obtained by Equation 2.1, and $\sum_k$ stands for $\sum_{k=1}^{N_{tg}}$. Others, like Gröger and Plag (1993) preferred to use the median of the distribution to minimize the possible influence of exceptionally large values of the trends. Nowadays it is recognized that evaluating the uncertainty associated with m is of utmost importance. However, as it appears from Table 2.1, in early studies published until the 1980s no uncertainty was generally provided. Subsequently, we will consider three possible error estimates for g. The first is the root mean square:

$$rms = \sqrt{\frac{\sum_k (r_k - g)^2}{N_{tg} - 1}}, \tag{2.6}$$

which characterizes the average uncertainty of the individual trends r_k. The second is the standard deviation of the mean

$$sdom = \frac{rms}{\sqrt{N_{tg}}}, \tag{2.7}$$

which represents the uncertainty of the best estimate g (see *e. g.* Taylor 1997). Since in the definition of *rms* and *sdom* above the individual uncertainties σ_k do not play any role, it is sometimes convenient (see *e. g.* Mitrovica et al. 2001) to consider a third estimate of the error to properly account for the large variability of the σ_k values (see Fig. 2.5). This is defined as the weighted root–mean–square

$$wrms = \sqrt{\frac{\sum_k (r_k - g)^2 w_k}{\sum_k w_k}}, \tag{2.8}$$

where the weights are defined as $w_k = 1/\sigma_k^2$. To characterize the GMSLR estimates obtained in the following from a given set of TGs, these will be written as

$$\mu = g \pm sdom, \tag{2.9}$$

and the corresponding numerical values of *rms* and *wrms* will be also provided for the sake of completeness.

2.2.3 GMSLR from uncorrected TG data

In Fig. 2.6a, we show the histogram of the distribution of the rates of sea level change r_k for all TGs with a minimum number of yearly records $N^v_{min} \geq 3$ (the ALL set, see Fig. 1.1). For this

set our GMSLR estimate is $\mu = 1.4 \pm 0.2$ mm yr^{-1}, where the small value of *sdom* compared to *m* indicates that the latter is, in this case, quite well constrained (the fractional uncertainty is $sdom/|m| \approx 15\%$). According to Equation 2.7, this does not result from a small *rms* value, which in fact amounts to 5.8 mm yr^{-1}; rather, it is due to the large number of TGs belonging to the ALL set ($N_{tg} = 1213$). In spite of the small *sdom*, the relatively large *rms* value clearly confirms that the one obtained using the whole set of available TGs is not a robust GMSLR estimate.

The overall accuracy of the result shown in Fig. 2.6a is difficult to assess, since this would imply the knowledge of the "true value" of *g* (see *e. g.* Taylor 1997), which here is not given *a–priori*. It is certain, however, that because of its global character, GIA potentially constitutes a source of systematic errors which can deteriorate the accuracy of the estimate (Nakiboglu and Lambeck, 1991; Mitrovica and Davis, 1995; Peltier, 1996). At individual TGs, these errors cannot be eliminated by increasing the record length, since the rates of sea level change associated with GIA can be safely assumed to be constant on a century time scale. Regarding the propagation of GIA–induced systematic errors into the best estimate *g*, we observe that the GIA contribution to present day sea level change is globally vanishing across the oceans, on the average (see section 2.3). However, since the TG distribution is certainly not uniform across the oceans (Fig. 1.1), we should not expect that the cumulative effect of GIA will vanish leaving *g* unaffected. For these reasons, the distribution of Fig. 2.6a is likely to be biased by GIA by an unknown amount. While a quantitative assessment will be given starting from section 2.3, we note that the un–corrected estimate provided in Fig. 2.6a, though possibly inaccurate, is not totally inconsistent with some of the previous, GIA–uncorrected estimates listed in Table 2.1, which in some cases are based on the thorough selection of a limited number of TGs meeting specific criteria. In Fig. 2.6b, we illustrate the particularly important case of D97. The data are taken from Table 2.2. We observe that the GMSLR estimate obtained in this case ($\mu = 1.6 \pm 0.1$ mm yr^{-1}), is consistent with that obtained from the ALL set in Fig. 2.6a, where $\mu = 1.4 \pm 0.2$ mm yr^{-1}. Hence, in spite of the sparse distribution of the ALL stations, decadal and inter–decadal fluctuations and gaps in the time series and spurious tectonic effects, when taken collectively the TG observations appear to provide a reliable (though imprecise, because of the large *rms*) GMSLR estimate.

In Fig. 2.7, sites with short records are progressively removed from the ALL set considered in Fig. 2.6a; the corresponding distribution of rates r_k are shown in the right frames. In particular, in Fig. 2.7(a), (b), (c) and (d), we consider the TG sites with a number of valid yearly observations $N_k^v \geq N_{min}^v$, for $N_{min}^v = 30$, 60, 90, and 110, respectively. Ideally, assuming negligible systematic errors from *e. g.* GIA, with increasing N_{min}^v we would expect that the computed rates are less and less influenced by the inter–decadal components of oceanographic origin that affect individual time series. Consistent with Fig. 2.5a, the number N_{tg} of sites considered in each of the maps of Fig. 2.7 is strongly decreasing with increasing N_{min}^v, which deteriorates the estimate of μ and the smoothness of the histograms of the r_k values. In this respect, we note that for $N_{min}^v = 60$ (Fig. 2.7b), the histogram is similar to that in Fig. 4 of Douglas (1991), corresponding to $N_{min}^v = 50$. A smooth best–fitting normal curve is clearly questionable for such a distribution, contrary to what we have seen in Fig. 2.6a above for very large N_{tg} values (the ALL set). Even a cursory inspection of the histograms reveals that the *rms* values are virtually unaffected by the reduction of N_{min}^v, and

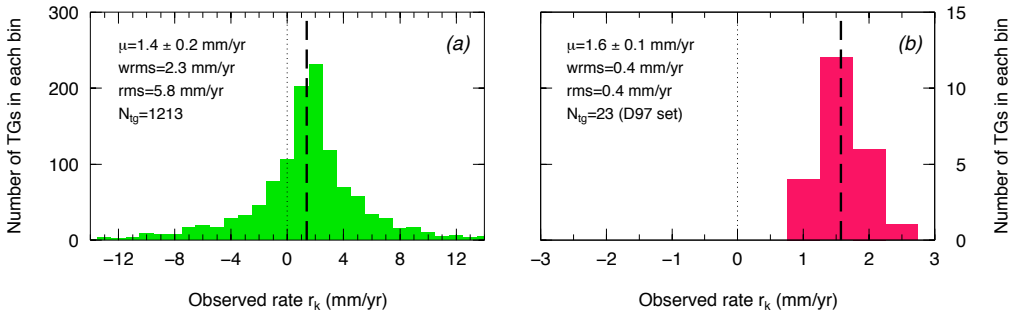

Figure 2.6: Distributions of the rates of sea level change obtained from Equation 2.1 for the ALL set of TGs (a), and for the D97 set (b). A vertical dashed segment marks the average value m. Other statistics are given in the insets.

the same can be observed for *wrms*. As a consequence, the *sdom* value progressively increases until the average sea level μ becomes largely undetermined, and eventually falls to values close to zero. Figs. 2.7c and 2.7(d) show that negative values of μ, corresponding to an average sea level *fall* cannot be discounted by our analysis for $N^v_{min} = 110$ and $N^v_{min} = 120$. This effect is clearly associated with the increasingly dominant role, in the assessment of μ, of strongly negative sea level trends from sites located in areas deeply covered by ice at the LGM. According to the maps of Fig. 2.7, these sites with long records are predominantly located in northern Europe, and particularly in the Baltic Sea. Gröger and Plag (1993) have reached similar conclusions, observing that the median of sea level trends decreases with increasing N^v_{min}, due to the increasing weight of the Scandinavian records.

The dependence of μ and of the respective errors upon N^v_{min} and N_{tg} is better illustrated in Fig. 2.8. The increase of *sdom* with increasing N^v_{min} and the insensitivity of *rms* and *wrms* in a very broad range of N^v_{min} values are now apparent. We note that g is monotonically decreasing for $N^v_{min} \leq 70$, while for larger values it follows a more erratic curve that reflects the progressively increasing spread of the histograms shown in Fig. 2.7. Also because of the relatively large *sdom* values for $N^v_{min} > 70$, the estimate $\mu = g \pm sdom$ becomes progressively unstable. However, all the μ values are swinging approximatively between 0 and 1 mm yr^{-1}. Incidentally, we note that the number of TGs for $N^v_{min} = 110$ is $N_{tg} = 23$, the same as the specific subset of tide gauges selected by D97 according to rigorous requirements not uniquely based on N^v_{min}. The geographical distribution of these sites, shown in Fig. 1.1, differs significantly from that in Fig. 2.7d, at least in two respects. First, the D97 set does not include TGs from formerly ice–covered areas and from the peripheral bulge. Second, it contains a small but significant number of TGs (four), from the southern hemisphere, which are totally absent if the selection of sites is merely based on the length of the record, as in Fig. 2.7. By the histogram of Fig. 2.6b, it is apparent that a careful selection of the sites implies a much better constrained value of μ ($sdom = 0.1$ mm yr^{-1}) and a considerably

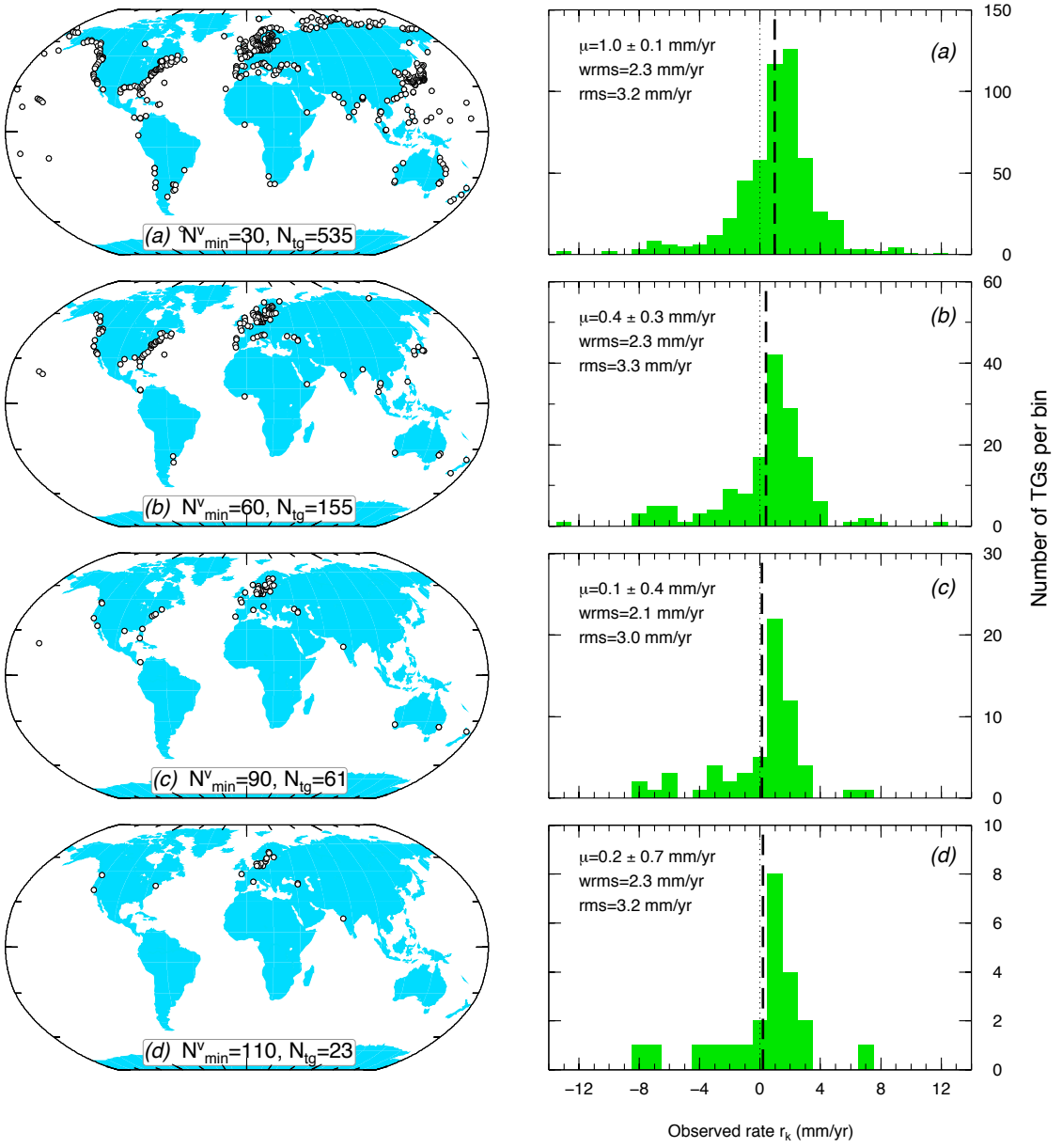

Figure 2.7: Spatial distribution (left) and histogram of observed rates (right) for the TGs with a number of valid RLR annual records $N^v_{min} \geq 30$, 60, 90 and 110 (from top to bottom). For each subset, the right frames also show the basic statistics (μ, *rms* and *wrms*). The effect of GIA corrections on these distributions is shown in Fig. 2.10.

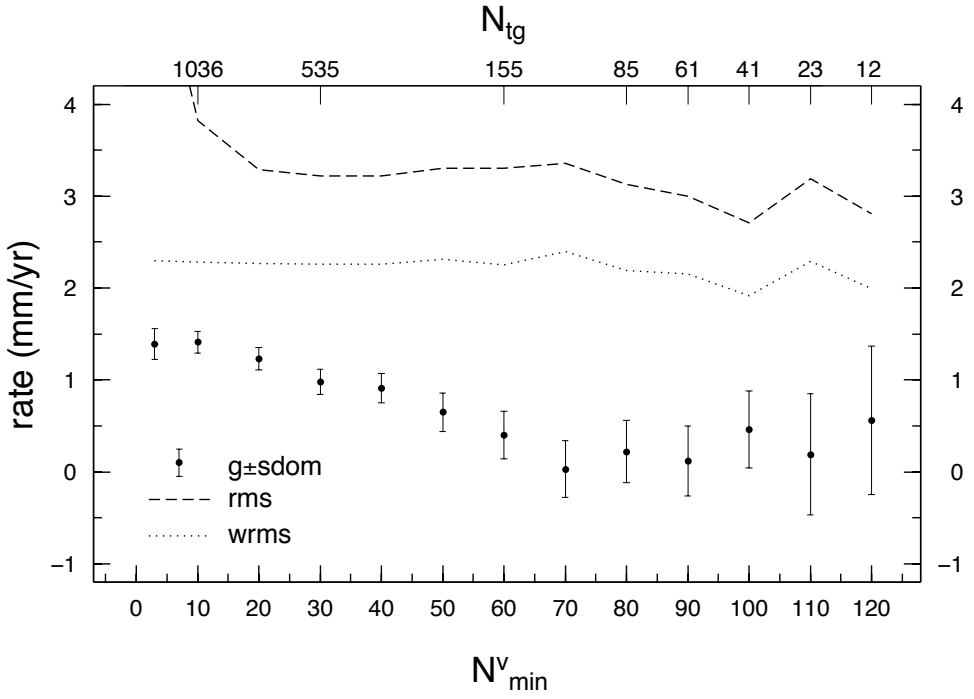

Figure 2.8: Statistics for sets of TG stations containing records with a minimum number N^v_{min} of RLR annual records, as a function of N^v_{min}. The corresponding value of N_{tg} is shown in the second x–axis on top. No GIA correction is applied before the statistics are computed.

reduced *rms* compared to Fig. 2.7d. This confirms that the estimate of μ involves a more thorough approach than the simple decimation of the ALL set and that, in general, it cannot be performed by a straightforward automatic selection.

2.3 GIA correction of TG observations

2.3.1 GIA modeling for GMSLR estimate

As anticipate in subsection 1.4.2, to address the role of GIA corrections upon the estimate of GMSLR, in this work we will consider the three previously published time–histories of the late–Pleistocene ice sheets: ICE–3G (Tushingham and Peltier, 1991), ICE–5G (Peltier, 2004) and KL05 (Fleming and Lambeck, 2004). Details of numerical implementation of the SLE (Equation 1.22) here applied, are illustrated in subsection 1.4.1. Maps of the GIA component of present–day rate of sea–level change obtained with the SELEN code (described in section 1.4) have been presented in Fig. 1.7 of chapter 1. In Fig. 2.9, we present the comparison of the same fingerprints for mod-

els ICE–3G, ICE–5G and KL05, obtained neglecting (left frames) and including (right frames) the effects of Earth rotation on sea–level variations. As discussed in subsection 1.4.2, the GIA–induced sea–level pattern shows local differences according with the three models used. The sea–level change patterns suggested in Fig. 2.9 by ICE–5G (c) and KL05 (e) across north America and the north Atlantic differ significantly from those of ICE–3G (a), and we expect that this may have significant impact on the GIA correction at the numerous nearby tide gauges. These remarkable differences remain in the simulations that include rotational effects (right frames). Another major difference concerns the contour lines in the southern hemisphere, and it could be explained by the differences between the total amount of meltwater from Antarctica (see Fig. 1.6) and the details of the history of melting in this regions in the models considered. This feature, along with the recognized role played by rotational effects (Milne and Mitrovica, 1998), is expected to influence the rates of sea–level change at tide gauges in south America.

2.3.2 GIA correction of sea–level trends

GIA corrections at TGs are directly obtained from the maps of Fig. 2.9. Following Equation 1.2 in section 1.3, they can be expressed as

$$r_k^{gia} = \frac{dS}{dt}(\omega_k, t_p), \tag{2.10}$$

where $\omega_k = (\theta_k, \lambda_k)$ are the coordinates of k–th TG and t_p is present time. Hence, the GIA–corrected rates of sea level change are

$$r'_k = r_k - r_k^{gia}, \tag{2.11}$$

where r_k^{gia} and r_k are given by Eqs. 2.10 and 2.1, respectively. Assuming that GIA corrections are "exact", the uncertainty on r_k will directly propagate on r'_k. Hence, the GIA–corrected rates are

$$\rho'_k = r'_k \pm \sigma_k, \tag{2.12}$$

where σ_k is given by Equation 2.2. Statistics derived by corrected rates will be indicated with primed symbols (*e. g.* g', $wrms'$, ...). These are obtained by substituting r_k with r'_k and m with m'_k in eqs (2.5-2.8). In particular, we note that

$$g' = g - g^{gia}, \tag{2.13}$$

where

$$g^{gia} = \frac{1}{N_{tg}} \sum_{k=1}^{N_{tg}} r_k^{gia} \tag{2.14}$$

simply represents the average of the GIA corrections at TGs. Recalling Equation 1.15 in chapter 1 and according to Equation 2.10, this term would vanish (hence providing $g' = g$) only in the very idealized case of a regularly spaced, dense network of TGs located across the oceans. Obviously,

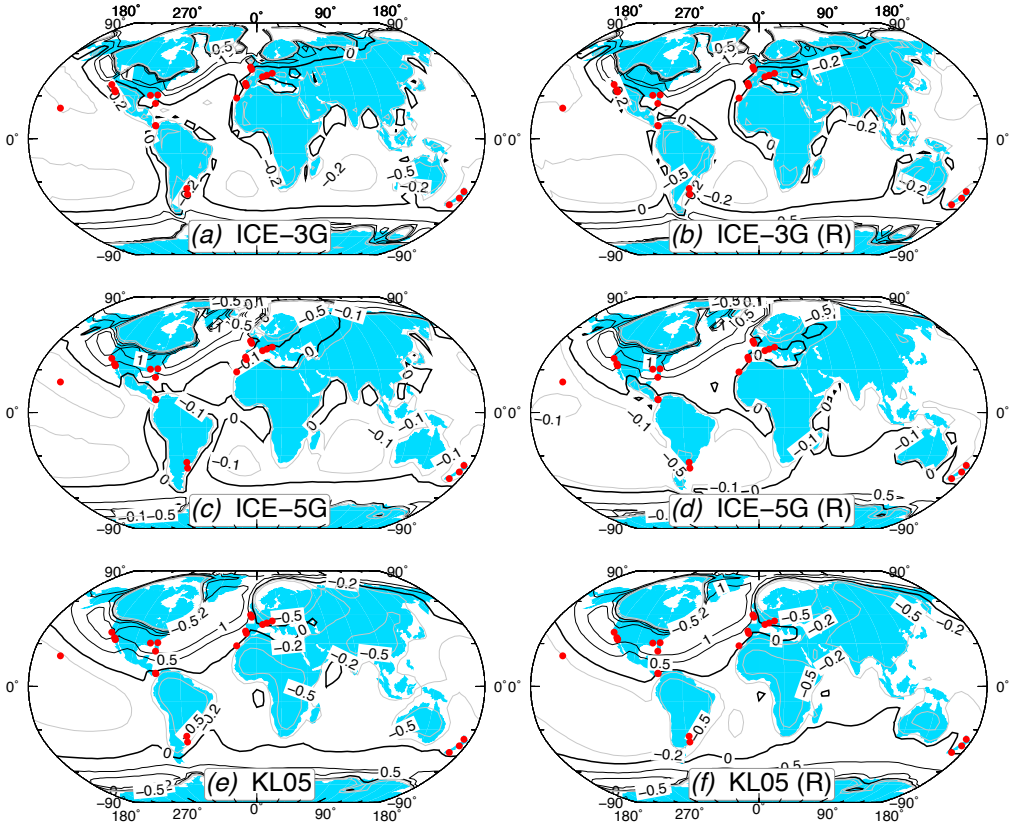

Figure 2.9: GIA component of present day rate of sea level change, evaluated according models ICE–3G (a), ICE–5G (c) and KL05 (e). Frames (b), (d) and (f) show results of computations based on the same ice models, but taking into account for the effects of the Earth's rotation on sea level change. The contour corresponding to $\dot{S} = 0$ is marked by thick curves; positive and negative values of $\dot{S}$ are shown by black and grey thin lines, respectively. Contour lines are also plotted through the continents. TG sites belonging to the D97 set are marked by red dots.

in view of the spatially inhomogeneous distribution of TGs in the real world (see *e. g.* Fig. 1.1), we should not expect that average GIA effects at TGs vanish.

With the aid of Equation 1.1 it is possible to discuss how much the GIA–corrected GMSLR g' contributes to assess a volume change of global oceans, and show the relevance of this quantity. In Fig. 2.10 we show the distributions of the GIA–corrected rates for various subsets of tide gauges. In this example, we have used GIA predictions by model ICE–3G, since it has been widely employed in the past (see Table 2.1); corrections for GIA models ICE–5G and KL05 will be discussed in next sections. In Figs. 2.10a to 2.10e, the minimum number of valid yearly observations is increased from $N^v_{min} = 3$ (set ALL) to $N^v_{min} = 110$, while in Fig. 2.10f, the D97 set is considered. Solid and stairs–step histograms, characterized by the same area, show the distribution of r'_k and of r_k, respectively (these latter are reproduced from Figs. 2.6 and 2.7). Vertical dashed segments show the GIA–corrected average m' (Equation 2.13); other primed statistics obtained from Eqs. 2.6 and 2.8 are also shown. The effect of GIA corrections, which can be appreciated even visually, is that of reducing the spread of the distributions around their average value, hence increasing the overall coherence of the tide gauge observations. The weighted variance reduction, estimated by a Fisher F–test for the ratio $wrms'/wrms$, is significant at the 95% confidence level for all the sets considered from Fig. 2.10a to Fig. 2.10e. For the D97 set in Fig. 2.10f, the variance reduction obtained by applying the GIA correction is not significant (at the same confidence level), and the average value of sea–level change $\mu' = 1.7 \pm 0.1$ mm yr^{-1} overlaps the un–corrected estimate ($\mu = 1.6 \pm 0.1$, see Fig. 2.6b and Table 2.6). However, from the statistics in Fig. 2.10f, it is apparent that the five requirements introduced by D97 produce a sizeable variance reduction with respect to the case when the only criterion is minimizing the number of yearly records ($N^v_{min} = 110$, see Fig. 2.10e).

The statistics for the corrected rates, shown in frame Fig. 2.10g as a function of N^v_{min}, confirm that with increasing N^v_{min} the GIA correction plays an increasing role. Furthermore, they differ from the corresponding uncorrected statistics, shown in Fig. 2.8, in several respects. First, m' shows a reduced sensitivity to N^v_{min} compared to m. Second, the standard error of the mean (*sdom*) is smaller, especially for the longest records, as an effect of the reduced *rms*. Third, m' and $wrms'$ broadly follow the same trend with varying N^v_{min}. According to Equation 2.8, this indicates that for the time series with the longest record (hence, from Fig. 2.10, those having generally the largest weight w_k in the expression of $wrms'$), the GIA correction is removing a large fraction of the observed trend, *i.e.*, $r_k \approx r^{gia}_k$. As pointed by D97, since these series are from the regions deeply covered by ice during the Last Glacial Maximum, even small errors in the GIA predictions for these regions can be comparable to the expected value of m'. This justifies, in D97, the exclusion of these sites from the analysis by the applivation of criterion *5*.

2.3.3 Uncertainties in GIA modeling

A major drawback of the approach followed so far is the assumption that the GIA correction r^{gia}_k is perfectly determined. This is not the case, however. In fact, there are at least three sources of error that can affect r^{gia}_k. The first is associated with the physical ingredients implemented in the SLE (Equation 1.22). For instance, the sea–level variations associated with fluctuations of

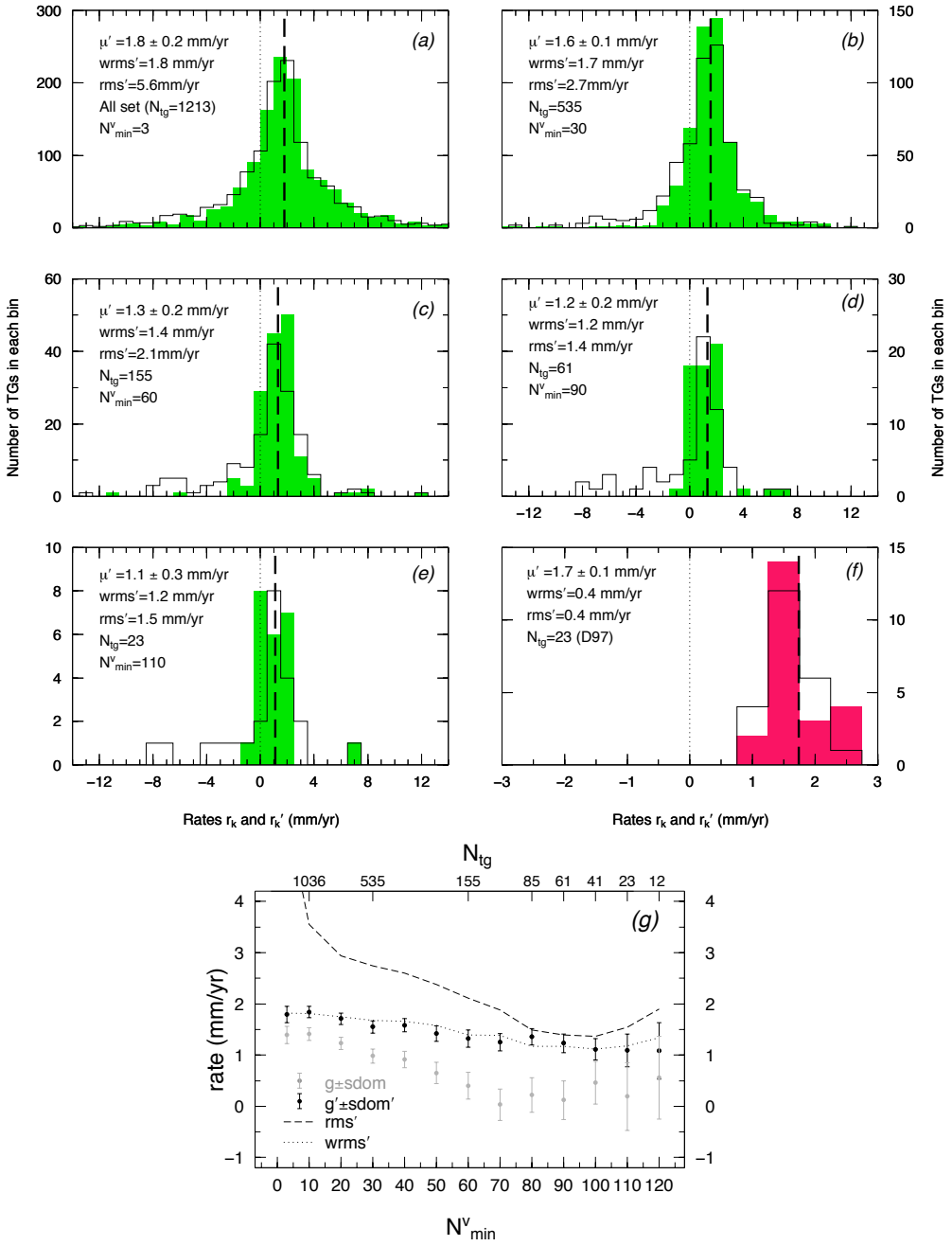

Figure 2.10: Frames from (a) to (e) show the effects of the GIA correction (by ICE–3G) on the distributions of the sea–level trends for increasing values of N^v_{min} (corrected and un–corrected distributions are shown by solid and stairs–step histograms, respectively). The D97 set is considered in frame (f). The statistics are summarized in (g) for more values of N^v_{min}.

the Earth's rotation vector (Milne and Mitrovica, 1998) can be included or not in the SLE (indeed, this can be accomplished in various ways, as discussed by Spada et al., 2011a). Similarly, to minimize the computational burden, the SLE can be solved assuming fixed shorelines or, alternatively, allowing for the development of a "gravitationally self–consistent" paleo–topography (Peltier, 2004). Accounting for or neglecting these effects can certainly have some impact on the GIA correction, both on a global and a regional scale. Once the physics of the SLE is set, a second source of uncertainty is associated with the numerical implementation of the SLE, and particularly to the procedures employed to retrieve its solution numerically. For instance, different temporal discretization schemes (the SLE is normally solved assuming stepwise or, alternatively, a linear piecewise discretization), as well as different geometries and spatial resolutions of the spatial grids are factors that can potentially impact the numerical results. Third, there are uncertainties associated with the spatio–temporal features of the late–Pleistocene ice sheets, which derive from errors in the RSL data that constrain the ice models itself (see the review of Whitehouse 2009). In this respect, GIA models are continuously improved, since the amount and the overall quality of the RSL observations is increasing with time. Consequently, GIA predictions are not given once and for all. A rigorous evaluation of all the possible sources of errors described above is certainly not feasible in this work, since it would imply running a very large number of sensitivity experiments. Hence, we use our code SELEN to estimate the GIA uncertainties adopting the three ice models described in subsection 1.4.2 above and the viscosity profiles recommended by their authors, shown in Table 1.1. This is done assuming that they provide three reliable (though not completely error–free) descriptions of the sea–level variations associated with the GIA phenomenon.

To illustrate the uncertainties inherent to the GIA correction, in Fig. 2.11 we compare the rates of sea–level change at the D97 tide gauges (see top frame) with the GIA corrections based on models ICE–3G, ICE–5G and KL05 (bottom). The three GIA models show comparable corrections (to within ± 0.3 mm yr^{-1}) at most of the sites, but the ICE–5G and the KL05 predictions strongly disagree with those of ICE–3G at those located along the North American West coast (13–16) and in South East North America (21–23). The reason of this mismatch is found in the larger extent of the Laurentian ice sheet in models ICE–5G and KL05 compared to ICE–3G, as it is illustrated by the ESL time histories and in the maps shown in Fig. 1.6 for the three models. This has important consequences on the assessment of the GMSLR . In fact, the lateral extent of the peripheral forebulge of ICE–3G is significantly smaller than in ICE–5G and KL05 (see Fig. 2.9), and tide gauges in the North American West coast and South East North America regions can be safely considered outside the collapsing region. However, this is not the case when ICE–5G and KL05 are considered. This means that, by a rigorous application of criterion five of D97, these sites should be excluded from the analysis, unless ICE–5G and KL05 are considered fully unreliable compared to the previolusy released ICE–3G. In the following, we denote by D97R the set of 16 TGs obtained excluding these sites (these are marked by a star in Table 2.2). We anticipate that, in contrast to D97, using the D97R set produces GIA–corrected estimates of GMSLR which are basically insensitive to the model adopted for the correction. This finding suggests a modification of the D97 criteria for the selection of the TGs suitable for the assessment of GMSLR, which is discussed below.

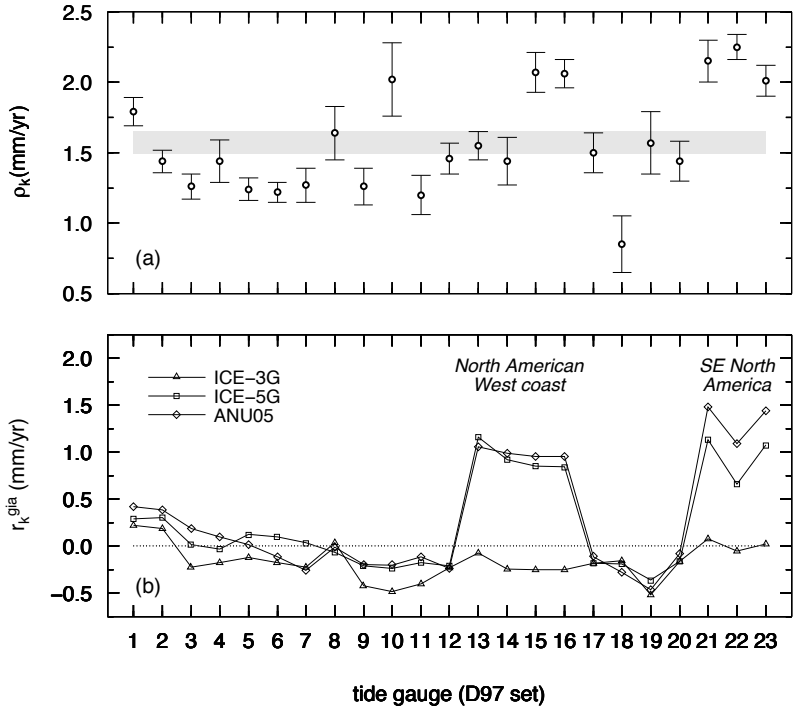

Figure 2.11: (a) Rates of sea–level change and their uncertainties at the 23 sites of the D97 set (the shaded region shows $\mu = m \pm sdom = 1.6 \pm 0.1$ mm yr^{-1}). The numerical values of the rates are listed in Table 2.2. (b) GIA corrections for the rates shown in (a), computed for the GIA models ICE–3G, ICE–5G and ANU05, respectively.

2.4 Secular GMSLR assessment

2.4.1 TGs selection

A new, GIA–based selection criterion: the SGX set

In Fig. 2.12a, we show the rates of sea–level change for 44 TGs from which at least $N^v_{min} = 60$ years of valid RLR annual records are available. In the following, this requirement will be referred to as criterion *I)* (the new or revised criteria introduced in this study are summarized in Table 2.3 and compared with those by D97). Criterion *I)* constitutes a stronger constraint compared to its counterpart *1)* in D97, which is based on the record length of possibly non–RLR records. As an additional constraint, we impose that the GIA corrections are nearly the same for all stations, regardless of the ice model employed. This is realized by the constraint

$$|r^{gia}_{M_1} - r^{gia}_{M_2}| \leq \Delta r, \tag{2.15}$$

where M_1 and M_2 are two GIA models, and Δr is a small tolerance parameter. Hereinafter, we will use $\Delta r = 0.3$ mm yr^{-1}, which represents $\sim 20\%$ of the expected magnitude of GMSLR (≈ 1.5 mm yr^{-1}), based on previous assessments (see Table 2.1). The resulting set, presented in Table 2.4, is referred to as "SGX set" in the following. Note that the constraint expressed by Equation 2.15 is applied to GIA simulations that do not include the effects from the rotational feedback. This is motivated, *a posteriori,* by the negligible role played by this modeling feature on the assessment of the GMSLR, as it will be discussed below. Since constraint in Equation 2.15 will substitute criterion *5)* of D97 (see introduction), it will be referred to as criterion *V)* in the following.

Table 2.3: The D97 selection criteria compared with those proposed in this work.

D97	This study
1). The TG series must be at least 60 years in length.	*I).* It must contain at least 60 years of valid "Revised Local Reference" (RLR) annual records[a].
2). The TG site must be sufficiently distant from collisional tectonic boundaries.	*II).* See *2).*
3). The series must have a sufficient completeness ($> 80\%$).	*III).* The series must have a sufficient completeness[b] ($> 70\%$).
4). The series must be in reasonable agreement with nearby gauges at low frequencies.	*IV).* See *4).*
5). The TG site must not belong to previously ice–covered areas during the Last Glacial Maximum (LGM) ~ 21 kyrs ago nor to the peripheral bulge adjacent to these areas.	*V).* The GIA correction should be essentially model independent (see Equation 2.15).
6). Not formally expressed in D97. See *VI).*	*VI).* TG series showing suspect accelerations and/or jumps, or affected by known human–driven effects should not be considered

([a]) Valid annual RLR records are obtained by averaging twelve monthly records.
([b]) For the TG series k, completeness is the ratio $N_k^v/span$ where N_k^v if the number of valid annual records and $span$ is the difference between the newest and the oldest valid annual RLR record.

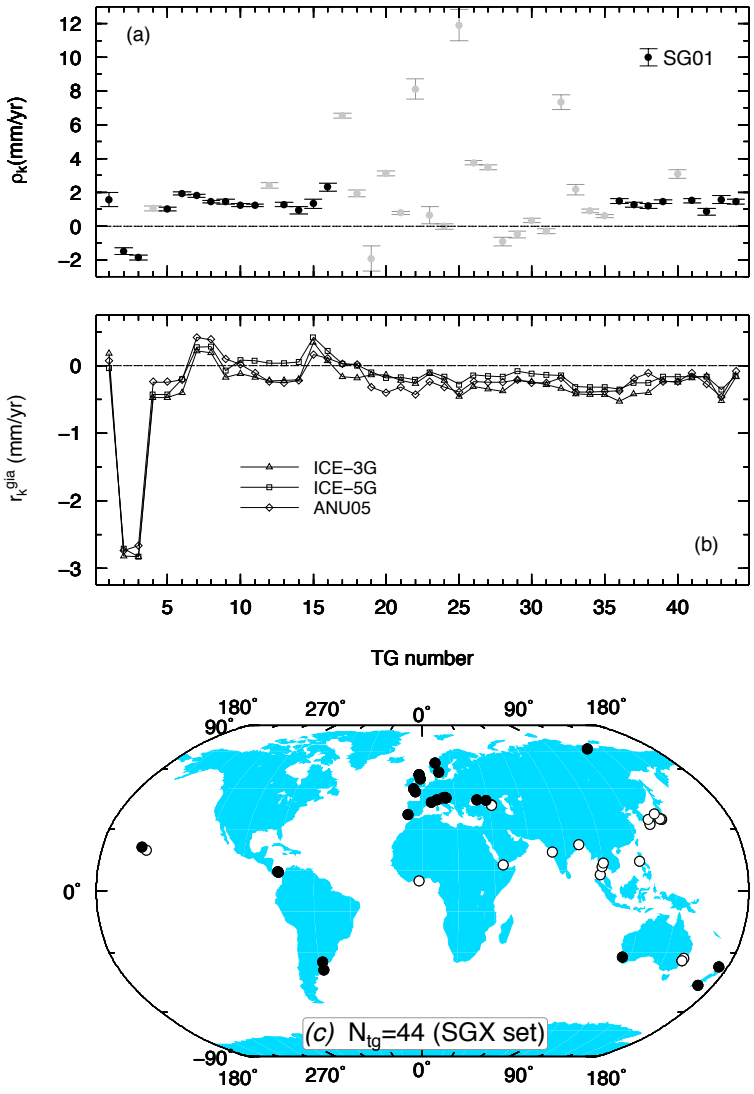

Figure 2.12: (a) Observed rates of sea–level change at the 44 TGs belonging to the SGX set. Black symbols denote sites of the SG01 subset, obtained by decimation of SGX according to the discussion below. In (b) the GIA corrections are shown for all sites. The spatial distribution of TGs is shown in (c), where black dots denote the location of the SG01 TG sites.

Imposing constraints *V)* and *I)* simultaneously to the three models considered in this study (namely, ICE–3G, ICE–5G and ANU05), our aim is to discard short records from TGs at which different GIA parameterizations produce too conflicting predictions. The SGX sites so selected, shown in Fig. 2.12b, in principle, should be only sensitive to the gross features of the spatial pattern of GIA–induced sea–level change, shared by any realistic model. An obvious hypothesis is that one of these features is the amplitude of the S^{hi} term of the SLE (see Equation 1.22), which is mainly determined by the time history of the meltwater loading and follows broadly similar curves for the three models considered (see the Equivalent Sea level – ESL – curves in Fig. 1.6a). This is confirmed by the geographical distribution of the TG sites belonging to SGX (see Fig. 2.12c), showing that the constraint *V)* is very effective (with a few exceptions, discussed below) in eliminating the TGs located in the vicinity of the major formerly ice–covered areas and those across the collapsing forebulges, where the three GIA models provide broadly different predictions, as a consequence of the different time–histories of ice melting at a regional scale. These are expected to be mostly affected by the S^{gi} term of the SLE and, only to a lesser extent, by hydro–isostatic effects. Since it is unlikely that the future GIA models will adopt ESL curves that dramatically diverge from those displayed in Fig. 1.6a, we believe that SGX constitutes the most natural set of TGs on which to rely upon for assessments of GMSLR.

Decimating SGX: the SG01 set

The anomalous rates of sea–level change observed for a significant number of the SGX sites (in some cases as large as several millimeters per year, see Fig. 2.12a), demands the application of selection criteria in addition to *I)* and *V)*, introduced above. They are: *II)* the TG station must be sufficiently distant from collisional tectonic boundaries, *III)* have a sufficient completeness ($> 70\%$, where completeness is the ratio $N_k^v/span$ where $span$ is the difference between the newest and the oldest annual RLR record), *IV)* the low–frequency sea–level trend from each TG must reasonably agree with that of nearby instruments. Criteria *II)* and *IV)* are directly borrowed from *2)* and *4)* of D97. We note that sites showing "suspect accelerations" or those where human–driven effects are ascertained, will be eliminated following a general prudence criterion finalized to avoid data contamination. In previous studies, this approach has been often implicitly or explicitly applied (see *i. e.* Hagedoorn et al., 2007). Here, it will be referred to as selection criterion *VI)*. The SGX TGs surviving the selection based on all requirements *II)–IV)* and *VI)* constitute set SG01 (see Table 2.5), which will be employed below in order to produce new GMSLR estimates.

Based on criterion *II)*, we have first expunged from the SGX set all TGs located close to active collisional tectonic boundaries. These include, in particular, the stations along the coast of Japan, whose low–frequency signals (periods longer than 50 yr) have long been recognized to be associated to the subduction of the Pacific and Philippine plates beneath Japan (Aubrey and Emery, 1986). According to the current RLR PSMSL record, at the six Japanese SGX sites of Mera, Aburatsubo, Uchiura, Hosojuma, Tonoura, and Wajima, the long–term rates of sea–level change show a considerable spread (with values ranging between ~ -0.5 to $\sim +4$ mm yr^{-1}), which prohibits the assessment of a reliable regional average value. We note that other sites that could be poten-

Table 2.4: TGs belonging to the SGX set. This is characterized by at least 60 valid yearly records and obey the constraint expressed by Equation 2.15. The rates with error bars are displayed in Fig. 2.12.

Tide gauge site	Period year–year	N_k^v years	$c_k^{(a)}$ %	$\rho_k = r_k \pm \sigma_k$ mm yr^{-1}
Tiksi Bukhta	1949–2009	61	100	1.6 ± 0.4
Heimsjo	1928–2009	71	77	−1.5 ± 0.2
Smogen	1911–2010	99	99	−1.9 ± 0.1
Aberdeen I	1932–2008	68	88	1.0 ± 0.2
Aberdeen II	1880–1965	85	99	1.2 ± 0.1
North Shields	1896–2009	103	90	1.9 ± 0.1
Newlyn	1916–2009	93	99	1.8 ± 0.1
Brest	1880–2009	121	93	1.4 ± 0.1
Lagos	1909–1987	69	87	1.4 ± 0.2
Marseille	1885–2009	119	95	1.2 ± 0.1
Genova	1884–1996	85	75	1.2 ± 0.1
Venezia	1909–2000	83	90	2.4 ± 0.2
Trieste	1905–2010	100	94	1.3 ± 0.1
Bakar	1930–2008	66	83	0.9 ± 0.2
Sevastopol	1910–1994	82	96	1.3 ± 0.3
Tuapse	1917–2009	91	98	2.3 ± 0.2
Poti	1874–2009	127	93	6.6 ± 0.1
Batumi	1882–2009	110	86	1.9 ± 0.2
Takoradi	1930–2008	62	78	−1.9 ± 0.7
Aden	1880–2008	60	46	3.1 ± 0.1
Mumbai/Bombay	1878–2006	114	88	0.8 ± 0.1
Calcutta	1932–2007	67	88	8.1 ± 0.1
Ko Taphao Noi	1940–2009	64	91	0.6 ± 0.5
Ko Lak	1940–2009	66	94	−0.0 ± 0.2
Ft. Phrachula C.	1940–2009	65	93	1.9 ± 0.9
Mera	1931–2009	73	92	3.7 ± 0.1
Aburatsubo	1930–2009	77	96	3.5 ± 0.1
Uchiura	1944–2009	64	98	−0.9 ± 0.2
Hosojima	1930–2009	78	97	−0.5 ± 0.2
Tonoura	1894–1983	85	94	0.3 ± 0.1
Wajima	1930–2009	78	97	−0.3 ± 0.1
Manila	1902–2009	82	76	7.3 ± 0.4
Newcastle III	1926–1988	63	100	2.2 ± 0.3
Sydney, Ft. Den. 2	1915–2009	92	97	0.9 ± 0.1
Sydney, Ft. Den.	1886–1993	108	100	0.6 ± 0.1
Fremantle	1897–2009	100	88	1.5 ± 0.2
Auckland II	1904–1998	92	97	1.3 ± 0.1
Dunedin II	1900–2009	64	58	1.2 ± 0.1
Honolulu	1905–2009	105	100	1.5 ± 0.1
Hilo, Hawaii	1947–2009	63	100	3.1 ± 0.3
Balboa	1908–2003	95	74	1.5 ± 0.1
Quenquen	1918–1982	64	98	0.9 ± 0.2
Buenos Aires	1905–1987	83	100	1.6 ± 0.2
Cristobal	1909–1979	71	100	1.4 ± 0.1

(^{a}) Completeness c_k is computed as the ratio between N_v^k and the total time span of each time series.

tially affected by tectonic deformations along the San Andreas Fault, like those along the North American West coast (San Francisco, Santa Monica, La Jolla and San Diego), which are included in the D97 set (see Table 2.2), have been automatically removed by the application of constraints in Equation 2.15.

Applying criterion *VI)*, several sites have been removed from the SGX set for possible contaminations from human–driven subsidence, as in the case of Venice (see *e. g.* Hagedoorn et al., 2007; Carbognin et al., 2010), whose sea–level trend exceed significantly those at other Mediterranean TGs located at approximately the same latitude (*e. g.* Trieste). For some other sites in SGX, suspect accelerations are apparent in the time series. This is particularly evident for the sites of Batumi and Poti (Black Sea), Takoradi (Ghana), Mumbai and Calcutta (India), Ko Lak, Ko Taphao Noi and Fort Phrachula Chomklao (Thailandia), Manila S. Harbor (Filippine) and Hilo (Hawaii Island). Possible origins of these anomalous trends, discussed in the land movement page of PSMSL (*http://www.pol.ac.uk/psmsl/˜landmove.html*), include increased groundwater extraction, recent deposit from river discharges, land reclamation works, various coastal processes and possibly volcanic deformations as for Hilo (Hawaii).

Anomalous sea–level trends at the sites above have been reported and discussed in a number of previous studies. The subsidence at Batumi and Poti is confirmed by Garcia et al. (2007) and by Stanev and Peneva (2002). Caccamise et al. (2001) have evidenced an inconsistency of the TG record at Hilo TG compared to the nearby Honolulu TG, whereas Yanagi and Akaki (1994) and Emery et al. (1991) have explained the anomalous increase in sea–level from 1965 to 1982 at Manila and Fort Phrachula Chomklao invoking a large withdrawal of groundwater; the anomalies in Manila TG trend are attributed by Douglas (1991) besides the tectonic movements in that area, to harbor development. For the indian TGs, in addition to the subsidence problems (Subrahmanya, 1996), it is recognized that the records were influenced by the high frequency of tropical cyclones and storm surges (Das and Radhakrishna, 1991). Lastly, a large interannual variability is the cause of the unreliability of the trend observed at the Ko Taphao Noi TG (Unnikrishnan and Shankar, 2007). Following the most simple and prudent approach, these sites have been eliminated from SGX.

The SGX set contains the Northern UK sites of Aberdeen and North Shields, which were discarded by D97 because of their proximity to the peripheral bulge adjacent of the former ice sheets. However, from our GIA computations, it appears that the rate of sea–level change at these sites is not anomalously large to motivate their exclusion. Actually, as shown in Table 2.5, the observed rates at these sites have a negative sign (contrary to what it is expected for sites located across the lateral forebulge region) and comparable with rates of far field sites, such as Buenos Aires. Thus, in agreement with Douglas (1991), these Northern UK sites are not discarded (though this is done for Aberdeen I, whose trend of sea–level change duplicates that of the nearby location of Aberdeen II).

By similar arguments, the two North European sites of Smogen (Sweden) and Heimjso (Norway), approximately located along the margins of the former Fennoscandian ice sheet, have not been excluded by our analysis. Among the SGX sites, these are the only two that are not located in the far field of the former ice sheets, and are experiencing secular rates of sea–level change of

-1.5 ± 0.2 and -1.9 ± 0.1 mm yr^{-1}, respectively. At these sites, the three ice models considered in this study coherently indicate a sea–level fall of ≈ 2.5 mm yr^{-1} (see Fig. 2.12). We note that Smogen was indeed included in the analysis of Douglas (1991) but it was later discarded by D97 since it is placed in the vicinity of the former ice sheets. Hemisjo was not considered by Douglas (1991) probably because, at that time, the TG record was not long enough to merit attention (the Smogen TG record starts only in 1928). Presently, Smogen and Heimjso are meeting the requirements of minimum length and of completeness (77% for Heimjso and 99% for Smogen). We observe that the strongly negative values of the rate of sealevel change observed for these TGs, if corrected for the GIA effect becomes largely coherent with the values found for the other TGs selected. Contrary to D97, we did not find any motivation to exclude the site of Tiksi (Tiksi Buktha, Siberia), which is remarkably complete (100%) but has not been included in the D97 set. Since the Tiksi record has been employed in previous studies aimed to a regional assessment of sea–level trend (see Pavlov, 2001; Proshutinsky et al., 2004, 2007), it will not be discarded here.

The SGX set contains five Australian TGs (namely, Sydney, Fort Denison, Fort Denison II, Newcastle and Fremantle). Since the two TGs located at Sydney provide inconsistent trends (see Table 2.4) and it is impossible to determine which one is effectively correct, both have been excluded from our assessment, also in agreement with criterion *4)*. In addition, we also note that the observed sea–level rate from the nearby site of Newcastle is largely inconsistent with the two Sydney trends (as pointed by Douglas (1991), the major discrepancy between Newcastle and Sydney is observed during the period 1950–1980). Consequently, we have prudentially expunged also the site of Newcastle from set SGX. However, in view of its considerable distance from Sydney and Newcastle and the fairly long and complete record (see Table 2.4), we did not discard the site of Fremantle. Its recognized ENSO–related variability does not appear to deteriorate the assessment of the secular sea–level trend obtained from this site, as pointed by Church et al. (2004). Previous authors have assumed distinct viewpoints regarding the Australian TG sites. For instance, D97 excluded Sydney and Newcastle and did not consider the TG of Fremantle, apparently without any explicit motivation. We als note that more recently, Hagedoorn et al. (2007) considered various Australian sites in their study, including Sydney and Fremantle but excluding Newcastle.

2.4.2 New GMSLR estimate

The basic data pertaining the SG01 sites, surviving the decimation of SGX, are displayed in Table 2.5. The rates of sea–level change for these sites are marked in Fig. 2.12a by black symbols, while those discarded from set SGX are shown by gray symbols. The corresponding GIA corrections are shown in Fig. 2.12b for the three models considered in this study. As shown in Fig. 2.12c by filled circles, the spatial coverage of set SG01 appears not too severely biased towards the northern hemisphere.

The various GMSLR estimates obtained in this work are summarized in Table 2.6. As anticipated in previous sections, for set D97R we obtain GIA–corrected values which are broadly consistent (to within ± 0.1 mm yr^{-1}), independently from the model employed to compute the GIA corrections. This is evidently in contrast with the estimates based on D97, which show a

Table 2.5: Basic data and computed rates of sea–level change for the SG01 set of TGs, determined according to the discussion in subsection 2.4.1. The average number of valid yearly RLR records for this set is 87 years. GIA corrections corresponding to models ICE–5G are also shown. According to Equation 2.15, those pertaining to ICE–3G and ANU05 do not differ from those shown by more than 0.3 mm yr^{-1}. The last column shows ICE–5G GIA corrections in which the effects of the rotational feedback on sea–level are taken into account.

Region	Tide gauge site	Period year–year	Span years	N_k^v years	$\rho_k = r_k \pm \sigma_k$ mm yr^{-1}	r_k^{gia} mm yr^{-1}	$r_k^{gia(b)}$ mm yr^{-1}
Siberia	1 Tiksi Bukhta	1949–2009	61	61	1.6 ± 0.4	-0.0	-0.2
Northern Europe	2 Heimsjo	1928–2009	82	71	-1.5 ± 0.2	-2.7	-2.7
	3 Smogen	1911–2009	99	99	-1.9 ± 0.2	-2.8	-2.8
Scotland	4 Aberdeen II	1880–1965	86	85	1.0 ± 0.1	-0.4	-0.4
	5 North Shields	1896–2009	114	103	1.9 ± 0.1	-0.2	-0.2
English Channel	6 Newlyn[a]	1916–2009	94	93	1.8 ± 0.1	$+0.3$	$+0.3$
	7 Brest[a]	1880–2009	130	121	1.4 ± 0.1	$+0.3$	$+0.3$
Atlantic	8 Lagos[a]	1909–1987	79	69	1.4 ± 0.2	$+0.0$	-0.0
Mediterranean	9 Marseille[a]	1885–2009	125	119	1.2 ± 0.1	$+0.1$	$+0.1$
Sea	10 Genova[a]	1884–1996	113	85	1.2 ± 0.1	$+0.1$	$+0.1$
	11 Trieste[a]	1905–2010	106	100	1.3 ± 0.1	$+0.0$	$+0.0$
	12 Bakar	1930–2008	79	66	0.9 ± 0.2	$+0.0$	$+0.0$
Black Sea	13 Sevastopol	1910–1994	85	82	1.3 ± 0.3	$+0.4$	$+0.3$
	14 Tuapse	1917–2009	93	91	2.3 ± 0.2	$+0.2$	$+0.1$
Australia	15 Fremantle	1897–2009	113	100	1.5 ± 0.2	-0.3	-0.2
New Zeland	16 Auckland II[a]	1904–1998	95	92	1.3 ± 0.1	-0.3	-0.2
	17 Dunedin II[a]	1900–2009	110	64	1.2 ± 0.1	-0.3	-0.2
Central America	18 Balboa[a]	1908–2003	96	95	1.5 ± 0.1	-0.2	-0.1
	19 Cristobal[a]	1909–1979	71	71	1.4 ± 0.1	-0.2	-0.1
South America	20 Quenquen[a]	1918–1982	65	64	0.9 ± 0.2	-0.2	-0.4
	21 Buenos Aires[a]	1905–1987	83	83	1.6 ± 0.2	-0.4	-0.5
Pacific	22 Honolulu[a]	1905–2009	101	105	1.5 ± 0.1	-0.2	-0.1

[a] Sites that also belong to the D97 set (see Table 2.2).
[b] Includes the effect of rotational feedback on sea–level change.

significant sensitivity to the model employed, with μ' in the range between 1.3 ± 0.1 and 1.7 ± 0.1 mm yr^{-1}. As discussed in section 2.3 and Fig. 2.5, the reasons of this sensitivity resided in the largely different predictions provide by the GIA models at TGs located along the North American West coast and in South East North America. Another appealing feature of D97R is the relatively small difference between the GIA un–corrected and corrected estimates (0.1 mm yr^{-1}). This indicates that thought the tide gauges of D97R are sparsely distributed, the average GIA corrections for these site is close to zero, as it would be for a set of TGs uniformly spaced across the oceans (see Equation 2.13). We also observe a systematic reduction of rms' and $wrms'$ with respect to D97, which indicates that the assessment of GMSLR obtained by D97R is slightly more precise than the one based upon D97.

Table 2.6: Estimates of GMSLR ($\mu = m \pm sdom$) obtained in this work, corresponding to different subsets of TGs and GIA corrections evaluated using code SELEN (see section 1.4). These trends have not been corrected for any tectonic effect. The statistics *rms* and *wrms* are also shown. Our preferred estimate is starred.

Estimate n.	TG set	N_{tg}	$\mu = m \pm sdom$ mm yr^{-1}	*rms* (*wrms*) mm yr^{-1}	GIA correction
1	ALL	1213	1.4 ± 0.2	5.8 (2.3)	no
2	”	”	1.8 ± 0.2	5.6 (1.8)	ICE–3G
3	D97	23	1.6 ± 0.1	0.4 (0.4)	no
4	”	”	1.7 ± 0.1	0.4 (0.4)	ICE–3G
5	”	”	1.5 ± 0.1	0.4 (0.3)	ICE–5G
6	”	”	1.3 ± 0.1	0.5 (0.4)	ANU05
7	D97R	16	1.4 ± 0.1	0.3 (0.2)	no
8	”	”	1.6 ± 0.1	0.3 (0.2)	ICE–3G
9	”	”	1.5 ± 0.1	0.3 (0.3)	ICE–5G
10	”	”	1.5 ± 0.1	0.3 (0.3)	ANU05
11	SG01	22	1.1 ± 0.2	1.0 (0.7)	no
12	”	”	1.5 ± 0.1	0.4 (0.3)	ICE–3G
13	”	”	1.4 ± 0.1	0.4 (0.3)	ICE–5G
14	”	”	1.5 ± 0.1	0.4 (0.3)	ANU05
15	SG01	22	$1.5 \pm 0.1^*$	0.4 (0.3)	ICE–3G, ICE–5G or ANU05[a]
16	SG01	22	1.5 ± 0.1	0.4 (0.3)	ICE–5G[b]

[a] Accounts for the effect of the rotational feedback on sea level change according to the theory outlined by Milne and Mitrovica (1998).
[b] Includes simulation of the horizontal migration of shorelines (rotational effects are neglected).

As a possible alternative to D97 and D97R, in section 2.4.1 and in the subsequent discussion we have defined set SG01 (the 22 SG01 TGs, with individual rates and basic data, are listed in Table 2.5). According to Equation 2.15, TGs belonging to SG01 are characterized by a GIA correction that is essentially independent from the particular model employed to determine it. The

application of this constraint makes the process of TG selection less prone to contamination from possible errors in GIA models and, consequently, the assessment of GMSLR more robust overall. The SG01 results of Table 2.6 (see estimates 11.–14.) reveal that for this set of TGs the application of the GIA correction implies a sizable modification of μ, contrary to what we observe for D97. The reason is the presence, in SG01, of the two sites of Heimsjo and and Smogen, located close to the former Fennoscandian ice sheet, and characterized by neatly negative sea–level trends (see Fig. 2.12). Consistently with the constraint of Equation 2.15, after GIA correction the GMSLR obtained using the SG01 TGs is largely independent on the model adopted for compute the correction, and point to a value of $\mu' = 1.5 \pm 0.1$ (*rms*=0.4, *wrms*=0.3 mm yr^{-1}). This value represents our "preferred" GMSLR estimate so far. By further computations, we have verified that excluding from SG01 the two sites of Heimsjo and Smogen, which clearly would appear as outliers with respect to the ρ_k values listed in Table 2.5, would not change the value of μ' nor that of *rms* and *wrms* at the 0.1 mm yr^{-1}level. In this case, similarly to D97R, the condition $\mu' \approx \mu$ would be attained.

In all the GMSLR estimates of Table 2.6 discussed so far (n. 1–15), our GIA modeling has been performed neglecting the effects on sea–level variations from the rotational feedback on sea–level variations (Milne and Mitrovica, 1998). Even a cursory inspection of Fig. 2.9 reveals that polar motion produces long–wavelength sea–level variations of a few fractions of millimeters per year, which are particularly visible in the southern hemisphere, where they are not overwhelmed by the sea–level changes directly associated with the melting of the major ice sheets of the northern hemisphere. Their pattern is dominated by a degree 2 order 1 harmonic term, with is associated with the variations of the Earth's centrifugal potential (Munk and Macdonald, 1975). A site–by–site analysis (see last columns of Table 2.5), shows that that present–day rates of sea–level change at the SG01 TGs are perturbed by as much as 0.2 mm yr^{-1}, well above the typical *sdom* in Table 2.6. This is in perfect agreement with the estimates of Milne and Mitrovica (1998), although these were totally based on rates of sea–level change extrapolated from the analysis of Relative Sea Level (RSL) curves in response to the melting of late–Pleistocene ice sheets. Of course, the significance of individual GIA corrections does not necessarily imply that the Earth's rotational response is effectively affecting the GMSLR estimate, since according to Equation 2.13 the value of m' depends on the TG–averaged r_k^{gia} values. When this average is computed, all the GIA–corrected GMSLR estimates indicate the same μ' value (see estimate n. 16), which does not depart (at the 0.1 mm yr^{-1} level), with our "preferred estimate" $\mu' = 1.5 \pm 0.1$ (*rms*=0.4 mm yr^{-1}, *wrms*=0.3 mm yr^{-1}), obtained neglecting the rotational effects on sea–level change. As a further test on the effects of approximations in GIA modeling, we have abandoned the fixed–shorelines approximation. In particular, we have implemented, for model ICE–5G, the iterative method outlined by Peltier (2004), which allows for a reconstruction of the paleo–topography since the Last Glacial Maximum. However, as shown by estimate n. 16 of Table 2.6, adding the realistic feature of migrating shorelines doest not modify, at the 0.1 mm yr^{-1}level, our preferred value of GMSLR .

Since the SG01 set does not contain TGs that are "too close" to active plate boundaries, tectonic vertical deformations can never be totally discounted (see *http://www.pol.ac.uk/psmsl/˜landmove.html*). As anticipated in subsection 1.3.4, previous studies (Melini et al., 2004; Melini and Piersanti, 2006), have demonstrated that estimates of secular sea–level variations that do not account for the

effects of global seismicity are likely to be overestimated by ~ 0.2 mm yr^{-1}. This will not change dramatically our estimates listed in Table 2.6, but nevertheless such effects exceed the *sdom* associated with the secular sea–level trend and therefore call for further investigations, also in view of some recent advancements of the theory framework (Melini et al., 2010).

Although a direct modelization is not possible, by simple arguments we can estimate the potential effect that regional tectonic deformations could have in the GMSLR estimates of Table 2.6. For instance, let us assume that the four Mediterranean TGs belonging to the SG01 set (Marseille, Genova, Trieste, and Bakar, see Table 2.5) are coherently affected by a rate of secular sea–level change of tectonic origin of constant amplitude r^{tect}, while it is assumed that random deformations acting on the remaining sites have a cumulatively negligible effect. Using Equation 2.5, it is easy to see that in order to affect the value of m by an amount $\geq 2 \cdot sdom$, the condition $r^{tect} \geq 1$ mm yr^{-1}should be approximately met if one assumes $sdom \approx 0.1$ mm yr^{-1}. This appears to be unrealistic as an order of magnitude of the typical tectonic trend in the Northern Mediterranean area (Tsimplis et al., 2011). Thought not supported by rigorous quantitative arguments, the above suggests that estimates of μ obtained by the D97, D97R and the SG01 sets are reasonably devoid of important tectonic effects, although individual sites can be certainly affected by local deformations associated with the global seismic activity (Melini et al., 2004).

Finally, using the series in the SG01 set, we have also estimated the GMSLR for the period 1993–2009 (Church and White, 2011). Starting from 1993, altimeter satellite data became available and this now makes it possible a comparison with results based on the TG record. The sea–level trend for the recent period 1993–2009 is broadly recognized to exceed the average secular value. Our ICE–5G corrected result $\mu' = 3.6 \pm 0.5$ mm yr^{-1}, which is based on the 12 TGs with completeness $> 75\%$ during this time period, is found to be consistent with the independent evaluation by Church and White (2011) for the same period, based on altimetry data ($\mu' = 3.2 \pm 0.4$ mm yr^{-1}) and is comparable with that assessed by the same authors using only TG observations ($\mu' = 2.8 \pm 0.8$ mm yr^{-1}). According to Bindoff et al. (2007) these increases may partly reflect decadal variability rather than a genuine acceleration, since in this period thermal expansion is much larger then during the whole 20th century and the melting of continental ice contributes for 1.2 ± 0.4 mm yr^{-1}to total sea–level rise.

Chapter 3

Sea level patterns at low harmonic degree

3.1 Spatial variability in sea–level change

The present day sea–level spatial variability is one of the most important issues related to climate change (Bindoff et al., 2007). As well as the assessment of a spatial average (the global mean sea–level), the understanding of the sea level spatial variability, originating from significant geographically non–uniform sea level fluctuations, is of great importance, having a direct impact on coastal hazard and society (Spada and Galassi, 2012).

Sea–level variability is the expression of climate variability and ocean dynamics. On short time scales (days to months) the factors that mostly influence sea–level variability are those linked to meteorology (oceanic currents, change in atmospheric pressure, ...). For longer time scales (from decade to century), as discussed in section 1.3, other factors have to be taken into account (GIA, present ice melting, thermosteric variations). Unfortunately, the incomplete understanding of ocean thermal expansion, uncertainties in the estimates of glaciers mass balance, and the stability of ice sheets limit our understanding of sea–level variability.

In this chapter, the sea–level variability at low wavelenght has been analyzed using a spherical harmonic (SH) approach. The spatial characteristic of variability at low–degree can be used to identify the physical causes. A similar approach has been used in previous studies, using Empirical Orthogonal Functions (EOFs) instead of harmonic decomposition (see Nerem and Mitchum, 2001, and references therein). Here, starting from tide gauge measurements, we attempt to estimate the contribution of different factors to sea–level variability. In particular, following the work of Nakiboglu and Lambeck (1991), low–degree signals have been investigated. In addition, similarly to what Mitrovica et al. (2001) have done, we attempt to constrain the mass balance of glaciers and ice sheets during the last century.

The chapter is divided in two parts. In the first, the classical spherical harmonics expansion, proposed to investigate similar issues by Nakiboglu and Lambeck (1991), is applied in order to

understand the possible contribution of ice melting to sea–level change. Being our interest focused on the last century, tide gauge measurements have been used. In the second part, we apply the more accurate method proposed by Hwang (1993) to test the robustness of the use of spherical harmonic decomposition in sea–level variability.

3.2 The Spherical Harmonic Expansion (SHE) approach

In this first step, classical Spherical Harmonic Expansion (SHE) method has been used for the assessment of spatial variability of sea–level trend. The maximum degree achievable depends on the density of data points used and on their spatial distribution: considering the structure of the tide gauge network, only a low–degree expansion seems to be possible *a priori*. Nevertheless, this kind of expansion can give information on the leading mechanisms of the spatial variability. The SHE method for the spatial variability of sea–level trend was used first by Nakiboglu and Lambeck (1991). They expanded in surface spherical harmonic series the secular trends estimated from tide gauges trends averaged across $10^\circ \times 10^\circ$ regions. As far as we know, the method of Nakiboglu and Lambeck (1991) has not been followed by others.

The convention for the SHE is the same used in Spada and Stocchi (2005):

$$Y_{lm}(\theta,\lambda) = \mu_{lm} P_{lm}(cos\theta) e^{im\lambda}, \tag{3.1}$$

where $i = \sqrt{-1}$, P_{lm} is the associated Legendre function of degree l ($l = 0,1,2,...$) and order m ($m = 0,1,2,...,l$), and θ and λ are colatitude and longitude, respectively. The normalization constant

$$\mu_{lm} = \sqrt{\frac{(2l+1)(l-m)!}{4\pi(l+m)!}} \tag{3.2}$$

ensures that the following orthogonality relationship holds

$$\int_\Omega Y^*_{l'm'}(\theta,\lambda) Y_{lm}(\theta,\lambda) d\Omega = \delta_{ll'}\delta_{mm'}, \tag{3.3}$$

where the asterisk denotes complex conjugation, δ_{ij} is the Kronecker delta, spherical harmonics with negative order are obtained by

$$Y_{l-m}(\theta,\lambda) \equiv (-)^m Y^*_{lm}(\theta,\lambda), \tag{3.4}$$

and, for any function $(\cdot)$,

$$\int_\Omega (\cdot) d\Omega = \int_0^{2\pi}\int_0^{\pi} (\cdot) sin\theta d\theta d\lambda. \tag{3.5}$$

The rates of sea–level at a given location is expanded as follows

$$r(\theta,\lambda) = \sum_{l=0}^{l_{max}} \sum_{m=-l}^{l} C_{lm} Y_{lm}(\theta,\lambda). \tag{3.6}$$

Assuming for $r(\theta,\lambda)$ a δ–like distribution

$$r(\theta,\lambda) = \sum_k r_k \delta(\omega - \omega_k), \tag{3.7}$$

one obtains

$$C_{lm} = \sum_k r_k Y^*_{lm}(\omega_k). \tag{3.8}$$

Considering the real spherical harmonic expansion we can write

$$r(\theta,\lambda) = \sum_{l=0}^{l_{max}} \sum_{m=0}^{l} (a_{lm} cos\ m\lambda + b_{lm} sin\ m\lambda) P_{lm}(cos\ \theta) \tag{3.9}$$

where

$$\begin{Bmatrix} a_{lm} \\ b_{lm} \end{Bmatrix} = (2 - \delta_{0m}) \begin{Bmatrix} +Re(C_{lm}) \\ -Im(C_{lm}) \end{Bmatrix}. \tag{3.10}$$

While $r(\theta,\lambda)$ is a function defined on the whole ocean, r_k^{obs} is defined only at tide gauge locations. The system

$$r_k^{obs} = \sum_k C_{lm} Y_{lm}(\theta_k, \lambda_k) \tag{3.11}$$

can be cast in a last–squares form and solved by means of SVD method. The system of equation has the form

$$\vec{b} = A\vec{x} \tag{3.12}$$

where $\vec{b}$ is contains the k–sea–level observations, the array A contains the SH computed at θ_k, λ_k and $\vec{x}$ is the vector of the unknowns C_{lm}. In this way, the vector of the unknown solution $\vec{x}$ gives us the complex spherical harmonic coefficients that minimize the different between the field $r(\theta,\lambda)$ and the tide gauge sea–level observations. In the following we will refer to this approach as SVD–SHE. The uncertainty has been extracted from a random uniform distribution and computing the rms of the distribution of $1,000$ solutions obtained (Press et al., 1992; Baker, 1997).

To compare the spherical harmonic coefficients obtained with SVD–SHE for two different input sets, the coefficient k_l was used, defined as:

$$k_l = \frac{\sum_{m=0}^{l} (C^A_{lm} \cdot C^B_{lm})}{\sqrt{\sum_{m=0}^{l} (C^A_{lm})^2 \cdot \sum_{m=0}^{l} (C^B_{lm})^2}}, \tag{3.13}$$

where $C^A_{l,m}$ and $C^B_{l,m}$ represent the harmonic coefficients obtained with two different input sets. For each harmonic degree l, the values of k represent the correlation between the fields, that ranges between 1 (perfect correlation) and 0 (no correlation).

3.3 Observed sea level data for spatial analysis

3.3.1 Tide gauges selection for spatial analysis

As illustrated at length in chapter 2, there are many factors that, locally, can invalidate reliability of a TG data set and that suggest the adoption of an appropriate selection.

The use of TGs for a SHE entails other problems: the SHE is sensitive to the quantity and distribution of the input points as well as the quality of data. If restrictive criteria for TG selection are imposed, too few points will remain for the SVD-SHE. Here, we use the ALL set introduced in chapter 2 as the basis for further selections. In order to obtain a TG set representative of secular sea–level trend and suitable for the work planned here, the following criteria have been applied:

i. the TG time series must be of sufficient length (at least 60 years);

ii. the series must have a sufficient completeness ($> 70\%$);

iii. the series must be in reasonable agreement with nearby gauges;

iv. the TGs must be sufficiently distant from collisional tectonic boundaries.

These criteria have been used in previous works for the assessment of secular global mean sea level rise, as discussed in chapter 2. The first two criteria (i. and ii.) address the concern that the period recorded from each TG selected is representative of the secular sea level trend. Douglas (1997), in his seminal work, has pointed out that for a secular assessment of sea level rise the TG series must be at least 60 years in length and must have a completeness $> 80\%$. In Spada and Galassi (2012) a completeness of 70% is also considered. The other criteria are used to ensure the reliability of the data for the TGs selected, as they remove TGs with clear problems in the series. Criterion *iii* removes TGs whose trends differ from those of near gauges (distance < 200 km) more than 1 σ (computed on the distribution selected with the first two criteria). Criterion *iv* has been used by Douglas (1997) and excludes TGs with persistent tectonic problems. In addition, we excluded also TGs sampling inland water (as for those on the Black Sea or those on the Saint Lawrence River, Canada). Applying the above criteria, we obtained a set of 101 TGs, the T60C70 set, whose distribution in shown in Fig. 3.1, where the histogram shows the distribution of sea level values during the selection procedure.

In Fig. 3.2 we show the results of a synthetic test performed to verify the reliability of the selected set for the SVD–SHE. The vector $\vec{b}$ in Equation 3.12 is constructed considering an arbitrary amount (1 mm yr^{-1}) at tide gauge locations, for the T60C70 and the ALL sets, respectively. The aim of the test in to verify the compliance between the fingerprint reproduced with the SHE using only the TG points (from the ALL or from the T60C70 set) and the shape of SHE expected for the same harmonic degree with an uniform coverage of the sphere. For degrees 1 and 2, the patterns obtained are those expected for the corresponding harmonic degrees; this is true for both the T60C70 and the ALL sets. For the harmonic degree 3, the shape of the fingerprint departs from the expected one, and this departure is more evident for the T60C70 because of the poorer

Table 3.1: Lithospheric thickness and mantle viscosity for the GIA models employed in this study. MT1 uses the VM2 viscosity profile of Peltier (2004) while S-I5G values have been obtained by volume–averaging the original VM2 viscosity profile; S-KL05 values are taken from Fleming and Lambeck (2004).

Rheological parameter	GIA model			
	S-I5G	S-KL05	MT1	MT2
Lithospheric thickness (km)	90	65	90	71
Upper mantle viscosity ($\times 10^{21}$ Pa·s)	0.5	0.3	$VM2$	0.3
Lower mantle viscosity ($\times 10^{21}$ Pa·s)	2.7	10	$VM2$	10

distribution of input points. This test suggests that a SVD–SHE analysis for the T60C70 is likely to be possible only until the degree two.

3.3.2 GIA effects at tide gauge locations

Based on Equation 1.3, we know that sea–level trend observed at a particular location, is the sum of different contributions. In the following, we model some of these contributions (namely, GIA, STE and MAS, for the present ice melting components) and we obtain their distribution up to harmonic degree 2.

To address the effect of GIA upon the estimate of sea level variability at low–degree, in this work two different approaches have been used. In both, the the GIA component of sea level change is evaluated solving the "Sea Level Equation" (see Equation 1.22 in subsection 1.4.1).

The first approach (a pseudospectral iterative solution of the Equation 1.22 using an improved version of code SELEN) is described in subsection 1.4.2, as well as the two time–histories of the late–Pleistocene ice sheets are used (ICE–5G and KL05). The second approach follows the theory presented in Kendall et al. (2005) and Tamisiea (2011): the GIA-induced perturbation in global sea level is computed by a pseudospectral approach (Mitrovica and Peltier, 1991). In this approach, two different models are used to reproduce the fingerprint of sea–level change (S^{GIA} in Equation 1.1) and its rate (r^{GIA} in Equation 1.3), both using ICE-5G model. In the following we will refer to the first two as S-I5G and S-KL05, respectively, while the latter will be named MT1 and MT2, respectively. The rheological profiles used for the models considered here are shown in Table 3.1.

To test the sensitivity of the SVD–SHE to the GIA-model used, the correlation between coefficients derived from the spherical harmonic expansion for corrected rate have been evaluated with Equation 3.13: the results are presented in Fig. 3.3. It is interesting to note that for the ALL-set (red symbols in Fig. 3.3) the correlation at degree 2 is significantly lower than at degree 1 or 3: this reflect the fact that GIA effects are dominant ad degree 2 and little differences in the models result in large differences in final outcomes. When ice thickness and distribution and rehological profile are similar, as is the case of S-I5G and MT1 (marked by square in Fig. 3.3), the correlation

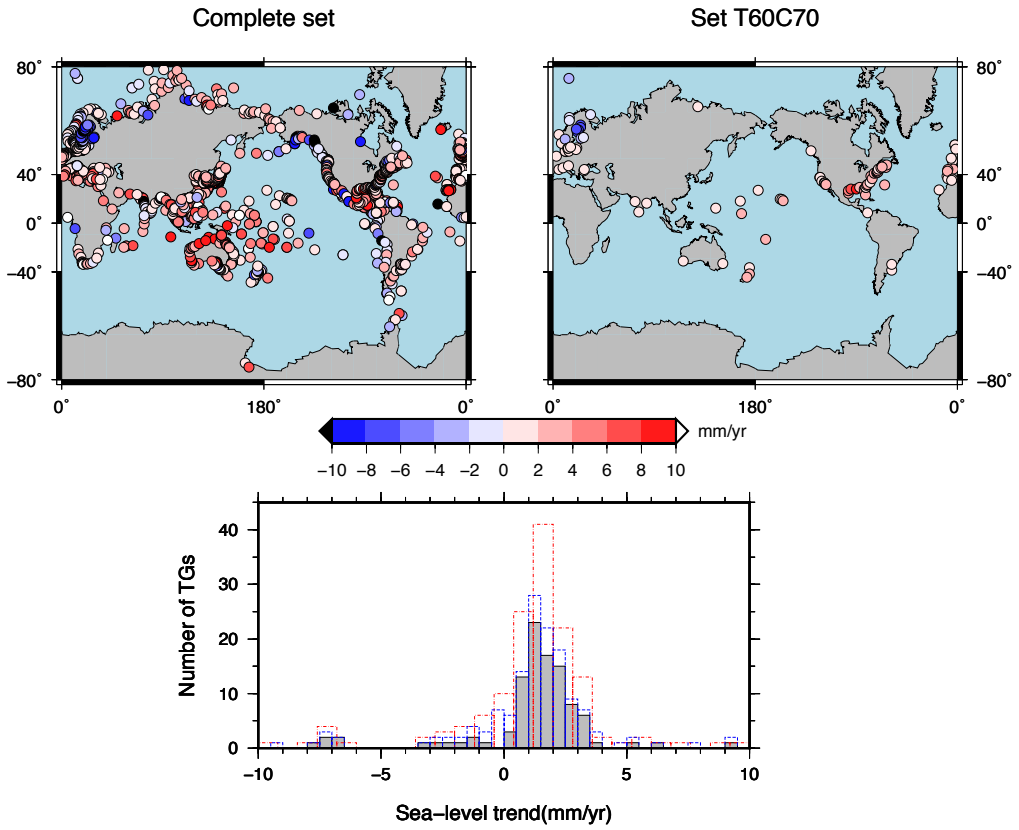

Figure 3.1: Tide gauges distribution for T60C70 set: the colors show the sea level trend (mm yr^{-1}) at each station. The histogram shows the frequency of sea level values in the selection procedure (red-dashed/dotted line for the set obtained selecting for the time length and completeness only, blue-dashed line adding the comparison between near TGs and full gray bar for the complete selection).

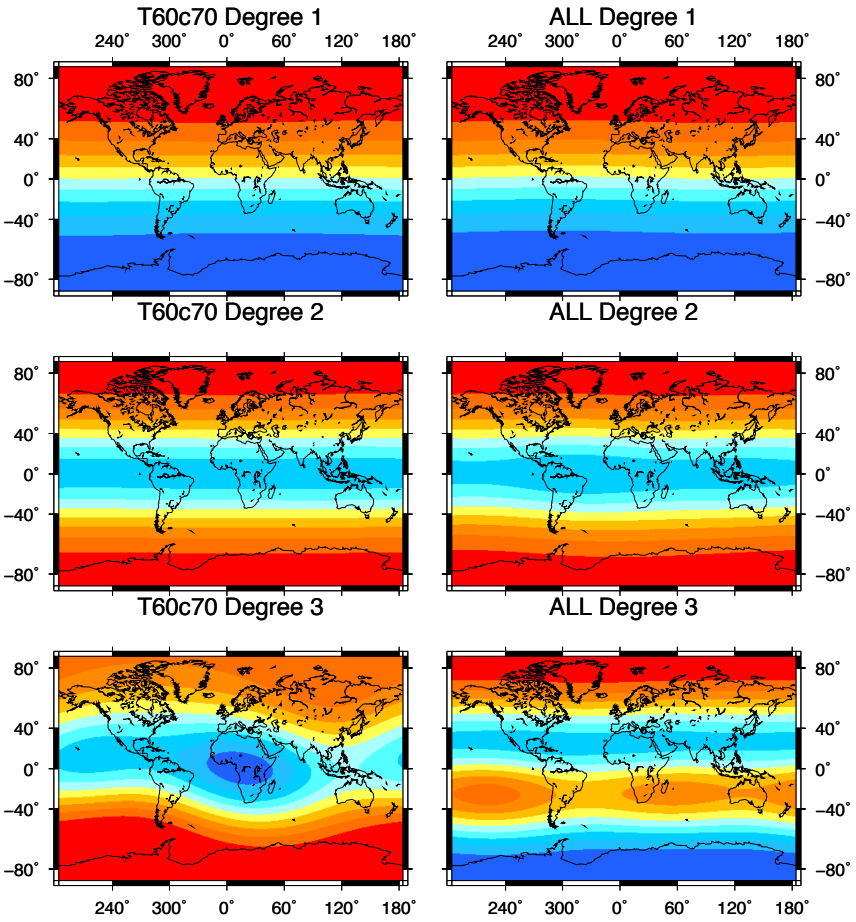

Figure 3.2: SVD–SHE based on tide gauges distribution, using for the $\vec{b}$ in Equation 3.12 synthetic values, instead of observed sea–level values.

coefficient assumes high values even at degree 2 ($k_2 = 0.991$). With T60C70 set (black symbols in Fig. 3.3), degree 1 shows low values of correlation (even anti–correlation for MT2 compared with other models). This could be explained by the number and the distribution of TGs in this set: the location of the few TGs available in North Europe and in North America (both areas strongly influenced by GIA) maximize the effect of the difference between models.

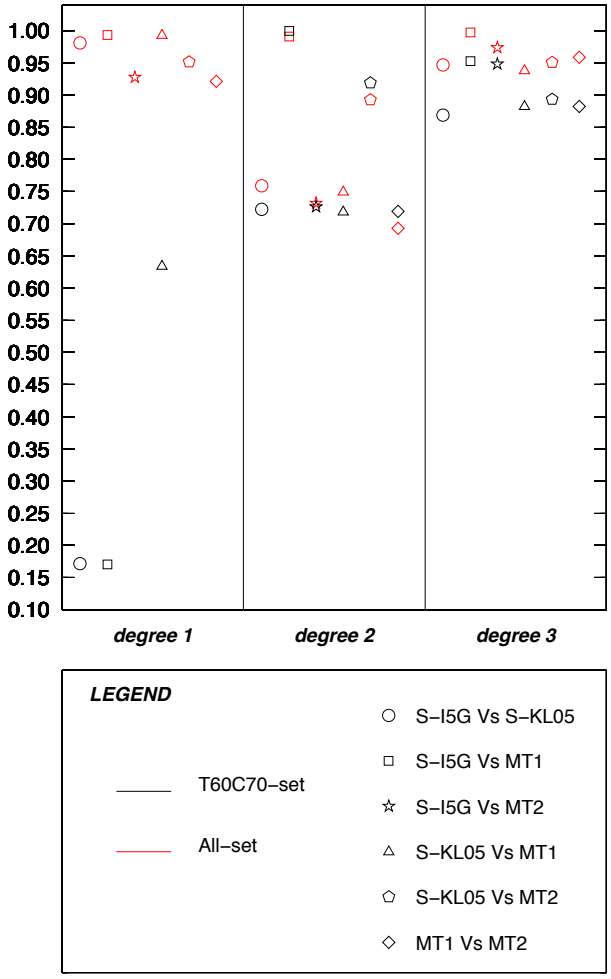

Figure 3.3: Correlation coefficient for SVD–SHE of corrected rate: the sea–level trends corrected with different GIA models have been compared in pairs.

Finally, spherical harmonic coefficients for the GIA predictions are compared to those obtained with the SVD–SHE of the GIA values of the corresponding model at the TG points. The k_l resulting

are shown in Table 3.2. These results show that the SVD–SHE is not completely suitable to detect the spatial variability of GIA, especially if a limited number of input points is used. Thereby, in the following analysis the GIA contribution to sea level variation will be subtracted from the observed rate at each TG points before the SVD–SHE.

Table 3.2: Correlation k_l at degree 2 between C_{lm} for the GIA computation obtained directly from GIA models and from SVD–SHE.

Gia-Model	ALL-set	T60C70 -set
S-I5G	0.855	0.687
S-KL05	0.841	0.971
MT1	0.851	0.853
MT2	0.884	0.742

3.4 SVD–SHE results

The SVD–SHE has been applied to TG observed sea–level for both ALL and T60C70 sets: the results are shown in Table 3.3. Initially, no corrections (GIA or thermo–steric) have been applied. The first column of Table 3.3 shows the C_{lm} values (with the subscripts a and b labeling the cosine and sine coefficents, respectively) obtained in Nakiboglu and Lambeck (1991): the correlation between these coefficients and those obtained with SVD–SHE is large, being $k_2 = 0.978$ for the ALL-set and $k_2 = 0.944$ for the T60C70-set. The C_{00a} coefficient, representing the global mean sea–level trend, ranges between 1.4 and 1.6 mm yr^{-1}, in agreement with that resulting from the analysis of TGs performed in chapter 2. The relevance of coefficient C_{20a} in all the three situation considered, reveals the importance of the two main sources of present ice melting (Antarctica and Greenland) in sea–level variability. The presence of other coefficients with non negligible values, especially C_{21b} for all the case, C_{11b} for the ALL-set and C_{10a} for the T60C70-set, evidences the relevance of processes with and hight spatial variability (as present melting of small glaciers, oceanic processes, etc.).

The sea–level trends detected from TGs in the ALL- and T60C70- sets are then corrected for the GIA and for thermo–steric effects. The correction consists in removing the signals deriving form specific sources (in the case, from GIA and thermosteric effects) from the sealevel signal directly observed by each TGs, before the SVD–SHE. For thermo–steric correction, EN66 (Ishii and Kimoto, 2009) and IS45 (Ingleby and Huddleston, 2007) datasets, presented in subsection 1.3.1, have been used. The trends thermo–steric sea–level in EN66 and in IS45 are referred to relatively long periods (1966–2010 and 1945–2010, respectively) and are then adequate for a correction on the secular observed sealevel trend. For the GIA correction, since different GIA models show a good correlation in SVD–SHE, we use here only the S-I5G model. The results are shown in

Table 3.3: Spherical harmonic coefficients C_{lm} from SVD–SHE for the ALL set (1211 TGs) and the T60C70 set (101 TGs) without GIA correction applied, compared with the C_{lm} value obtained by Nakiboglu and Lambeck (1991). Cosine and sine coefficients are labelled with subscripts a and b respectively. Units are in mm yr^{-1}.

	N-L 1991	at ALL-set	T60C70-set
C_{00a}	$+1.50 \pm 0.38$	$+1.60 \pm 0.11$	$+1.42 \pm 0.03$
C_{10a}	-0.14 ± 0.30	-0.03 ± 0.13	-0.40 ± 0.04
C_{11a}	-0.07 ± 0.27	-0.16 ± 0.06	-0.38 ± 0.02
C_{11b}	-0.24 ± 0.26	$+0.43 \pm 0.04$	-0.28 ± 0.01
C_{20a}	-0.86 ± 0.25	-0.81 ± 0.11	-1.52 ± 0.03
C_{21a}	-0.01 ± 0.23	$+0.15 \pm 0.02$	-0.11 ± 0.01
C_{21b}	-0.54 ± 0.23	-0.47 ± 0.03	-0.60 ± 0.01
C_{22a}	$+0.12 \pm 0.20$	$+0.04 \pm 0.00$	$+0.20 \pm 0.00$
C_{22b}	$+0.27 \pm 0.21$	$+0.37 \pm 0.02$	-0.03 ± 0.02

Table 3.4, where the forth and fifth columns show what remains to the observed trend after the sea–level induced by GIA and thermo–steric effects has been removed, respectively. According to Equation 1.3, these corrected trends can be explained with the contribution of present ice melting.

The global values of the corrected trend (C_{00a}) range between $+1.34$ and $+1.61$ mm yr^{-1} for the ALL set and between $+0.59$ and $+0.95$ mm yr^{-1} for the T60C70 set. This is in agreement with the total contribution of terrestrial ice melting (TIM) to sea–level rise assessed by IPCC. The IPCC AR4 (Bindoff et al., 2007) has assessed that for the period 1961–2003 the contribution of the three major ice source (Glaciers and ice caps, Antarctica and Greenland ice sheets) to sea–level trend was ~ 0.59 mm yr^{-1}, and that it was grown to 1.19 mm yr^{-1} considering only the period 1993–2003. The main contributor is Greenland, with 0.50 ± 0.18 and 0.77 ± 0.22 mm yr^{-1} in the two periods considered, respectively. According to AR5 (Church et al., 2013) the total contribution during 1993–2010 was 1.47 mm yr^{-1}. This suggests the importance to investigate the spatial variability of TIM contribution to sea–level.

To evaluate the contribution to the sea–level pattern resulting from land ice mass variations and to compare it with TG observed sea–level trend and with the residue remaining after GIA and thermo–steric correction, we need estimates of land ice changes within a given time interval. Unfortunately, as illustrated in section 1.2, even if many recent studies have investigated these mass balances using varying methods, they are usually referred to the period 1993 till present, corresponding to the satellite era. Lack of agreement between techniques and the small number of estimates explains the large differences between different studies and precludes the assignment of statistically rigorous error bounds (Lemke et al., 2007).

To solve this problem, two different approaches have been here applied. First, using published mass balance for glaciers and ice–sheets, the sea–level fingerprint of present ice melting have been reconstructed and the harmonic coefficients to degree 2 have been extracted. In addition, following

Table 3.4: SVD–SHE results for uncorrected and corrected TG data. The correction for the GIA effect was computed with S-I5G; for the thermosteric field, EN66 and IS45 were used. Units are in mm yr^{-1}.

C_{lm}	Uncorrected	With GIA correction	With GIA and Steric EN66 correction	With GIA and Steric IS45 correction
ALL set				
C_{00a}	$+1.60 \pm 0.11$	$+1.83$	$+1.34$	$+1.61$
C_{10a}	-0.03 ± 0.13	-0.14	-0.16	-0.15
C_{11a}	-0.16 ± 0.06	-0.10	-0.01	-0.12
C_{11b}	$+0.43 \pm 0.04$	$+0.50$	$+0.50$	$+0.48$
C_{20a}	-0.81 ± 0.11	-0.23	-0.23	-0.23
C_{21a}	$+0.15 \pm 0.02$	-0.05	-0.08	-0.03
C_{21b}	-0.50 ± 0.03	-0.20	-0.23	-0.19
C_{22a}	$+0.04 \pm 0.00$	-0.09	-0.15	-0.06
C_{22b}	$+0.37 \pm 0.02$	$+0.29$	$+0.26$	$+0.30$
T60C70 set				
C_{00a}	$+1.42 \pm 0.03$	$+1.24$	$+0.59$	$+0.95$
C_{10a}	-0.40 ± 0.04	$+0.34$	$+0.47$	$+0.30$
C_{11a}	-0.38 ± 0.02	$+0.50$	$+0.50$	$+0.48$
C_{11b}	-0.28 ± 0.01	-0.47	-0.54	-0.53
C_{20a}	-1.52 ± 0.03	-0.50	-0.56	-0.49
C_{21a}	-0.11 ± 0.01	-0.48	-0.57	-0.49
C_{21b}	-0.60 ± 0.01	$+0.39$	$+0.46$	$+0.45$
C_{22a}	$+0.20 \pm 0.00$	-0.22	-0.33	-0.27
C_{22b}	-0.03 ± 0.02	$+0.00$	$+0.22$	$+0.00$

the example of Mitrovica et al. (2001), we have extrapolated a mass balance for present ice sources, minimizing the difference between the residual and the fingerprint obtained with an uniform ice loss.

In both approaches, the sea–level fingerprint of present ice melting has been computed solving the SLE with the code SELEN, as illustrated in subsection 1.4.3, at degree 128 with a uniform mass loss of 100 Gt yr^{-1}. The SVD–SHE has been then applied to fingerprint values at tide gauges location and the harmonic coefficients up to degree two have been obtained for the ALL and the T60C70 sets.

To obtain an assessment of present ice melting contribution to observed sea–level trend, the harmonic coefficients obtained have been scaled with the published mass balances shown in table 3.5. Results are presented in Table 3.6, where last two columns ("residuals") show what remain subtracting from the observed trend (corrected for GIA and steric effects, this latter with EN66 and IS45 respectively) the contribution of terrestrial ice melting.

Table 3.5: Mass balance and in equivalent sea level (esl), for the melting of the three ice sources considered, during period 1961–2003. Negative values for the mass balance correspond to ice loss and imply a positive rate of ESL.

	GIS	AIS	GIC
Ice loss (Gt yr^{-1})	-50.4	-68.4	-183
ESL (mm yr^{-1})	$+0.14$	$+0.19$	$+0.51$

For both the ALL and T60C70 TG sets, the residuals show negative values for C_{00a}, namely -0.97 mm yr^{-1} for EN66 and -0.61 mm yr^{-1} for IS45. This suggest that mass balances used for GIC, GIS and AIS are over–estimated. The overestimation of mass balance used is confirmed by the positive, non negligible residual for the coefficient C_{20a} ($+0.45$ for EN66 and $+0.52$ for IS45). Since the C_{20a} represents the zonal pattern with negative values at the pole, positive values for the residual imply that an excess signal has been subtracted from the corrected sea–level. Probably, the reason resides in the period to which the balances are referred: during 1961–2003 the rate of melting could be larger than in the whole 20^{th} century. The other coefficient with non negligible residual is the C_{11b}: this reflects the sectorial distribution of sea–level along the East-West gradient. The interpretation of possible causes of this residual is not straightforward, but it is likely associated with the distribution of small glaciers.

In the second approach, through an inversion process, we have found mass balance that minimizes the difference between harmonic coefficients of the TIM fingerprint and the observed sea–level rate. This approach has been presented for the first time by Mitrovica et al. (2001). The TIM fingerprint has been obtained with a uniform loss of 100 Gt yr^{-1}, according to models presented in subsection 1.4.3; the observed rate has been corrected for GIA effects with S-I5G; in addition, according to Mitrovica et al. (2001), an uniform trend of 1 mm yr^{-1} has been removed to take in to account thermo–steric effects. Three tests have been performed. In the first (Test 1), the three

Table 3.6: Spherical Harmonic Coefficients (C_{lm}) from SVD–SHE for sea level fingerprint of present ice melting at TG locations (ALL set and T60C70 respectively), considering mass balances presented in table 3.5. Column Residuals shows what remain subtracting from the observed trend (corrected for GIA and steric effects, this latter with EN66 and IS45 respectively) the contribution of terrestrial ice melting.

C_{lm}	ALL set					
	AIS	GIS	GIC	Total fingerprint	Residuals EN66	IS45
C_{00a}	+0.44	+0.34	+0.92	+1.71	−0.36	−0.09
C_{10a}	+0.09	−0.06	−0.06	−0.03	−0.13	−0.12
C_{11a}	+0.01	+0.02	−0.03	−0.00	−0.01	−0.12
C_{11b}	+0.00	−0.00	+0.06	+0.06	+0.44	+0.42
C_{20a}	−0.06	−0.08	−0.53	−0.68	+0.44	+0.44
C_{21a}	+0.00	+0.05	−0.10	−0.05	−0.03	+0.02
C_{21b}	−0.00	+0.03	+0.05	+0.08	−0.31	−0.27
C_{22a}	+0.01	+0.01	+0.05	+0.07	−0.22	−0.13
C_{22b}	−0.00	−0.01	+0.15	+0.14	+0.12	+0.16
C_{lm}	ALL set					
	AIS	GIS	GIC	Total fingerprint	Residuals EN66	IS45
C_{00a}	+0.48	+0.35	+0.73	+1.57	−0.97	−0.61
C_{10a}	+0.05	−0.08	+0.14	+0.11	+0.36	+0.19
C_{11a}	+0.01	−0.01	+0.21	+0.22	+0.29	+0.27
C_{11b}	−0.00	+0.00	−0.14	−0.14	−0.40	−0.39
C_{20a}	−0.03	−0.12	−0.86	−1.00	+0.45	+0.52
C_{21a}	+0.00	+0.04	−0.37	−0.33	−0.24	−0.16
C_{21b}	+0.00	+0.01	+0.17	+0.18	+0.28	+0.27
C_{22a}	+0.00	+0.01	−0.08	−0.06	−0.26	−0.20
C_{22b}	+0.01	−0.02	+0.11	+0.09	+0.12	−0.10

ice sources AIS, GIC and GIS are inferred simultaneously. Mass balances resulting from Test 1, shown in Table 3.7, are quite in agreement with those published for the AIS but significantly greater for the GIS. The value obtained for GIC is not realistic, corresponding to 8.8 mm yr^{-1} of ESL. This suggest to perform Test 2, in which the mass balance for GIC is *a priori* set to an established value. The mass balance used to obtain result of Table 3.6, corresponding to -183 Gt yr^{-1}, is not adequate to represent the GIC contribution to sea–level rise referred to the last century. For this reason, in Test 2 we have set the mass balance for the GIC to -122 Gt yr^{-1}, corresponding to ~ 0.34 mm yr^{-1}, as previously done by Mitrovica et al. (2001). Whit this assumption the GIS mass balance is similar to that found in Test 1, but the one for the AIS is negative (indicating accretion) and near to balance. Following the work of Mitrovica et al. (2001), we have performed Test 3 introducing for the AIS a uniform loss of 36 Gt yr^{-1}, corresponding to ~ 0.1 mm yr^{-1} of ESL. In this way, the mass balance resulting for the GIS is $+179$ Gt yr^{-1}, still significantly larger than

published estimates.

Table 3.7: Mass balance estimates for present ice melting from spherical harmonic coefficients, for T60C50. Units are in Gt yr^{-1}.

	Test 1	Test 2	Test 3
GIS	-258	-234	-179
AIS	-68	$+14$	-36
GIC	-3168	-122	-122

The three tests performed show that the SVD–SHE approach gives back a mathematical solution of the problem, but that this solution is not apparently consistent previously estimates of TIM mass balances. Possible reasons are:

i. the poor input spatial distribution of data;

ii. possible inadequacies of method adopted (SVD–SHE);

iii. the small variance shown by TIM fingerprints compared to the other sea–level components.

The importance of the number and distribution of TG series used as data input has been extensively debated in subsection 3.3.1. As previously outlined, the limitation of method adopted mainly resides in the reproduction of harmonic functions on the whole surface of the sphere, even on the part not covered by oceans. In addition, results shown in the last part of this section, suggest that the contribution of TIM to sea–level, certainly important at global scale, has not enough energy to allowed detection in terms of spatial variability. In order to corroborate this latter hypotheses, it is necessary to explore the same problem with uniformly distributed data and possibly adopting a more suitable mathematical method.

3.5 An alternative approach: the Hilbert-Hwang method

The results obtained in section 3.4 do not explain properly all the contributions of sea–level signal at low–degree. In particular, it seems not possible to extrapolate the contribution of present ice melting from the observed sea–level trend. This difficulty is probably inherent in the method employed, which shows a number of limitations. First, SVD–SHE is strongly influenced by the distribution of the TGs used. Secondly, the classical harmonic expansion assumes that the signals is defined over the whole sphere, *i. e.* also across the continents. In addition, being the spherical harmonics non–othogonal over the oceans, the traditional spectral analysis of oceanic signals may lead to misleading results and consequently to wrong conclusions (Hwang, 1993). In order to test the opportunity of using a low–degree expansion in sea–level analysis, here an other approach has been applied.

Following the work of Hwang (1993) the SHs have been orthonormalized using a Gram–Schmidt process in a function space, constructing new sets of orthonormal (ON) functions. Hereinafter, we will refer to this method to as HH–SHE method. The classical SH functions, here succintly indicated by y_i, are orthonormal on the sphere:

$$\int_{sphere} y_i y_j^* dA = 4\pi\delta_{ij} \tag{3.14}$$

where i (and j) is a unique index representing order and degree of the harmonic function, being $i = \frac{l(l+1)}{2} + m + 1$.

According with the HH-SHE method it is possible to find a new ensemble of functions (y_i') orthonormal on an arbitrary finite domain, as the surface of the oceans:

$$y_i' = \int_{ocean} y_i' y_j'^{\star} dA \tag{3.15}$$

where the new set of "spherical" harmonic functions are mutually orthogonal on the oceans:

$$y_i' = \int_{ocean} y_i' y_j'^{*} = 4\pi\delta_{ij} \tag{3.16}$$

and are connected with the SHs by

$$y_i' = \sum_{j=1}^{i} c_{ij} y_j, \tag{3.17}$$

where c_{ij} are the combination coefficients in the orthonormalizing process. To compute C, the matrix of coefficients c_{ij}, following Hwang (1991) the Cholesky decomposition of the Gram matrix G is used,

$$G = CC^{+}, \tag{3.18}$$

$$G = LL^{+} \tag{3.19}$$

$$C = L^{-1}, \tag{3.20}$$

where L is the lower triangular matrix from the Cholesky decomposition (Wilkinson et al., 1965). Being known the coefficients c_{ij}, it is possible to perform a reconstruction of the set of image functions obeying to the orthonormality condition on the domain. The reconstruction on the chosen domain is then given by:

$$f = \sum_{j=1}^{n} f_j' y_j' = \sum_{i=1}^{n} \sum_{j=1}^{i} f_i c_{ij} y_j, \tag{3.21}$$

were f and f' are the harmonic coefficients of old and new functions, respectively (the new ON are found through Equation 3.17), y and y' are the old and new harmonic functions, respectively.

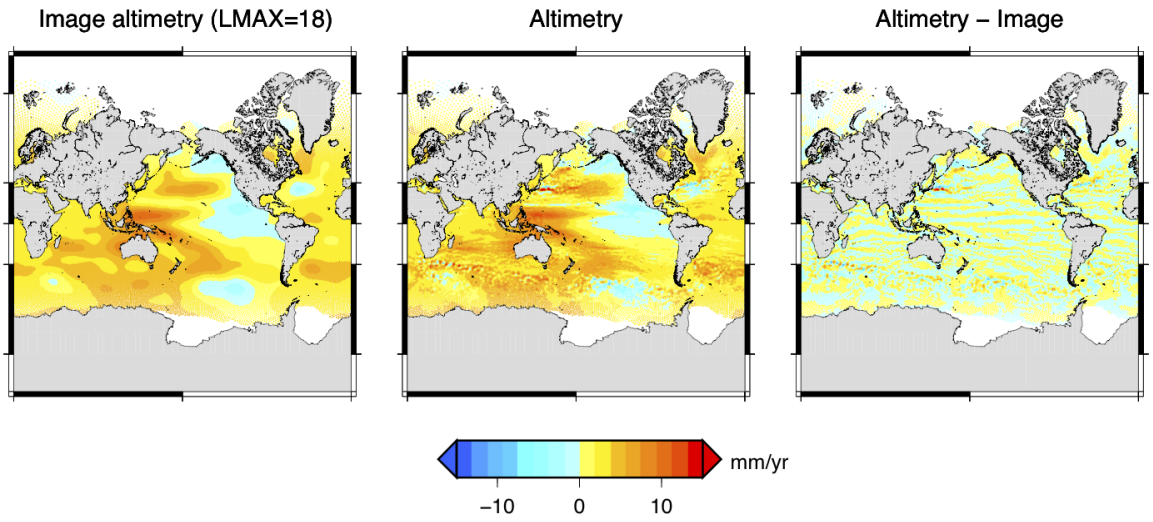

Figure 3.4: HH–SHE for altimeter sea–level data: image function (LMAX=18) for the altimeter observed sea–level trend (left frame), observed sea–level trend (central frame) and their difference (right frame).

3.6 Application of HH–SHE to sea–level data

The scope of the application of this method, is here to understand how much spherical harmonics are able to separate single components of sea–level variability. In order to minimize other possible source of uncertainty, and to drive the expansion to high degree (higher then the 2 allowed by TGs data) uniformly spaced data are needed. For this reason, we have used satellite altimeter measurements obtained from Mean Sea Level TOPEX/POSIDON altimetry sea–level global data for the period 1992–2005 from the AVISO database (*http://www.aviso.oceanobs.com*, see section 1.2 for further details).

With equation Equation 3.21 we have reconstructed the function for altimeter observed sea–level trend. In Fig. 3.4 are shown the image functions (left frame, for LMAX=18), the observed sea–level signal (central frame) and their difference (right frame). The difference between original and reconstructed is negligible, being its average lower than e 0.1 mm yr^{-1}. This confirms that with the HH–SHE method it is possible to satisfactory decompose our reconstructed observed signal.

Confident on the ability of the method, we have applied HH–SHE to the other main component of sea–level change, namely steric effects, GIA and TIM. For the steric component, data from National Oceanographic Data Center (NODC) of the NOAA have been used (see subsection 1.3.1). We have computed the trend for pendadal average from 1955–1959 to 2007–2011 of steric data at two different depths: 0–2000 m and 0–700 m respectively. For GIA and TIM we have obtained

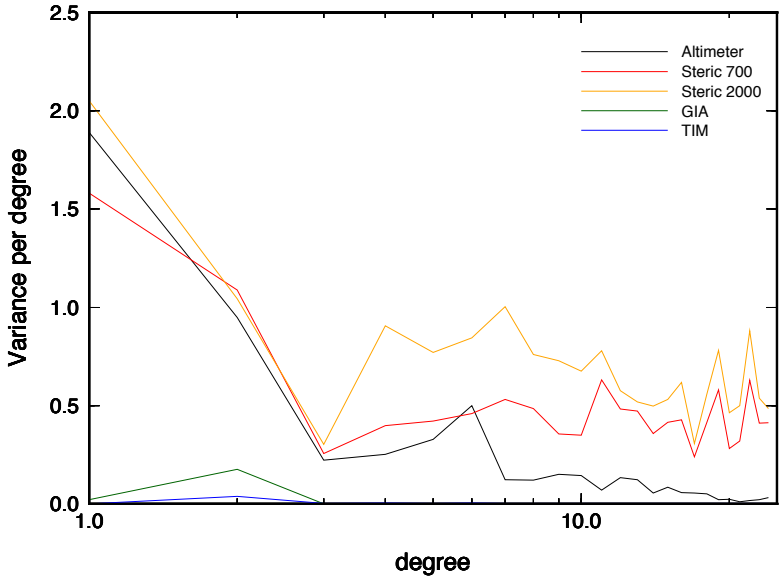

Figure 3.5: Spectrum (expressed in terms of variance per degree) for the reconstructed components of sea–level.

sea–level fingerprint using theory and models presented in section section 1.4. For GIA, ICE–5G (Peltier, 2004) has been used. For TIM, similarly to what done for SVD–SHE, the fingerprint has been obtained, according to subsection 1.4.3.

The image functions obtained for the altimeter observed sea–level trend and for each sea–level components with HH–SHE, have been analyzed in term of variance for degree. The scope was to understand if, at the same degree, the different components of sea–level variability have comparable energy. In Fig. 3.5 is clearly shown that only the steric component have a variability comparable, and even higher, to those shown by the observed trend at medium and high degree (> 3). GIA signal shows a detectable variance (~ 2.1) only at degree 2, reflecting the variability between north–south hemisphere of GIA signal. TIM components shows a degree of variance not appreciable in comparison with those exhibit by observed signal (in the order of magnitude of 10^{-2}): this is in agreement with the smoothed shape of the fingerprint obtained for TIM by models.

3.7 Main findings on SHE methods for sea–level analysis

In this chapter, the SHE has been used in order to analyze spatial variability of sea–level. The classical SH expansion, that reproduces functions on the whole sphere, has been used together with a singular values decomposition (SVD–SHE) on observed or modeled sea–level data. As observed sea–level trend, we have put in input TGs data that, in reason of theirs sparse and non–

uniform distribution, have only permitted a low–degree expansion (LMAX=2). The SVD–SHE reconstruction of the observed sea–level trend from TGs, corrected for GIA and thermo–steric effects, have been compared with modeled TIM fingerprint, in order to assess de magnitude of mass balance for glaciers and ice sheets at secular scale. Results have suggested that TIM contribution is not easily detectable in observed signal, even at low–degree, prompting to investigate through an other SHE approach.

Consequently, the Hilbert Hwang Empirical Orthogonal Function approach for SHE used by Hwang (1993) (HH–SHE) has been applied to altimeter data. The HH–SHE is able to reproduce image function (orthonormal to the classical harmonic function) for a chosen spatial domain (in this case, the ocean surface). In addition, the use of altimeter data avoids problems linked to non–uniform distribution of data and allows to drive the expansion till high degree. The analysis of variability at different degree of the image functions of altimeter observation, of steric data and of modeled GIA and TIM component shown that GIA and TIM contain to less variability, even at low–degree, to be detected in observed signal.

Chapter 4

Non–linear sea–level variations at tide gauges

As discussed in chapter 2, observations from the global array of tide gauges show that sea–level has been rising on average with rate of 1.5–2 mm yr^{-1} during the last $\sim$ 150 years. Although a global sea–level acceleration was initially ruled out (Douglas, 1992), subsequent studies have coherently proposed values of $\sim$ 1 mm yr^{-2} (Church and White, 2006; Jevrejeva et al., 2008). More complex non–linear trends and abrupt sea–level variations have also been recognized (Olivieri and Spada, 2013). Globally, these could manifest a regime shift between the late Holocene and the current rhythms of sea–level rise, while locally they result from ocean circulation anomalies, steric effects and wind stress.

In previous chapters, linear variations of sea–level have been investigated. In this chapter, the attention is focused on non–linear components of sea–level through the analysis of TG data. To do that, different approaches have been applied to address different questions. For each of them, the general theory has been applied to a specific case of study. Differently from the previous chapters, devoted to global analysis, the attention here is on the regional scale.

4.1 Detecting oscillations: the Empirical Mode Decomposition

Inter–annual sea–level variations are caused by several mechanisms, as exposed in chapter 1, including ocean mass variations and volume changes. Furthermore, meteorological and oceanographic fluctuations are responsible for cyclic sea–level variations; at a global scale, these are primarily caused by the El Niño Southern Oscillation (ENSO), the North Atlantic Oscillation (NAO), and the Atlantic multi–decadal oscillation (AMO). Regional sea–level variability induced by interannual and interdecadal cycles can temporarily magnify or reduce the amplitude of long–term sea–level trend (Tsimplis et al., 2013).

To study periodic components of the sea–level signals and to verify possible relationships with oceanographic fluctuations, the EMD method (Huang et al., 1998) is adopted. Non–linear and non–

stationary time series are decomposed into a sequence of N empirical orthogonal Intrinsic Mode Functions (IMFs) describing cyclic variations, not necessarily characterized by constant amplitudes and phases. Contrary to a simple regression, the EMD is not requiring *a–priori* assumptions about the functional expression of the regression model (Huang et al., 1998). By the EMD, it is possible to isolate terms with dominating periodicities from the tide gauge record and to obtain a residual, which reveals the long–term "natural trend" of the signal.

The EMD method has been previously used in sea–level studies by Ezer and Corlett (2012) and Ezer et al. (2013) to correlate variations in the Gulf Stream with variations in coastal sea level. Here we use an improved version of the EEMD method (the "ensemble EMD", see Wu and Huang, 2009), namely the Complete Ensemble Empirical Mode Decomposition with Adaptive Noise (CEEMDAN), described by Torres et al. (2011) and implemented in MATLAB. The EEMD method has been used by Breaker and Ruzmaikin (2011) to study the San Francisco tide gauge time series and recently by Spada et al. (2014a) to analyze the Nuuk/Godthab (Southwest Greenland) tide gauge record.

The EEMD requires the definition of two parameters. The first (*Nsdt*), is defined as the ratio of the standard deviation of IMF1 to the standard deviation of the original time series, and it determines the noise level. The second (*NE*), defines the number of realizations required to construct each IMFs. Proper values have been chosen by trial and error. To avoid the "end effect" problem, a mirroring technique has been employed (Barnhart, 2011). To assess the uncertainty on the residual time serie, we have computed the mean variance of each IMFk obtained from the *NE* realizations, $\hat{\sigma}^2_{IMFk}$. The error on the residual is then $\sigma_{res}=\sqrt{\sum_{k=1}^{N}\hat{\sigma}^2_{IMFk}}$, where N is the number of modes.

4.2 A case study: Empirical Mode Decomposition analysis for the Adriatic Sea tide gauge records

The Adriatic Sea is a semi–enclosed basin communicating with the Mediterranean through the Otranto Strait. It is bounded by Italy on its northern and western sides and by Croatia, Bosnia, Slovenia, Montenegro and Albania on the eastern side (see Fig. 4.1). Sea–level variability across the Adriatic Sea is a key issue principally because of its low–lying sandy shorelines. Most of the coastal zones are located at an elevation only slightly in excess (or sometimes even lower) than mean sea–level. A possible impact of sea–level rise is further enhanced by the presence, particularly along the cost of the northern Adriatic Sea, of high–value economical activities and densely populated areas.

In the Adriatic Sea, sea–level changes are mainly driven by steric effects (Tsimplis and Rixen, 2002). However, since $\sim$ 1960, an important role of atmospheric forcing has been evidenced by Tsimplis et al. (2012), who have attributed a significant component of total sea–level change to land movements and to the coupling with the Mediterranean Sea through the Otranto strait. The influences of the ocean modes, as the NAO, on sea–level fluctuations in the Adriatic Sea have been first evidenced by Tsimplis and Josey (2001) and later reassessed by Tsimplis et al. (2013).

The problem of sea–level rise in the Adriatic Sea has been tackled in a number of studies, based

on both tide gauges observation and oceanographic models. Since the tide gauges with longest records (Venice and Trieste, Italy) are located in the northern Adriatic, most of the studies have focused on this area (see for example Ferla et al., 2007; Masina and Lamberti, 2013). With the aim of assessing the vulnerability of coastal cities and infrastructures, several studies have investigated the frequency and magnitude of surges (see, for example Pirazzoli and Tomasin, 2002). Sea–level measurements have been interpreted in terms of oceanographic and climatic processes using appropriate models (Tsimplis and Rixen, 2002, Marcos and Tsimplis, 2007, Tsimplis et al., 2012).

In the following, the Empirical Mode Decomposition (EMD) method is applied to the Adriatic sea–level curve obtained by stacking all the tide gauge observations currently available on the Basin. The aim is to enlighten the existence of cyclic sea–level variations possibly related with the NAO and the AMO modes. This part of the Thesis is based on the work of Galassi and Spada (2015).

4.2.1 Sea–level observations for the Adriatic Sea

The analysis is based on Revised Local Reference (RLR) tide gauge monthly and annual data from the Permanent Service for Mean Sea Level (PSMSL) (see section 1.2). On August 2012, the RLR database was extended with the introduction of new data from 22 italian tide gauges: among these, seven are facing the Adriatic Sea. Most of the newly introduced RLR Adriatic tide gauges have recorded more than 10 years of data, thus providing a significantly extended dataset that motivates our study. All the tide gauge data employed here have been extracted from the PSMSL web page (*http://www.psmsl.org/*), and extracted from database on September 25, 2013. Since here we are mainly interested into non–linear sea–level variations, no correction has been applied for the effects of Glacial Isostatic Adjustment (GIA). Following the approach of Spada and Galassi (2012), no other corrections have been performed. The absence of steep changes in the tide gauge time–series suggests a negligible effect for co–seismic deformations. Furthermore, since local subsidence is not expected to drive cyclic effects on sea–level, no corrections for subsidence have been applied even in cases, like Venice, where its role is recognized to be particularly important (Carbognin et al., 2004).

The location of the 30 RLR tide gauges considered in this study is displayed in Fig. 4.1a, which also shows the number of valid years of data from each station (a valid year is one for which ≥ 10 monthly averages are available). Figs. 4.1b and 4.1c show annual data at each station for the western and the eastern sides of the basin, respectively. Information about the tide gauges are listed in Table 4.1. Record lengths range between 3 years (Porto Corsini and Porto Garibaldi, in northern Italy) and 138 years (Trieste), with this latter containing 116 valid annual records. The completeness of records varies between 33% (Ortona) to 100% for 14 stations out of 30. Altogether, the record of the RLR Adriatic tide gauges spans 141 years, starting in 1872 (Venezia Porto S. Stefano) and ending to present. Although following the PSMSL recommendation here we only analyse RLR tide gauge data, we note that for some Northern Adriatic sites (e.g., Porto Corsini), the metric record is considerably more extended. This would probably merit efforts to update these records to the RLR standard.

Table 4.1: Basic data of the Adriatic tide gauges considered in this study, listed in alphabetic order. Symbols N_{val} and c denote, for each time series, the number of valid yearly records and the completeness (%), respectively. Starred (*) tide gauges are those introduced into the RLR PSMSL dataset on August, 2012.

Station name	PSMSL Id	Period year–year	N_{val} years	c %
Ancona	101	1967–1971	2	40
Ancona II *	2098	2001–2011	11	100
Bakar	353	1930–2011	69	84
Bar *	1075	1965–1990	26	100
Bari	2075	2001–2011	11	100
Dubrovnik	760	1956–2010	53	96
Gazenica	1577	1983–1988	6	100
Koper	1009	1962–1991	26	87
Luka	1817	1992–2003	11	92
Manfredonia	1262	1969–1971	3	100
Ortona	972	1961–1972	4	33
Ortona II *	2097	2001–2011	10	91
Ploce	1945	2006–2011	6	100
Porto Corsini	100	1970–1972	3	100
Porto Garibaldi *	2144	2010–2012	3	100
Rovinj	761	1956–2011	55	98
Split G. Luka	352	1955–2011	57	100
Split RT Marjana	685	1953–2011	56	95
Sucuraj	1706	1987–2004	17	94
Trieste	154	1875–2012	116	84
Trieste II *	2099	2001–2011	11	100
Ubli	1718	1987–1990	4	100
Venezia P. Salute	168	1909–2000	83	90
Venezia P.S. Stefano	39	1872–1919	46	96
Venezia Arsenale	87	1889–1913	22	88
Venezia II *	2100	2002–2011	10	100
Vieste *	2087	2001–2011	10	91
Vis-Ceska	1574	1983–1990	7	88
Zadar	1859	1995–2011	17	100
Zlarin	1578	1983–1987	5	100

To construct a sea–level curve representative of the whole time period covered by the Adriatic tide gauges and to increase the signal–to–noise ratio, we have stacked the individual monthly time series. Stacking techniques are commonly used in seismic data processing (see e.g. Gilbert and Dziewonski, 1975) and have been also employed in global sea–level studies (Trupin and Wahr, 1990; Jevrejeva et al., 2006; Olivieri and Spada, 2013). At local scale, by an averaging approach equivalent to stacking, Scarascia and Lionello (2013) have constructed a synthetic sea–level curve for the North Adriatic Sea starting from the longest tide gauge records available. Following Olivieri and Spada (2013), here the stack has been obtained by averaging, at each time step, the sea–level values available from the Adriatic tide gauges.

The curve resulting from the stack of Adriatic tide gauge monthly time series is shown in gray in Fig. 4.2. Hereinafter, this curve will be referred to as the "AS curve". A cursory analysis of the AS curve has been performed by a linear regression (black line), which provides a rate of sea–level rise $r_{AS} = (1.23 \pm 0.05)$ mm yr^{-1} during the time period 1872–2012, where the uncertainty defines the 95% confidence level, according to statistics described by Spada and Galassi (2012). However, the linear regression provides a poor description of the AS curve, and a 10–years moving average, shown by the red curve in Fig. 4.2, suggests the existence of cyclic sea–level variations with a period of about ~ 20 years, which will receive further attention.

The values of the sea–level trend and acceleration obtained from tide gauge time series generally vary significantly according to the time span considered (e.g., Olivieri and Spada, 2013). To study this sensitivity in the case of the AS curve, in Fig. 4.3 we have performed a multi–scale dynamical analysis (MSDA, see Scafetta, 2013) showing the average rate of sea–level change (Fig. 4.3a) and the acceleration (Fig. 4.3b), obtained for different time windows centered at a given epoch (bottom axis). Rates and accelerations are computed as first and second differences of the AS curve, respectively. The rate attains neatly positive values (yellow and orange hues) only for windows of width > 60 years. Negative trends (cyan) are observed, in particular, for windows of a few decades (< 30 years) after ~ 1980. For time windows exceeding 20 years, the acceleration (Fig. 4.3b) shows values of the order of 10^{-1} mm yr^{-2} with a relative uncertainty of $\sim 50\%$, hence relatively small compared to the average global values (e.g., Olivieri and Spada, 2013).

The time series that contain data from the last few years in Fig. 4.1, are all characterized by a neat sea–level high–stand occurring after year 2000. To focus on this feature, in the left part of Fig. 4.4 we show the monthly records available for decade 2003–2012. For the same time span, the annual values are shown on the right. The red thick curves at the bottom show the stacked monthly and annual data. Even from a cursory inspection, the time series show broadly similar features. We find linear correlations as large as 0.9, with average values in the range of ~ 0.7–0.9 for couples of overlapping tide gauge records longer than 50 years (95% confidence level). The correlation between the AS curve and records of Trieste and Venice is in the range ~ 0.8–0.9, at the same confidence level; while the correlation between the AS curve and the remaining tide gauge records varies in the average range ~ 0.6–0.8. Effects on sea–level from the difference in temperature and salinity between the Eastern and the Western Adriatic evidenced at seasonal time scale (e.g., Artegiani et al., 1997) are not visible at decadal periods.

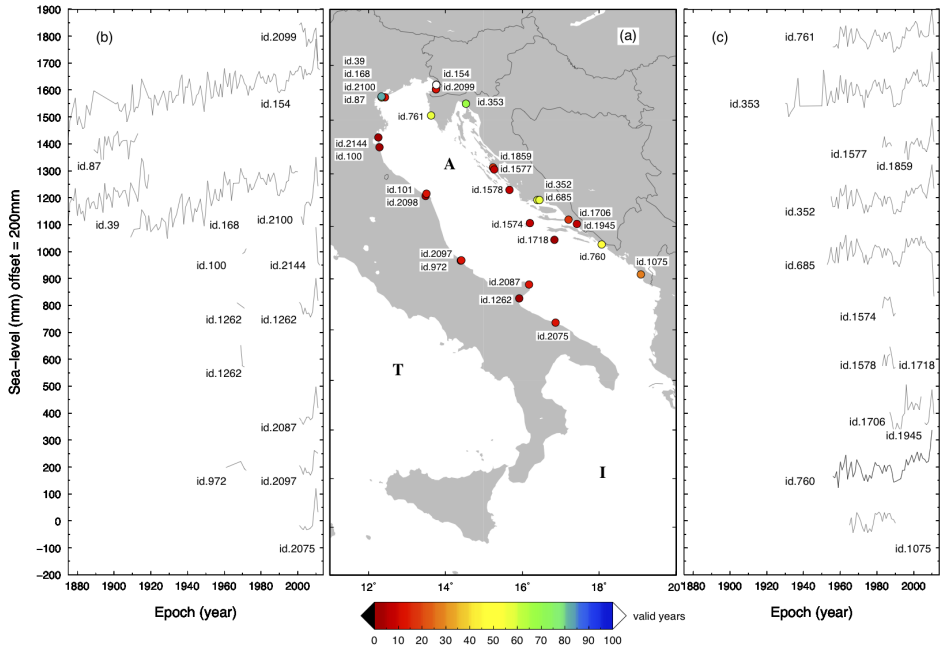

Figure 4.1: (a) Location of the RLR PSMSL tide gauges in the Adriatic Sea (Ids are also indicated). Letters A, I and T denote the Adriatic, the Ionian and the Tyrrhenian Seas, respectively. The number of valid years N_{val} is key–coded by the color palette. (b) and (c) show the annual time series available at each station (see Table 4.1). The time series are shifted by 200 mm to facilitate visualization.

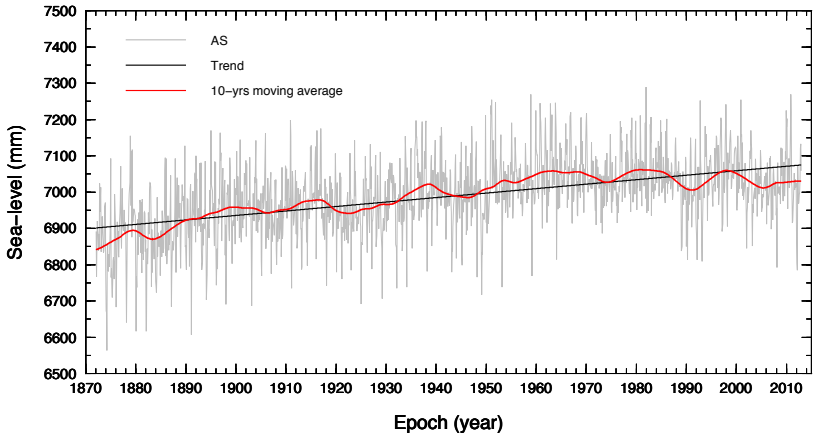

Figure 4.2: Stack of the Adriatic tide series from monthly data (AS curve). The black and the red curves show the best–fitting linear trend and the 10–years rolling average, respectively.

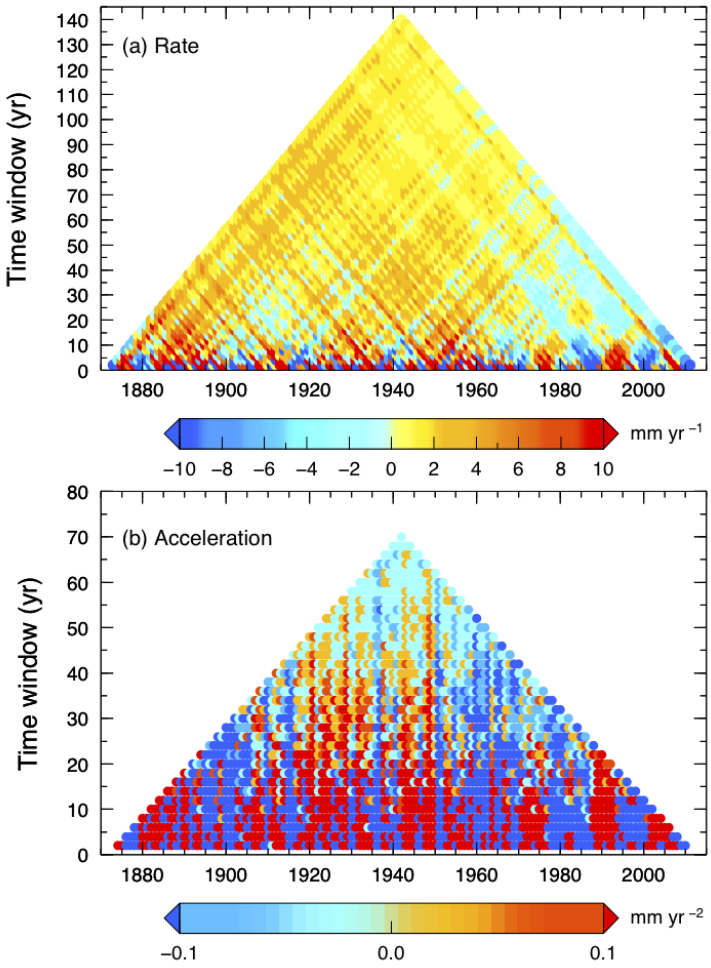

Figure 4.3: MSDA for the rate of sea–level change in (a) and acceleration (b) obtained by differencing the AS curve of Fig. 4.2.

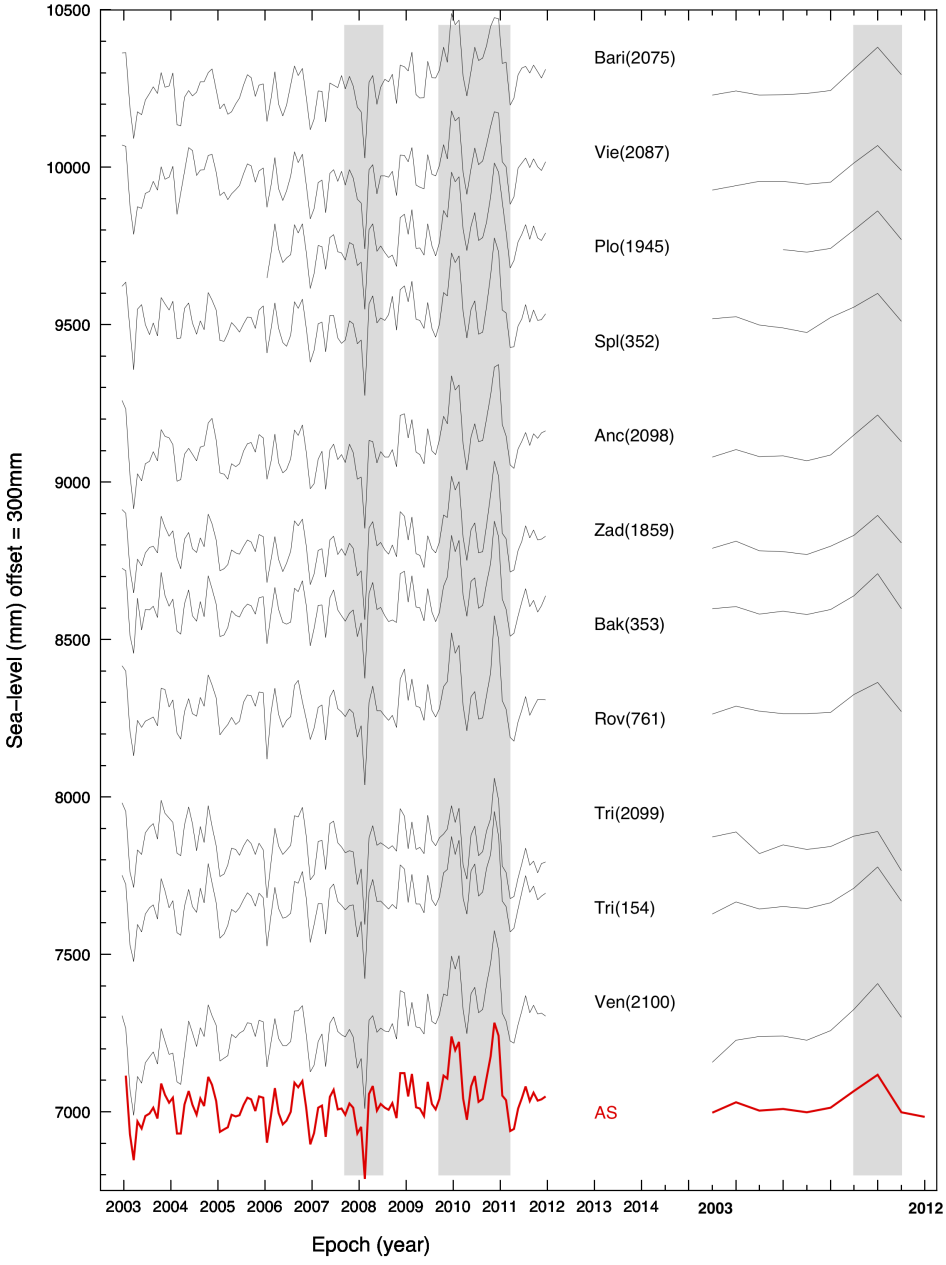

Figure 4.4: Adriatic time series (monthly on the left and annual on the right), and their stack (red) for the decade 2003–2012. The shaded rectangles mark the occurrence of the sea–level anomalies discussed in the text.

From the monthly time series in Fig. 4.4, two peculiar features appear, marked by the shaded rectangles. The first is a short–lived (~ 2 months) low–stand at the beginning of 2008, a feature that is not discernible in the annual averages. The second is represented by a couple of sea–level high–stands during the winters of years 2010 and 2011. In the annual records, these two peaks merge into a single maximum. The existence of this latter anomaly was previously detected for the whole Mediterranean Sea by Tsimplis et al. (2013), on the basis of observations from altimetry and model predictions of the steric component of sea–level change. In particular, they noted that during period 2008–2011, the absolute mean sea–level was 2–3 cm above the average altimetric datum, and they also remarked a very strong steric signal in the winter of 2011. Landerer and Volkov (2013), using both altimetry measurements (AVISO products) and gravity observations from the Gravity Recovery and Climate Experiment (GRACE), evidenced two sea–level anomalies in January 2010 and in December 2010, which reached an amplitude of 12 and 10 cm, respectively. The occurrence of significant positive and negative sea–level anomalies in the past few decades was also evidenced by Raicich (2003) for the northern Adriatic.

4.2.2 EEMD decomposition for the Adriatic sea–level stack

To establish the nature of the sea–level anomalies displayed in Fig. 4.4 and to study the cyclic components suggested by the moving average in Fig. 4.2, we have adopted an improved version of the EEMD method (see section 4.1). The AS curve has been mirrored (for the 5% of its length). The two parameters *Nsdt* (the noise level) and *NE* (number of realizations), described in section 4.1, have been set to $Nstd = 0.44$ and $NE = 300$.

The time variations of the sea–level trend and acceleration in the Adriatic Sea, shown in Figs. 4.5b and 4.5c, are obtained evaluating the first and second differences of the EEMD residual, respectively. Starting from $\sim$ 1900, the rate of sea–level change has remained almost stable until $\sim$ 1950, with values in the range of 1.5–2 mm yr^{-1}, comparable with the global secular rate of sea–level change (Spada and Galassi, 2012). In the ensuing four decades, it has declined significantly to reach values < 0.5 mm yr^{-1} after $\sim$ 1990 and even slightly negative values during the last decade. The average value of the rate of sea–level change for the whole period is (1.02 ± 0.63) mm yr^{-1}. The sea–level acceleration (Fig. 4.5c) has shown a strong variability during the time span considered, with a number of oscillations and no apparent trend. However, the acceleration of the residue has never exceeded the value of 0.01 mm yr^{-2}, somewhat less than the values obtained in the MSDA analysis in Fig. 4.3b, which was based on the full and comparatively more noisy AS curve. The average acceleration is negative and its amplitude is negligible compared to the global average sea–level acceleration during the same time span (see values in Table 1 of Olivieri and Spada, 2013).

The presence of cyclic sea–level variations in the Adriatic Sea, qualitatively suggested by the stack of Fig. 4.2, cannot be evidenced studying the EEMD residual. With this purpose, in Fig. 4.6, we show the whole set of 10 IMFs obtained from the EEMD decomposition of the AS curve. The existence of a significant cyclic pattern in the IMFs is visually evident, with a period increasing with k. The dominating period of each IMFs, obtained by standard Fourier transform methods,

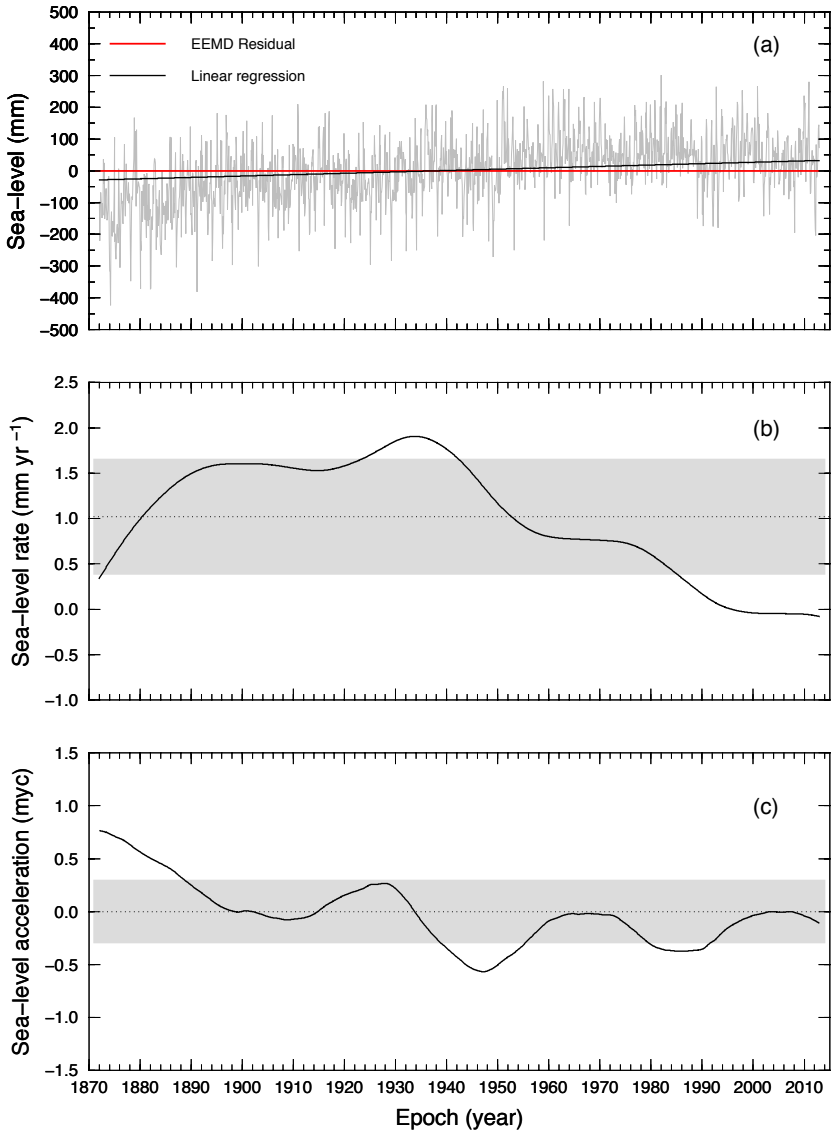

Figure 4.5: (a) EEMD residual (red) and its linear regression (black) for the AS (gray). (b) First difference (in mm yr^{-1}) and (c) second differences on the residual (in myc, where 1 myc = mm/yr/century). Average values of first and second differences (dotted lines) and their uncertainty (shaded).

is shown in Fig. 4.7a. A clear semi–annual periodicity is shown by both IMF2 and IMF3, while IMF4 is essentially an annual term. The characteristic periods of the remaining IMFs are regularly increasing with k, approximately following a power law. The longest period ($\sim$ 70 years) is that obtained for IMF10. Fig. 4.7b shows the values of the Fourier power spectra for the various IMFs, computed at the dominating periods shown in Fig. 4.7a. The power is normalized by the value obtained for IMF2. The power attains the largest values for the semi–annual (IMF3) and the annual (IMF4) terms; for the remaining IMFs, it oscillates at relatively low levels. The power spectrum clearly shows that for periods in the range between ~ 5 and ~ 40 years the dominating oscillations are those described by IMF6 (4.8 years) and IMF8 (20.4 years). This latter periodicity ($\sim$ 20 years) was also qualitatively suggested by inspection of the 10-years moving average in Fig. 4.2. The power of the oscillation with the longest period (IMF10, 70.5 years) exceeds that of all the other IMFs with $k > 4$. This is a manifestation of the "red spectrum" problem in tide gauge observations illustrated by e.g. Sturges and Hong (2001), which substantially hinders the detection of a genuine sea–level trend from records shorter than $\sim$ 60 years (Douglas, 1997).

4.2.3 Empirical Mode Decomposition analysis of Atlantic modes and their influence on the Adriatic sea–level

To investigate possible connections between sea–level variations and the ocean-atmosphere oscillations in the Adriatic Sea, henceforth we consider the NAO and the AMO Atlantic modes. The NAO index represents the difference between the normalized sea–level pressure in Lisbon (Portugal) and in Stykkisholmur/Reykjavik (Iceland) since 1864 (Hurrel, 1995). A positive NAO index signifies an increased pressure gradient and stronger westerlies over the middle latitudes (Grossmann and Klotzbach, 2009). The AMO is a mode of variability occurring in the North Atlantic Ocean, defined from the patterns of sea–surface temperature once the linear trend has been removed. A positive AMO phase corresponds to an almost uniform warming of the North Atlantic (Enfield et al., 2001). The existence of periodicities in the Atlantic modes NAO and AMO is well known and it is based on mechanisms of positive and negative feedbacks and of delay (Suarez and Schopf, 1988). In this framework, Grossmann and Klotzbach (2009) have recognized that the variability of convection due to salinity and temperature changes takes place in the seas facing Greenland, Iceland, and Norway, in the Labrador Sea and, to a lesser extent, in Mediterranean Sea.

The influence of the NAO on the Mediterranean sea–level has been the subject of various investigations. Jordà and Gomis (2013) have related the negative temperature trend in the Mediterranean Sea (in contrast with the global mean temperature) to the highly positive NAO phase dominating the 1960s to 1990s decades. Tsimplis and Josey (2001) have analyzed the link between the sea–level variability in Mediterranean and the NAO concluding that the strengthening of the latter from the 1960s to the 1990s explains a significant part of the reduction in Mediterranean sea–level over this period. Tsimplis et al. (2013) have analyzed the effect of the NAO on sea–level in Mediterranean Sea during 1993–2011, outlining the mechanism through which this oscillation influences the sea–level variability. Calafat et al. (2012) have provided evidence of an anti–correlation between NAO and sea–level at Mediterranean tide gauges, particularly at decadal time scale. A link

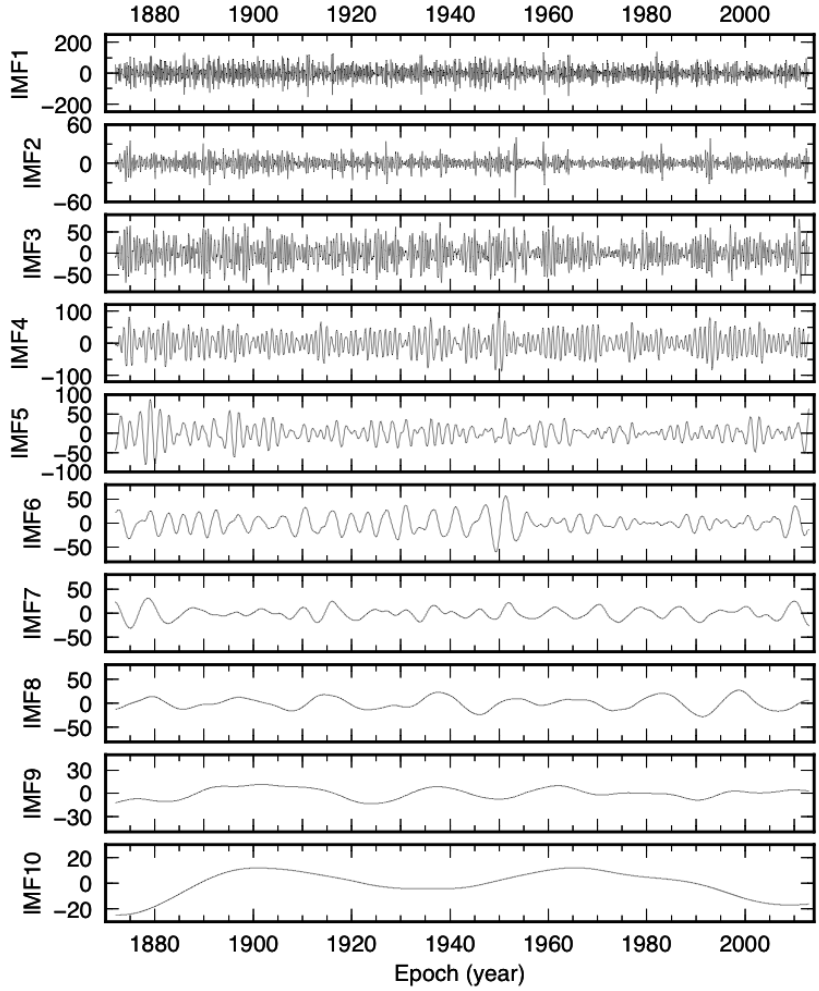

Figure 4.6: Image functions IMFk ($k = 1, .., 10$) resulting from the EEMD analysis of the AS curve shown in Fig. 4.2. Note the different scales on the y-axis.

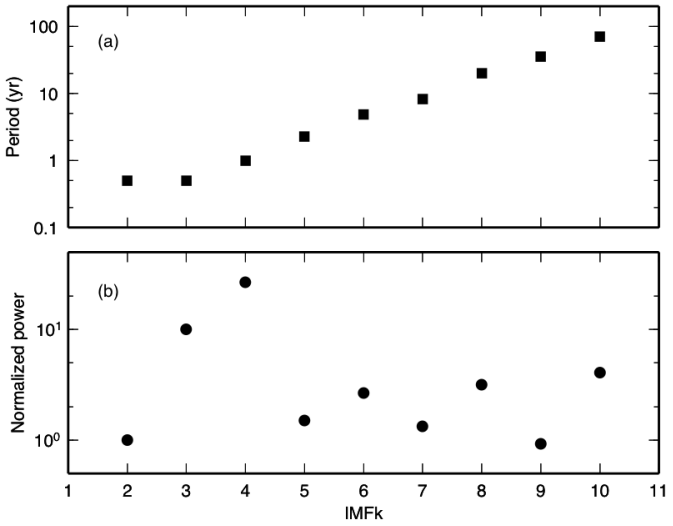

Figure 4.7: Fourier power spectrum analysis for the image functions IMFk components of the AS curve. (a) Dominating period (in years); (b) Maximum power, normalized by the IMF2 maximum power.

between the oscillation of sea–level record detected by the tide gauge of Venezia and the AMO was noticed by Scafetta (2013). The simultaneous effects of NAO and AMO on the sea–level variability in the Mediterranean Sea has been previously investigated by Raicich (2012). He has found a correspondence between the negative sea–level anomaly in the early 1970s with a negative AMO and a positive NAO and a simultaneous shift in the positive sea–level anomaly in the mid 1990s with a positive AMO and a negative NAO.

Here, we use the station–based NAO indices produced by the NCAR Climate Analysis Section[1], based on Hurrel (1995), and the AMO index calculated at NOAA PSD from the Kaplan SST dataset [2] (Enfield et al., 2001). The annual time–series for the NAO and the AMO are shown in Fig. 4.8a by red and blue colors, respectively, while Fig. 4.8b shows the same time–series after the application of a 10–years moving average. The AS curve is displayed at the bottom of each frame. The AMO and NAO indices are tightly interrelated, especially during recent decades, and characterized by a complex and non–stationary relationship (Walter and Graf, 2002). Grossmann and Klotzbach (2009) have shown that long–term positive (or negative) phases of the NAO correspond to negative (or positive) phases of the AMO, generally with a time lag of several years. To establish the nature of the cyclic sea–level variations suggested by the EEMD analysis, we study the correlations between the NAO and AMO indices and the sea–level signals observed across the Adriatic Sea.

[1] *https://climatedataguide.ucar.edu/climate–data/hurrell–north–atlantic–oscillation–nao–index–station–based.*
[2] *http://www.esrl.noaa.gov/psd/data/timeseriesimeseries/AMO/.*

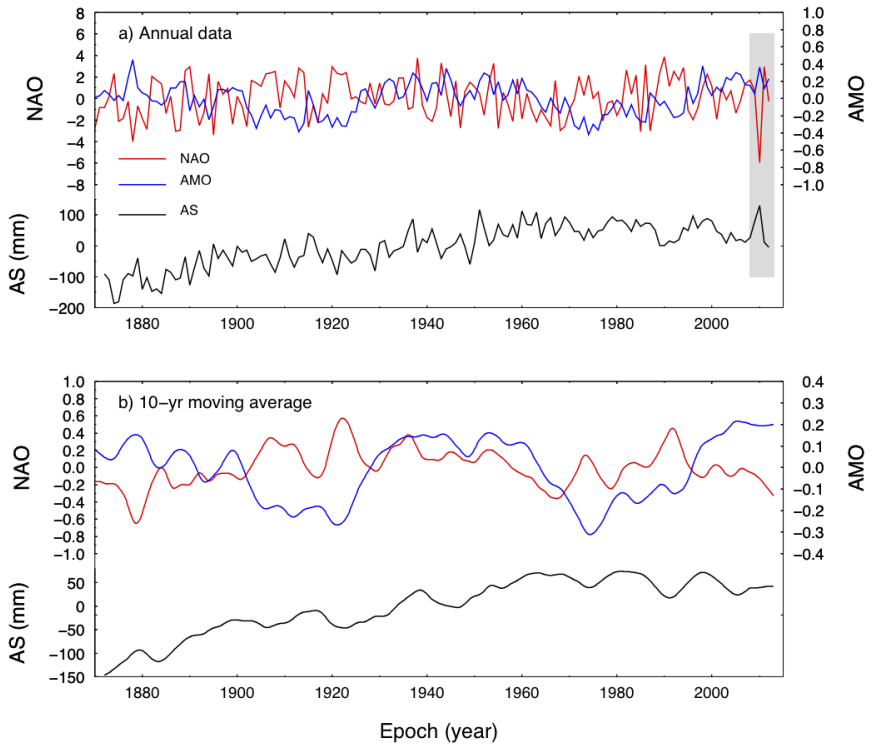

Figure 4.8: Comparison between NAO (red line), AMO (blue) and sea–level stack for the Adriatic tide gauges (AS, black). Frame (a) shows annual data for the three time series; while (b) shows their 10-years moving average. The 2010–2011 anomaly is marked by a shaded rectangle in (a).

The existence of an anti–correlation between AMO and NAO was already qualitatively clear from Fig. 4.8a and it is even more evident from inspection of the smoothed curves in Fig. 4.8b. Similarly, a correlation between the AS curve and AMO and an anti-correlation between AS and NAO, is qualitatively suggested by the same figure. The correlation and anti–correlation phases are separated by periods of variable length, which are often close to ~ 20 years.

In Fig. 4.9, the sample cross-correlations between the two Atlantic modes and the AS curve have been quantitatively evaluated using the method outlined by Box et al. (2007). The three top frames refer to the time period 1880–2012, while the time window 2009–2012 is considered in the bottom; the correlations are shown at different time lags expressed in years and months, respectively. The results show that an anti–correlation at lag 0 effectively exists between AS and NAO and between NAO and AMO for both the time windows considered (95% confidence level). This confirms our guess above based on Fig. 4.8. A clear correlation pattern between AS and AMO is not evident for period 1880–2012 (Fig. 4.9b), but during 2009–2012 we observe a significantly large correlation at lag ~ 0 (Fig. 4.9e).

The EEMD analysis of the NAO and AMO indices, shown in Fig. 4.10 and in Table 4.2, indicate that for the NAO the power is mostly concentrated in the IMF7 at a period $p = 7.8$ years. At a comparable period ($p = \sim 9.2$ years), the AMO shows a peak in the power spectrum (IMF7). However, for the AMO, the maximum power is found at a multi–decadal time scale (IMF10, $p = \sim$ 79 years). The values of the periods found for the IMF7's of AMO and NAO suggest that opposite phases are met every ~ 21 years. We have further analyzed the relationship between these cyclic components by a coherence test (Kay, 1988) with a time window of 30 years, which has revealed a significant coherence (95% confidence) at a period of ~ 22 years, with a phase lag of 180°. Applying a coherence test to the AS curve and the AMO, a significant coherence is found at a period of 21.7 years, with a phase close to 0°. These results suggest that the ~ 20 years cycle shown by the IMF8 for the AS curve (see Fig. 4.6) can be associated to the ~ 21 years cycle resulting from the combination of AMO and NAO.

The amplitude of the oscillations of the three signals considered here (AMO, NAO and AS) varies with time (see Figs. 4.6 and 4.10), and the opposition or synergy of phases does not occur regularly. As evidenced in Fig. 4.9, in 2009–2012 opposite phases for AMO-NAO and AS-NAO occurred simultaneously also accompanied by a synergic phase for AS-AMO; the 2010-2011 anomaly occurred exactly during this lapse of time and, furthermore, it fell inside the AMO warm phase. Alternate warm and cold phases for AMO have a long periodicity, of the order of that evidenced by the EEMD analysis (IMF10 ~ 78 years), well in excess of the ~ 20 years cycles shown by the AS curve. In North America and Europe, the warm AMO phase has been related to a decrease in sea–level pressure (SLP) and in sea surface temperature (SST) (see, *i.e.,* Knight et al., 2006). In the same regions, Sutton and Hodson (2005) have evidenced a role of AMO in modulating the summer boreal climate and the frequency of extreme events. A direct relationship between the AMO and the Mediterranean sea–level variations has not been pointed out yet. Nevertheless, the relationship between SST and SLP in the Atlantic Ocean and sea–level across the whole Mediterranean Sea is well documented (see, in particular Tsimplis and Josey, 2001).

The EEMD analysis clearly reveals the annual and the semiannual periodicities in the AS curve,

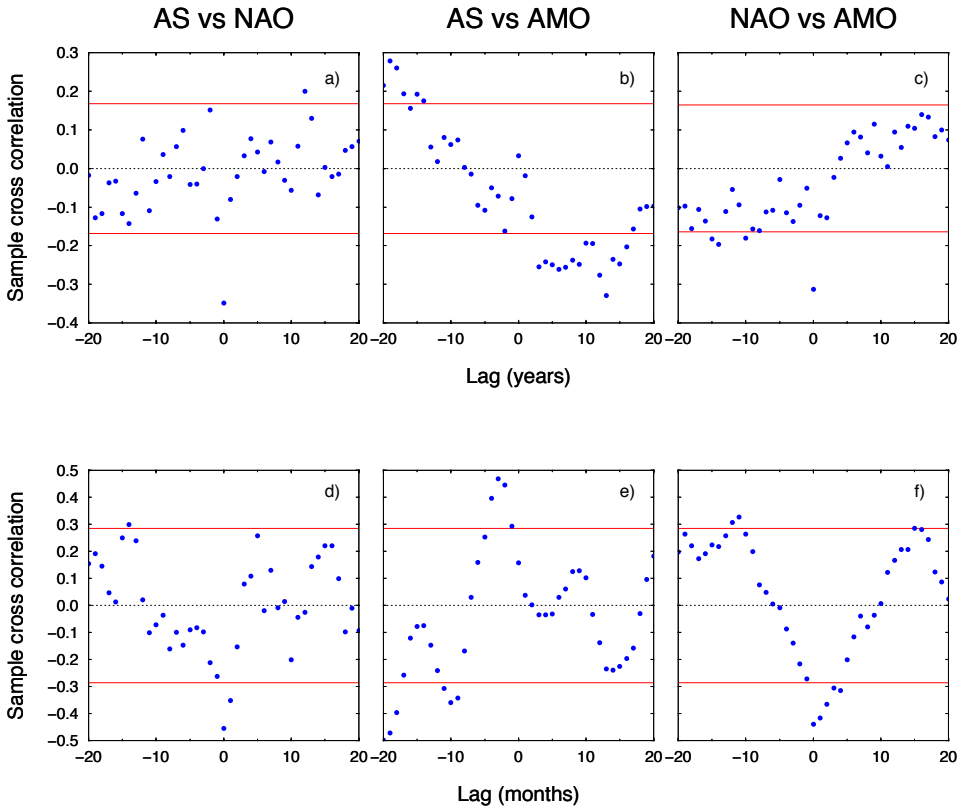

Figure 4.9: Sample cross correlation between AS, AMO and NAO (the 95% confidence intervals are denoted by red horizontal lines). Frames a), b) and c): whole period (1880-present) with annual data; d), e) and f): from 2009 with monthly data.

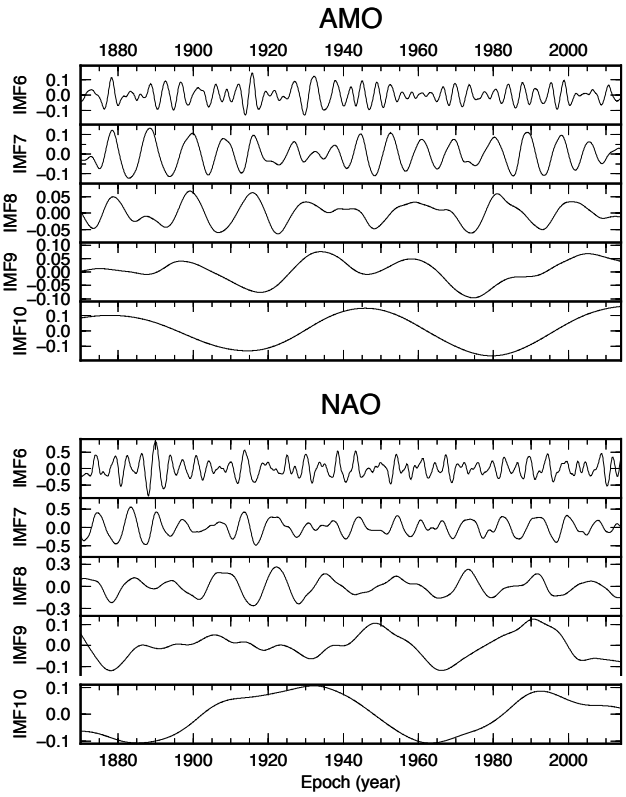

Figure 4.10: Image functions IMFk ($k = 6, .., 10$) resulting from the EEMD analysis of the NAO and AMO indices.

Table 4.2: Period (p, in year) and corresponding power (npw) resulting from the Fourier transform for each IMF of NAO and AMO indices (npw is normalized by the power of IMF2). For the EEMD analysis, we set $NE = 300$ for AMO and $NE = 400$ for NAO.

IMF	NAO		AMO	
	p (yr)	npw	p (yr)	npw
2	0.4	1	0.4	1
3	0.6	14	0.6	21
4	1.0	12	1.0	201
5	2.4	11	2.5	127
6	3.7	8	3.6	153
7	7.8	22	9.2	744
8	16.8	5	17.4	133
9	49.3	2	52.3	325
10	74.0	5	78.5	$5.6 * 10^3$

and shows a powerful oscillation with a period of ~ 20 years. The analysis on NAO, AMO and AS signals has shown that a negative phase of sea–level corresponds to a negative phase of the AMO and to a positive phase of NAO. The EEMD analysis suggests that the periodic occurrence of opposite phases in the AMO and NAO indices (with a period of ~ 20 years), corresponds to the ~ 20 years cycle identified for the sea–level trend in the Adriatic Sea. The coincidence of AMO-NAO phase opposition and warm AMO phase could explain the anomalous sea–level high–stand detected during 2010–2011 and possibly help to forecast future anomalous sea–level fluctuations within the Adriatic Sea.

4.3 Detecting tipping points in sea–level records

A complete comprehension of the past century sea–level trend and variability, is essential in understanding possible future development. Olivieri and Spada (2013) using tide gauge observations from Permanent Service of Mean Sea Level (PSMSL), have noticed change points or abrupt inflections that influence sea–level trend and acceleration, both at global and at local scale. These change points represent transitions from a statistically stable state to another which occur in many dynamical system (Ditlevsen and Johnsen, 2010). Such transitions, known as tipping points, can be the result of a massive external shock, or stepwise change in the conditions, or it is also possible that a slight perturbation can invoke a massive shift to a contrasting and lasting state (van de Leemput et al., 2014).

Several types of tipping point exist, including reversible and rate–dependent ones. Strongly non–linear but reversible transitions are expected to resemble bifurcation-type behavior (Lenton,

2011). Even when the dynamic of a system is not perfectly known, its behavior at bifurcation can be identified, and the transition should be prevented (see, *i.e.* Ditlevsen and Johnsen, 2010; Scheffer et al., 2009). This makes the early warning (EW) approach a useful tool for tipping point detection and for the study of the dynamics of the systems. For this, recently, a growing attention is devoted on early warning methods for tipping point detection in climate signals (Lenton, 2011), mainly with paleorecords and models data (see Table 1 of Lenton, 2011, for a syntesis).

A tipping point, in a particular moment in time, is defined as the critical point at which a small change can lead to large, long–term consequences in a dynamic system (Lenton, 2011). For a system generated by a general process

$$dx = f(x\theta)dt + g(x\theta)dW, \tag{4.1}$$

where x is the state of the system, $f(x\theta)$ describes the deterministic part of the system, $g(x\theta)dW$ determines how stochasticity interacts with the state variable and dW is a white noise process, slow change in the underlying conditions (θ) moves the system near to a threshold, and a change in its state (a transition into an alternative dynamic regime) could occur.

According to Dakos et al. (2012), the indicators of critical transitions can be grouped in two main categories: the metric–based and the model–based indicators. Both are finalized to detect changes in the correlation structure of the system considered, but while the metric–based simply quantify variations in the statistical property of the time series, the model–based methods attempt to fit the data with a specific model structure.

Different metric–based indicators exist: in the following there is a brief description of those used in this section. For a system that is gradually approaching a bifurcation, the recovery from perturbation tends to be infinitely slow: this phenomenon is termed "critical slowing down" (Lenton, 2011). As complex systems (such as the climate ones) approach a tipping point, their dynamics tend to become dominated by the critical slowing down phenomenon. Slowing down causes the intrinsic rates of change in a system to decrease, and the "short term memory" tends to increase. As a consequence, the autocorrelation at lag–1 (AR(1)) prior of a transition tend to increase (Dakos et al., 2012).

According to the fluctuation-dissipation theorem (Kubo, 1966), an increase in the variance of observed signal is also expected approaching a bifurcation. Variance is the second moment around the mean, and it can be measured as standard deviation (sd) or coefficient of variation (cv). These two signals, sd (or cv) and AR(1), are connected and only the detection of both can be considered as a sign of an approaching tipping point (Ditlevsen and Johnsen, 2010). This happens when the system is lead by some external control parameter and its jump happens in proximity of a bifurcation (the potential barrier is small in comparison to noise intensity); in this case we can detect a change in both the indicators (autocorrelation and standard deviation) prior to the jump. If only one between AR(1) and sd (or cv) changes, the jump is not indicating a bifurcation. Rather, the jump is only driven by internal noise (short time fluctuations) and the potential does not change. This implies that the jump will be not predictable until it actually is about to happen (Ditlevsen and Johnsen, 2010).

Other metric–based indicators used here are skewness and kurtosis. Skewness (sk) is the standardized third moment around the mean and it is expected to increase near a transition towards an alternative state greater than the present one and to decrease if the alternative state is smaller (Dakos et al., 2012). Kurtosis (ku) is the standardized fourth moment around the mean of a distribution: if the variance results from infrequent and extreme deviations the kurtosis distribution has sharper peak and longer and fatter tails (Fossion et al., 2013).

For the model–based indicator, we need a general model to interpolate the time series that we are analyzing, which are generated by an unknown process. The non–parametric drift-diffusion-jump (DDJ) model can approximate a wide range of non–linear processes without the need specifying an explicit equation (Dakos et al., 2012). Following Dakos et al. (2012), our system can be approximated by fitting a drift-diffusion-jump model:

$$dx(t) = f(x(t), \theta(t))dt + g(x(t), \theta(t))dW + dJ(t), \tag{4.2}$$

where x is the state variable, $f(.)$ and $g(.)$ are non–linear functions, dW is white noise, and jumps J are relatively large shocks that occur intermittently. If $x(t)$ can be observed at discrete intervals of time, and the unknown $\theta(t)$ moves towards a threshold, even if $f(.)$ and $g(.)$ are not known, we can estimate drift, diffusion and jump statistics that may serve as early warnings of the bifurcation (Carpenter and Brock, 2011). By a regression, it is possible to estimate drift (through $f(.)$), total variance, jump intensity, and diffusion variance (through $g(.)$). The conditional variance of x (that rises to infinity at the critical transition) can be estimated using standard non–parametric regression techniques (Dakos et al., 2012). Similarly than the autocorrelation and variance, conditional variance and diffusion estimates in the drift–diffusion–jump model can help to discern bifurcations that occur in the drift from bifurcations that occur in the diffusion (so-called noise-induced transitions: an abrupt shift in the shape of the stationary distribution). A bifurcation in the drift only may be indicated in advance by conditional variance but not diffusion. A bifurcation in the diffusion may be indicated by increases in both conditional variance and diffusion.

The Potential Analysis is used to detect possible alternative states, inferring the shape of the underling potential of a system (Livina et al., 2010). The assumption is that time series can be modelled by a stochastic potential equation

$$dZ = \frac{dU}{dz}dt + \sigma dW, \tag{4.3}$$

where $\frac{dU}{dz}$ is a polynomial potential and σ is the intensity of the unit variance white noise dW. The number of potential system states of the time series correspond to the order of the best fit polynomial.

In the following section, the EW methods have been used on observed data for climate variables, especially on past century sea–level observations. The aim is to understand if the sea–level observed at tide gauges shows tipping points and if these can be related to other climate variables. In addition, we would understand if tipping points in sea–level signal can be anticipated. To do that, we focused our attention to the North Est Pacific Ocean (hereinafter NEP) which hosts

some of the tide gauges with the longest records. Furthermore, the NEP is sensitive to global processes (Merrifield, 2011) as the El Niño Southern Oscillation (ENSO), the Pacific Decadal Oscillation (PDO) and the North Pacific Gyre Oscillation (NPGO).

4.4 A case study: the North Est Pacific Ocean

4.4.1 Sea–level and oceanic modes in the North Est Pacific

In the US West Coast, facing on North Est Pacific Ocean (NEP), are located some of the tide gauges with longest and more complete sea–level records in the world. Here we use data from PSMSL Revised Local Reference (RLR) database (Holgate et al., 2012). Information about the three longest tide gauges in the NEP are listed in Table 4.3. The tide gauges time series of San Francisco (SFO) and Seattle (SEA) have a completeness of 100%, and cover with data a period of 160 and 115 years, respectively. The tide gauge of San Diego (SDO) covers a time span of 108 years with a lack of 3 years of data.

Following Olivieri and Spada (2013), to obtain sea–level information on the whole region considered, we have performed a stack of the three original tide gauge curves. The result (hereinafter "NEP-stack") is shown in Fig. 4.11 that also displays the sea–level monthly data for the tide gauges of SFO, SEA and SDO, respectively. Colored curves in Fig. 4.11 show result of the application of a smoothed 10–years filter.

Table 4.3: Basic informations for the tide gauges facing the NEP.

Name and abbreviation	PSMSL id	Period (yr)	Completeness (%)
S. Francisco (SFO)	10	1854–2013	100
Seattle (SEA)	127	1899–2013	100
S. Diego (SDO)	158	1906–2013	98

Bromirski et al. (2011) suggest that at least two main change points can be detected from sea–level data observed by tide gauges in the NEP: one in $\sim$ 1930 and the other in $\sim$ 1980. In Table 4.4 the linear trends for each periods and for the whole time series are displayed. The two change points identified by Bromirski et al. (2011) bound a linear sea–level trend (obtained with a simple linear regression, according to Spada and Galassi, 2012) that ranges between 1.86 (for SFO and SDO) and 2.38 (SEA) mm yr^{-1}. The sea–level trend of the Stack-NEP for the whole period, is 1.62 mm yr^{-1} , in fair agreement with the 1.5 mm yr^{-1} assessed for the period 1901–1990 by the AR5–IPCC report (Church et al., 2013). After 1980, even if according to Bromirski et al. (2011) the linear trend is not statistically significant for all the three tide gauges, it is evidently that coastal sea–level has remained approximately stationary, in disagreement with the global mean sea level

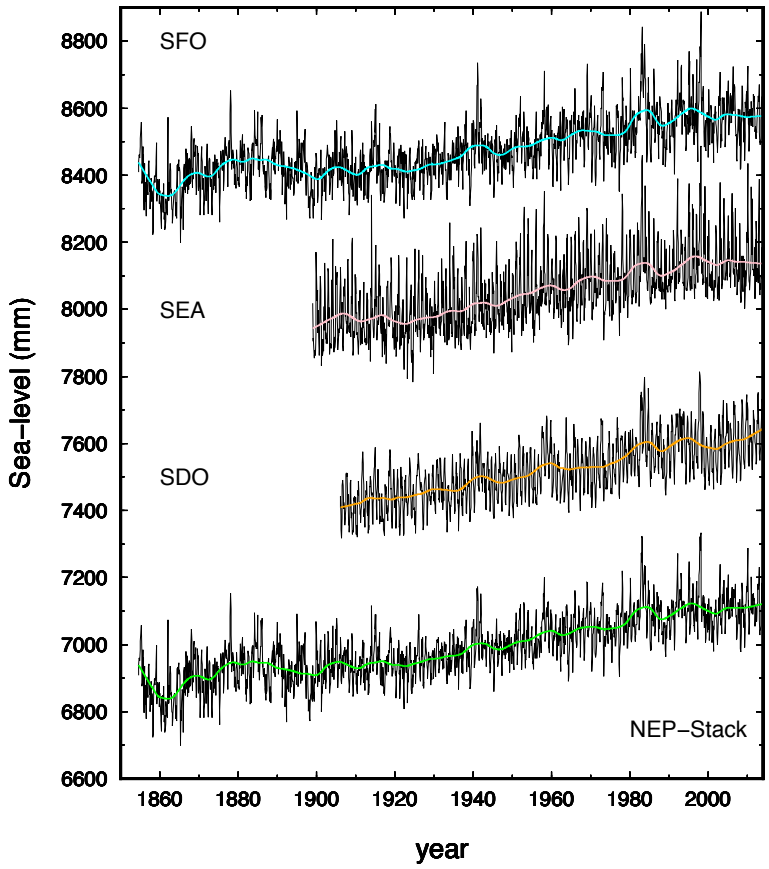

Figure 4.11: Longest PSMSL RLR tide gauge records in the North Est Pacific and their stack. The black curves represent the monthly data, whereas the colored smoothed curves are the result of a lowpass filter with a 10–year (120 moths) span. Data are shifted of 500 mm for visualization purpose.

Table 4.4: Linear trend for TG sea–level series and for their stack at different time span and for the whole recording period.

Period	SFO (mm yr^{-1})	SEA (mm yr^{-1})	SDO (mm yr^{-1})	NEP-Stack
up to 1930	0.51 ± 0.10	-0.138 ± 0.50	1.76 ± 0.50	0.98 ± 0.10
1930–1980	1.86 ± 0.20	2.38 ± 0.20	1.89 ± 0.20	2.04 ± 0.10
after 1980	-0.18 ± 0.00	0.47 ± 0.50	0.76 ± 0.50	0.38 ± 0.30
whole period	0.41 ± 0.03	1.96 ± 0.07	2.05 ± 0.06	1.62 ± 0.030

assessed by Church et al. (2013) for the period 1993–2010 (3.2 mm yr^{-1}) and for the period 1971–2010 (2.8 mm yr^{-1}).

Sea–level in the NEP is strongly influenced by oceanic modes, namely El Niño Southern Oscillation (ENSO), Pacific Decadal Oscillation (PDO) and North Pacific Gyre Oscillation. Several studies have shown the influence of these modes on sea–level variability at regional scale, and particularly in the NEP. Bromirski et al. (2011) evidence that present regional values of sea–level rise in NEP differs from those assessed at global scale in reason of the influence of these modes of vriability. Zhang and Church (2012) highlight the implication of decadal variability induced by PDO to decreasing in observed sea–level in East Pacific.

The ENSO is a coupled ocean–atmosphere phenomenon that causes the most important global climate variability on interannual time scales. Here we use the Multivariate ENSO Index (MEI, extracted from the NOAA web site *http://www.esrl.noaa.gov/*) that is based on the six main observed variables over the tropical Pacific: sea–level pressure, zonal and meridional components of the surface wind, sea surface temperature, surface air temperature, and total cloudiness fraction of the sky (Wolter and Timlin, 1998).

Similar to the ENSO, the Pacific Decadal Oscillation (PDO) is a long-lived El Niño-like pattern of Pacific climate variability. The PDO index is defined as the leading principal component of North Pacific monthly sea surface temperature (SST) variability. Here we use standardized values for the PDO index[3], derived as the leading PC of monthly SST anomalies in the North Pacific Ocean, poleward of 20°N.

The ENSO and the PDO oscillations have similar spatial fingerprints, even though the PDO has a stronger signature in the North Pacific–North American sector, while the ENSO in the tropics. On the other hand, their behavior in time is somewhat different. While typical ENSO events (warm or cold phase) persist for short period (6 to 18 months), the PDO events persist for longer time (20 to 30 years, see Gedalof et al., 2002). According to Minobe (2000), in the 20th century PDO has shown two main periodicities, one from 15 to 25 years, and the other from 50 to 70 years. Zhang et al. (1997) evidenced a regime shift that occurred around 1976–1977.

[3]http://jisao.washington.edu/pdo/PDO.latest

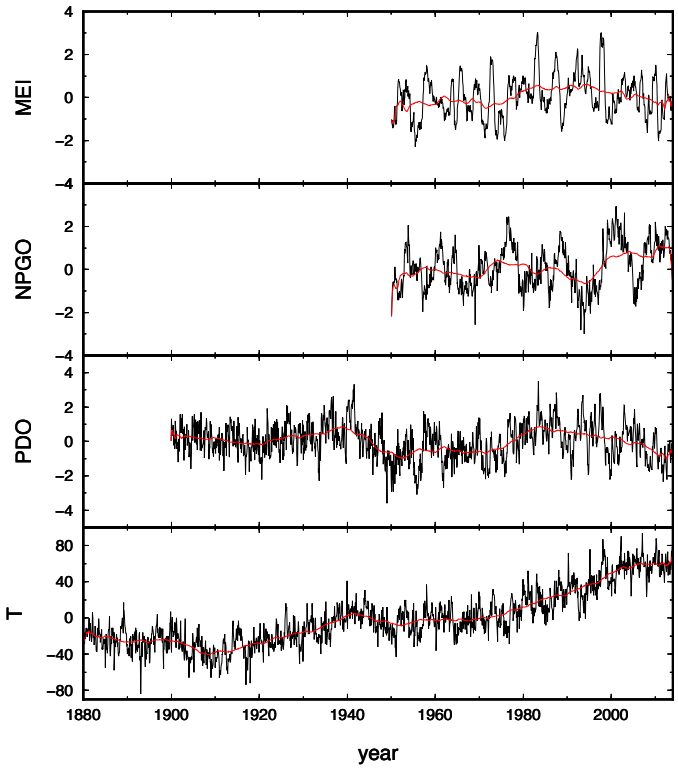

Figure 4.12: Oceanic modes for the NEP. The colored smoothed curves represent the 10–year (120 moths) moving average.

According to Merrifield (2011) we consider also the North Pacific Gyre Oscillation (NPGO, see Di Lorenzo et al., 2008). The NPGO is a mode of climate variability, driven by the atmosphere through the North Pacific Oscillation (NPO, in turn linked to ENSO cycle) and reflecting regional and basin–scale variations in wind–driven upwelling and horizontal advection (Di Lorenzo et al., 2008).

In Fig. 4.12, monthly data (black curve) and their 10–years running average (red) for the three oceanic modes are plotted. Being the ocean variability strongly linked to the temperature, Fig. 4.12 also shows the global data of GISS Land–Ocean Temperature Index (in 0.01 degrees Celsius, base period: 1951–1980, Hansen et al., 2010). GISS Surface Temperature analysis is carried by NASA and provides a measure of the changing global surface temperature with monthly resolution (*http://www.data.giss.nasa.gov/gistemp/*).

4.4.2 Tipping point of North Est Pacific

In Fig. 4.13 are shown the metric tipping point indicators for the NEP stack and for the San Francisco tide gauge observations. The autocorrelation at lag-1 and the standard deviation show a considerable rise around year 1983 and a minor jump around 1998, for both the signal considered. These features is confirmed by an increase, in the same years, in the kurtosis, skewness and coefficient of variation. According to Ditlevsen and Johnsen (2010), the simultaneous increase in AR(1) and sd could indicate that we are assisting to a "real" jump, with a change in the state of potential. This means that some external variable is leading the observed phenomenon (in this case, the sea–level variations).

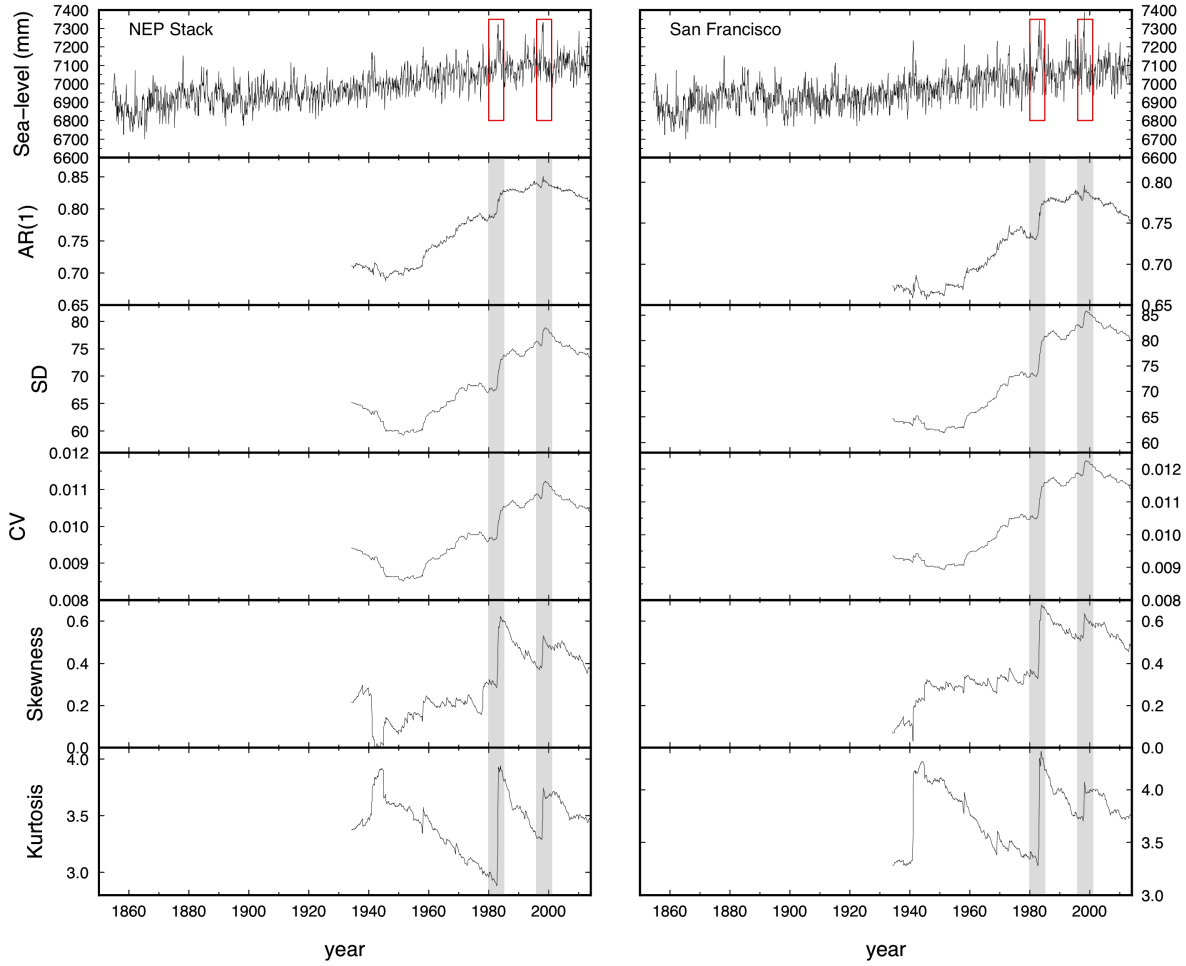

Figure 4.13: Basic metric tipping point indicators for the NEP stack and for the San Francisco tide gauge observations.

A DDJ analysis has been performed on the entire NEP stack and it is shown in Fig. 4.14. The conditional and the total variance as well the jump intensity increase for the last part of the time series. The increase is particularly evident in $\sim$ 1980, $\sim$ 2000 and $\sim$ 2013. On the opposite, in the same time steps, the diffusion term decreases. The indicators are noisy, but they became very clear when plotted against sea–level values (due to smoothing, see Dakos et al., 2012). In this representation (right frames of Fig. 4.14) it is more clear that the indicators start to signal an upcoming transition from sea–level values higher than 7200.

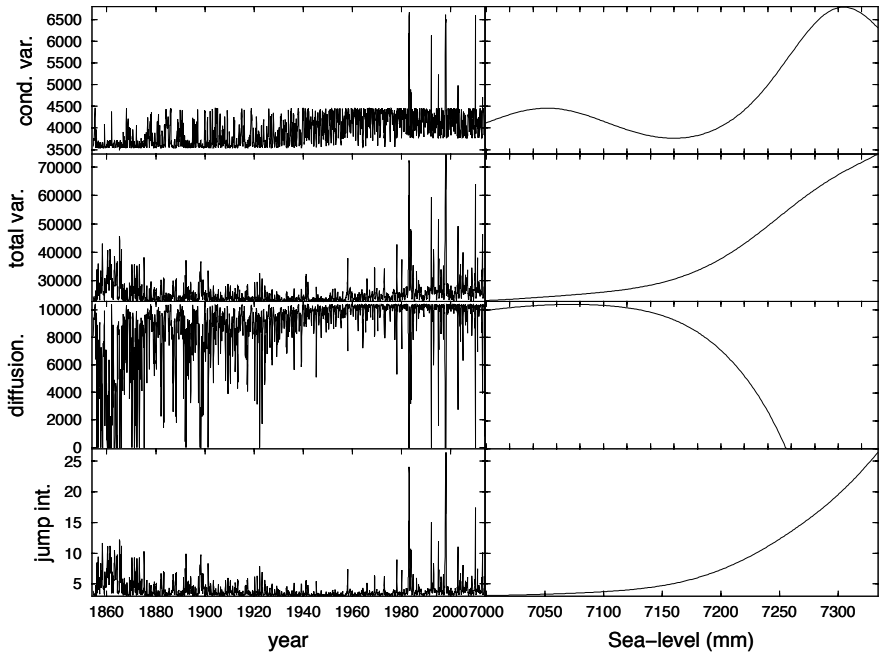

Figure 4.14: Drift – diffusion – jump (DDJ) analysis for the NEP stack.

The analysis of potential for the NEP stack in Fig. 4.15 shows a main well around $\sim$ 6900 mm and a second well around $\sim$ 7100. The first corresponds to the long period of "stability" of the beginning of the 21th century ($\sim$ 1900–1950) wile the second points to a more brief and dubious stable period, starting after 1980.

The indicators used partially confirms the findings of Bromirski et al. (2011), indicating the period around 1980 as crucial point, in which sea–level shifts from a state (uniform increase) to another (closer to stability). The possible break point underlined by Bromirski et al. (2011) in 1930 is not evident by our analysis because the time windows used in the method does not allow to have information for first part of the time series. In addition to the Bromirski et al. (2011) findings, our work evidences an other shift around year 2000.

The same analysis has been performed on the oceanic modes presented above. The scope is to

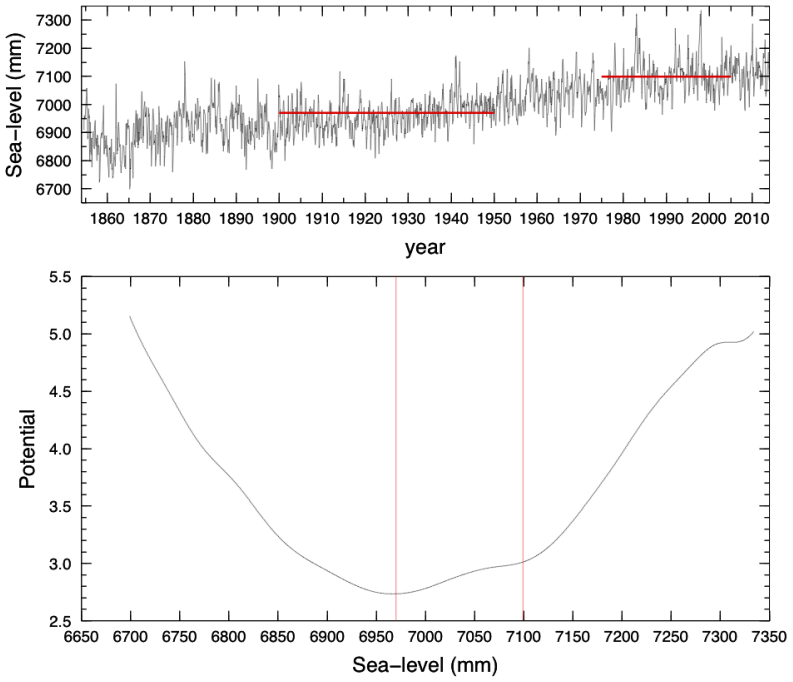

Figure 4.15: Potential analysis for the NEP stack. The bottom frame show the potential in function of the sea–level heigh (mm). In the top, NEP curve is shown with the indication (red lines) of the sea–level heigh for which the potential shows a well (6900 and 7100 mm).

investigate if similar shifts exist in oceanic process that influence the sea–level heigh. In addition we aim to understand if the oceanic modes drive sea–level change in NEP or if there is an other external variable forcing both oceanic modes and sea–level change. For this reason, we have also analyzed the ocean–land temperature monthly curve. In Fig. 4.16 are presented the AR(1) and sd indicators for temperature and oceanic modes.

The MEI index shows an increase starting immediately after 1980 in both AR(1) and sd. The same increase is present, less marked, in PDO and NPGO, even if this latter shows a decrease in both AR(1) and sd after 1980. The shift in sea–level detected for the NEP stack around year 2000 is evident in the MEI index, but no evidence in AR(1) and sd have been found for PDO and NPGO; in the same period, PDO shows a decrease in both AR(1) and sd. Finally, the possible shift indicated by the DDJ analysis of NEP stack (see Fig. 4.14) around 2012 is partially confirmed by MEI and in PDO metric indicators.

The interpretation of the mechanism of interaction between the oceanic modes and sea–level variability is not straightforward. Lluch-Cota et al. (2001) stress the importance of combined effects of PDO and ENSO on sea–level variability in Northestern Pacific, at varying degree both in time and latitude. From the present analysis results that the correlation between MEI and sea–level in NEP shown in several studies (see *e. g.* Zhang and Church, 2012) is reflected also in the critical tipping points. Merrifield (2011) evidences the relationship between wind anomalies associated with Oceanic modes and sea–level in NEP, suggesting a sea–level response to modulations in mean wind fields. He concludes that sea–level fluctuation in NEP are correlated with NPGO index and not with PDO. The correlation existing in trend and fluctuation is not evident in the current analysis, finalized to tipping point detection. The NPGO seems not to follow (neither to anticipate) any critical point shown by NEP stack. This would be related to the nature of the index itself, significantly correlated with fluctuations of specific parameter (salinity, nutrients and chlorophyll-a, see Di Lorenzo et al., 2008). Probably, these parameters are not those the driving the sea–level tipping points detected here.

On the other hand, it is not open to question that sea–level is influenced by change in temperature. Observation and modeling suggest a strong influence of increasing atmospheric temperature in weakening tropical circulation in the Pacific and in enhanced ENSO–like state. The analysis on PDO index, representing the SST in North Pacific, partially shows the same behavior shown for NEP stack: this suggest to investigate more in depth this index. In addition, we have analyzed data of land–ocean global temperature and compared the result with those obtained for the sea–level and the oceanic modes.

In Fig. 4.16d the AR(1) and sd indicators for GISS Temperature (T) are presented. The two jumps in ~ 1980, ~ 2000 detected for the NEP sea–level are shown also by AR(1) and sd for the T curve, confirming a link between temperature change and sea–level variation in NEP. The T curve used here, represent the global average monthly data, and thus it is not suitable for further analysis on NEP interactions.

Results of potential and DDJ analysis for PDO are presented in Figs. 4.17 and 4.18. The DDJ analysis on PDO suggests a jump around ~ 1984, neatly marked also by the total and the conditional variance indicators. According to the potential analysis (Fig. 4.18) , this apparent

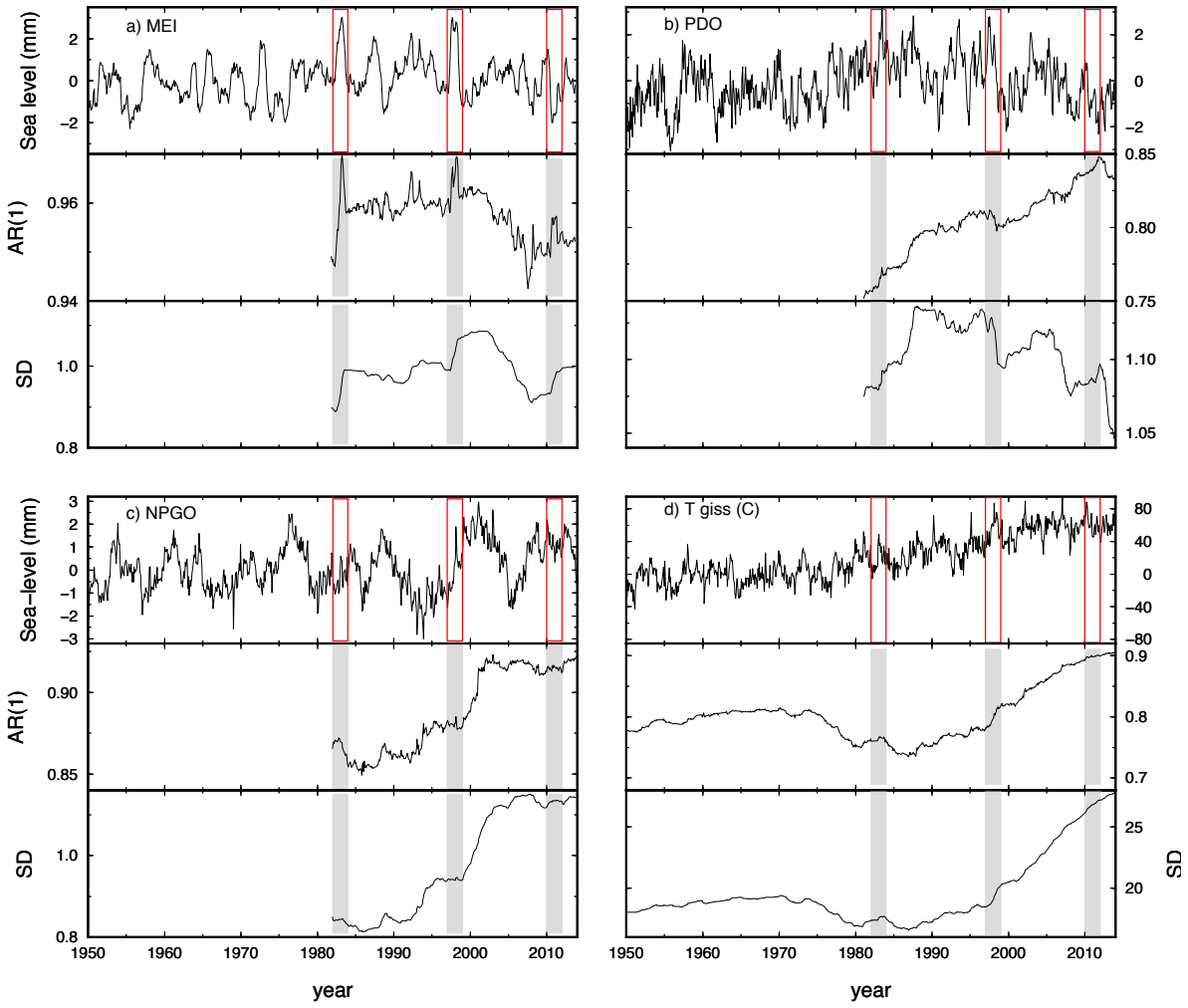

Figure 4.16: Metric indicators (autocorrelation at lag-1 and standard deviation) for a) Multivariate ENSO index (MEI), b) Pacific Decadal Oscillation (PDO), c) North Pacific Gyre Oscillation (NPGO) and d) GISS Land–Ocean Temperature Index.

change in the state of the system does not correspond to a change in the potential. Being the PDO defined as the principal component of the SST in North Pacific, we can hypothesize that the change detected with DDJ and metric indicators represent the "internal" change in the state of SST, and that this latter could be a driving force for sea–level change in NEP.

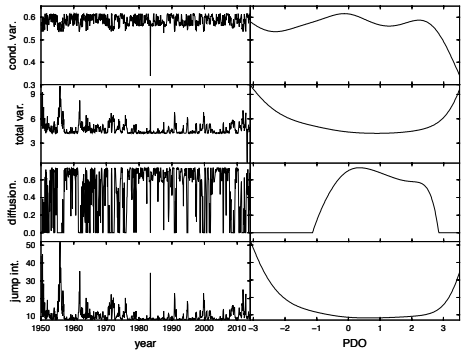

Figure 4.17: Drift – diffusion – jump (DDJ) analysis for the PDO index.

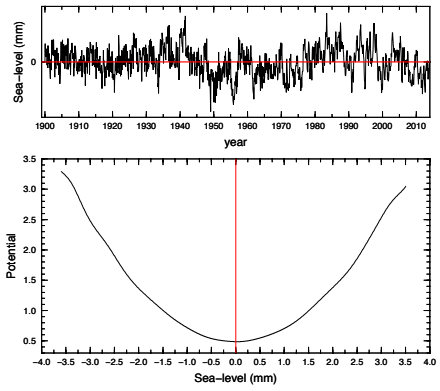

Figure 4.18: Potential analysis (right) for the PDO index.

4.5 Gleaning other information from tide gauge records

4.5.1 Constraining mass balance of the Greenland Ice sheet: the Nuuk/Gotab record

In view of rapid changes affecting the polar ice sheets (see the IPCC AR4 report, Bindoff et al., 2007), in situ instrumental observations of sea–level from these regions would be potentially very important. In particular, it is expected that relative sea–level observations from tide gauges located in the vicinity of major ice sheets could help to constrain the recent time–history of their mass unbalance. Before year $\sim$ 2000, this was only poorly determined because of the limited resolution of remote sensing techniques (Bindoff et al., 2007). However, despite significant collaborative efforts, at the end of the nineties the state of the polar tide gauges was generally unsatisfactory. The whole subject was reviewed by Plag (2000), who pointed out the degradation of the observing system and emphasized the relevance of Arctic tide gauge data for the geophysical community.

At the year 2000, only few tens of tide gauges where in operation along the Arctic shores of Russia, Greenland, Iceland, Norway, Canada and USA (Plag, 2000). Among these, only a few where characterized by a record length exceeding a few decades, and thus potentially suitable to estimate the long–term sea–level trend. The situation was (and still remains) particularly problematic in Greenland, where the PSMSL database now collects only eight sites (Fig. 4.19), mostly located along the southwestern margins of the Greenland Ice Sheet (GIS). The instrumental record from the Nuuk/Godthab (hereafter referred to as NG) tide gauge is remarkably long (>40 years) compared

to the other sites in Greenland ($\leq$10 years), and covers a time span ($\sim$ 1958–2003) during which only a few assessments of the GIS mass balance are available (Hanna et al., 2005; Bindoff et al., 2007; Rignot et al., 2008). The tide gauge time series are visualized in Fig. 4.20.

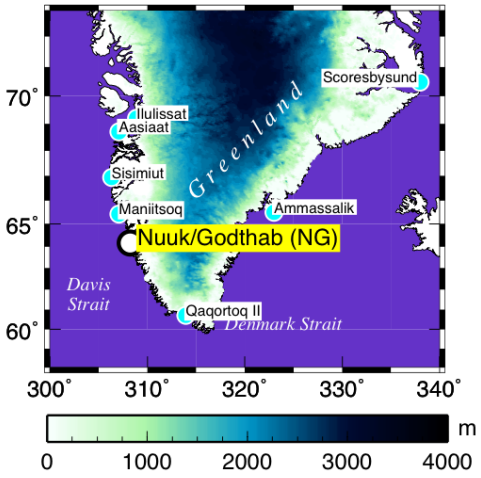

Figure 4.19: Map of southern Greenland, showing the location of the NG tide gauge (NG), and the present–day ice thickness of the GIS (in meters). Ice thickness data are a courtesy of Jonathan Bamber, 2012. Also shown are other PSMSL sites in Greenland: Ilulissat, Aasiaat, Sisimiut, Maniitsoq, Qaqortoq II, Ammassalik and Scoresbysund.

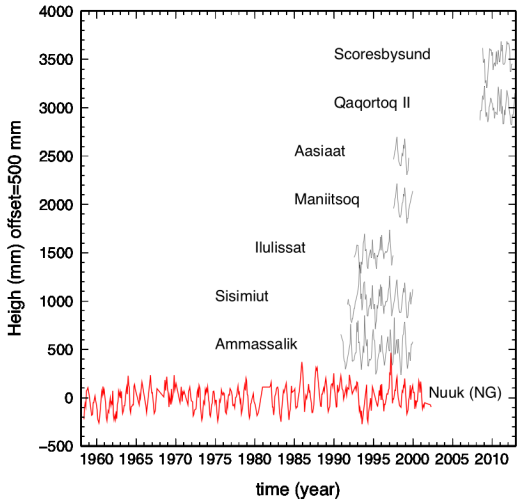

Figure 4.20: Overview of the PSMSL metric monthly time series available from the sites shown in the map. For visualization purposes, the average has been subtracted from each time series and these have been shifted by an arbitrary amount. The period and completeness of each time series is also shown.

The context outlined above encourages an analysis of the NG record, which as far as we know has never been attempted to date. In the following we will ascertain whether relative sea–level data from NG could be useful to constrain volume changes in the GIS and possibly other contributions to local sea–level rise, such as those associated to glacial isostatic adjustment (GIA) and to the melting of remote ice aggregates. We extend the previous analysis of Plag (2000), who recognized that trends shown by Arctic tide gauges are in broad agreement with an overall un–loading of the Arctic land–based cryosphere. However, in comparison with Plag (2000), we perform a more quantitative study taking advantage of IPCC AR4 assessments (Bindoff et al., 2007) and numerical modeling based on the solution of the "Sea Level Equation" (Farrell and Clark, 1976) and the computation of sea–level "fingerprints" (Mitrovica et al., 2001; Tamisiea et al., 2011). Although we focus on an individual tide gauge record, the method outlined can be extended to other Arctic records with sufficient length. The material which follows is broadly based on the findings of Spada

et al. (2014a).

The Nuuk/Godthab tide gauge data

The NG tide gauge record, obtained from the database of the PSMSL (see section 1.2), contains monthly mean values between years 1958.4 and 2002.3. The total time span of the record is thus 43.9 years and its completeness is $c = 79\%$. In 2002, the instrument was damaged and no longer maintained by DMI (the Danish Meteorological Institute). Coincidentally, the time period of the NG tide gauge almost exactly overlaps the one adopted in IPCC AR4 report (Bindoff et al., 2007) in their assessments of the total budget of the global mean sea–level change during the second part of the 20$^{\text{th}}$ century (namely, 1961–2003). This will greatly facilitate inter–comparisons between the observed rate at the NG site and the AR4 assessments.

The NG time series, reproduced in Fig. 4.21a, shows a clear linear trend and large amplitude oscillations with approximately a period of 2 decades, which are likely to represent the effects of the 18.6 years nodal tide (Trupin and Wahr, 1990). The oscillations are particularly evident after application of a 10–years running average to the time series (thick line in Fig. 4.21a), clearly showing that the tide attains almost exactly two full cycles within the time window of the NG data. Therefore, it is expected that the assessment of the trend is not too biased by the oscillating component of the signal. A few interruptions are also present in the time series, which however do not seriously affect its completeness.

Although our goal here is not to use the NG record for a new estimate of global secular sea–level rise, its overall quality can be assessed with reference to the constraints adopted in chapter 2 (labeled I–VI in Table 2.3). The NG time series is not meeting criterion (I), since its length is <60 years. Furthermore, the series is not belonging to the RLR PSMSL dataset. Rather, the data currently belong to the Metric dataset. Criterion (II) is met, since Nuuk is located along the western coast of Greenland (see Fig. 4.19, sufficiently distant from collisional tectonic boundaries. In spite of the gaps (see Fig. 4.21), the completeness of the NG monthly record is remarkable (79%) and thus largely meeting requirement III, which was however thought for annual time series. Criterion IV cannot be applied since in the neighborhood of the NG tide gauge no other instrumental observations of comparable length are available (see Figs. 4.19 and 4.20). As we will see below, the GIA correction is quite model–dependent (criterion V). This has been verified running various GIA models and by inspection of GIA results presented in the literature. Last, since the NG record is not showing suspect accelerations and/or jumps, and could be hardly affected by anthropogenic effects because of the very low urbanization in the Nuuk region, criterion VI is met.

To estimate the local long term sea–level trends from the NG data, we first performed a straight–forward linear regression. Assuming a linear model, during the whole time period of the NG record the observed rate of sea–level change is $(+1.9 \pm 0.7)$ mm yr^{-1}, where the uncertainty has been evaluated by Equation 2.3 in chapter 2 and corresponds to the 95% confidence level. The trend is shown by a red line in Fig. 4.21a). The sea–level acceleration (twice the quadratic term of a polynomial regression) for the NG time series is $a^{OBS} = (-0.05 \pm 0.04)$ mm yr^{-2}. By a Fisher F–test performed on the variances of the residues of the linear and quadratic regressions, we have

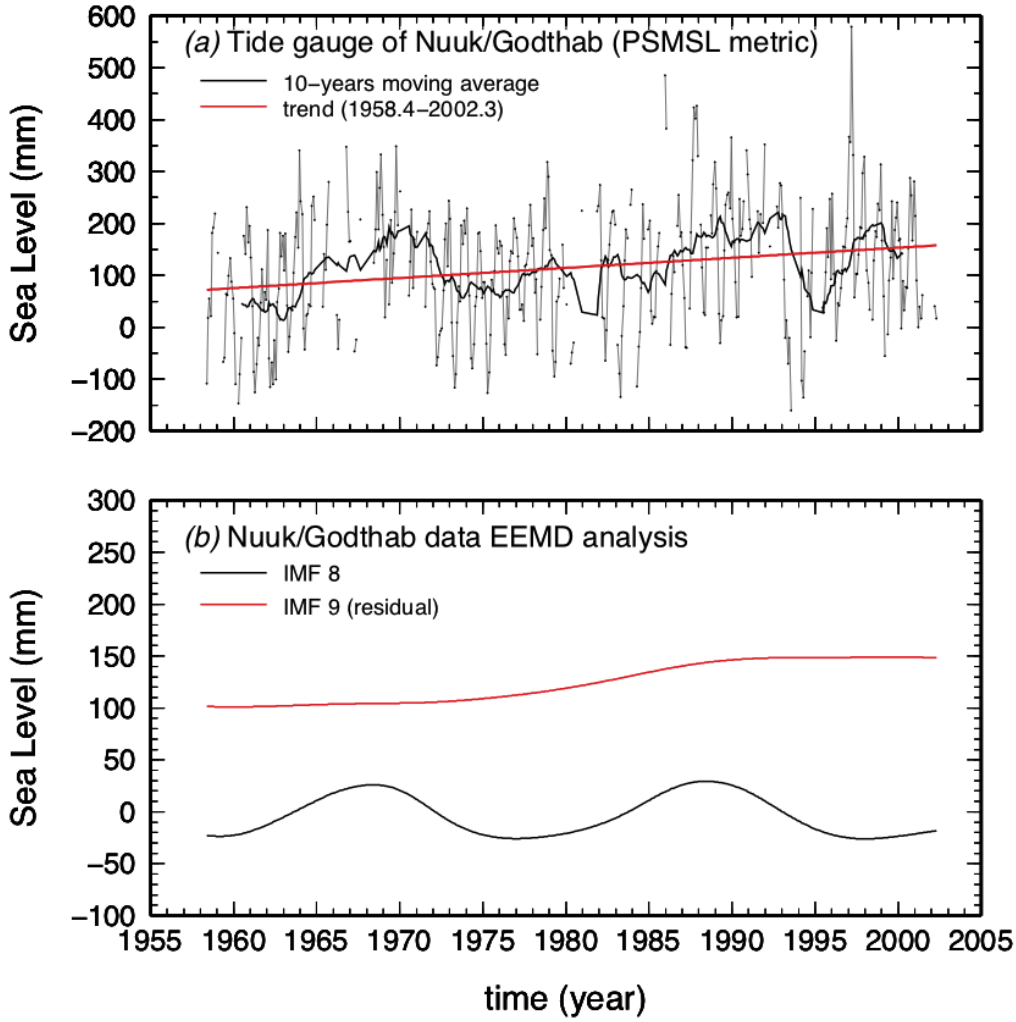

Figure 4.21: (a): the NG time series (thin line and dots), the 10–years moving–average (thick line), and the linear trend over the whole observation period (red) obtained by least squares. (b) the Image Function IMF8 corresponding to the longest period ($\sim$ 18 years) in the EEMD analysis described in the body of the paper (black curve), and the long term residual trend (red).

verified that the latter is not improving the fit with respect to the former, at the 95% confidence level.

The record of NG has been then analyzed using the improved version of the EEMD method (the CEEMDAN, Torres et al., 2011) presented in section 4.1. The two parameters required by the EEMD method, have been set to $Nstd = 0.30$ and $NE = 300$, respectively (see above for their definition).

In Fig. 4.21b we show the residual for the NG time series after interpolation (with a cubic spline, see De Boor, 1978) and mirroring, the residual (red curve) obtained after subtracting the IMFs, and the IMF8 (black curve) which represents the oscillation with the longest period ($\sim$ 18 years). To obtain a linear trend from the residual, we have performed a standard linear regression, which provides a rate of (1.93 ± 0.03) mm yr^{-1}. Adding in quadrature the uncertainty in the residual itself, we obtain

$$r^{OBS} = +1.93 \pm 0.18 \quad \text{mm yr}^{-1}, \tag{4.4}$$

(95% confidence), for the time period 1958.4–2002.3 (extrapolating our assessment to the time interval 1961–2003, the same considered in the AR4, does not significantly change the estimate). While the value obtained is consistent with the one gained above by a standard linear regression, the strong improvement in its precision results from the removal of the cyclic components implied in the EEMD approach. Note that in Equation 4.4 and in the following, the uncertainty will be expressed using two significant figures, even when the fractional uncertainty is large. This is generally contrary to common practice (see e.g., Taylor, 1997), but it facilitates comparison with the AR4 results.

The value of r^{OBS} in Equation 4.4 is comparable with the average rate of global sea–level change during the period 1961–2002 $(+1.8 \pm 0.8)$ mm yr^{-1} (95% confidence) assessed by AR4. According to Wahl et al. (2013) (see their Table 3), these values of the sea–level trend are also in broad agreement with the rate of global sea–level rise during 1950–2009 (namely, 1.80 ± 0.11 mm yr^{-1}), and with the regional rate for the North Sea (1.62 ± 0.29 mm yr^{-1}) during the same period. However, in view of the large local effects expected at the NG tide gauge from GIA and in particular from the isostatic effects associated with the melting of the nearby GIS, this agreement is certainly fortuitous.

Sea–level components at the NG tide gauge

The long–term rate of relative sea–level change observed at the NG tide gauge stems from the combination of several components. Following the general approach of Slangen et al. (2012) and presented in chapter 1, the total observed rate r^{OBS} coincides with r^{TOT} of Equation 1.3, and can be written as:

$$r^{OBS} = r^{GIA} + r^{MAS} + r^{STE} + r^{OTH}, \tag{4.5}$$

where the sea–level components on right–hand side have been described in chapter 1 and r^{OBS} here represents the observed rate constrained by Equation 4.4. The term r^{OTH} includes the contribution of tectonic movements (r^{TEC}) and those due to terrestrial mass exchange (including dams

impoundment and groundwater mining, r^{TER}). In turn, the mass term in (4.5) can be expressed as

$$r^{MAS} = r^{AIS} + r^{GIC} + r^{GIS}, \tag{4.6}$$

where the terms in the right hand side are the contributions associated with mass variations of the Antarctic Ice Sheet (AIS) and of Glaciers and Ice caps (GIC), the one due to the melting of the Greenland Ice Sheet (GIS) during the same time period. The various terms of Eqs. (4.5) and (4.6) are individually discussed in the following.

Fig. 4.22 shows the sea–level fingerprints associated with GIA at regional scale. The global fingerprint is that presented in Fig. 2.9 of chapter 2. Since the time scale of GIA is of the order of a few kilo–years (Turcotte and Schubert, 2002), the rates of sea–level change can be assumed of Peltier (2004) to be constant over the time period of concern here (a few decades). The maps are obtained using the ice model ICE5G(VM2) and the theory presented in section 1.4. Since for this model the ice sheets melting ends $\sim 4,000$ years ago, GIA is not currently causing any alterations in the total mass of the oceans, but is of course producing regional sea–level variations due to the Earths on–going adjustment to the changes following the LGM. As a consequence, for the global fingerprints, the average sea–level is

$$\left\langle r^{GIA} \right\rangle = 0, \tag{4.7}$$

where $\langle \cdots \rangle$ denotes the average over the surface of the oceans. However, this property does not hold for the mass terms in Equation 4.5 since, in contrast with GIA, they currently involve a net mass variation of the oceans, as well as surface displacements due to local changes.

Across the Davis Strait (*i.e.*, between Greenland and Canada), a sea–level rise of several millimeters per year results from the combined effects of two processes, namely the the collapse of the the isostatic forebulge surrounding the former Laurentian ice sheet and the melting of the Greenland ice sheet. The relative contribution of these two processes have been separately studied by Fleming and Lambeck (2004). The rate of sea–level rise is strongly reduced along the coasts of southwest Greenland and it changes its sign to the south. According to the current version of model ICE5G(VM2), the rate of GIA–induced sea–level change at the NG tide gauge is

$$r^{GIA}_{ICE-5G(VM2)} = +0.66 \text{ mm yr}^{-1}, \tag{4.8}$$

with an unspecified uncertainty (for NG and all the other PSMSL tide gauges, numerical predictions for sea–level change are available from *http://www.atmosp.physics.utoronto.ca/ peltier/*). In view of the large gradients of GIA–induced sea–level variations in southwest Greenland shown in Fig. 4.22, we expect that details in the GIA modeling assumptions, both in terms of the ice mass descriptions and Earth rheology used, could lead to significantly different results. To estimate the uncertainty associated with r^{GIA}, we have carried two further GIA runs (R1 and R2) in which two different global chronologies for the melting history of the late–Pleistocene ice sheets have been employed (the computations have been made using an improved version of the program SELEN presented in section 1.4. The chronologies are ICE–5G and KL05 described in subsection 1.4.2 of chapter 1.

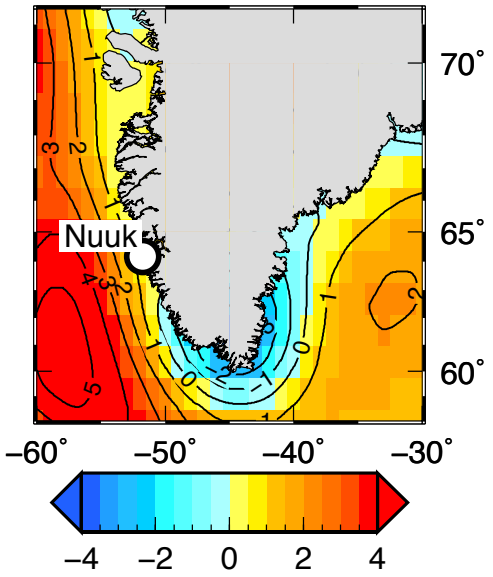

Figure 4.22: Rate of present–day sea–level change due to GIA from LGM (r^{GIA}) obtained using model ICE5G(VM2) for southern Greenland.

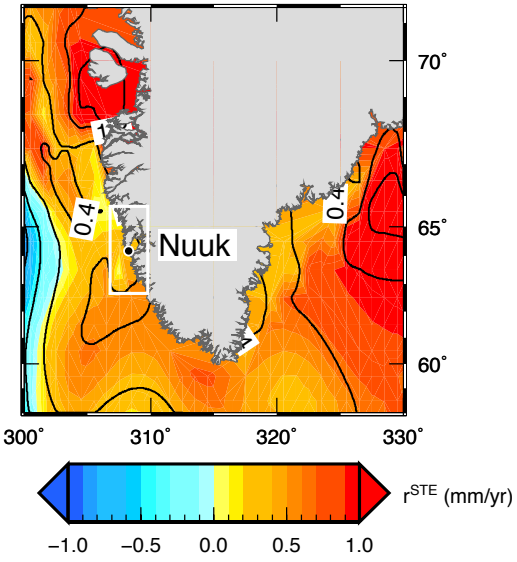

Figure 4.23: Steric component of sea–level change (r^{STE}) in southern Greenland between 1958–1962 and 2000–2005 according to the NODC data.

For run R1, we have employed a three layer viscosity profile for the mantle, obtained by volume averaging the multi–layered VM2 profile of Peltier (2004). The upper mantle, transition zone, and lower mantle Maxwell viscosities are 0.5, 0.5 and 2.7 x 10^{21} Pas, respectively, and the lithospheric thickness is 90 km. For run R2, we have adopted the nominal viscosity profile of Fleming and Lambeck (2004), which is constrained by Holocene relative sea–level observations in Greenland. In this case, the upper mantle, transition zone, and lower mantle viscosities are 0.4, 0.4 and 10 x 10^{21} Pa$*$s, respectively, with a lithospheric thickness of 80 km. We did not vary these viscosity values, since this would alter the match of the GIA model predictions with the Holocene relative sea–level variations used to constrain their parameters. The formulation by Milne and Mitrovica (1998) has been employed to account for the impact of Earth rotation variations on sea–level change. Runs R1 and R2 have in turn been repeated adopting the recipe by Tanaka et al. (2011) in order to mimic the effects of mantle compressibility. Despite the significant spatial variability shown by the GIA response in southwest Greenland, in all the computations performed, the GIA–induced rate of sea–level change tends to decrease close to the shorelines. The values of GIA–induced sea–level rise predicted at the NG site are 1.54, 1.03, 0.81, and 0.64 mm yr^{-1}, for models R1, R2, R3 and R4, respectively. Along with the value corresponding to the nominal

ICE5G(VM2) model (Equation 4.8), these values define the relatively narrow interval

$$r^{GIA} = +1.1 \pm 0.5 \text{ mm yr}^{-1}, \tag{4.9}$$

which represents our preferred estimate for the current rate of GIA–induced sea–level change at NG.

For the thermosteric component, Bindoff et al. (2007) have evaluated the ocean–average steric contribution to total sea–level rise during two distinct time periods: 1961–2003 and 1993–2003, respectively. Their assessments are presented in Table 5.3 of the IPCC AR4. For the former period, which is almost exactly overlapping the time span of the NG tide gauge record, they provide an average sea–level of

$$\left\langle r^{STE}_{AR4} \right\rangle = +0.42 \pm 0.12 \text{ mm yr}^{-1}, \tag{4.10}$$

(90% confidence), while during the latter there is evidence of a significant increase of the steric component, with values close to 1.5 mm yr^{-1}. Estimate (4.10), which accounts for thermal expansion to the depth of 3,000 m, combines results from Antonov et al. (2005) and Ishii et al. (2006).

The geographic distribution of linear trends in thermal expansion for 1955 to 2003, is highly non–uniform, especially across the equatorial oceans (see Fig. 5.16 of the IPCC AR4, based on Ishii et al. 2006). From visual inspection of this figure, in the Davis Strait the trend of the thermosteric component of sea–level change has been positive during that time period, with values possibly below the global average (4.10). To obtain a more refined estimate of the total steric component of sea–level rise at Nuuk, we have analyzed the data available from the National Oceanographic Data Center (NODC, see *http://www.nodc.noaa.gov/*). In particular, we have considered fields of the steric sea–level anomaly down to a depth of 2000 m, during the time period between the pentads 1958–1962 and 2000–2005. The regional pattern of the average rate for southwest Greenland is displayed in Fig. 4.23. Using values from ocean pixels within the $3^\circ \times 3^\circ$ area marked by a rectangle in Fig. 4.23 we obtain

$$r^{STE} = +0.39 \pm 0.14 \text{ mm yr}^{-1}, \tag{4.11}$$

where the uncertainty represents the standard deviation of the mean. This overlaps with the estimate (4.10) based on the AR4 report. Using steric anomalies to a depth of 700, also available from the NODC, would not change appreciably the value of r^{STE} in the area surrounding Nuuk. We note that Equation 4.11 does not account for possible bottom pressure variations caused by ocean warming and circulation changes. However, using a coupled Atmosphere–Ocean General Circulation Model under the IPCC A1B scenario, Landerer et al. (2007) have shown that these will play a role, especially in shelf areas, during the 21st and 22nd centuries.

For the r^{MAS} component of Equation 4.5, we have used fingerprints obtained with the models presented in subsection 1.4.3 of chapter 1. Maps of present–day sea–level fingerprint for the three ice sourced considered (namely, AIS, GIS and GIC) are shown in Fig. 1.9 of chapter 1. For the mass term r^{AIS} in Equation 4.6, the ocean–averaged assessment suggested by the IPCC AR4 is

$$\left\langle r^{AIS}_{AR4} \right\rangle = +0.14 \pm 0.41 \quad \text{mm yr}^{-1}, \tag{4.12}$$

during the period 1961–2003 (again, see Table 5.3 of Bindoff et al., 2007). As discussed more in detail in the following, this is rather a guess, since no supporting data effectively exist for the mass balance of the AIS during this period of time.

Since the NG tide gauge is located in the extreme far–field of Antarctica, (4.12) is expected to constitute a valid approximation for the rate of local sea–level change. In fact, one fundamental properties of the sea–level fingerprints is that of reaching, at very large distances of the ice sources, a value slightly in excess of the ocean–averaged value (Mitrovica et al., 2001). This is confirmed by the results in Fig. 4.24a where is shown the regional (normalized) sea–level fingerprint (*i.e.* the ratio $r/\langle r\rangle$, where $\langle r\rangle$ is the ocean–average of relative sea–level rate) corresponding to the melting of the AIS. Using the IPCC assessment for in (Equation 4.12 above and the numerical values obtained in Fig. 4.24a our estimate for the AIS component of total sea–level change at NG is

$$r^{AIS} \simeq 1.1 \ \left\langle r^{AIS}_{AR4} \right\rangle = +0.15 \pm 0.45 \text{ mm yr}^{-1}. \tag{4.13}$$

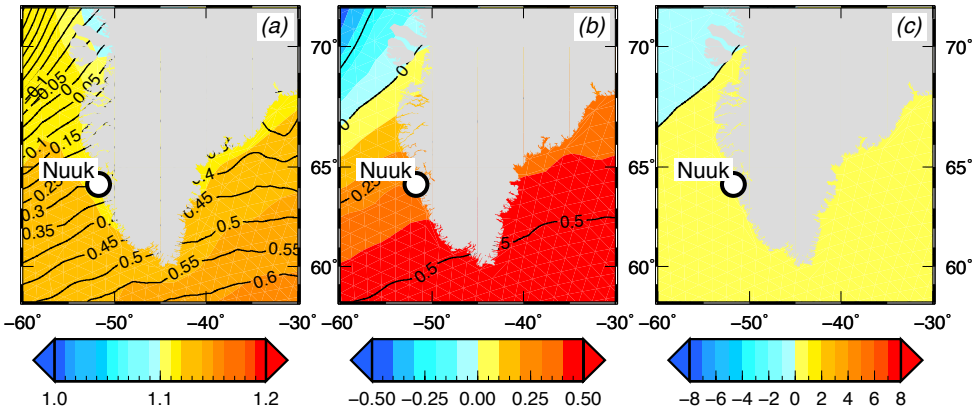

Figure 4.24: Normalized TIM sea–level fingerprints ($r/\langle r\rangle$) for the AIS (left), GIC (middle) and GIS (right) in Southern Greenland.

For the mass term r^{GIC} in Equation 4.6, the regional normalized sea–level fingerprint is shown in Fig. 4.24b. At global scale, in comparison with AIS and GIS, the GIC fingerprints show a larger spatial variability, which reflects the scattered distribution of the global system of the ice sources. The site of NG is very close to the nodal line of the sea–level fingerprint corresponding to a vanishing sea–level change. This is consistent with the results obtained by Mitrovica et al. (2001) (see their Fig. 1c), who however did not assume a uniform mass variation across the GIC. The same is found in Slangen et al. (2012). From the numerical results of Fig. 1.9d in chapter 1, we directly obtain:

$$r^{GIC} \simeq +0.25 \ \left\langle r^{GIC}_{AR4} \right\rangle = +0.13 \pm 0.05 \quad \text{mm yr}^{-1}, \tag{4.14}$$

where

$$\left\langle r^{GIC}_{AR4} \right\rangle = +0.50 \pm 0.18 \quad \text{mm yr}^{-1}, \tag{4.15}$$

represents the spatially averaged sea–level variation assessed by is the IPCC AR4 for the period 1961–2003. This value includes glaciers and ice caps around the ice sheets and its uncertainty represents the 90% confidence interval. The large discrepancy of r^{GIC} from the globally averaged value is the consequence of the relatively small distance separating the NG tide gauge from the major GIC sources in the northern polar region.

The GIS sea–level fingerprint is shown in Fig. 4.24c. Since we do not dispose of a detailed mass balance for the GIS during the time period 1961–2003, these fingerprints have been obtained assuming a uniform mass variation over the GIS, as previously done above for the GIC and the AIS components.

For rate of equivalent sea–level rise associated on the GIS melting during the period 1961–2003, the IPCC AR4 estimate is

$$\left\langle r^{GIS}_{AR4} \right\rangle = +0.05 \pm 0.12 \quad \text{mm yr}^{-1}, \tag{4.16}$$

which is largely based on the work of Hanna et al. (2005), but it also accounts for other mass balance estimates obtained for the period 1993–2003 (see Fig. 4.18 of the AR4). Since $\left\langle r^{GIS}_{AR4} \right\rangle$ results from a very small number of assessments, its uncertainty has not a statistically rigorous significance and does not represent a specific confidence level. We note that within the range of uncertainty, $\left\langle r^{GIS}_{AR4} \right\rangle$ also includes negative values that would correspond to a positive mass balance for the GIS (ice mass accretion) during the period 1961–2003.

After the publication of the IPCC AR4, the work of Hanna et al. (2005) has been extended and updated by Rignot et al. (2008). By averaging the total mass balance estimates given in their Fig. 3 over the time period 1960–2000 a second estimate for the average sea–level rise can be obtained

$$\left\langle r^{GIS}_{R08} \right\rangle = +0.20 \pm 0.08 \quad \text{mm yr}^{-1}, \tag{4.17}$$

which suggests a larger contribution of the GIS compared to (4.16).

A third estimate has been recently given by Slangen et al. (2012), who combined surface mass balance data from Ettema et al. (2009) with the dynamical component of ice loss from (Rignot et al., 2011), suggesting:

$$\left\langle r^{GIS}_{S12} \right\rangle = ++0.14 \pm 0.16 \quad \text{mm yr}^{-1}, \tag{4.18}$$

which only marginally includes negative values, indicative of an increase of the GIS mass.

Taken all together, estimates (4.16), (4.17) and (4.18) point to an average sea–level rise $\left\langle r^{GIS} \right\rangle$ in the range between $+0.1$ and $+0.2$ mm yr^{-1}. From the normalized fingerprint values in Fig. 4.24c, one has

$$r^{GIS} \simeq -5.5 \left\langle r^{GIS} \right\rangle \tag{4.19}$$

which allows for a straightforward computation of the local rate of sea–level rise expected at the NG tide gauge during 1961–2003 according to the 4three estimates above for $\left\langle r^{GIS} \right\rangle$. Note that, in (4.19), the large scaling factor in front of $\left\langle r^{GIS} \right\rangle$ denotes the large departure from eustasy arising from NG being in the near–field of the GIS. Various results, reviewed by Alley et al. (2010),

strongly indicate that during last decade, $\langle r^{GIS} \rangle$ has increased considerably above the values reported for the period 1961–2003, implying a significant acceleration (Rignot et al., 2011). In particular, according to the recent ICESat–based estimate of Sørensen et al. (2011) Spada et al. (2012); **?**, the average sea–level rise associated with the melting of the GIS has been $\langle r^{GIS} \rangle$ = 0.67 0.08 mm yr^{-1} between 2003 and 2008, exceeding by an order of magnitude the AR4 assessment for 1961–2003 (4.16).

Since Nuuk is located along the western coast of Greenland (see Fig. 4.19), distant from collisional boundaries, tectonic deformations are not expected to significantly contaminate the observations. Thus, the term r^{OTH} will be mainly composed by r^{TER}, referred to the terrestrial mass exchange.

The TER global sea–level fingerprint has been constructed for the time period 1961–2003 by Slangen et al. (2012), as presented in subsection 1.3.4. At global level, the two main processes combined to obtain the TER fingerprint (namely, groundwater extraction and reservoir impoundment) contribute to produce a sea–level fall and a total ocean-averaged effect of

$$\langle r^{TER} \rangle = -0.20 \pm 0.26 \quad \text{mm yr}^{-1}, \tag{4.20}$$

where the uncertainty has been estimated adding the individual uncertainties of the contributing mechanisms (see the summary Table 3.1 of Slangen et al., 2012). In the region of the Davis Strait (see Fig. 4.24), the TER component of sea–level rise is

$$r^{TER} = -0.07 \pm 0.09 \quad \text{mm yr}^{-1}, \tag{4.21}$$

which therefore represents the smallest mass term in Eq. (4.6), and the one characterized by the largest fractional uncertainty.

Constraining the mass balance of the GIS

In Fig. 4.26, the top lines (black) summarize the numerical values obtained in section 4.5.1 for the various sea–level contributions (Eqs. 4.5 and 4.6). While the GIA term is only obtained from modeling, the others are based on various assessments in the literature. For the mass terms, estimates of local sea–level variations have been obtained with the aid of the sea–level fingerprints. Concerning the GIS, three rates are given, corresponding to three different estimates for the average sea–level change discussed above. It is apparent that the GIA and the GIS terms are those providing the largest contribution to sea–level variations at NG during period 1961–2003. The two terms, however, are counteracting, with the GIA producing a relative sea–level rise and the changes in the GIS having the tendency to produce a sea–level fall, according to the three estimates considered here. The remaining mass terms (AIS, GIC) and the TER have a minor role, and, in general, are characterized by a large fractional uncertainty. However, with the STE term, they act in the same direction of the GIA term. The three MOD lines in Fig. 4.26 (blue) show the total modeled and/or assessed values for the rate of sea–level change at NG. They result from adding the terms of lines 1.–5. with each of the three GIS contributions corresponding to the estimates of AR4, of Rignot et al. (2008) and of Slangen et al. (2012), respectively.

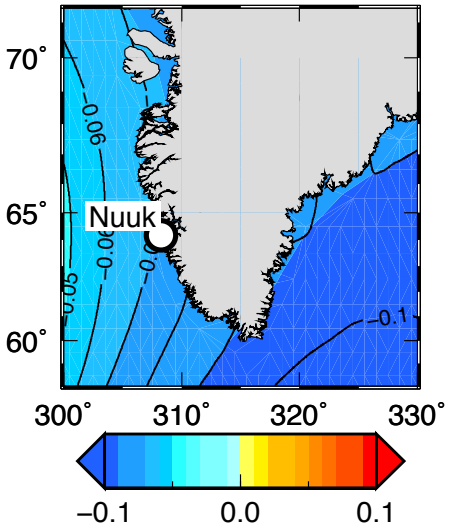

Figure 4.25: Regional views of the mass term r^{TER} of sea–level change for the time period 1961–2003.

Although the fractional uncertainties on the MOD values are relatively large, a comparison with the observed rate (red in Fig. 4.26) is possible, at least qualitatively. All the MOD rates indicate positive rates of sea–level change, as seen in the observed trend. The observed trend is fully consistent (the error bars completely overlap) with the model predictions based on the AR4 assessment for the GIS component, while the agreement is only marginal if we consider the MOD value based on the Slangen et al. (2012) estimate. The observed rate is clearly inconsistent with the MOD rate inferred from the Rignot et al. (2008) results. Overall, the results in Fig. 4.26 indicate that the level of disagreement between the rate of sea–level change inferred from NG and the predictions resulting from modeling or obtained from the literature is of the order of 0.5–1 mm yr^{-1}, which represents a significant fraction of the observed rate.

The general misfit between the observations and model predictions in Fig. 4.26 could be attributed to an erroneous evaluation of one or more of the terms in Equation 4.5 or to some unmodeled effects. Since the GIA and the GIS have the largest amplitudes, errors in the evaluations of these two terms could be a major cause of disagreement. Due to the very low urbanization in the Nuuk region, anthropogenic effects can safely be excluded. Systematic errors associated with the instrumentation, however, cannot be ruled out. Another possible source of misfit could, in principle, be associated with tectonic deformations associated with the r^{TEC} term in Equation 4.5. These have been often invoked as a possible cause of long–term sea–level variations at tide gauges (Spada and Galassi, 2012; Olivieri et al., 2015). Previous work (*e.g.,* Chung and Gao, 1997) has suggested that Greenland is a tectonically stable region with a low level of seismicity (Johnston,

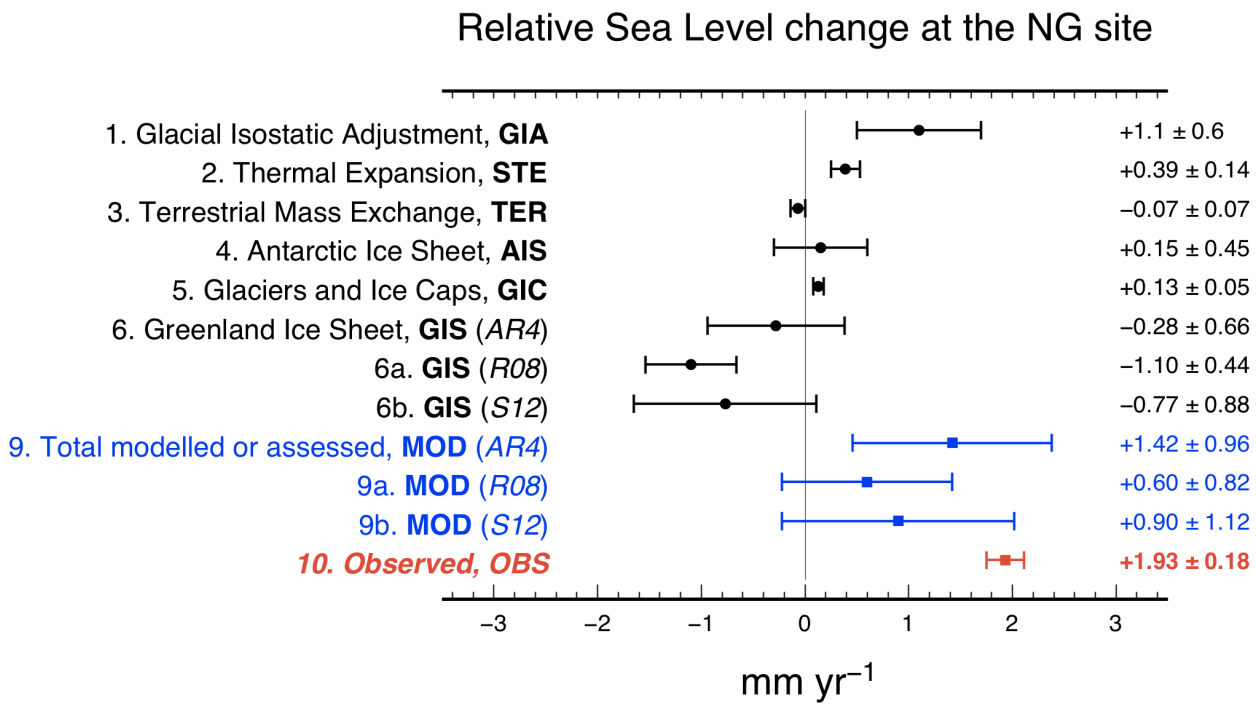

Figure 4.26: Summary of individual modeled (or assessed) contributions to the sea–level trend expected at the NG tide gauge during 1961–2003 (black), the total modeled or assessed sea–level change (MOD, blue) and the observed trend (OBS, red) at the NG tide gauge. The error bars on the total MOD rate are obtained by adding in quadrature the individual (independent) uncertainties of the individual sea–level contributions. Note that for the GIS, three estimates are available, and thus three MOD rates. The right column shows the numerical values of the estimates, to two significant figures.

1987) possibly controlled by on–going GIA (Chung, 2002). Furthermore, observations of vertical rates of crustal uplift observed by Global Positioning System (GPS) along the coasts of Greenland can be satisfactorily explained, at least during 2003–2008, by combining GIA effects based on model ICE–5G of Peltier (2004) with isostatic deformations associated with the present elastic response to ice unloading, without invoking tectonic deformations (Spada et al., 2012). Although the agreement between predictions of isostatic models and GPS vertical rates is particularly good at the GPS site of KELY in southwest Greenland, relatively close to the location of the NG tide gauge, a role for tectonic subsidence cannot be ruled out at the 0.5 mm yr^{-1} level, since the uncertainty on the longest GPS vertical rates is still above the 1 mm yr^{-1} level (see Table 3 of Spada et al., 2012). Possible effects from the vertical deformations associated with cryospheric fluctuations during the Little Ice Age (LIA) are expected to produce small effects in SW Greenland, even assuming an extremely low asthenospheric viscosity (Valentina Barletta, personal communication, 2013).

Assuming that the trend of sea–level change observed at the NG tide gauge is not significantly affected by tectonic deformation, and that the proposed estimates at lines 1.–5. can be trusted, the results of Fig. 4.26 can be used to refine previous estimates of $\langle r^{GIS} \rangle$. In particular, they suggest that $\langle r^{GIS} \rangle$ could be somewhat biased toward positive values. The bias appears to be larger for the estimates by Rignot et al. (2008) and Slangen et al. (2012) compared with the AR4 assessment. Because of Equation 4.19, this produces exceedingly negative values of the local sea–level trend at NG, which prevent a full agreement with the observed rate of sea–level change. A disagreement at the ~ 1 mm yr^{-1} level between MOD and OBS, suggested by Fig. 4.26, would imply, according to Equation 4.19, a reduction of ~ 0.2 mm yr^{-1} in $\langle r^{GIS} \rangle$. Hence, estimates (4.17) and (4.18) would be consistent with a substantial equilibrium of the mass balance of the GIS during period 1961–2003 (i.e. $\langle r^{GIS} \rangle \approx 0$), which would match the AR4 assessment (4.16). For the moment, the existence of a slight, but significant mismatch between the observations at NG and the ASL estimates of Rignot et al. (2008) and Slangen et al. (2012) remains an hypothesis, based on the assumption that the various sea–level contributions at NG, and their uncertainties, have been evaluated correctly. Nevertheless, according to the results above, the possibility that the mass balance of the GIS during 1961–2003 was closer to equilibrium than expected, cannot be discounted.

4.5.2 Acceleration in GIA– induced sea–level changes: the Baltic Sea

Although isostatic readjustment affects the local rates of secular sea–level change, a possible impact on regional acceleration have been so far discounted (Douglas, 1992; Woodworth et al., 2009), since the process evolves on a millennium time scale (Turcotte and Schubert, 2002). Here we report a previously unnoticed anomaly in the long–term sea–level acceleration of the Baltic Sea tide gauge records, and we explain it by the classical post–glacial rebound theory and numerical modeling of glacial isostasy. Contrary to previous assumptions, our findings demonstrate that isostatic compensation plays a role in the regional secular sea–level acceleration. Results of this part have been published in Spada et al. (2014b).

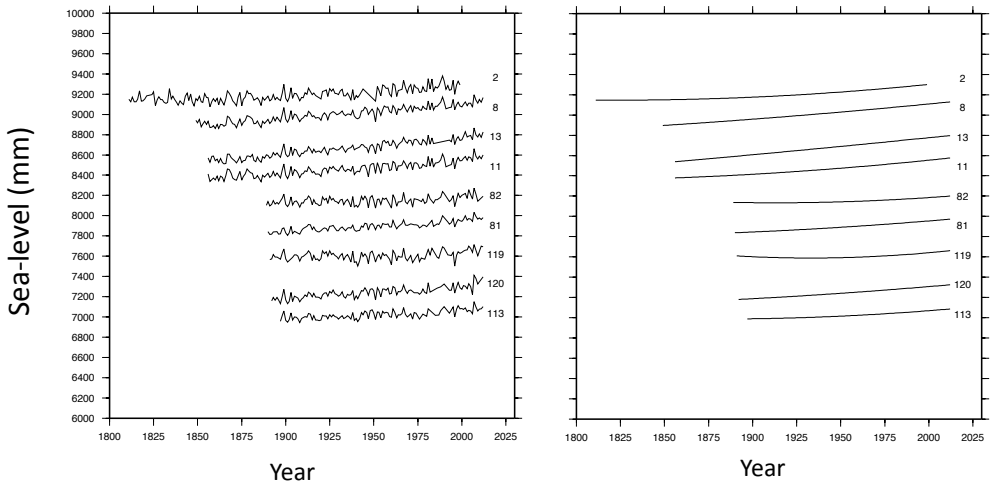

Figure 4.27: Baltic tide gauge observations. Annual sea–level observations (left) and their parabolic fit (right) at a selection of tide gauges facing the Baltic Sea. The numbers represent the PSMSL ID codes.

Regional pattern of sea–level acceleration

The regional patterns of the global sea–level acceleration (GSLA, Olivieri and Spada, 2013) (GSLA), shows accelerations in secular tide gauge time series from the Baltic Sea that tend to exceed, albeit slightly, those from records of comparable length and quality from elsewhere. Tide gauges from this region are generally not exploited in GSLA studies (Church and White, 2006; Woodworth et al., 2009) because these are believed to be too strongly influenced by local circulation Jevrejeva et al. (2008) and possibly by GIA. To confirm the existence of an anomalous acceleration, we have now compared the sea–level trends obtained from 60 validated Baltic Sea records (see Figs. 4.27 and 4.28a, BS) with those shown by the global set of tide gauge time–series previously employed by Douglas (Douglas, 1991, 1997) and obeying rigorous quality constraints in terms of record length and completeness. Contrary to the former, the latter are not from regions that were deeply covered by ice at the Last Glacial Maximum ($\sim 21,000$ years ago) where isostatic disequilibrium is still causing crustal uplift, and consequently a relative sea–level fall of several millimeters per year (Steffen and Wu, 2011). We have augmented the global set with ten records of comparable length, used in chapter 2 to minimize the contamination from Glacial Isostatic Adjustment (GIA) and the sensitivity to the model adopted to perform the GIA correction. The resulting global set consists of 32 records (Fig. 4.28b, GL); it includes sites largely insensitive to GIA and thus more suitable to constrain the long term sea–level changes driven by current climate variations.

Following DouglasDouglas (1992), sea–level accelerations in Fig. 4.28 have been computed as twice the quadratic term of a second–degree best–fitting olynomial. The distribution of the acceler-

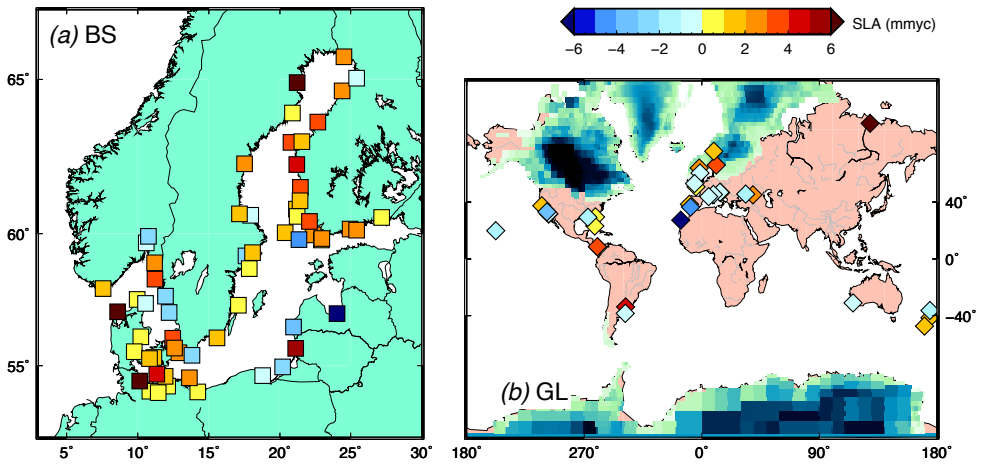

Figure 4.28: Location of tide gauge instruments. (a) Location of Baltic Sea (BS) tide gauges ($N = 60$, minimum record length: 100 years, average completeness: 92%). In (b) the global (GL) set is considered ($N = 32$, 56 years, 58%). Shades of blue in (b) depict the thickness of the ice sheets at the Last Glacial Maximum according to the GIA model ICE–5G(VM2) Peltier (2004). Colors of squares and diamonds denote the local sea–level acceleration (1 mmyc = 1 millimeter per year per century). All time series and tide gauge station information are extracted from the PSMSL database of annual RLR (revised local reference) recordsWoodworth and Player (2003).

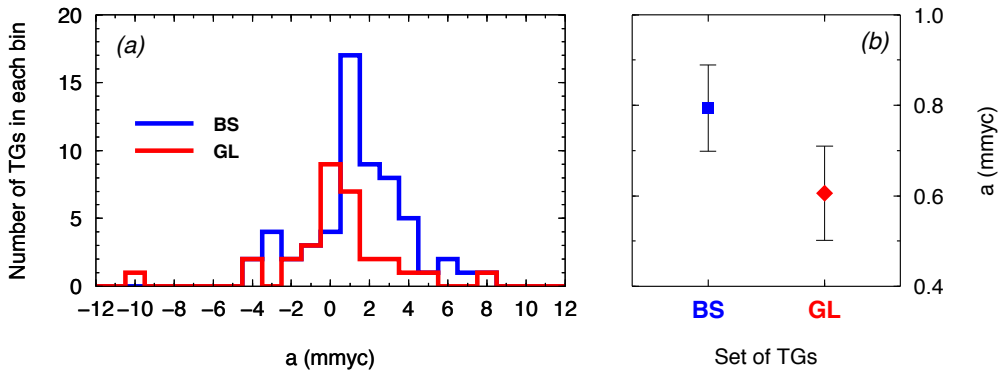

Figure 4.29: Distribution of observed sea–level accelerations. (a) Sea–level accelerations observed for the Baltic Sea (BS, blue) and the global (GS, red) sets of tide gauges. (b) Average sea–level accelerations for the two sets and their standard deviations. For BS and GL, the accelerations have average values of (0.8 ± 0.1) and (0.6 ± 0.1) mmyc, respectively. Their difference defines the anomalous sea–level acceleration $N_a = (0.2 \pm 0.2)$ mmyc.

ations obtained for sets BS and GL are shown by the histograms of Fig. 4.29a (here, we have found convenient to express accelerations in units of mmyc = 1 mm/yr/century). By a Student t–test with Welch correction(Welch, 1947) we have verified that the weighed averages of the two distributions, shown Fig. 4.29b, are significantly different at the 95% confidence level. This supports the hypothesis that the sea–level accelerations for the BS tide gauges are, on the average, larger than those belonging to the GL set. According to our computations, the anomaly (i.e. the difference in the average sea–level accelerations for the two sets), can be quantified as $N_a = (0.2 \pm 0.2)$ mmyc. The anomaly is small, but it is not negligible compared to GSLA estimates so far obtained in the literature, which are close to 1 mmyc (Olivieri and Spada, 2013).

Glacial isostatic sea–level acceleration

The positive sign for N_a can be explained, in a straightforward way, invoking the physics of post–glacial rebound (Turcotte and Schubert, 2002). In formerly glaciated regions like the Baltic Sea, relative sea–level has been gradually falling since the end of deglaciation $\sim 8{,}000$ years ago, as a direct consequence of the post–glacial uplift of the Earths crust (Steffen and Wu, 2011). According to the classical post–glacial rebound theory for a Newtonian viscous Earth (Turcotte and Schubert, 2002), after unloading, the free surface relaxes toward isostatic equilibrium following an exponential law. Hence the rate of relative sea–level fall was larger immediately after the end of ice melting and it is now progressively increasing toward less and less negative values. At the BS tide gauges in Fig. 4.28a, this today implies an excess positive sea–level acceleration compared to distant sites,

which are less (or not at all) influenced by the post–glacial rebound process; this explains why the observed anomaly N_a is positive.

By more quantitative arguments, it is possible to predict the order of magnitude of the anomalous acceleration. For a simplified half–space model the post–glacial displacement $u(t)$ of the Earth's free surface decays with time exponentially (Turcotte and Schubert, 2002). Hence the rate of vertical uplift $v(t)$ scales with $v(t) = -u(t)/\tau_r$ where t is time and τ_r is the Maxwell relaxation time of the Earth's mantle (Turcotte and Schubert, 2002). Since vertical uplift dominates the relative sea–level variations $s(t)$ in formerly glaciated regions (Steffen and Wu, 2011), neglecting gravitational effects (Peltier, 2004) we can write $s(t) = -u(t)$, which taking the second derivative gives $a(t) = v(t)/\tau_r$ where $a(t)$ is the local sea–level acceleration. We note that the rate of present day sea–level change and its acceleration are negatively correlated, namely $r(t) = -a(t)\tau_r$. The relaxation time τ_r is obtained analytically in terms of the bulk properties of the Earth and the spatial wavelength of the ice load (Turcotte and Schubert, 2002). Assuming a characteristic uplift rate $v \sim 10$ mm yr^{-1}, representative of the Baltic region (Steffen and Wu, 2011), for $\tau_r = 4,400$ years (Turcotte and Schubert, 2002) (suitable for the size of Fennoscandia) and a bulk mantle viscosity (Haskell, 1936) of 10^{21} Pa $\cdot$ s, we obtain $a \sim 0.2$ mmyc at present time, consistent with the amplitude of the observed anomaly N_a in Fig. 4.29b. Since $a(t)$ scales with $v(t)$, the anomalous acceleration is doomed to disappear as soon as the surface of the Earth will reach, in a few millennia, a full isostatic compensation ($v(t) = 0$).

To substantiate the order–of–magnitude estimates above, we have employed a realistic GIA model to compute and visualize the fingerprints (Milne and Mitrovica, 1998; Mitrovica et al., 2001) describing patterns of present–day sea–level rates and acceleration associated with GIA. We have implemented model ICE–5G(VM2) (Peltier, 2004) following the approach described in subsection 1.4.2, including the horizontal migration of shorelines and the impact of Earth rotation variations on sea–level change. The two fingerprints are shown in Fig. 4.30a and Fig. 4.30b, respectively; the second is obtained from the first by numerical differentiation. We have verified that their global shape would not change perturbing the viscosity profile of the mantle within reasonable bounds, nor adopting alternative GIA models, characterized by different assumptions about the Earth's viscosity profile and including a distinct time chronology for the melting of the late–Pleistocene ice sheets (Lambeck and Johnston, 1989; Lambeck et al., 1998).

The GIA fingerprint for the rate of sea–level change in Fig. 4.30a clearly reflects the direct effect of un–loading, which dominates across the previously glaciated regions causing an enhanced sea–level fall. Finer details of the map have been quantitatively explained in terms of "continental levering" (tilting of coastal regions due to ocean water loading) and "ocean syphoning" (migration of water from the far field of former ice sheets to fill the space left by the collapsing isostatic forebulges Mitrovica and Milne, 2002). However, the fingerprint of sea–level acceleration in Fig. 4.30b has been shown for the first time in Spada et al. (2014b), since previous studies have assumed that GIA has negligible effects on the GSLA (Douglas, 1992, 1997; Church and White, 2006; Jevrejeva et al., 2008; Woodworth et al., 2009; Olivieri and Spada, 2013) and its importance has been overlooked.

Similarly to the correction for the rate of sea–level rise (Fig. 4.30a), that for the accelera-

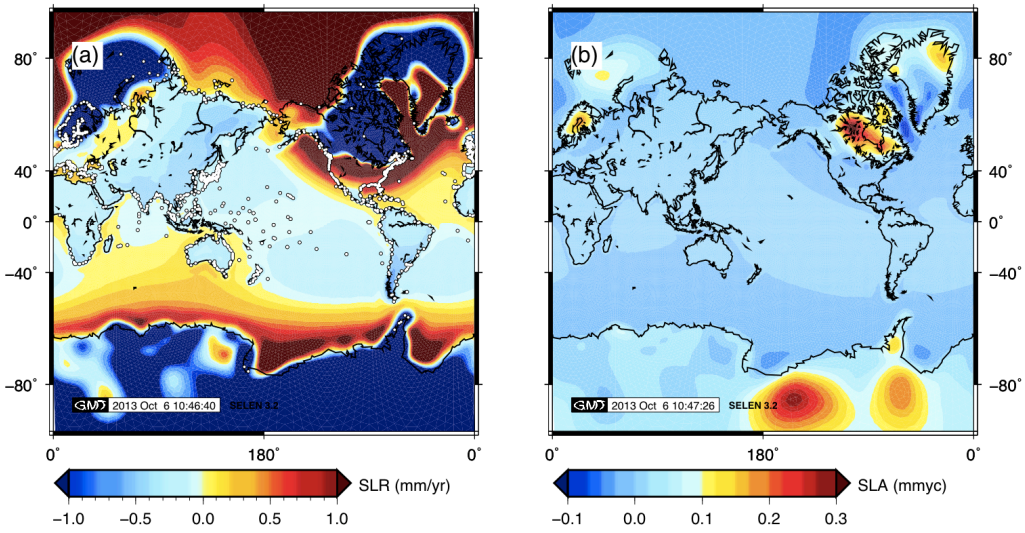

Figure 4.30: GIA fingerprints for the rate of sea–level rise (a) and its time–derivative (sea–level acceleration) (b), computed for model ICE–5G(VM2) (Peltier, 2004) and obtained by code SELEN (Spada and Stocchi, 2007; Spada et al., 2012). In (a) the dots show the PSMSL tide gauges, and the actual rates in polar regions far exceed the range of color table. Since relative sea–level is defined by the offset between the geoid height and the Earth's solid surface (Milne and Mitrovica, 1998), these fingerprints are also defined across the continents.

tion (Fig. 4.30b) has a vanishing average across the oceans, and the mean value at the locations of the global set of PSMSL tide gauges is effectively negligible ($< 10^{-2}$ mmyc), which justifies the assumptions in previous GSLA studies. However, the regional impact of GIA–induced sea–level acceleration is apparent, especially in areas which are still subject to significant isostatic disequilibrium like the Baltic Sea, the Hudsons Bay region, northern Greenland and West Antarctica. Across the Baltic Sea, the GIA acceleration amounts to ~ 0.1–0.2 mmyc, in agreement with the order of magnitude observed in this study and with the classical post–glacial rebound theory. The anomaly attains its largest amplitude (> 0.3 mmyc) in West Antarctica and in central Canada. Since century–long tide gauge observations from the Hudsons Bay region are not available, it is impossible to compare predictions for this region with instrumental data. The negative correlation between the two fingerprints in Figs. 4.30a and 4.30b is apparent and consistent with the extremely simplified post–glacial rebound theory discussed above. However, their ratio, which can be interpreted as the GIA "relaxation time", is not constant since the complex rheological layering of the GIA model employed here implies a multi–exponential relaxation (Peltier, 2004; Spada and Stocchi, 2007). Using directly the results from 4.30, for the Baltic Sea region we obtain $\tau_r \sim 5,000$ years, in agreement with the classical Haskell theoryHaskell (1936).

In response to GIA, tide gauge records located along the coasts of the Baltic Sea exhibit a small – but significant – long–term sea–level acceleration in excess to those in the far field of previously glaciated regions. The sign and the amplitude of the anomaly is consistent with the post–glacial rebound theory and with realistic numerical predictions of GIA models routinely employed to decontaminate the tide gauges observations from the GIA effectsPeltier (2004). Model computations predict the existence of anomalies of similar amplitude in other regions of the globe where GIA is still particularly vigorous at present, but no long–term instrumental observations are available to support their existence. We confirm that a GIA correction for secular sea–level acceleration is not required in GSLA assessments because its average value is vanishingly small at the locations of the PSMSL tide gauges (Douglas, 1992). Nevertheless, here we have shown that GIA is contributing significantly on a regional scale, and therefore it should be recognized as one of the processes responsible for local, long–term sea–level acceleration.

Chapter 5

Sea level projections

The prediction of future sea–level is one of the major challenges of climate science (Church et al., 2013). Although sea–level rise is generally considered a relatively slow process on human time scales (but see Cronin, 2012), it has a very significant long–term impact, influencing the dynamics of coastal erosion, groundwater salinization and change in natural ecosystems (Nicholls and Cazenave, 2010).

Recently, we are assisting to the development of process–based models, which require the understanding of numerous components acting on sea–level variations, as the warming of oceans, the present and past ice melting and the associated crustal deformation. The IPCC AR5 (Church et al., 2013), using results from 21 CMIP5 AOGCMs, for different Representative Concentration Pathways (RCP) scenarios, has assessed the likely process–based projections of global mean sea–level rise in 0.4 (RCP2.6) to 0.6 (RCP8.5) meters at 2081–2100 with respect to 1986–2005. Jevrejeva et al. (2012) have forced a physically plausible sea–level model constrained by observations, with the RCP radiative forcing scenarios (Moss et al., 2010); their projections up to 2500 show that sea–level will continue to rise (with a maximum rate of 10 mm yr^{-1} for the medium RCP6.0 scenario) even after stabilization of radiative forcing, mainly because of the long–term response time of sea–level.

Semi–empirical models, based on past observations, have been proposed as a complementary approach (Bittermann et al., 2013). Semi–empirical models do not require the understanding of all the processes acting on sea–level variations, because they do not attempt to explicitly attribute sea–level rise to its individual physical components. Instead, they consider any change in sea–level as an integrated response of the entire climate system, using simple physically motivated relationships (Church et al., 2013). Semi–empirical models need observed data over their period of calibration to provide projections (see, *e. g.*, Rahmstorf, 2007). Rahmstorf (2007) use AR4 temperature scenarios and observed sea–level data to demonstrate that the rate of sea–level rise is roughly proportional to the warming above the temperature of pre–industral era and obtaining a projection at 2100 between 0.5 to 1.4 m above the 1990 level. Grinsted et al. (2010) have calibrated theirs projections using past sea–level reconstruction (for the last 2000 years), tide gauge observations

(after $\sim$ 1900) and temperature data. They found that the likely rates of 21th century sea–level rise exceed by roughly factor of 3 the 2090–2099 scenarios proposed by the fourth Assessment Report (AR4) of the IPPC (Bindoff et al., 2007). Schaeffer et al. (2012) calibrated their semi–empirical model on sea–level data of the past millennium to project sea–level rise in a warming scenario between 2° C and 1.5° C above pre–industrial temperature. Their results point to a rise of 75–80 cm in 2100 with respect to year 2000.

In this chapter, the two approaches (model–based and semi-empirical) have been applied. This work is in progress in collaboration with the Science and Information Technologies of the University of Urbino (E. Lattanzi and D. Di Lucido). For the semi–empirical, the neural–network method has been applied on a global synthetic sea–level curve. For the model–based approach results of model for the different components of sea–level change, have been combined in the case of the Mediterranean Sea.

5.1 Semi-empirical sea–level projection by neural network

An Artificial Neural Network (ANN) is a synthetic computational model inspired by the biological notion of neural network. ANNs are composed of interconnecting artificial neurons (programming constructs that mimic the properties of biological neurons), able to calculate an output signal starting from an input signal.There are several kinds of ANNs which differ in their network architecture, in the neuron behavior, and in the way the network learns (*i. e.*, the way to change the interconnections weights and bias levels between neurons).

The most widely used ANN for time series forecasting is a single hidden layer feed forward network (Zhang et al., 1998). This network is characterized by three layers of simple processing units connected by links, schematized in Fig. 5.1. The relationship between the outputs and the inputs for a generic signal y is described by the following equation:

$$y_t = w_0 + \sum_{j=1}^{q} w_j \cdot g\left(w_{0,j} + \sum_{i=1}^{p} w_{i,j} \cdot y_{t-i}\right) + \varepsilon_t, \tag{5.1}$$

where g is a transfer function, $w_{i,j}$ are connection weights between input and hidden layer and w_j are connection weights between the hidden and the output layers. Finally p is the number of input nodes and q is the number of hidden nodes. Note that the output layer contains only one node whose output is y_t. The network represented by Equation 5.1 is a powerful computational model which is able to approximate the arbitrary function as the number of hidden nodes q is sufficiently large (Khashei and Bijari, 2010).

To construct an ANN, input series of sufficient length are needed. In this work, we use a sea–level reconstruction calculated from 1023 tide gauge records by Jevrejeva et al. (2006), using the virtual station method to solve the sampling problem of station locations. All records used in the reconstruction have been previously corrected for the GIA (Peltier, 2001) and low pass filtered to remove quasi–periodic oscillations shorter than 30 years. The record was extended backwards to 1850 using data from the three long tide gauge records of Amsterdam, Liverpool and Stockholm.

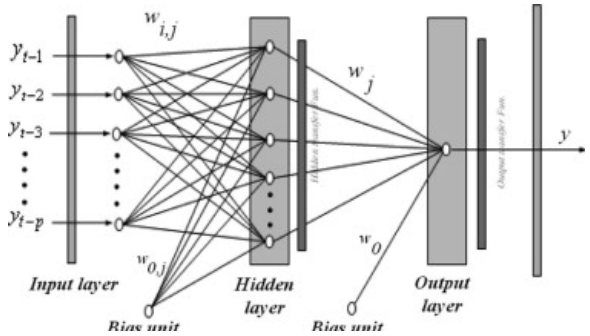

Figure 5.1: Single hidden layer feed forward network structure.

The resulting global sea–level curve (hereinafter "JEV reconstruction") starts in 1700 and ends in 2002; it is shown in Fig. 5.2.

5.1.1 The neural network method for sea–level projection

In the construction of the ANN architecture, the setting of q and p plays a fundamental role. The choice of the parameter q (number of hidden nodes) depends on input data. An high number of hidden nodes increases the ability of the network to recall the training set, entailing a decline in the generalization capability (*i. e.* the network does not perform well in out-of-sample prediction). To maintain the ability of the network to generalize it is necessary to set low values of q. The selection of the number of lagged observations p, plays a fundamental role in determining the nonlinear autocorrelation structure of the time series.

The optimal architecture of an ANN can be found following different approaches (see Khashei, 2005, for a discussion), but most of these methods are usually quite complex and are difficult to implement. Furthermore, none of these methods can guarantee the optimal solution for all real forecasting problems. To date, there is no simple clear-cut method for determination of these parameters and the usual procedure is to test numerous networks with varying numbers of input and hidden units (p and q), to estimate generalization error for each of these and to select the network with the lowest generalization error (Hosseini et al., 2006).

Here, to find the optimal ANN's architecture the method proposed by Gautama et al. (2003) has been adopted. This method calculates both the optimal embedded dimension (M) and the time lag (τ) of a time series by finding τ sub-series of M samples in the original time series so that they minimize its entropy level. The so determined M parameter is then used to choose p and q through an iterative process, in which each ANN generated uses a couple of p and q multiple of M. The generated ANN has then been tested by using the whole JEV reconstruction series; ten years of samples have been subtracted to the JEV reconstruction and used to calculate the prediction error according to the out-of-sample prediction schema (*i. e.* samples on the prediction window are totally unknown to the network). The ANN which generates a lower prediction error is saved as

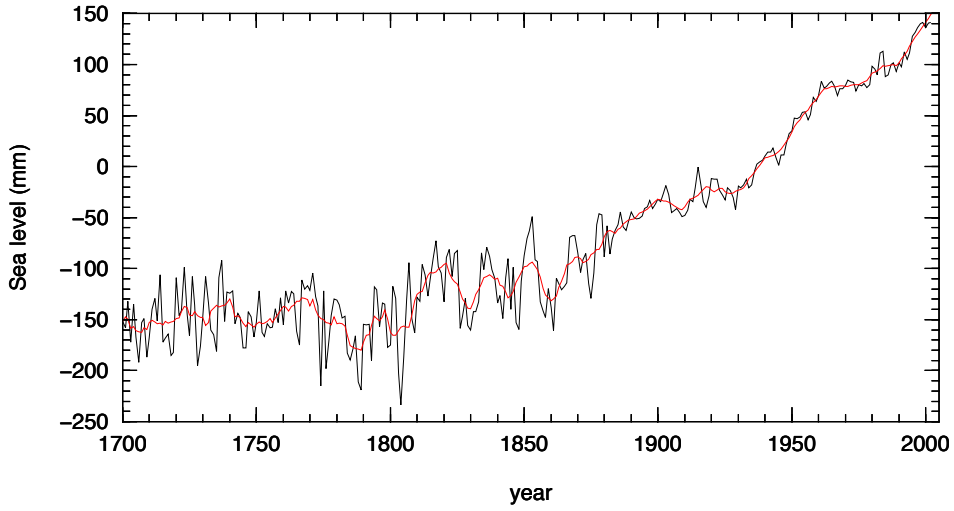

Figure 5.2: Synthetic global sea–level curve from Jevrejeva et al. (2006) ("JEV reconstruction") and its 10–years moving average (red curve).

the *best network*. The prediction error has been calculated according to the following formula:

$$E = \frac{1}{N}\sum_{i=1}^{N} \delta\xi_i, \tag{5.2}$$

where N is the number of error terms. By executing the Gautama algorithm on the *JEV reconstruction* we obtain a value of 6 as optimal embedded dimension (M) and a value $\tau = 50$ years. The *best network*, showing a prediction error of 0.22, has been obtained using $p = 120$ and $q = 24$, respectively. All tested networks are trained by means of the Gradient Descent Back Propagation Algorithm (GDAM, Rehman and Nawi, 2011) and are characterized by a simple Hyperbolic tangent sigmoid transfer function (Vogl et al., 1988).

The validation process has been carried out in three different training configurations, with prediction windows equal to 50, 100, and 180 years, to verify if with the reduction of the training window the out-of-sample prediction characteristics are maintained. As expected, tan increase in the prediction window corresponds to an increase in the measured error. The cause resides in two main reasons: i) the boundedness of the original numerical series increasing the prediction window reduces the training window; ii) the increase of the prediction window increases the error magnification in the predicted values.

Sea–level projection with artificial neural network method

The architecture of the ANN obtained so far has been used to project in the future (to year 2300) the JEV reconstruction. The reference sea–level value for the projection has been set to the av-

erage value for the period 1986–2005, in order to facilitate comparison with the Representative Concentration Pathway (RCP) scenarios presented in the AR5 (Church et al., 2013). From the observed sea–level data outwards, the variance around the mean tends to increase. Considering the projection from 2002 to 2300, the variance significantly exceeds those associated to the sea–level observations, with a standard deviation of $\sigma = 107$ mm, against the $\sigma = 49$ mm for the projection to year 2100. The whole JEV–reconstruction (from 1700 to 2002) has $\sigma = 91$ mm, but neglecting data before year 1850 (when only few tide gauges were operating) it reduces to $\sigma = 76$ mm. For this reason here we presents only values obtained up to year 2100. Results are presented in Fig. 5.3a where the black curve represents the observed annual values of JEV reconstruction while in blue are drawn the projected annual values (hereinafter JEV-projection).

The projected sea–level for 2081–2100 in respect to 1986–2005 is ~ 195 mm. This is significantly lower than values obtained in the IPCC AR5 (see Fig. 5.3b). The AR5 projection for RCP 2.6 in the same time interval is ~ 400 mm, with a low limit of ~ 260 mm. All the other RCP scenarios present values significantly higher than our estimate (~ 470 mm and ~ 480 mm for RCPs 4.5 and 6.0 respectively, and ~ 630 mm for RCP 8.5 with an upper bound of ~ 820 mm).

Fig. 5.3c shows a comparison between the JEV-projection and the results obtained by Rahmstorf (2007). As previously introduced, Rahmstorf has applied a semi–empirical approach that uses the connection between global sea–level rise and global mean surface temperature to obtain sea–level projections, based on IPCC Third Assessment Report (Houghton et al., 2001) scenarios. The sea–level projections so obtained give values at 2100 (relative to 1990) ranging from ~ 500 to ~ 1400 mm, with a lowest plausible limit of ~ 380 mm, obtained assuming that the value of temperature stops increasing in a few years. The sea–level at 2100 relative to 1990 obtained with the JEV-projection is ~ 253 mm.

The reason of the low values of projected sea–level obtained with the ANN approach resides mainly in the method itself. The observed sea–level data in input have been used without introducing any constraint: no physical processes related to sea–level change (as change in temperature, oceanic forcing or ice melting) have been considered to validate the ANN. The lack of these further constrains, is possibly causing a bias in the projection obtained. The JEV-reconstruction used here, is based, in its first part (around year 1850), only on a few tide gauges. The high uncertainty until ~ 1850, appears as shows an almost stable behavior (high oscillation around a stable value). After the mid of 19th century we assist to a general increase of sea–level, with an alternation of neatly positive with negligible or even negative rates. This is evident in the multi–scale dynamical analysis (MSDA, see Scafetta, 2013), shown in Fig. 5.4. The trend of the whole JEV-reconstruction (computed with a standard linear regression) is 1.65 mm yr^{-1}, but this increases up to 2.4 mm yr^{-1} if we consider only the period after 1985. This is true also considering subsets of the curve after ~ 1985, which show in general a sea–level rate in excess of 2 mm yr^{-1} (for time windows of few decades, see Fig. 5.4a). In the same period, the acceleration mainly shows positive values, even near to ~ 0.1 mm yr^{-2} (see Fig. 5.4b). The JEV-projection (from 2003 to 2100) shows a rate of 1.61 mm yr^{-1}, in accordance with that of the whole JEV-reconstruction, but that does not account for the increasing rate of the last period (1985–2002); this latter period is probably too short compared with the whole JEV-reconstruction series and the ANN "forgets" the increasing rate, bearing

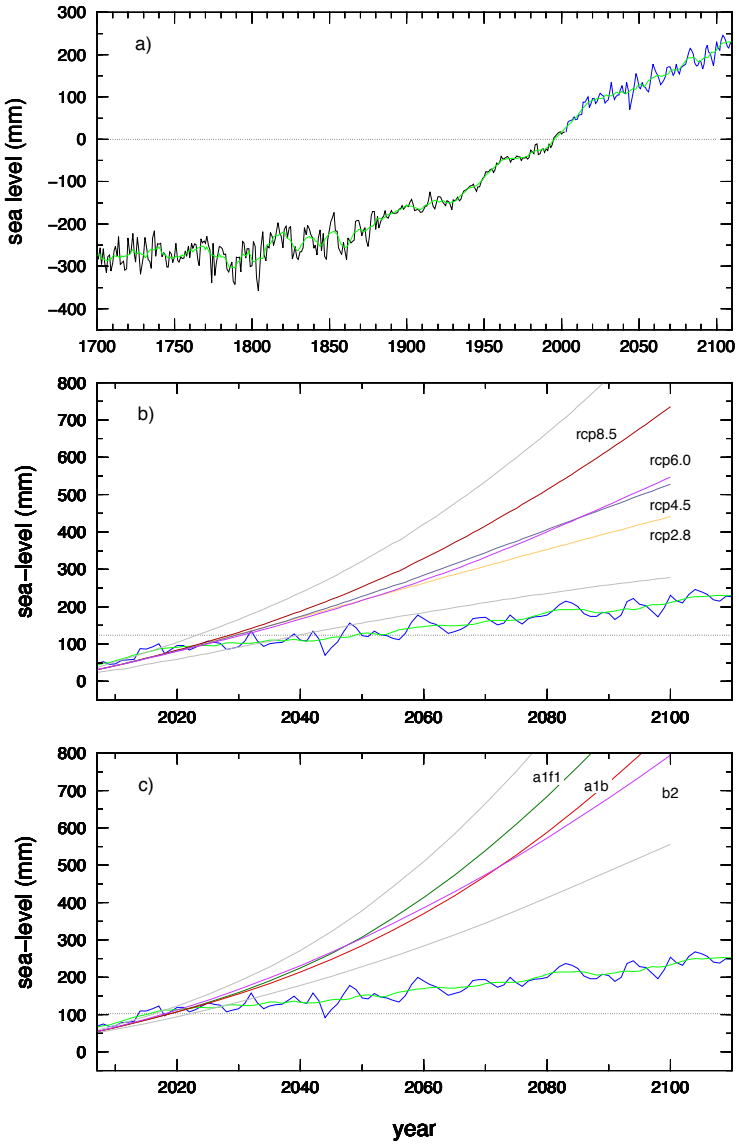

Figure 5.3: JEV reconstruction (black), its 10–year moving average (green) and its projections (blue) with neural network methods (frame a) and comparison with sea–level scenarios according to IPCC AR5 (b) and to Rahmstorf (2007) (c). Gray lines in (b) and (c) shows the low and the upper limit of the projections (in b) which correspond to the upper limit of RCP 8.5 and to the lower limit of the RCP 2.6. To facilitate comparison with the AR5 results, in (a) and (b) the projection is referred to the average sea–level values in the period 1986–2005; in (c), similarly to Rahmstorf (2007), the projection is referred to the 1990 value.

in mind the more statical behavior of the previous part of the series.

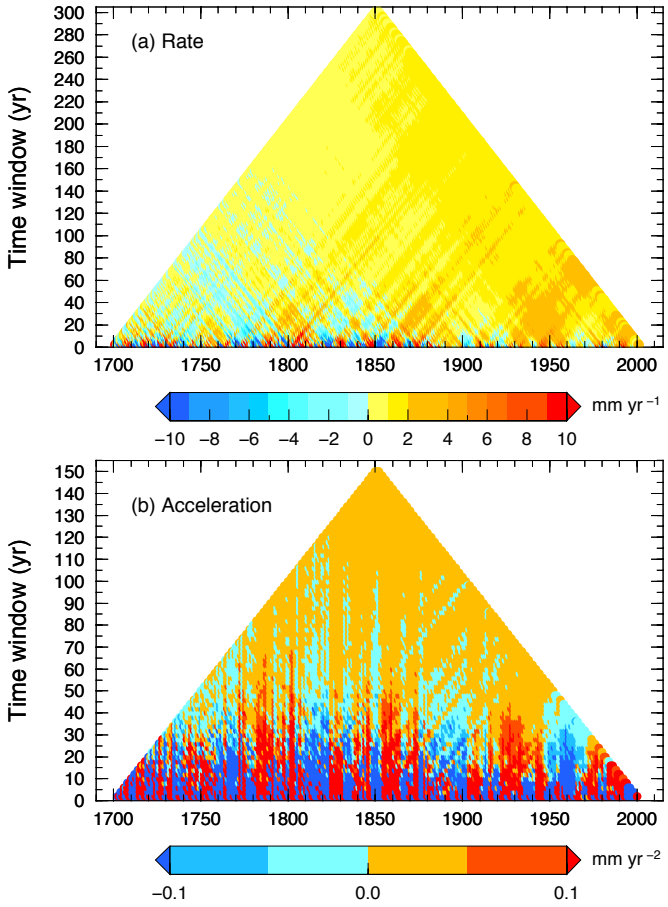

Figure 5.4: Multi–scale dynamical analysis (MSDA) for the rate of sea–level change in (a) and acceleration (b) obtained by differencing the JEV reconstruction.

A remarkable property of the ANN is to reproduce not only the trend, but the overall behavior of the input series. In our experiment, this is confirmed by the EEMD analysis applied to detect possible oscillations (for details on the method adopted, see section 4.1 in chapter 4). Using here annual data as input for the EEMD, only few IMFs are extracted. The results for this analysis are shown in Table 5.1. The IMF2 shows a periodicity of $\sim$ 10 years for the JEV-reconstruction (more evident for the series truncated before 1850) and for both the projections. The $\sim$ 20 years periodicity is apparent for the JEV-projection up to 2300 and for the truncated JEV-reconstruction, but it is not evident in the other two cases. Longer cyclicalities have not been found for the JEV-projection.

Table 5.1: EEMD analysis for JEV-reconstruction and JEV-projection: period (in years) for each IMFs.

	JEV-reconstruction		JEV-projection	
	1700–2002	1850–2002	2003–2100	2003–2300
IMF2	8.6	11.8	11.0	10.8
IMF3	14.5	22.0	16.5	20.3
IMF4	38.0	77.0	–	–
IMF5	76.0	–	–	–

5.2 Model–based projection: the case of the Mediterranean Sea

The model–based AR5 projections presented above represent globally averaged sea–level variations which cannot be immediately translated into regional scenarios. Indeed, all the processes responsible for future sea–level rise are characterized by a strong regional signature, which makes local projections particularly challenging (Meehl et al., 2007). These, however, are of fundamental importance for the possible impact of sea–level rise on society and to improve management and planning of coastal defense. Several contributions to sea–level rise which have small or negligible globally averaged effects, can indeed have a significant amplitude on regional scale. This occurs, for example, for the sea–level changes expected from salinity variations (Antonov et al., 2002) or for those associated with GIA (Farrell and Clark, 1976). The pattern of the sea–level change expected from future mass loss from GIC and continental ice sheets shows significant variations even at the 100–km spatial scale (Spada et al., 2013). These will add up to the spatially heterogeneous contribution expected from the ocean response to global warming that includes thermo–steric, halo–steric and dynamic effects (Spada et al., 2013). The material of this chapter follows the reasoning of Galassi and Spada (2014). who have considered model–based projections for the particularly interesting case of the Mediterranean Sea.

In view of the high and increasing population density (Cori, 1999) and of the numerous coastal areas potentially vulnerable to flooding, erosion and loss of wetlands (Nicholls et al., 1999), in the Mediterranean region the problem of future sea–level rise is particularly felt. In key zones, like the Moroccan coast (Snoussi et al., 2008) and the Venetian Lagoon (Carbognin et al., 2010), future sea–level rise will exacerbate existing human pressure, will impact the development of tourism (Cori, 1999) and will influence the migration fluxes (Black et al., 2011). Because of $\sim 46,000$ km of populated coasts belonging to 22 countries, the socioeconomical and political implications of a growing risk of inundation demand, for the Mediterranean countries, serious consideration of long term sea–level variability into costal planning (Nicholls and Hoozemans, 1996). Low–elevation coastal zones (LECZ, see Fig. 5.5) have a considerable extension in the Mediterranean basin and are highly vulnerable to environmental events, like floods, which can directly or indirectly affect the coastal community. Some Mediterranean densely populated areas are LECZ. For example $\sim 30\%$ of the Egyptian population (about 27 million people) lives in the LECZ of the Nile delta (Black

et al., 2011) and highly populated cities, as Tunis ($\sim$ 2.2 million inhabitants) are in LECZ.

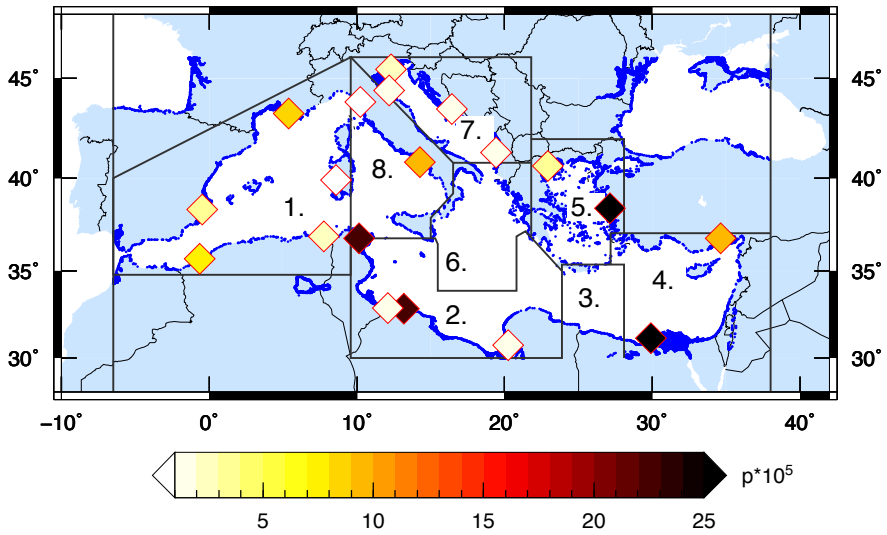

Figure 5.5: LECZs (defined as lands with an elevation $<$ 10 m relative to present sea–level, see McGranahan et al., 2007, and *http://sedac.ciesin.columbia.edu/data/collection/lecz*) along the coasts of the Mediterranean Sea (blue, obtained from model ETOPO2, see *http://www.ngdc.noaa.gov/mgg/fliers/06mgg01.html*), with principal cities in LECZ marked by diamonds (the population is color–coded in units of 10^5 inhabitants). Also shown are the political boundaries and the Mediterranean Sea sub–basins outlined by Carillo et al. (2012). This same partitioning is adopted in the body of the paper to facilitate an inter–comparison of the various components of sea–level change. The Western Mediterranean (1.) is the largest sub–basin, adjacent to the Tyrrhenian Sea (8.). This latter is connected with the Southern Central Mediterranean (2.) through the Channel of Sicily. The Adriatic Sea (7.) extends northwards between Italy and the Balkans and communicates with the Ionian Sea (6.) through the Strait of Otranto. The Aegean Sea (5.) extends between Greece and Turkey, and is connected to the South Creete (3.) and the Levantine Seas (4.) through several straits in the Grecian Island Arc.

Previous investigations on the future sea–level rise across the Mediterranean Sea (Tsimplis et al., 2008; Marcos and Tsimplis, 2008; Carillo et al., 2012; Jordà and Gomis, 2013) have mainly focused on the modeling of the steric component of sea–level change, which describes the effects of water density variations. While at global scale the thermo–steric effects dominate the steric sea–level variations (Antonov et al., 2002), at a regional scale and in particular in the Mediterranean Sea halo–steric and thermo–steric effects can be comparable (see *e. g.* Tsimplis and Rixen, 2002). It has been recently pointed out, however, that neglecting the contribution of the salinity increase to the mass component could lead to a severe underestimation of total sea–level rise, especially

within semi–enclosed basins as the Mediterranean Sea (Jordà and Gomis, 2013).

A common feature to all previous approaches to the problem of future sea–level rise in the Mediterranean Sea has been the adoption of simplified models for the mass component (coming from melting glaciers, ice caps, and ice sheets, see subsection 1.3.2), and of terrestrial mass exchange, including dams impoundment and groundwater variations (see subsection 1.3.4). Tsimplis et al. (2008), who have first tackled the problem of future sea–level changes in the Mediterranean Sea, have used the IPCC AR4 projections for the mass term (Meehl et al., 2007) and modulated it according to the amplitude of the GIA "sea–level fingerprint" (Mitrovica et al., 2001) predicted for the Mediterranean region as a whole, thus neglecting possible spatial variabilities at a sub–basin scale. An even more simplified approach has been adopted by Marcos and Tsimplis (2008), who only accounted for a globally–averaged mass term according to the IPCC AR4 SRES A1B and A2 scenarios (Meehl et al., 2007). In Carillo et al. (2012), no attempts have been made to combine estimates for the mass–induced term to their projections of steric variations to 2050. Furthermore, none of the above studies have considered nor realistically modeled the effects on future sea–level change expected from GIA, in spite of its recognized importance in the Mediterranean basin at decadal and secular time scales (Stocchi and Spada, 2009). A notable exception is the study of Lambeck et al. (2011), who projected future sea–level combining GIA effects (including glacio– and hydro–isostatic components) to the IPCC AR4 and Rahmstorf (2007) scenarios to 2100, also estimating the future relative sea–level variations of tectonic origin. The study of Lambeck et al. (2011), however, is limited to the Italian coasts.

The aim of this work is to estimate the future sea–level variations in the Mediterranean Sea to 2040–2050 relative to 1990–2000, combining the patterns of TIM, GIA, and steric components of sea–level change following the approach first outlined on a global scale by Slangen et al. (2012) and later adopted by Spada et al. (2013). Recalling Equation 1.1, we will find the total future sea–level change in Mediterranean Sea as

$$S^{TOT}_{MED} = S^{GIA}_{MED} + S^{MAS}_{MED} + S^{OR}_{MED} + S^{OTH}_{MED}, \tag{5.3}$$

where the term S^{OR} accounts for ocean circulation in addition to steric components and substitutes the S^{STE} of Equation 1.1. The general features of each term have been described in chapter 1. The chosen time frame is dictated by the specific projections employed for the steric component of sea–level rise. Up to now, for the Mediterranean Sea these components have only been considered separately, and often their spatial variations have been neglected across this relatively small, semi–enclosed basin. Although Tsimplis et al. (2008) have recognized the importance of the mass addition into the oceans due to the future melting of the GIC, up to now a realistically modeled TIM component has not been included in the future sea–level budget of the Mediterranean Sea. Similarly, as far as we know, the future effect of GIA has never been evaluated before at the Mediterranean scale using different models. Recent projections for the twenty–first century by Slangen et al. (2014) have emphasized the regional patterns of all the sea–level components, but have not provided clues on the Mediterranean Sea.

Since predictive models for tectonic deformations are still unavailable, possible effects from tectonics and coastal processes on future sea–level rise are non accounted for in this study. A

similar approach has been followed by Church et al. (2013). When estimates of local past long–term tectonic uplift are available from independent sources (see Lambeck and Purcell, 2005 for the whole Mediterranean Sea Lambeck et al., 2004a and Antonioli et al., 2009 for the Italian and Istrian coastlines), these can be combined to our results by linear extrapolation. The same also holds for the possible local effects of sediments compaction. Zerbini et al. (1996) have shown that in the Mediterranean Sea, vertical crustal movements are small compared to the decadal or multidecadal sea–level variability. It should be noted, however, that in some cases the tectonic movements are not directly assessed from field evidence, but defined to include all movements that are not eustatic nor isostatic (Antonioli et al., 2009). As such, they will depend on the isostatic model employed to estimate the S^{GIA} term in Equation 5.3. Previous work has shown that co–seismic and post–seismic deformations from the global seismic activity had, during last decades, only a modest role on local sea–level change at tide gauges (Melini et al., 2004). These are not taken into account here, but making specific assumptions on the future rates of seismic activity within the Mediterranean basin and the surroundings, they can be estimated by forward modeling (see *e. g.* Piersanti et al., 1995) and combined to our projections.

The S^{MAS} term in Equation 5.3 can be expressed as the sum of contributions from the AIS, the GIS, and GIC (see Equation 1.4 in chapter 1) Below, estimates for the terms in Equation 5.3 and Equation 1.4 and their spatial variability will be separately obtained from previous literature and from modeling, and combined together. The term S^{OTH} in Equation 5.3, is included only in respect to the contribution from terrestrial mass exchange (S^{TME}, see subsection 1.3.4). As discussed above, tectonic effects will not be considered.

5.2.1 Components of future sea–level in the Mediterranean Sea

Terrestrial Ice Melting (TIM)

The TIM components of future sea–level rise (S^{MAS} in Equation 5.3) have been obtained following the approach outlined in subsection 1.4.3 and the global fingerprints to 2040–2050 relative to 1990–2000 for MR and HE scenarios are shown in Figs. 1.10 and 1.11, respectively.

The TIM sea–level fingerprints across the Mediterranean Sea are shown in Fig. 5.6. Since the basin is located in the intermediate far–field of the TIM sources employed here, these sea–level variations exhibit sub–eustatic values (*i. e.* they do not exceed the ocean–averaged values) and due to the long–wavelength global patterns (see Figs. 1.10 and 1.11 in subsection 1.4.3), they show only a very modest variations across the basin. To 2040–2050, the TIM component of relative sea–level change across the Mediterranean Sea amounts to ~ 8 cm and ~ 18 cm for the MR (a) and the HE (b) scenarios, respectively. We have verified that the slight deviations from a uniform response in the northern Tyrrhenian and in the Adriatic Seas are the effect of the melting of the nearby Alpine glaciers and of the distant GIS.

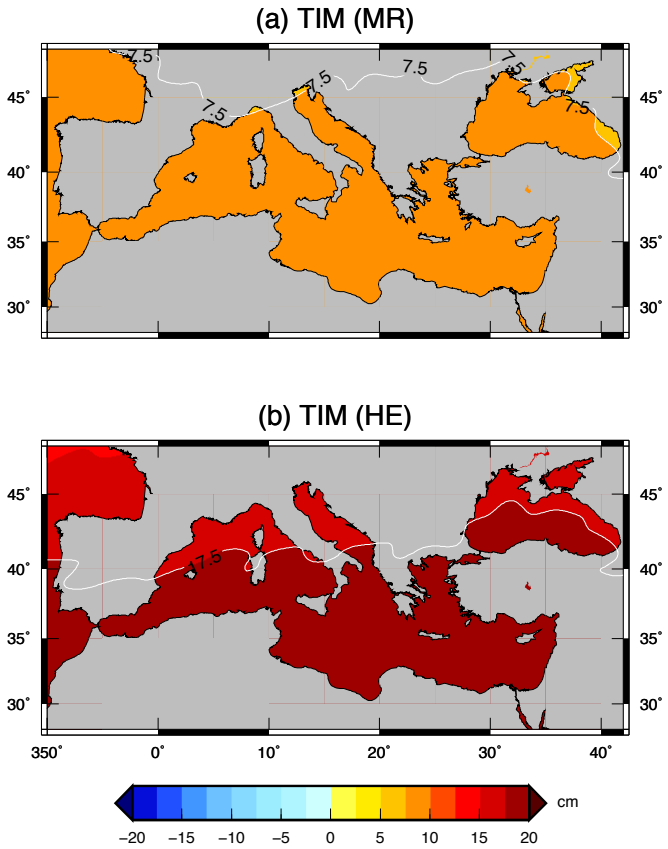

Figure 5.6: Relative sea–level variation expected to 2040–2050 relative to 1990–2000 in the Mediterranean Sea, according to the TIM MR (a) and HE (b) scenarios, respectively.

Terrestrial Mass Exchange

The contribution to sea–level variation from terrestrial mass exchange (the term S^{TME} defined in subsection 1.3.4), is due to change in water stored on continents as snow, lakes, permafrost, groundwater or dams. The processes contributing to S^{TME} are related with climate changes (melting of permafrost or snow, increase in lake evaporation) and human activities (mainly building of dams and groundwater extraction). Climate–related changes in water and snow storage on land show inter–annual to decade fluctuations (Nerem et al., 2010), and have not displayed significant trends during recent decades (Church et al., 2013).

The future projection of IPCC AR5 (Church et al., 2013) assesses a contribution from land water storage of 4 cm (median value) of sea–level to 2081–2100 relative to 1986–2005, regardless of the RCP scenario adopted. Inspection of the S^{TME} AR5 fields available from the Integrated Climate Data Center (ICDC, see *http://icdc.zmaw.de/*) shows that, for the Mediterranean Sea, a significant sub–basin variability is predicted. Nevertheless, to year 2050, the projected s^{TME} slightly exceeds the 1 cm level only in the northwestern Mediterranean, a small value compared to S^{TIM} and to the basin–averaged s^{GIA} contribution. Especially in view of the large uncertainties in the S^{OR} component, discussed below, the S^{TME} term will be therefore neglected.

Global Isostatic Adjustment (GIA)

The S^{GIA} term is estimated by two distinct and independently developed GIA models: ICE–5G (VM2) (Peltier, 2004) and KL05 (Lambeck et al., 1998), described in subsection 1.4.2. In the IPCC AR5 report (Church et al., 2013), the uncertainty in the GIA component of future sea–level rise has been estimated using slightly different implementations of these same GIA models (see, in particular, the Supplementary Material of Chapter 13 of the report). The two models predict, for the Mediterranean region, distinctly different rates of present–day vertical uplift (Serpelloni et al., 2013) and relative sea–level change (Stocchi and Spada, 2009).

The future sea–level variations expected to 2040–2050 relative to 1990–2000 from GIA have been obtained by a straightforward time–integration of the rate of present–day sea–level change predicted by the two GIA models, which is approximately constant during the relatively short time period considered here. Differences in the ESL curve and ice distributions between the two models employed (see section 2.3 for a in–depth discussion), imply that the sea–level predictions obtained show ignificant differences on a regional scale, including the Mediterranean Sea.

In Fig. 5.7, the modeled future pattern of relative sea–level change associated with GIA is shown in detail across the Mediterranean Sea and the Black Sea, for models ICE–5G (VM2) (a) and KL05 (b). Both predict a maximum sea–level rise in the bulk of the basins, with the largest values expected in the Tyrrhenian and in the Ionian Seas between Sicily and Greece. Maximum values range between ~ 2 and ~ 4 cm for ICE–5G (VM2) and KL05, respectively. Localized regions of sea–level fall are predicted in the Alboran Sea, along the coast of Southest Tunisia, across the Gulf of Sirte, and in the Levant. As pointed by Stocchi and Spada (2009), the pattern of sea–level change shown is Fig. 5.7 is explained by the loading effect of melt water since the LGM,

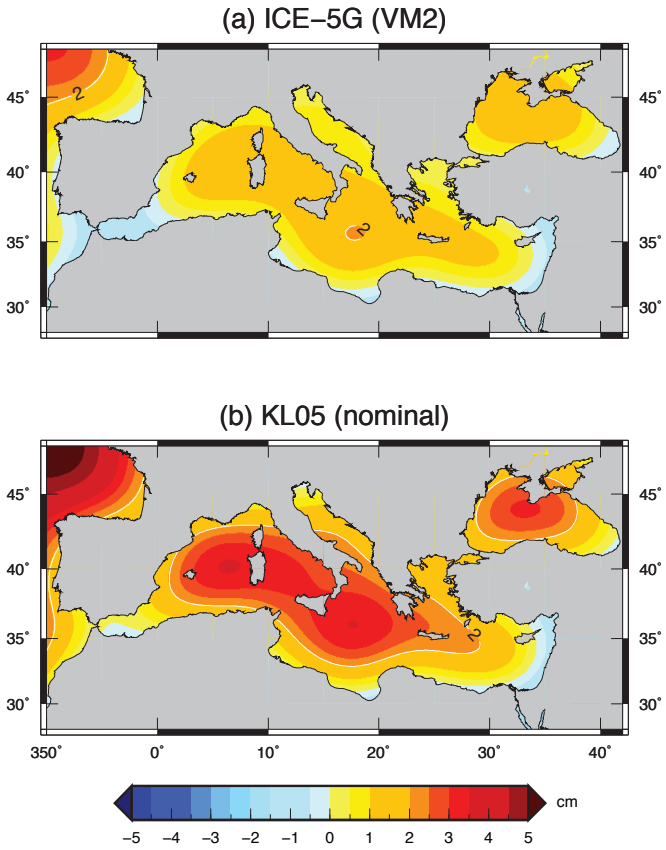

Figure 5.7: GIA sea–level fingerprints to 2040–2050 relative to 1990–2000 in the Mediterranean Sea, obtained using model ICE–5G (VM2) (a) and model KL05 (b).

causing a general subsidence accompanied by a collapse of the geoid at a lower rate, hence a relative sea–level rise. This flexural response is maximized at the centre of the basin, while along the coasts it is hampered by the effects of continental levering (Mitrovica and Milne, 2002), causing a relative sea–level fall in some places. Model KL05 Fig. 5.7b) predicts the largest sea–level variations since it assumes a relatively large lower mantle viscosity compared to ICE–5G (VM2), this implying a largest isostatic disequilibrium at present time, hence enhanced rates of adjustment.

Ocean Response (OR)

The Mediterranean Sea is a mid–latitude, semi–enclosed, deep sea that exchanges water, salt and heat with the North Atlantic Ocean only through the Strait of Gibraltar. The circulation is forced by water exchange, wind stress, buoyancy flux at the surface due to freshwater, and heat fluxes (Robinson et al., 2001). Due to this peculiar dynamic regime, sea–level variations within the

Mediterranean Sea have not always reflected the global ones nor those in the Atlantic Ocean (Tsimplis and Baker, 2000). Using runs from a suite of atmosphere–ocean general circulation models (AOGCMs), Marcos and Tsimplis (2008) have projected changes of steric sea–level in the range of -22 to 31 cm for 2100 within the Mediterranean Sea. The range includes values obtained for a committed climate change scenario (where concentrations of greenhouse gases are kept fixed at year 2000 levels), and the SRES A1B and SRES A2 scenarios, but do not include any mass addition contributions. In their study, Marcos and Tsimplis (2008) have found that AOGCMs sometimes provide a large spread of results. Furthermore, they display a non–coherent behavior and provide inconsistent projections with each other that prevents the definition of the spatial pattern of projected sea–level across the Mediterranean Sea.

For the reasons above, AOGCMs are generally not considered fully adequate to describe the complex dynamic conditions of the Mediterranean Sea (Mark Carson, 2014, personal communication). This has stimulated, in the past few years, the development of regional, high–resolution coupled models that have been used to project the steric and atmospheric pressure contributions to sea–level change to the 21^{th} century (Tsimplis et al., 2008; Carillo et al., 2012). Here, the steric component of future sea–level rise (including thermo–steric and halo–steric contributions) is directly taken from the regional model of Carillo et al. (2012). They have performed two 50–year regional experiments under the SRES A1B scenario (referred to as EA1B and EA1B2, respectively), using coupled ocean–atmosphere regional circulation MITgcm–RegCM3 models (Pal et al., 2007) with boundary conditions from model ECHAM5–MPIOM (Roeckner et al., 2003). Since the simulations by Carillo et al. (2012) extend to year 2050, the same limit is adopted here. In the simulations of Carillo et al. (2012), the horizontal spatial resolution for the ocean component (MITgcm) is $^1/_8\,^\circ \times\, ^1/_8\,^\circ$, while for the atmospheric model a uniform horizontal grid spacing of 30×30 km is used (the vertical resolution of the models is detailed in the work of Carillo et al., 2012). The two experiments only differ in the boundary conditions for the oceanic component in terms of salinity between the Atlantic Ocean and the Mediterranean Sea through the Strait of Gibraltar. Henceforth, the outcomes of these experiments represent the ocean component (OR) of future sea–level variations in the Mediterranean Sea. It has been recently pointed out, however, that the use of the steric component in the Mediterranean Sea is not a good approximation to sea–level change (Jordà and Gomis, 2013). It would be the case only if a geostrophic adjustment is established, which often happens in the open ocean but not in the Mediterranean Sea, due to the presence of topographic barriers. For instance, a salinization of the basin would imply a large decrease of the steric component while in reality sea–level would not decrease (see Jordà and Gomis 2013 for more details). In this perspective, our results below should be considered as preliminary since they could underestimate the actual sea–level projections across the Mediterranean Sea in a significant way.

Fig. 5.8 shows the OR component of sea–level variations in the Mediterranean Sea expected during the decade 2040–2050 relative to 1990–2000. The maps have been constructed digitizing the time series in Figure 11 of Carillo et al. (2012); the uncertainty on the sea–level values averaged over these two decades is of the order of 1 cm. The future sea–level OR fingerprints are spatially–averaged across each of the eight sub–basin listed in Table 5.2, whose boundaries are displayed in Fig. 5.5. Since the boundary conditions of simulations EA1B and EA1B2 of Carillo et al. (2012)

differ essentially in the upper layers of the Atlantic Sea (about 1°C in temperature and 0.5 psu in salinity) the spatial variations of projected sea–level change in the two simulations are driven by the sea–water inflow through the Strait of Gibraltar. The values of future steric sea–level averaged over the entire basins are about 0.4 and 5.3 cm in the two scenarios, respectively. The fresher and warmer climatology that characterizes the EA1B2 scenario produces a strong impact on future sea–level change, with a maximum contribution in the Ionian Sea of 8.8 cm (against 2.3 cm obtained with EA1B). Large differences can be found also in the eastern Mediterranean Sea, in the South Creete sub–basin where the OR contribution to future sea–level change is -3.6 and 3.4 cm in the EA1B and EA1B2 simulations, respectively, and in the Levantine sub–basin, with 0.6 and 6.0 cm.

Establishing a quantitative range of uncertainty for the OR component of future sea–level change in the Mediterranean Sea is not straightforward. The reasons are the rather limited set of model runs performed in previous studies, the large number of variables involved and the numerous emissions scenarios existing. In addition, it has been recently suggested that steric and mass components have been possibly misinterpreted in previous works, leading to erroneous and contradictory conclusions on regional sea–level variability within the Mediterranean Sea (Jordà and Gomis, 2013). Previous works have adopted coupled models and boundary conditions that differ from those of Carillo et al. (2012). For example, Tsimplis et al. (2008), using an Atmosphere–Ocean Regional Climate Model coupled over the Mediterranean Sea, have obtained a maximum steric sea–level rise of 23 cm between periods 2070–2099 and 1961–1990, with a mean steric sea–level rise of 13 cm, with lower values in the eastern Mediterranean Sea and higher values at the western Mediterranean Sea. These results, obtained adopting only one model under the high level anthropogenic gas emission SRES A2 scenario, cannot be directly compared with the outcomes of the regional simulations by Carillo et al. (2012), who have adopted the more optimistic A1B scenario, and a different time frames for their projections. Also in view of the methodological points raised by Jordà and Gomis (2013), the large spread of the projections so far obtained demonstrates that a consensus on the amount of future sea–level rise (and on its uncertainty) is still far from being reached.

5.2.2 Total sea–level change in Mediterranean Sea to 2050

To estimate the total amount of relative sea–level variation expected to 2050 across the Mediterranean Sea, the TIM and GIA components previously obtained, have been superimposed to the OR component above. Among the eight combinations of TIM+GIA+OR simulations so obtained, we consider the low–end MR+ICE5G+EA1B and the high–end HE+KL05+EA1B2 combinations, which will be referred to as MIN50 and MAX50 scenarios in the following, respectively. In the following two subsections, the total projected sea–level change will be considered at sub–basin scale, at tide gauges and at LECZ, respectively.

Sea–level change at Mediterranean sub–basins

The numerical values obtained in each of the sub–basins are summarized in Table 5.2. The bins in Fig. 5.9 display the results for the total TIM (blue), GIA (green), OR (red) and the total sea–

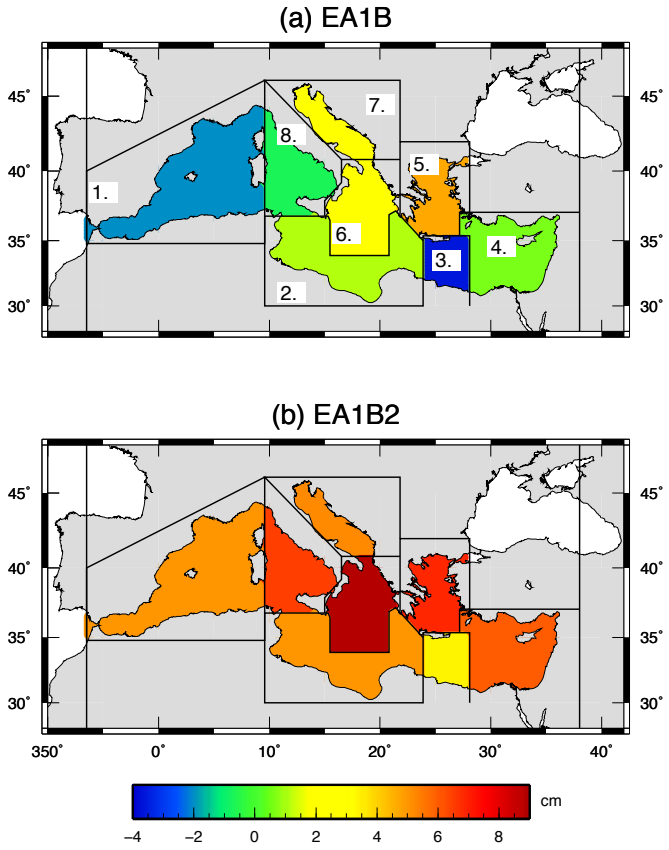

Figure 5.8: OR component for sea–level to 2040–2050 (relative to 1990–2000) for the EA1B (a) and EA1B2 (b) scenarios according to predictions by Carillo et al. (2012). The eight Mediterranean Sea sub–basins (1.–8.) shown in (a) are defined in Fig. 5.5.

Table 5.2: Sea–level projections to 2040–2050 across the Mediterranean sub–basins, decomposed in TIM, GIA and OR components. The total sea–level rise for scenarios MIN50 and MAX50 are shown in the last columns.

Mediterranean	TIM AIS (cm)		TIM GIS (cm)		TIM GIC (cm)		GIA (cm)		OR (cm)		Total (cm)	
sub–basin	MR	HE	MR	HE	MR	HE	ICE–5G	KL05	EA1B	EA1B2	MIN50	MAX50
1. W Med	3.4	8.2	0.5	1.8	4.6	7.9	0.7	2.1	−2.0	3.4	7.2	23.4
2. SC Med	3.2	7.8	0.8	3.2	4.8	8.1	0.8	1.7	1.1	5.0	10.7	25.8
3. S Creete	3.1	7.6	0.8	3.6	4.7	7.9	0.8	1.4	−3.6	3.4	5.8	23.4
4. Levantine	3.1	7.4	0.9	3.9	4.5	7.7	0.3	0.6	0.6	6.0	9.4	25.6
5. Aegean	3.1	7.6	0.8	3.2	4.5	7.7	0.9	2.0	4.7	6.9	14.0	27.4
6. Ionian	3.2	7.8	0.7	3.0	4.7	7.9	1.6	3.0	2.3	8.8	12.5	30.5
7. Adriatic	3.2	7.8	0.5	2.1	4.2	7.2	0.6	1.5	3.0	5.2	11.5	23.8
8. Tyrrhenian	3.3	8.0	0.5	2.0	4.5	7.7	1.3	2.8	−0.7	4.1	8.9	24.6
Weighed Average	3.2	7.8	0.7	2.8	4.6	7.8	0.9	1.9	0.4	5.3	9.8	25.6

level variation (white) for the two scenarios. Their patterns are shown in Fig. 5.10. Since the TME component of sea–level rise does not exceed the 1 cm level across the Mediterranean Sea (less than the uncertainty associated with the OR contribution during decades 1990–2000 and 2040–2050), this term is not included Fig. 5.9.

Despite the different geometries of their components, the combined sea–level fingerprints in scenarios MIN50 and MAX50 show some trends which are clearly visible in Fig. 5.9. First, in both scenarios, almost all the components are coherent and concur to a total sea–level *rise* across the Mediterranean Sea (the only exceptions are the negative OR values predicted for South Creete, West Mediterranean and Tyrrhenian, which however are not fully balancing the positive values of TIM and GIA in those sub–basin). Second, for two scenarios, the TIM component always largely exceeds the OR component; furthermore, in all sub–basins the TIM component of MIN50 is always larger than the OR component of MAX50. Third, in both scenarios, the GIA component generally contributes less than OR, but nevertheless it is apparent that GIA is not always negligible compared to TIM. According to our estimates, the 2040–2050 total sea–level change respect to 1990–2000 could range, across the sub–basins, between ~ 6 and ~ 14 cm for scenario MIN50, and between ~ 23 and ~ 30 cm for MAX50. Considering the smooth pattern shown by the TIM component of sea–level change (see Fig. 5.6), the regional variability of scenarios MIN50 and MAX50 is mainly caused by the OR component and, to a lesser extent, by the GIA contribution. At sub–basin scale (see Fig. 5.10), the sum of the three components reaches the largest amplitude in the bulk of the Mediterranean Sea, especially in the Ionian Sea, where the total future sea–level prediction reaches 12.5 cm for scenario MIN50 and 30.5 cm for MAX50, respectively, and in the Aegean Sea, with values of 14.0 and 27.4 for the two combinations. GIA mitigates sea–level rise along the continental coastlines of Mediterranean Sea, with the largest effects observed for small coastal curvature (see Fig. 5.7). However, the local magnitude of sea–level fall is not sufficient to contrast the effects of the other two components at sub–basin scale.

Across the whole Mediterranean Sea, the total sea–level rise will range, according to our results, between 9.8 (MIN50 scenario) and 25.6 cm (MAX50) to 2040–2050. The basin–averaged

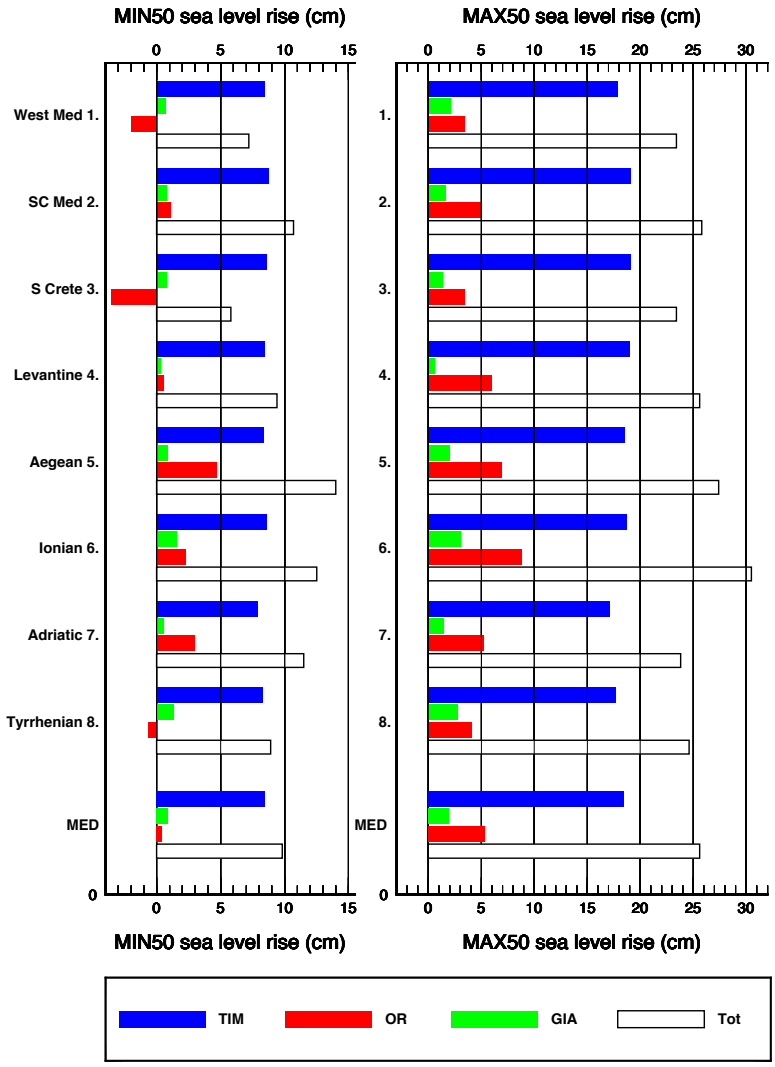

Figure 5.9: TIM (blue), GIA (green) and OR (red) components of total sea–level change in the eight sub–basins defined in Fig. 5.5 for the MIN50 (left) and MAX50 scenarios (right). White bins show total sea–level change, the bottom lines (MED) show weighed–averages across the whole Mediterranean Sea.

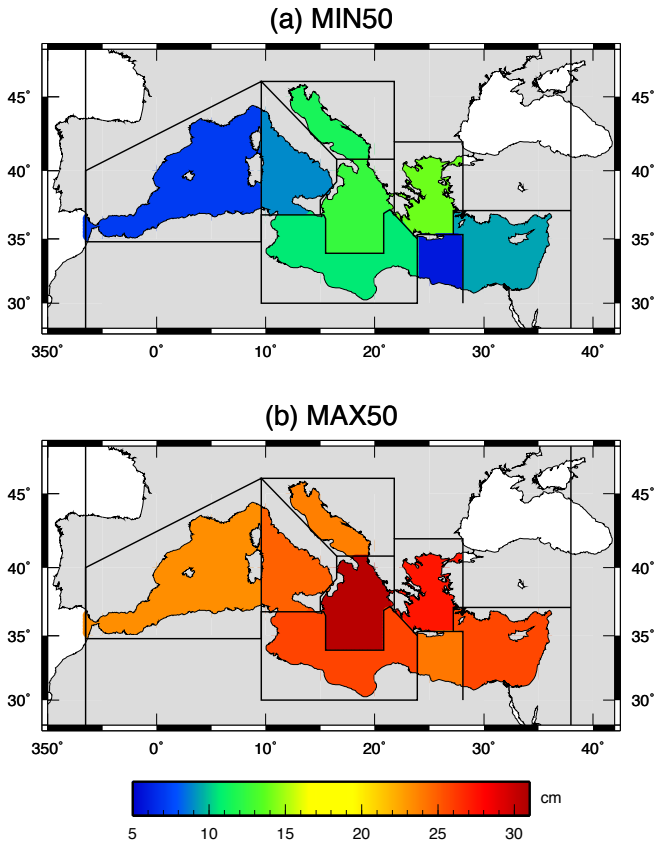

Figure 5.10: Projected sea–level variations in the Mediterranean Sea to 2040–2050 relative to 1990–2000, combining contributions from TIM, GIA and OR for the MIN50 (a) and MAX50 (b).

TIM component is, in both scenarios, exceeding the OR (adopting the basin–wide projections of Tsimplis et al. (2008) instead of those of Carillo et al. (2012) would not qualitatively change this conclusion). Furthermore, the MIN50 TIM value exceeds the MAX50 OR component. The dominance of TIM over OR suggested by our projections could indicate a significant change in the regime of the Mediterranean sea–level variations, which have been dominated, during the altimetry era (the last ~ 20 years), by steric effects (Criado-Aldeanueva et al., 2008). Our findings agree, at least qualitatively, with the global results of the IPCC AR5 report (Church et al., 2013), which indicate a slight dominance of the TIM over the OR contributions in all the RCP scenarios to year 2100 (see median values of Table 13.5 of the report).

Sea–level change variations at tide gauges and LECZ

A simple way to assess the sea–level projections obtained above is to compare them with observations of sea–level variations and their rates at tide gauges placed along the Mediterranean shorelines. The Permanent Service for Mean Sea Level (PSMSL) holds 134 records from Revised Local Reference (RLR) tide gauges facing the Mediterranean Sea. The longest record is that of Marseille (121 years); the completeness of records varies between 33 to 100%. The oldest tide gauge record is that of Venezia Santo Stefano (Italy), which started in 1872. The locations of the Mediterranean Sea tide gauges are shown by small circles in Fig. 5.11. To avoid contamination of decade and multi–decade sea–level fluctuations (Douglas, 1997; Sturges and Hong, 2001), the past trend of sea–level change has been only estimated for tide gauges with a minimum record > 60 years and a completeness $> 80\%$ (Spada and Galassi, 2012). The trends, obtained by a straightforward linear regression, are not corrected for GIA nor for any other possible contaminating effects. For the selected tide gauges, the best fitting model is indeed linear (Olivieri and Spada, 2013), which in this case motivates our choice of neglecting any sea–level acceleration.

Basic data for the six selected tide gauges obeying the criteria above are summarized in Table 5.3, while in Table 5.4 we estimate future sea–level variations according to the two scenarios MIN50 and MAX50. Table 5.4 shows that the sea–level rise to 2040–2050 could exceed that obtained by extrapolation of secular rates by a factor as large as ~ 6. Adopting scenario MIN50, in Trieste and Bakar (both placed in the northern Adriatic) sea–level will rise by ~ 11 cm by 2040–2050. However, assuming MAX50, this would amount to ~ 23 cm. Both values largely exceed those projected on the basis of the observed rates at these locations (as shown in Fig. 5.9, the TIM will be the major driving mechanism in the Adriatic sub–basin). The future trends at the six tide gauges indicate a minimum value of ~ 1 mm yr^{-1} for scenario MIN50, and of ~ 4 mm yr^{-1} for MAX50, which implies a sharp increase in the rate of sea–level change of factors ranging from ~ 1 to ~ 6 to 2040–2050. At the Mediterranean Sea scale, the sea–level variations expected at all the tide gauges to 2050 (Fig. 5.11), show a significant east–west gradient that mostly reflects the patterns of the OR component of total sea–level rise (Fig. 5.8) and, to a lesser extent, that of GIA (Fig. 5.7).

Projections of future sea–level rise are of particular importance in the Mediterranean Sea, in view of the large extent coastal areas vulnerable to flooding and of the high population density

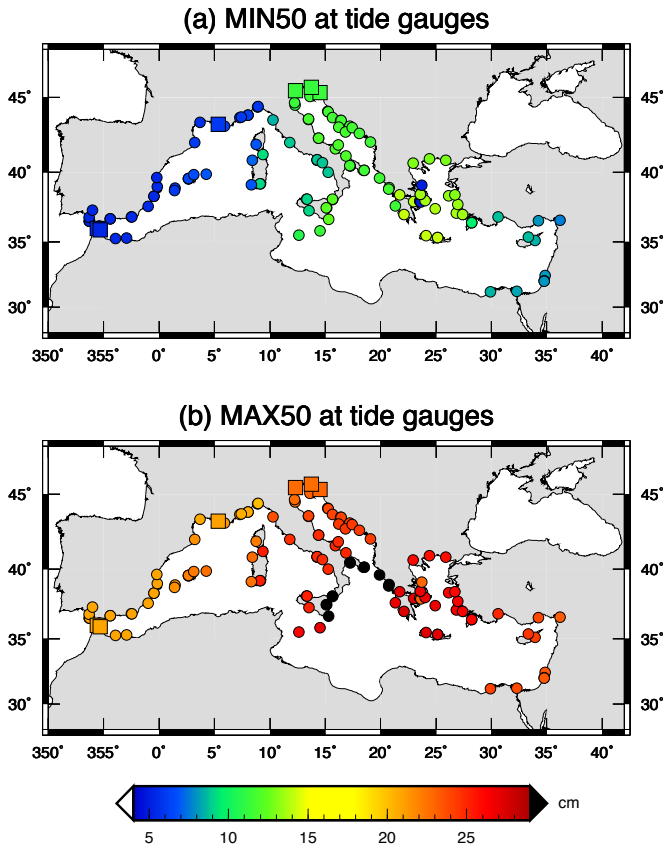

Figure 5.11: Amount of sea–level change at the location of all the Mediterranean PSMSL RLR tide gauges to 2040–2050, according to the MIN50 (a) and MAX50 (b) scenarios. Squares show the locations of tide gauges listed in Tables 5.3 and 5.4.

Table 5.3: Basic data of the Mediterranean Sea tide gauges with a record length sufficient for an estimate of the long–term trend. Data are from the PSMSL RLR dataset (extracted from database 20 May 2014). The rates of sea–level change are computed by linear regression.

PSMSL Station	PSMSL Id	Time span year–year	Valid yearly records	Observed rate mm yr^{-1}
Marseille (FR)	61	1885–2012	121	1.26 ± 0.05
Venezia P.S. (I)	168	1909–2000	83	2.44 ± 0.17
Trieste (I)	154	1875–2012	116	1.25 ± 0.10
Bakar (HR)	353	1930–2011	69	0.93 ± 0.21
Ceuta (E)	498	1945–2012	61	0.64 ± 0.12
Tarifa (E)	488	1944–2012	60	0.99 ± 0.13

Table 5.4: Total relative sea–level variations and their rates to 2040–2050 according to scenarios MIN50 and MAX50, at the six tide gauges considered in this study. Column "Extrapolation" shows the sea–level rise that would be observed assuming the secular rates of Table 5.3. The trend variations (last two columns) represent the ratios between the rates according to the two scenarios and the observed secular rates.

PSMSL station	Extrapolation to 2050 cm	Scenario MIN50 cm	Scenario MAX50 cm	Future trend MIN50 mm yr^{-1}	Future trend MAX50 mm yr^{-1}	Trend variation MIN50	Trend variation MAX50
Marseille	6.3	6.0	20.9	1.2	4.2	+0.9	+3.3
Venezia P.S.	12.9	11.3	22.7	2.3	4.5	+0.9	+1.9
Trieste	6.2	11.3	22.7	2.2	4.5	+1.8	+3.6
Bakar	4.6	11.3	22.9	2.3	4.6	+2.4	+4.9
Ceuta	3.2	5.4	20.8	1.1	4.2	+1.7	+6.5
Tarifa	4.9	5.4	20.8	1.1	4.2	+1.1	+4.2

(see *e. g.* Cori, 1999; Nicholls and Cazenave, 2010). To investigate the possible impacts of our projections, we have estimated the total sea–level variation that is expected to 2040–2050 at some densely populated Mediterranean LECZ whose locations are shown in Fig. 5.5. In Fig. 5.12, the amount of sea–level rise at these LECZ is shown for scenarios MIN50 and MAX50 (gray and red bins, respectively). Extreme values for both scenarios are predicted for Izmir and Tessaloniki, both facing the Aegean Sea. One critical area is the Nile delta, where in the highly populated area of Alexandria (over 2.2 million inhabitants), our projections are between 8.5 and 24.1 cm for the MIN50 and MAX50 scenarios, respectively. Since in Fig. 5.12 we do not include the local effects due to compaction and lack of sediments in the Nile delta, our estimates above are expected to represent a lower bound of the effective future sea–level rise. Extrapolating to 2050 the values of subsidence suggested by Ericson et al. (2006), our MAX50 scenario would be approximately doubled, although it has been recently suggested that Alexandria has been subject to a more moderate land subsidence over the past decade (Wöppelmann et al., 2013). An extended LECZ develops along the northern Adriatic Sea, between the cities of Ravenna and Venice. Despite the relatively modest population (150 and 270 thousands inhabitants, respectively), the two towns are included in the UNESCO heritage list for their recognized artistic and historical value. In this LECZ, the sea–level rise will be ~ 11.3 cm and ~ 22.7 in the two scenarios. Similarly to the case of the Nile delta, however, our estimates are not including the effects of local subsidence, which have been extensively considered in previous studies (see for example Carbognin et al., 2010; Teatini et al., 2005).

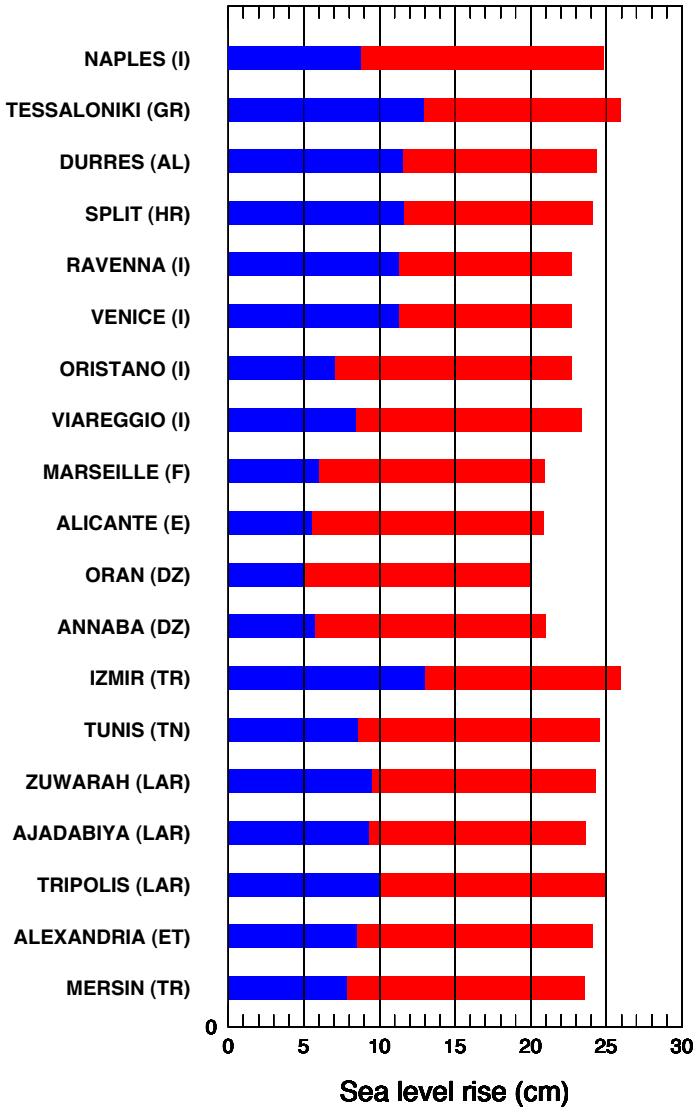

Figure 5.12: Sea–level rise expected to 2040–2050 as the result of the combined effect of the TIM, OR, and GIA sea–level components in densely populated coastal towns located in Mediterranean LECZ (see Fig. 5.5), for the MIN50 (blue) and the MAX50 (red) scenarios discussed in the body of the paper.

Chapter 6

Conclusions and final remarks

In this work, different issues related to some aspects of sea–level changes have been taken in to consideration. Using tide gauge measurements and geophysical models, the problem of sea–level change has been tackled for the recent past and for the future, both at global and at regional scales. Drawing the conclusions, it is important to stress out the main findings obtained in the different parts of this Thesis. In the following, we will summarize the achievement obtained for

- the sea–level changes at global scale;
- the relevance of geophysical process in sea–level changes understanding;
- the importance of tide gauge measurements for the detection of non–linearity in sea–level;
- the assessments of future sea–level change assessments.

6.1 Sea–level changes at global scale

After a revisitation of previous work and an overview of the currently available data, we have proposed a new solution to the long–standing problem of the assessment of GMSLR from secular TG observations. The TGs selection has been based on numerical results obtained from three specific GIA models widely employed in the literature and characterized by distinct viscosity profiles and ice sheets chronologies (namely, ICE–3G, ICE–5G and KL05). However, the approach outlined is easily reproducible and could be directly applied to any other plausible GIA model, provided that it is consistent with a specific set of Relative Sea Level observations since the LGM.

Using appropriate selection criteria, we have identified a restricted set of 22 TGs (SG01) which are useful for the assessments of the GMSLR. The imposed constraints make our "preferred" GMSLR estimate, namely $\mu' = 1.5 \pm 0.1$ mm yr^{-1} totally independent on the GIA model employed to compute the corrections. Furthermore, we have found that it is stable (at the 0.1 mm yr^{-1} level) with respect to the introduction of refined features in the numerical solution of the SLE such as the rotational component of the sea–level variations and the horizontal migrating of shorelines.

Our GMSLR estimate is found to be largely consistent with other GIA–corrected estimates obtained from TG observations during comparable time scales ($\sim$ one century), but based on different methods of analysis. Although the statistical meaning of the error bar on the GMSLR estimate by Bindoff et al. (2007) is not explicitly stated, our estimate is clearly consistent with the results of the fourth IPCC report. Since our GMSLR estimate is largely independent on assumptions regarding the GIA corrections, we have probably improved the robustness of the GMSLR assessment with respect to previous works.

After having assessed the global mean value of the rate of sea–level, we have investigated the spatial variability of observed sea–level signals. Sea–level variability at global scale has been addressed trough the Spherical Harmonic Expansion methods, applying the SVD–SHE approach (see chapter 3) to tide gauge dobservations. In addition to the ALL set (composed by all the RLR PSMSL tide gauge with more of three valid years in their records), we have performed a selection capable to leave sufficient TGs for the expansion but also able to extract TGs representative for sea–level changes in the last century. The set so obtained, the T60C70 set, contains 101 TGs. From a synthetic test, and from the literature, we have considered appropriate to lead the expansion based on the ALL and T60c70 sets only up to harmonic degree two.

The so obtained C_{00a} coefficient, representing the global mean sea–level trend, ranges between 1.4 and 1.6 mm yr^{-1}, in agreement with that resulting from the analysis of TGs performed in chapter 2. Regarding the other harmonic coefficients describing the spatial variability, the relevance of coefficient C_{20a} obtained for both the TG sets manifests a north–south pattern and reveals the importance of the two main sources of present ice melting (Antarctica and Greenland) in sea–level variability. The presence of other coefficients with non negligible values, especially C_{11b} for the ALL-set, C_{10a} for the T60C70-set and C_{21b} for both, evidences the relevance of processes with an high spatial variability (as the present melting of small glaciers, oceanic processes, etc.).

6.2 The role of solid Earth geophysical processes in sea–level change

Solid Earth processes responsible for sea–level change, namely GIA and TIM, have been modeled to understand their contribution to sea–level variations.

GIA models have been used as criteria for tide gauges selection in the assessment of GMSLR. GIA corrections to the sea–level trends obtained from specific sets of TGs have long been recognized to have an important role, but up to now, these have been generally computed *a posteriori*, once a suitable set of TG has been identified according to specific criteria. In this work, GIA corrections have been employed in a non–traditional way, since their amplitude is quantitatively adopted *a priori* as one of the selection criteria imposed to constrain the TG set appropriate for GMSLR assessment. In particular, we have proposed to substitute the criterion suggested by Douglas (1997) concerning the exclusion of the TGs belonging to regions which were deeply covered by ice at the LGM or to their surroundings, with a new requirement *i. e.*, that GIA corrections to TG series should be largely independent from the particular GIA model employed to compute them. Our motivation essentially resides in the markedly different ice distributions at the LGM

shown by current GIA models, which is the cause of distinct subsidence patterns, especially across the lateral forebulge regions.

Our estimate of GMSLR is consistent with the results of Douglas (1997) is only met for the GIA–uncorrected estimate. The corrected one ($\mu'_{D97} = 1.8 \pm 0.1$ mm yr^{-1}) is inconsistent with ours (1.5 ± 0.1 mm yr^{-1}), and exceeds it, essentially because of the significantly different set of criteria imposed for the selection of the TGs. According to our results, the discrepancy is specifically to be attributed to the assumption that the North America West coast and SE North America TGs are located outside the peripheral bulge of the formerly ice–covered regions. While this can be certainly assumed for GIA computations based on model ICE–3G, our computations have shown that this is not the case when models ICE–5G and KL05 are employed. This serious inconsistency between GIA model predictions has ultimately prompted us to propose our requirement for TGs selection instead of the D97 criterion.

The analysis of spatial variability with SVD–SHE has been used to understand the possible contribution of ice melting to sea–level change. The global values obtained as "residuals" (sea–level observed rate corrected for GIA and steric effect) range between $+1.34$ and $+1.61$ mm yr^{-1} for the ALL set and between $+0.59$ and $+0.95$ mm yr^{-1} for the T60C70, in agreement with the total contribution of TIM to sea–level rise assessed by IPCC (1.47 mm yr^{-1} during 1993–2010, Church et al., 2013).

The spatial variability of TIM contribution to sea–level has been investigated following the example of Mitrovica et al. (2001), and a mass balance for present ice sources has been extrapolated, minimizing the difference between the residual and the fingerprint obtained with an uniform ice loss. The solutions obtained are not apparently consistent with previously estimates of TIM mass balances. Possible reasons are in the method employed (SVD–SHE), which shows a number of limitations: first, SVD–SHE is strongly influenced by the distribution of the TGs used. Secondly, the classical harmonic expansion assumes that the signals is defined over the whole sphere, *i. e.* also across the continents.

In order to understand how much spherical harmonics are able to separate single components of sea–level variability, an other method, the HH–SHE, has been applied. The HH–SHE is based on the definition of "spherical" SH functions that are orthogonal over the irregular shape of the oceans. In order to avoid problems linked to non–uniform distribution of data and to drive the expansion to high degree (higher then the 2 allowed by TGs data) uniformly spaced satellite altimeter measurements (T/P) have been used. The analysis of variability at different degree of the image functions of altimeter observation, of steric data and of modeled GIA and TIM component shown that GIA and TIM contain to less variability, even at low–degree, to be detected in observed signals.

A further attempt to constrain mass balance from observed sea–level recordsv has been done using single TG record of sufficient length and located in proximity of the ice mass. The Nuuk/Godthab (NG) tide gauge record has both these requisites. The location of the NG station (Southwest Greenland) and its record length (~ 4 decades) makes it potentially useful to constrain volume changes in the GIS during a period (1958–2002) when only a few mass balance estimates exist for the GIS, often characterized by a considerable degree of uncertainty.

Analysis of the NG sea–level time series by standard regression methods clearly shows a lin-

ear sea–level rise and a negligible sea–level acceleration. Based on previous AR4 assessments, on results from the literature and on the sea–level fingerprint method, all the sea–level components have been evaluated, along with their uncertainties. During period 1961–2003, GIA and the isostatic disequilibrium associated with melting of the GIS have been the dominating causes sea–level variations at the NG tide gauge, but these processes have been acting in opposite directions: GIA has produced a sea–level rise, while GIS has contributed a sea–level fall. When combined with the other sea–level contributions, including the steric component and various mass terms, the total modeled rate of sea–level change at NG is found to be broadly coherent with the observed trend, but its amplitude is not fully explained. In view of the large uncertainties in the modeled components of sea–level change at NG, the misfit between predictions and observations cannot be interpreted unambiguously. A possible interpretation is that the evidence from NG could indicate that the mass balance of the GIS was, during 1961–2003, closer to equilibrium than suggested by several estimates in the literature that followed the AR4 assessment.

Another relevant issue addressed is that concerning GIA–induced sea–level acceleration. Although isostatic readjustment affects the local rates of secular sea–level change (Milne and Mitrovica, 1998; Peltier, 2004), a possible impact on regional acceleration have been so far discounted (Douglas, 1992; Jevrejeva et al., 2008; Woodworth et al., 2009) since the process evolves on a millennium time scale (Turcotte and Schubert, 2002). Analyzing tide gauge records located along the coasts of the Baltic Sea we have detected a previously unnoticed anomaly in the long–term sea–level acceleration and we have demonstrated that this can be explained by the classical post–glacial rebound theory and numerical modeling of glacial isostasy. The sign and the amplitude of the anomaly, ~ 0.2 mm/yr/century, is consistent with the post–glacial rebound theory and with realistic numerical predictions of GIA models routinely employed to decontaminate the tide gauges observations from the GIA effects (Peltier, 2004). Model computations predict the existence of anomalies of similar amplitude in other regions of the globe where GIA is still particularly vigorous at present, but no long–term instrumental observations are available to support their existence.

6.3 Regional sea–level non–linearity

Complex non–linear trends and abrupt sea–level variations shown by TGs records have been investigated applying different approaches to regional case studies.

The Ensamble Empirical Mode Decomposition (EEMD) technique has been applied to sea–level record of TGs located in Adriatic Sea to investigate the existence of possible cyclic variations. The EEMD analysis clearly reveals the annual and the semiannual periodicities in the sea–level stack of all Adriatic tide gauges, and shows a powerful oscillation with a period of ~ 20 years. The analysis on Atlantic Modes (namely NAO and AMO) and on Adriatic sea–level signals has shown that a negative phase of sea–level corresponds to a negative phase of the AMO and to a positive phase of NAO. The EEMD analysis suggests that the periodic occurrence of opposite phases in the AMO and NAO indices (with a period of ~ 20 years), correspond to the ~ 20 years cycle identified for the sea–level trend in the Adriatic Sea. The coincidence of AMO-NAO phase

opposition and warm AMO phase could explain the anomalous sea–level high–stand detected during 2010–2011 and possibly help to forecast future anomalous sea–level fluctuations within the Adriatic Sea.

A Early Warning approach have been used to detect tipping points in sea–level records of North East Pacific (NEP). The analysis on TG sea–level records partially confirms the findings of Bromirski et al. (2011), indicating the period around 1980 as crucial point, in which sea–level shifts from a state (uniform increase) to another (closer to stability). In addition to the Bromirski et al. (2011) findings, our work evidences an other shift around year 2000. The same analysis has been performed on the oceanic modes acting on North East Pacific, namely the El Niño Southern Oscillation (ENSO), the Pacific Decadal Oscillation (PDO) and North Pacific Gyre Oscillation (NPGO), to investigate if the same shifts are detectable in oceanic process that influence the sea–level height. The analysis on PDO index, representing the SST in North Pacific, partially shows the same behavior of NEP stack, suggesting a jump around $\sim$ 1984. According to the potential analysis, this apparent change in the state of the system does not correspond to a change in the potential. Being the PDO defined as the principal component of the SST in North Pacific, we can hypothesize that the change detected represents the "internal" change in the state of SST, and that this latter could be a driving force for sea–level change in NEP.

6.4 Outlook

The problem of future sea–level assessment has ben tackled through two different approaches: the first, semi–empirical, is based on the artificial neural network system while the second, model–based, uses a model implementation for the single components of sea–level change.

The neural network method has been applied on a global synthetic sea–level curve reconstructed from 1023 tide gauge records (Jevrejeva et al., 2006). The artificial neural network (ANN) has projected this sea–level curve up to year 2100. The projected sea–level for 2081–2100 in respect to 1986–2005 is $\sim$ 195 mm, significantly lower than values obtained in the IPCC AR5 in the same time interval ($\sim$ 400 mm, with a lower limit of $\sim$ 260 mm for RCP 2.6). The reason of the lower values obtained with the ANN approach resides mainly in the method itself. The observed sea–level data in input, have been used without introducing any constraint so that what happened in the past is reproduced for the future by the network. The first part of the syntetic sea–level curve (from 1700 to about 1850) shows a trend significantly lower than those observed in the last part (from $\sim$ 1990) and this has strongly influenced the projection. Nevertheless, the projected sea–level curve has maintained the main characteristics (as the periodicity of oscillation) of the original sea–level signal. Results obtained here with the ANN suggest to improve the approach for the sea–level projection, introducing some external physical parameter (as the temperature) to help the system in the reproduction of the sea–level behavior.

Adopting a model–based approach, we have analyzed the case of future sea–level rise in the Mediterranean Sea. Using published estimates for the TIM and steric components of future sea–level change and GIA modeling, we have obtained spatial patterns of low–frequency sea–level vari-

ations across the Mediterranean Sea to 2040–2050. The spatially–averaged projected sea–level rise to 2040–2050 will be 9.8 and 25.6 cm in the Mediterranean Sea in our MIN50 and MAX50 scenarios, respectively. These two values are slightly smaller than the minimum and maximum likely ranges of variation assessed by the IPCC AR5 under the RCP6.0 scenario, akin to the SRES A1B scenarios used to obtain the TIM and steric–oceanic (OR) projections in this study ($\sim$ 15 and $\sim$ 30 cm). During next decades, the mass component of sea–level rise (TIM), will largely exceed the OR in the Mediterranean Sea (this ratio of TIM to OR sensibly exceeds the one assessed globally by AR5 to 2100). This result, however, is contingent to the assumption that a geostrophic adjustment is established in the Mediterranean Sea, a condition that could not be fully met (Jordà and Gomis, 2013).

In the Mediterranean Sea, the largest deviations from a uniform response will be associated with the steric component. The expected TIM–induced sea–level variations will be quite uniform, since the ice sources that are driving this component are mostly located in the far–field of the basin. Compared to TIM, the regional imprint of GIA will be more pronounced, although its average amplitude will be comparatively small (this holds for both GIA models employed in this study). Despite the regional variability shown by the TIM, steric and GIA fingerprints, these three components of future sea–level rise will be to a great extent coherent at a sub–basin scale.

To assess the local impact of our projections, we have evaluated the variation in the rates of sea–level rise at PSMSL RLR tide gauges located along the coasts of the Mediterranean Sea. In the conservative MIN50 scenario, our computations suggest that the rate will increase by a factor of $\sim$ 2 compared to the secular rates observed at the tide gauges. To 2050, the MAX50 predicted rates of sea–level variation at Mediterranean tide gauges are at the lower bound of the AR5 RCP6.0 assessed global trends.

Bibliography

R. B. Alley, J. T. Andrews, J. Brigham-Grette, G. K. C. Clarke, K. M. Cuffey, J. J. Fitzpatrick, S. Funder, S. J. Marshall, G. H. Miller, J. X. Mitrovica, D. R. Muhs, B. L. Otto-Bliesner, L. Polyak, and J. W. C. White. History of the Greenland Ice Sheet: paleoclimatic insights. *Quaternary Science Reviews*, 29:1728–1756, 2010. doi: 10.1016/j.quascirev.2010.02.007.

J. B. Anderson, S. S. Shipp, A. L. Lowe, J. S. Wellner, and A. B. Mosola. The Antarctic Ice Sheet during the Last Glacial Maximum and its subsequent retreat history: a review. *Quaternary Science Reviews*, 21(1):49–70, 2002.

F. Antonioli, L. Ferranti, A. Fontana, A. Amorosi, A. Bondesan, C. Braitenberg, A. Dutton, G. Fontolan, S. Furlani, K. Lambeck, et al. Holocene relative sea–level changes and vertical movements along the italian and istrian coastlines. *Quaternary International*, 206(1):102–133, 2009.

J. I. Antonov, S. Levitus, and T. P. Boyer. Steric sea level variations during 1957–1994: Importance of salinity. *Journal of Geophysical Research*, 107, C12:8013, 2002. doi: 10.1029/2001JC000964.

J. I. Antonov, S. Levitus, and T. P. Boyer. Thermosteric sea level rise, 1955–2003. *Geophysical Research Letters*, 32:12602, 2005. doi: 10.1029/2005GL023112.

A. Artegiani, E. Paschini, A. Russo, D. Bregant, F. Raicich, and N. Pinardi. The Adriatic Sea general circulation. Part I: Air-sea interactions and water mass structure. *Journal of Physical Oceanography*, 27(8):1492–1514, 1997.

D. G. Aubrey and K. O. Emery. Relative sea levels of Japan from tide-gauge records. *BGeological Society of America Bulletin*, 97(2):194–205, 1986.

F. B. Baker. A note on the proper use of the Numerical Recipes RAN1 random number generator. *Computational Statistics & Data Analysis*, 25(2):237–239, 1997.

T. P. Barnett. The estimation of global sea level change: a problem of uniqueness. *Journal of Geophysical Research: Oceans (1978–2012)*, 89(C5):7980–7988, 1984.

T. P. Barnett. Recent changes in sea level and their possible causes. *Climatic change*, 5(1):15–38, 1990.

B. L. Barnhart. *The Hilbert-Huang Transform: theory, applications, development*. PhD thesis, University of Iowa, 2011.

N. L. Bindoff, J. Willebrand, V. Artale, A. Cazenave, J. M. Gregory, S. Gulev, K. Hanawa, C. Le Quere, S. Levitus, Y. Nojiri, et al. Observations: oceanic climate change and sea level. In S. Solomon, D. Qin, M. Manning, Z. Chen, M. Marquis, K. B. Averyt, M. Tignor, and H. L. Miller, editors, *Climate Change 2007: The Physical Science Basis: Contribution of Working Group I to the Fourth Assessment Report of the Intergovernmental Panel on Climate Change*, pages 385–433. Cambridge University Press, 2007.

K. Bittermann, S. Rahmstorf, M. Perrette, and M. Vermeer. Predictability of twentieth century sea–level rise from past data. *Environmental Research Letters*, 8(1):014013, 2013.

R. Black, W. N. Adger, W. Nigel, N. W. Arnell, S. Dercon, A. Geddes, and D. S. G. Thomas. Migration and global environmental change (Editorial). *Global Environmental Change*, 21S: S1–S2, 2011.

G. E. Box, G. M. Jenkins, and G. C. Reinsel. Time series analysis: forecasting and control, 2007.

L. C. Breaker and A. Ruzmaikin. The 154-year record of sea level at San Francisco: extracting the long-term trend, recent changes, and other tidbits. *Climate Dynamics*, 36(3-4):545–559, 2011.

P. D. Bromirski, A. J. Miller, R. E. Flick, and G. Auad. Dynamical suppression of sea level rise along the Pacific coast of North America: Indications for imminent acceleration. *Journal of Geophysical Research: Oceans (1978–2012)*, 116(C7), 2011.

C. Cabanes, A. Cazenave, and C. Le Provost. Sea level rise during past 40 years determined from satellite and in situ observations. *Science*, 294(5543):840–842, 2001.

D. J. Caccamise, M. A. Merrifield, M. Bevis, J. Foster, Y. L. Firing, M. S. Schenewerk, F. W. Taylor, and D. A. Thomas. Sea level rise at Honolulu and Hilo, Hawaii: GPS estimates of differential land motion. *Geophysical Research Letters*, 32:L03607, 2001.

A. Cailleux. Rècentes variations du niveau des mers et des terres. *Société Géologique de France*, 48:310–315, 1952.

F. M. Calafat, D. P. Chambers, and M. N. Tsimplis. Mechanisms of decadal sea level variability in the eastern North Atlantic and the Mediterranean Sea. *Journal of Geophysical Research: Oceans*, 117(C9), 2012.

L. Carbognin, P. Teatini, and L. Tosi. Eustacy and land subsidence in the venice lagoon at the beginning of the new millennium. *Journal of Marine Systems*, 51(1):345–353, 2004.

L. Carbognin, P. Teatini, A. Tomasin, and L. Tosi. Global change and relative sea level rise at Venice: what impact in term of flooding. *Climate Dynamics*, 35(6):1039–1047, 2010. doi: 10.1007/s00382-009-0617-5.

A. Carillo, G. Sannino, V. Artale, P.M. Ruti, S. Calmanti, and A. Dell'Aquila. Steric sea level rise over the Mediterranean Sea: present climate and scenario simulations. *Climate Dynamics*, 39 (9–10):2167–2184, 2012. doi: 10.1007/s00382-012-1369-1.

S. R. Carpenter and W. A. Brock. Early warnings of unknown nonlinear shifts: a nonparametric approach. *Ecology*, 92(12):2196–2201, 2011.

A. Cazenave and W. Llovel. Contemporary sea level rise. *Annual Review of Marine Science*, 2: 145–173, 2010. doi: 10.1146/annurev-marine-120308-081105.

B. F. Chao, Y. H. Wu, and Y. S. Li. Impact of artificial reservoir water impoundment on global sea level. *Science*, 320(5873):212–214, 2008. doi: 10.1126/science.1154580.

W-Y. Chung. Earthquakes along the passive margin of Greenland: evidence of postglacial rebound control. *Pageoph*, 159:2567–2584, 2002.

W-Y. Chung and H. Gao. The Greenland earthquake of 11 July 1987 and postglacial reactivation along a passive margin. *Bulletin of the Seismological Society of America*, 87:1058–1068, 1997.

J. A. Church and N. J. White. A 20th century acceleration in global sea-level rise. *Geophysical research letters*, 33(1):L01602, 2006.

J. A. Church and N. J. White. Sea-level rise from the late 19th to the early 21st century. *Surveys in Geophysics*, 32(4-5):585–602, 2011.

J. A. Church, J. M. Gregory, P. Huybrechts, M. Kuhn, K. Lambeck, M. T. Nhuan, D. Qin, and P. L. Woodworth. Changes in sea level. *, in: JT Houghton, Y. Ding, DJ Griggs, M. Noguer, PJ Van der Linden, X. Dai, K. Maskell, and CA Johnson (eds.): Climate Change 2001: The Scientific Basis: Contribution of Working Group I to the Third Assessment Report of the Intergovernmental Panel*, pages 639–694, 2001.

J. A. Church, N. J. White, R. Coleman, K. Lambeck, and J. X. Mitrovica. Estimates of the regional distribution of sea level rise over the 1950-2000 period. *Journal of Climate*, 17(13):2609–2625, 2004.

J.A. Church, P.U. Clark, A. Cazenave, J.M. Gregory, S. Jevrejeva, A. Levermann, M.A. Merrifield, G.A. Milne, R.S. Nerem, P.D. Nunn, A.J. Payne, W.T. Pfeffer, D. Stammer, and A.S. Unnikrishnan. Sea Level Change. In T.F. Stocker, D. Qin, G.-K. Plattner, M. Tignor, S.K. Allen, J. Boschung, A. Nauels, Y. Xia, V. Bex, and P.M. Midgley, editors, *Climate Change 2013: The Physical Science Basis. Contribution of Working Group I to the Fifth Assessment Report of the Intergovernmental Panel on Climate Change*, pages 1138–1191. Cambridge University Press, Cambridge, 2013.

B. Cori. Spatial dynamics of Mediterranean coastal regions. *Journal of Coastal Conservation*, 5: 105–112, 1999. doi: 10.1007/BF02802747.

F. Criado-Aldeanueva, J. Del Rao Vera, and J. Garcia-Lafuente. Steric and mass-induced mediterranean sea level trends from 14 years of altimetry data. *Global and Planetary Change*, 60(3-4): 563 – 575, 2008. doi: 10.1016/j.gloplacha.2007.07.003.

T. M. Cronin. Rapid sea–level rise. *Quaternary Science Reviews*, 56:11–30, 2012.

D. Dahl-Jensen, J. Bamber, C.E. Bŕggild, M. van den Broeke, E. Buch, J. Hesselberg Christensen, K. Dethloff, M. Fahnestock, S. Marshall, M. Rosing, et al. The Greenland Ice Sheet in a changing climate. Technical report, Artic Monitoring and Assessment Programme, 2009.

V. Dakos, S. R. Carpenter, W. A. Brock, A. M. Ellison, V. Guttal, A. R. Ives, S. Kefi, V. Livina, D. A Seekell, E. H. Van Nes, et al. Methods for detecting early warnings of critical transitions in time series illustrated using simulated ecological data. *PLoS One*, 7(7):e41010, 2012.

P. K. Das and M. Radhakrishna. An analysis of Indian tide-gauge records. *Proceedings of the Indian Academy of Sciences-Earth and Planetary Sciences*, 100(2):177–194, 1991.

J. L. Davis and J. X. Mitrovica. Glacial isostatic adjustment and the anomalous tide gauge record of eastern North America. *Nature*, 379:331–333, 1996.

C. De Boor. *A practical guide to splines*, volume 27, Applied Mathematical Sciences. Springer–Verlag New York, 1978.

E. Di Lorenzo, N. Schneider, K. M. Cobb, P. J. S. Franks, K. Chhak, A. J. Miller, J. C. McWilliams, S. J. Bograd, H. Arango, E. Curchitser, et al. North Pacific Gyre Oscillation links ocean climate and ecosystem change. *Geophysical Research Letters*, 35(8), 2008.

P. D. Ditlevsen and S. J. Johnsen. Tipping points: early warning and wishful thinking. *Geophysical Research Letters*, 37(19), 2010.

J. P. Donnelly, P. Cleary, P. E. Newby, and R. Ettinger. Coupling instrumental and geological records of sea-level change: evidence from southern New England of an increase in the rate of sea-level rise in the late 19th century. *Geophysical Research Letters*, 31:L05203, 2004.

B. C. Douglas. Global sea level rise. *Journal of Geophysical Research: Oceans (1978–2012)*, 96 (C4):6981–6992, 1991.

B. C. Douglas. Global sea level acceleration. *Journal of Geophysical Research: Oceans (1978–2012)*, 97(C8):12699–12706, 1992.

B. C. Douglas. Global sea level rise: a redetermination. *Surveys in Geophysics*, 18:279–292, 1997. doi: 10.1023/A:1006544227856.

B. C. Douglas. Sea level change in the era of the recording tide gauge. *International Geophysics*, 75:37–64, 2001.

M. B. Dyurgerov and M. F. Meier. *Glaciers and the changing Earth system: a 2004 snapshot*. INSTAAR, University of Colorado at Boulder, 2005.

A. M. Dziewonski and D. L. Anderson. Preliminary reference Earth model. *Physics of the Earth and Planetary Interiors*, 25(4):297–356, 1981.

K. O. Emery. Relative sea levels from tide-gauge records. *Proceedings of the National Academy of Sciences*, 77(12):6968–6972, 1980.

K. O. Emery, D. G. Aubrey, and L. Jansa. *Sea levels, land levels, and tide gauges*, volume 237. Springer-Verlag New York, 1991.

D. B. Enfield, A. M. Mestas-Nuñez, and P. J. Trimble. The Atlantic multidecadal oscillation and its relation to rainfall and river flows in the continental U.S. *Geophysical Research Letters*, 28 (10):2077–2080, 2001.

J. P. Ericson, C. J. Vörösmarty, S. L. Dingman, L. G. Ward, and M. Meybeck. Effective sea–level rise and deltas: causes of change and human dimension implications. *Global and Planetary Change*, 50(1):63–82, 2006. doi: j.gloplacha.2005.07.004.

J. Ettema, M. R. van den Broeke, E. van Meijgaard, W. J. van de Berg, J. L. Bamber, J. E. Box, and R. C. Bales. Higher surface mass balance of the Greenland ice sheet revealed by high-resolution climate modeling. *Geophysical Research Letters*, 36(12):n/a–n/a, 2009. doi: 10.1029/2009GL038110.

T. Ezer and W. B. Corlett. Is sea level rise accelerating in the Chesapeake Bay? A demonstration of a novel new approach for analyzing sea level data. *Geophysical Research Letters*, 39(19), 2012.

T. Ezer, L. P. Atkinson, W. B. Corlett, and J. L. Blanco. Gulf Stream's induced sea level rise and variability along the US mid-Atlantic coast. *Journal of Geophysical Research: Oceans*, 118(2): 685–697, 2013.

R. G. Fairbanks. A 17, 000-year glacio-eustatic sea level record: influence of glacial melting rates on the Younger Dryas event and deep-ocean circulation. *Nature*, 342(6250):637–642, 1989.

R. W. Fairbridge and O. A. Krebs. Sea level and the southern oscillation. *Geophysical Journal International*, 6(4):532–545, 1962.

W. E. Farrell and J. A. Clark. On postglacial sea level. *Geophysical Journal of the Royal Astronomical Society*, 46(3):647–667, 1976. doi: 10.1111/j.1365-246X.1976.tb01252.x.

M. Ferla, M. Cordella, L. Michielli, and A. Rusconi. Long-term variations on sea level and tidal regime in the lagoon of Venice. *Estuarine, Coastal and Shelf Science*, 75(1):214–222, 2007.

X. Fettweis. Reconstruction of the 1979–2006 Greenland ice sheet surface mass balance using the regional climate model MAR. *The Cryosphere Discussions*, 1(1):123–168, 2007.

K. Fleming and K. Lambeck. Constraints on the Greenland Ice Sheet since the Last Glacial Maximum from sea-level observations and glacial-rebound models. *Quaternary Science Reviews*, 23: 1053–1077, 2004. doi: 10.1016/j.quascirev.2003.11.001.

K. M. Fleming, P. Tregoning, M. Kuhn, A. Purcell, and H. McQueen. The effect of melting land-based ice masses on sea-level around the Australian coastline. *Australian Journal of Earth Sciences*, 59(4):457–467, 2012.

R. Fossion, D.A. Hartasánchez, O. Resendis-Antonio, and A. Frank. Criticality, adaptability and early-warning signals in time series in a discrete quasispecies model. *Frontiers in Biology*, 8(2): 247–259, 2013.

G. Galassi and G. Spada. Sea–level rise in the Mediterranean Sea by 2050: Roles of terrestrial ice melt, steric effects and glacial isostatic adjustment. *Global and Planetary Change*, 123:55–66, 2014.

G. Galassi and G. Spada. Linear and nonlinear sealevel variations in the Adriatic Sea from tide gauge records (18722012). *Annals of Geophysics*, in press, 2015.

D. Garcia, Chao Vigo, I., B. F., and M. C. Martinez. Vertical Crustal Motion along the Mediterranean and Black Sea Coast Derived from Ocean Altimetry and Tide Gauge Data. *Pure and Applied Geophysics*, 164:851–863, 2007.

T. Gautama, D. P. Mandic, and M. M. Van Hulle. A differential entropy based method for determining the optimal embedding parameters of a signal. In *Acoustics, Speech, and Signal Processing, 2003. Proceedings. (ICASSP'03). 2003 IEEE International Conference on*, volume 6, pages VI–29. IEEE, 2003.

Z. Gedalof, N. J. Mantua, and D. L Peterson. A multi-century perspective of variability in the Pacific Decadal Oscillation: new insights from tree rings and coral. *Geophysical Research Letters*, 29(24):57–1, 2002.

F. Gilbert and A. M. Dziewonski. An application of normal mode theory to the retrieval of structural parameters and source mechanisms from seismic spectra. *Philosophical Transactions for the Royal Society of London. Series A, Mathematical and Physical Sciences*, pages 187–269, 1975.

V. Gornitz. Sea-level rise: A review of recent past and near-future trends. *Earth Surface Processes and Landforms*, 20(1):7–20, 1995.

V. Gornitz and S. Lebedeff. Global sea-level changes during the past century. In D. Nummedal, O. H. Pilkey, and J. D. Howard, editors, *Sea-Level Fluctuations and Coastal Evolution*, pages 3 – 16. SEPM (Society for Sedimentary Geology), 1987. doi: 10.2110/pec.87.41.0003.

V. Gornitz, S. Lebedeff, and J. Hansen. Global sea level trend in the past century. *Science*, 215 (4540):1611–1614, 1982.

A. Grinsted, J. C. Moore, and S. Jevrejeva. Reconstructing sea level from paleo and projected temperatures 200 to 2100 AD. *Climate Dynamics*, 34(4):461–472, 2010.

M. Gröger and H.-P. Plag. Estimations of a global sea level trend: limitations from the structure of the psmsl global sea level data set. *Global and Planetary Change*, 8(3):161–179, 1993.

I. Grossmann and P. J. Klotzbach. A review of North Atlantic modes of natural variability and their driving mechanisms. *Journal of Geophysical Research*, 114:851–863, 2009. doi: 10.1029/2009JD012728.

B. Gutenberg. Changes in sea level, postglacial uplift, and mobility of the earth's interior. *Geological Society of America Bulletin*, 52(5):721–772, 1941.

J. M. Hagedoorn, D. Wolf, and Z. Martinec. An estimate of global mean sea-level rise inferred from tide-gauge measurements using glacial-isostatic models consistent with the relative sea-level record. *Pure and Applied Geophysics*, 164(4):791–818, 2007.

E. Hanna, P. Huybrechts, I. Janssens, J. Cappelen, K. Steffen, and A. Stephens. Runoff and mass balance of the Greenland ice sheet: 1958–2003. *Journal of Geophysical Research*, 110:D13108, 2005. doi: 10.1029/2004JD005641.

J. Hansen, R. Ruedy, M. Sato, and K. Lo. Global surface temperature change. *Reviews of Geophysics*, 48(4), 2010.

N. A. Haskell. The motion of a viscous fluid under a surface load, Part II. *Physics*, 7:56–61, 1936.

S. J. Holgate and P. L. Woodworth. Evidence for enhanced coastal sea level rise during the 1990s. *Geophysical Research Letters*, 31(7), 2004.

S. J. Holgate, A. Matthews, P. L. Woodworth, L. J. Rickards, M. E. Tamisiea, E. Bradshaw, P. R. Foden, K. M Gordon, S. Jevrejeva, and J. Pugh. New data systems and products at the Permanent Service for Mean Sea Level. *Journal of Coastal Research*, 29(3):493–504, 2012.

H. G. Hosseini, D. Luo, and K. J. Reynolds. The comparison of different feed forward neural network architectures for ECG signal diagnosis. *Medical Engineering & Physics*, 28(4):372–378, 2006.

J. T. Houghton, Y. D. Ding, D. J. Griggs, M. Noguer, P. J. van der Linden, X. Dai, K. Maskell, and C. A. Johnson. *Climate change 2001: the scientific basis*. The Press Syndicate of the University of Cambridge, 2001.

J. R. Houston and R. G. Dean. Sea-level acceleration based on us tide gauges and extensions of previous global-gauge analyses. *Journal of Coastal Research*, 27(3):409–417, 2011.

N. E. Huang, Z. Shen, S. R. Long, M. C. Wu, H. H. Shih, Q. Zheng, N.-C. Yen, C. C. Tung, and H. H. Liu. The empirical mode decomposition and the Hilbert spectrum for nonlinear and non-stationary time series analysis. *Proceedings of the Royal Society of London. Series A: Mathematical, Physical and Engineering Sciences*, 454(1971):903–995, 1998.

J. D. Hurrel. Decadal trends in the North Atlantic Oscillation: regional temperatures and precipitation. *Science*, 269:676–679, 1995.

C. Hwang. *Orthogonal functions over the oceans and applications to the determination of orbit error, geoid and sea surface topography from satellite altimetry*. PhD thesis, The Ohio State University, Columbus, 1991.

C. Hwang. Spectral analysis using orthonormal functions with a case study on the sea surface topography. *Geophysical Journal International*, 115(3):1148–1160, 1993.

B. Ingleby and M. Huddleston. Quality control of ocean temperature and salinity profiles – Historical and real-time data. *Journal of Marine Systems*, 65(1):158–175, 2007.

M. Ishii and M. Kimoto. Reevaluation of historical ocean heat content variations with time-varying XBT and MBT depth bias corrections. *Journal of Oceanography*, 65:287–299, 2009.

M. Ishii, M. Kimoto, K. Sakamoto, and Iwasaki S. Steric sea level changes estimated from historical ocean subsurface temperature and salinity analyses. *Journal of oceanography*, 62(2): 155–170, 2006.

E. R. Ivins and C. G. Sammis. Transient creep of a composite lower crust: 1. Constitutive theory. *Journal of Geophysical Research: Solid Earth (1978–2012)*, 101(B12):27981–28004, 1996.

S. Jevrejeva, A. Grinsted, J. C. Moore, and S. Holgate. Nonlinear trends and multiyear cycles in sea level records. *Journal of Geophysical Research: Oceans (1978–2012)*, 111(C9), 2006.

S. Jevrejeva, J. C. Moore, A. Grinsted, and P. L. Woodworth. Recent global sea level acceleration started over 200 years ago? *Geophysical Research Letters*, 35:L08715, 2008. doi: 10.1029/2008GL033611.

S. Jevrejeva, J. C. Moore, and A. Grinsted. Sea level projections to AD2500 with a new generation of climate change scenarios. *Global and Planetary Change*, 80:14–20, 2012.

A. C. Johnston. Suppression of earthquakes by large continental ice sheets. *Nature*, 330:467–469, 1987.

G. Jordà and D. Gomis. On the interpretation of the steric and mass components of sea level variability: The case of the Mediterranean basin. *Journal of Geophysical Research: Oceans*, 2013.

F. Justino, A. Timmermann, U. Merkel, and W. R. Peltier. An initial intercomparison of atmospheric and oceanic climatology for the ICE-5G and ICE-4G models of LGM paleotopography. *Journal of climate*, 19(1):3–14, 2006.

G. P. Kalinin and R. K. Klige. Variation in the world sea level. *World Water Balance and Water Resources of the Earth*, pages 581–585, 1978.

S. M. Kay. *Modern spectral estimation: theory and application*. Englewood Cliffs, NJ, 1988.

A. C. Kemp, B. P. Horton, J. P. Donnelly, M. E. Mann, M. Vermeer, and S. Rahmstorf. Climate related sea–level variations over the past two millennia. *Proceedings of the National Academy of Sciences*, 108(27):11017–11022, 2011.

R. A. Kendall, J. X. Mitrovica, and G. A. Milne. On post-glacial sea level – ii. numerical formulation and comparative results on spherically symmetric models. *Geophysical Journal International*, 161(3):679–706, 2005. doi: 10.1111/j.1365-246X.2005.02553.x.

R.A. Kendall, K. Latychev, J. X. Mitrovica, J. E Davis, and M. E. Tamisiea. Decontaminating tide gauge records for the influence of glacial isostatic adjustment: The potential impact of 3-D Earth structure. *Geophysical Research Letters*, 33(24), 2006.

M. Khashei. Forecasting the Isfahan steel company production price in Tehran metals exchange using artificial neural networks (ANNs). Master's thesis, Isfahan University of Technology, 2005.

M. Khashei and M. Bijari. An artificial neural network (p,d,q) model for timeseries forecasting. *Expert Systems with Applications*, 37(1):479 – 489, 2010. doi: http://dx.doi.org/10.1016/j.eswa.2009.05.044.

J. R. Knight, C. K. Folland, and A. A. Scaife. Climate impacts of the Atlantic multidecadal oscillation. *Geophysical Research Letters*, 33(17), 2006.

R. Kubo. The fluctuation-dissipation theorem. *Reports on Progress in Physics*, 29(1):255, 1966.

K. Lambeck and P. Johnston. The viscosity of the mantle: Evidence from analyses of glacial rebound phenonena. In I. Jackson, editor, *The Earth's Mantle: Composition, Structure, and Evolution*, pages 461–502. Cambridge Univ. Press, New York, 1989.

K. Lambeck and A. Purcell. Sea–level change in the Mediterranean Sea since the LGM: model predictions for tectonically stable areas. *Quaternary Science Reviews*, 24(18):1969–1988, 2005.

K. Lambeck, C. Smither, and P. Johnston. Sea-level change, glacial rebound and mantle viscosity for northern Europe. *Geophysical Journal International*, 134(1):102–144, 1998. doi: 10.1046/j.1365-246x.1998.00541.x.

K. Lambeck, F. Antonioli, A. Purcell, and S. Silenzi. Sea–level change along the Italian coast for the past 10,000 yr. *Quaternary Science Reviews*, 23(14):1567–1598, 2004a.

K. Lambeck, M. Anzidei, F. Antonioli, A. Benini, and A. Esposito. Sea level in Roman time in the Central Mediterranean and implications for recent change. *Earth and Planetary Science Letters*, 224(3):563–575, 2004b.

K. Lambeck, F. Antonioli, M. Anzidei, L. Ferranti, G. Leoni, G. Scicchitano, and S. Silenzi. Sea level change along the Italian coast during the Holocene and projections for the future. *Quaternary International*, 232(1):250–257, 2011.

F. W. Landerer and D. L. Volkov. The anatomy of recent large sea level fluctuations in the Mediterranean Sea. *Geophysical Research Letters*, 40(3):553–557, 2013.

F. W. Landerer, J. H. Jungclaus, and J. Marotzke. Ocean bottom pressure changes lead to a decreasing length–of–day in a warming climate. *Geophysical Research Letters*, 34, L06307, 2007. doi: 10.1029/2006GL029106.

P. Lemke, J. Ren, R. B. Alley, I. Allison, J. Carrasco, G. Flato, Y. Fujii, G. Kaser, P. Mote, R.H. Thomas, and T. Zhang. Observations: Changes in Snow, Ice and Frozen Ground. In S. Solomon, D. Qin, M. Manning, Z. Chen, M. Marquis, K.B. Averyt, M. Tignor, and H.L. Miller, editors, *Climate Change 2007: The Physical Science Basis: Contribution of Working Group I to the Fourth Assessment Report of the Intergovernmental Panel on Climate Change*, pages 337–386. Cambridge University Press, 2007.

J. T. M. Lenaerts, M. R. van den Broeke, W. J. van de Berg, E. van Meijgaard, and P. Kuipers Munneke. A new, high-resolution surface mass balance map of Antarctica (1979 2010) based on regional atmospheric climate modeling. *Geophysical Research Letters*, 39(4): n/a–n/a, 2012. doi: 10.1029/2011GL050713.

T. M. Lenton. Early warning of climate tipping points. *Nature Climate Change*, 1(4):201–209, 2011.

E. Lisitzin. Le niveau moyen de la mer. *Bulletin d'Information. Comite Central d'Oceanographie d'Etude des Cotes (COEC)*, 10:254–262, 1958.

E. Lisitzin. *Sea–level changes*, volume 8. Elsevier Science, 1974.

V. N. Livina, F. Kwasniok, and T. M. Lenton. Potential analysis reveals changing number of climate states during the last 60 kyr. *Climate of the Past*, 6(1), 2010.

D. B. Lluch-Cota, Warren S. Wooster, and S. R. Hare. Sea surface temperature variability in coastal areas of the northeastern Pacific related to the El Niño-Southern Oscillation and the Pacific Decadal Oscillation. *Geophysical Research Letters*, 28(10):2029–2032, 2001.

M. B. Lythe, D. G. Vaughan, and BEDMAP Consortium. BEDMAP: A new ice thickness and subglacial topographic model of Antarctica. *Journal of Geophysical Research*, 106:11335–11352, 2001. doi: 10.1029/2000JB900449.

M. Marcos and M. N. Tsimplis. Forcing of coastal sea level rise patterns in the North Atlantic and the Mediterranean Sea. *Geophysical Research Letters*, 34(18):L18604, 2007. doi: 10.1029/2007GL030641.

M. Marcos and M. N. Tsimplis. Comparison of results of AOGCMs in the Mediterranean Sea during the 21st century. *Journal of Geophysical Research*, 113:C12028, 2008. doi: 10.1029/2008JC004820.

M. Masina and A. Lamberti. A nonstationary analysis for the Northern Adriatic extreme sea levels. *Journal of Geophysical Research: Oceans*, 118:1–18, 2013. doi: 10.1002/jgrc.20313.

G. McGranahan, D. Balk, and B. Anderson. The rising tide: assessing the risk of climate change and human settlements in low elevation coastal zones. *Environment and Urbanization*, 19:17–37, 2007.

G. A. Meehl, T. F. Stocker, W. D. Collins, P. Friedlingstein, A. T. Gaye, J. M. Gregory, A. Kitoh, R. Knutti, J. M. Murphy, A. Noda, S. C. B. Raper, I. G. Watterson, A. J. Weaver, and Z.-C. Zhao. Climate Change 2007: The Physical Science Basis, Intergovernmental Panel on Climate Change. In S. Solomon, D. Qin, M. Manning, Z. Chen, M. Marquis, K. B. Averyt, M. Tignor, and H. L. Miller, editors, *Global Climate Projections*, pages 747–845. Cambridge University Press, Cambridge, 2007.

D. Melini and A. Piersanti. Impact of global seismicity on sea level change assessment. *Journal of Geophysical Research: Solid Earth (1978–2012)*, 111(B3), 2006.

D. Melini, A. Piersanti, G. Spada, G. Soldati, E. Casarotti, and E. Boschi. Earthquakes and relative sealevel changes. *Geophysical Research Letters*, 31(9), 2004.

D. Melini, G. Spada, and A. Piersanti. A sea level equation for seismic perturbations. *Geophysical Journal International*, 180(1):88–100, 2010.

M. A. Merrifield. A Shift in Western Tropical Pacific Sea Level Trends during the 1990s. *Journal of Climate*, 24(15), 2011.

G. A. Milne and J. X. Mitrovica. Postglacial sea-level change on a rotating Earth. *Geophysical Journal International*, 133(1):1–19, 1998. doi: 10.1046/j.1365-246X.1998.1331455.x.

S. Minobe. Spatio-temporal structure of the pentadecadal variability over the North Pacific. *Progress in Oceanography*, 47(2):381–408, 2000.

J. X. Mitrovica and J. L. Davis. Present-day post-glacial sea level change far from the Late Pleistocene ice sheets: Implications for recent analyses of tide gauge records. *Geophysical Research Letters*, 22(18):2529–2532, 1995.

J. X. Mitrovica and G.A. Milne. On the origin of late Holocene sea-level highstands within equatorial ocean basins. *Quaternary Science Reviews*, 21:2179–2190, 2002.

J. X. Mitrovica and V. R. Peltier. On post-glacial geoid subsidence over the equatorial oceans. *Journal of Geophysical Research*, 96:20 053–20 071, 1991.

J. X. Mitrovica, M. E. Tamisiea, J. L. Davis, and G. A. Milne. Recent mass balance of polar ice sheets inferred from patterns of global sea-level change. *Nature*, 409:1026–1029, 2001.

R. H. Moss, J. A. Edmonds, K. A. Hibbard, M. R. Manning, S. K. Rose, D. P. Van Vuuren, T. R. Carter, S. Emori, M. Kainuma, T. Kram, et al. The next generation of scenarios for climate change research and assessment. *Nature*, 463(7282):747–756, 2010.

W. H. Munk and G. J. F. Macdonald. The rotation of the earth: a geophysical discussion. In W. H. Munk and G. J. F. MacDonald, editors, *The rotation of the earth: a geophysical discussion*, volume 1, pages 19–323. Cambridge (UK): Cambridge University Press, 19+ 323 p., 1975.

M. Nakada and H. Inoue. Rates and causes of recent global sea-level rise inferred from long tide gauge data records. *Quaternary Science Reviews*, 24(10):1217–1222, 2005.

M. Nakada and K. Lambeck. Glacial rebound and relative sea-level variations: a new appraisal. *Geophysical Journal International*, 90(1):171–224, 1987.

S. M. Nakiboglu and K. Lambeck. Secular sea level change. In K. Lambeck R. Sabadini and E. Boschi, editors, *Glacial Isostasy, Sea Level and Mantle Rheology*, pages 237–258. Kluwer Academic Publ., 1991.

R. S. Nerem, D. P. Chambers, C. Choe, and G. T. Mitchum. Estimating mean sea level change from the TOPEX and Jason altimeter missions. *Marine Geodesy*, 33(S1):435–446, 2010.

R.S. Nerem and G.T. Mitchum. Observations of sea level change from satellite altimetry. In M. T Douglas, B.and Kearney and S. P. Leatherman, editors, *Sea Level Rise: history and consequences*, volume 75. Academic Press, San Diego, 2001.

J. Nicholls and A. Cazenave. Sea–Level rise and its impact on coastal zones. *Science*, 328, 5985: 1517–1520, 2010. doi: 10.1126/science.1185782.

R. J. Nicholls and F. M. J. Hoozemans. The Mediterranean: vulnerability to coastal implications of climate change. *Ocean & Coastal Management*, 31(2):105–132, 1996.

R. J. Nicholls, F. M. J. Hoozemans, and M. Marchand. Increasing flood risk and wetland losses due to global sea–level rise: regional and global analyses. *Global Environmental Change*, 9, Supplement 1(0):S69–S87, 1999. doi: http://dx.doi.org/10.1016/S0959--3780(99)00019--9.

C. Nostro, A. Piersanti, A. Antonioli, and G. Spada. Spherical versus flat models of coseismic and postseismic deformations. *Journal of Geophysical Research: Solid Earth (1978–2012)*, 104 (B6):13115–13134, 1999.

M. Olivieri and G. Spada. Intermittent sea–level acceleration. *Global and Planetary Change*, 109: 64–72, 2013. doi: 10.1016/j.gloplacha.2013.08.004.

M. Olivieri, G. Spada, A. Antonioli, and G. Galassi. Mazara del Vallo tide gauge observations (1906–1916): land subsidence or sea level rise? *Journal of Coastal Research*, 31(1):69–75, 2015. doi: 10.2112/JCOASTRES-D-12-00233.1.

J. S. Pal, F. Giorgi, X. Bi, N. Elguindi, F. Solmon, S. A. Rauscher, X. Gao, R. Francisco, A. Zakey, J. Winter, et al. Regional climate modeling for the developing world: The ICTP RegCM3 and RegCNET. *Bulletin of the American Meteorological Society*, 88(9):1395–1409, 2007.

V. K. Pavlov. Seasonal and long-term sea level variability in the marginal seas of the Arctic Ocean. *Polar research*, 20(2):153–160, 2001.

W. R. Peltier. Global sea level rise and glacial isostatic adjustment: an analysis of data from the east coast of North America. *Geophysical Research Letters*, 23(7):717–720, 1996.

W. R. Peltier. Global glacial isostatic adjustment and modern instrumental records of relative sea level history. *International Geophysics*, 75:65–95, 2001.

W. R. Peltier. Global glacial isostasy and the surface of the ice-age Earth: the ICE-5G (VM2) Model and GRACE. *Annual Review of Earth and Planetary Sciences*, 32:111–149, 2004. doi: 10.1146/annurev.earth.32.082503.144359.

W. R. Peltier. Closure of the budget of global sea level rise over the GRACE era: The importance and magnitudes of the required corrections for global glacial isostatic adjustment. *Quaternary Science Reviews*, 28(17):1658–1674, 2009.

W. R. Peltier and J. T. Andrews. Glacial-Isostatic Adjustment – I. The Forward Problem. *Geophysical Journal of the Royal Astronomical Society*, 46(3):605–646, 1976.

W. R. Peltier and X. Jiang. Mantle viscosity from the simultaneous inversion of multiple data sets pertaining to postglacial rebound. *Geophysical Research Letters*, 23(5):503–506, 1996.

W. R. Peltier and A. M. Tushingham. Global sea level rise and the greenhouse effect: might they be connected? *Science*, 244(4906):806–810, 1989.

A. Piersanti, G. Spada, R. Sabadini, and M. Bonafede. Geobal post-seismic deformation. *Geophysical Journal International*, 120(3):544–566, 1995.

P. A. Pirazzoli. Secular trends of relative sea-level (RSL) changes indicated by tide-gauge records. Technical report, CNRS-INTERGEO, 191 Rue Saint Jacques, 75005 Paris, France, 1986.

P. A. Pirazzoli. Global sea-level changes and their measurement. *Global and Planetary Change*, 8 (3):135–148, 1993.

P. A. Pirazzoli and A. Tomasin. Recent evolution of surge-related events in the Northern Adriatic area. *Journal of Coastal Research*, 18(3):537–554, 2002.

H. P. Plag. *Arctic tide gauges: a status report*. Intergovernmental Oceanographic Commission of UNESCO, 2000.

S. Polli. Gli attuali movimenti verticali delle coste continentali. *Annals of Geophysics*, 5(4):597–602, 1952.

W. H. Press, B. P. Flannery, S. A. Teukolsky, and W. T. Vetterling. *Numerical Recipes in FORTRAN 77: Volume 1, Volume 1 of Fortran Numerical Recipes: The Art of Scientific Computing*, volume 1. Cambridge university press, 1992.

A. Proshutinsky, I. M. Ashik, E. N. Dvorkin, S. Häkkinen, R. A. Krishfield, and W. R. Peltier. Secular sea level change in the Russian sector of the Arctic Ocean. *Journal of Geophysical Research: Oceans (1978–2012)*, 109(C3), 2004.

A. Proshutinsky, I. Ashik, S. Häkkinen, E. Hunke, R. Krishfield, M. Maltrud, W. Maslowski, and J. Zhang. Sea level variability in the Arctic Ocean from AOMIP models. *Journal of Geophysical Research: Oceans (1978–2012)*, 112(C4), 2007.

S. Rahmstorf. A semi-empirical approach to projecting future sea-level rise. *Science*, 315(5810): 368–370, 2007.

F. Raicich. Recent evolution of sea-level extremes at Trieste (Northern Adriatic). *Continental Shelf Research*, 23(3):225–235, 2003.

F. Raicich. Decadal variability of sea level in the Mediterranean Sea in connection with local climate and large-scale climate indicators. MedCLIVAR Conference, Madrid 26-28 September, Poster presentation, 2012.

M. Z. Rehman and N. M. Nawi. Improving the Accuracy of Gradient Descent Back Propagation Algorithm (GDAM) on Classification Problems. *International Journal of New Computer Architectures and their Applications (IJNCAA)*, 1(4):838–847, 2011.

M. Rhein, S. R. Rintoul, S. Aoki, E. Campos, D. Chambers, R. A. Feely, S. Gulev, G. C. Johnson, S. A. Josey, A. Kostianoy, et al. Observations: ocean. In T. F. Stocker, D. Qin, G.-K. Plattner, M. Tignor, S. K. Allen, J. Boschung, A. Nauels, Y. Xia, V. Bex, and P. M. Midgley, editors, *Climate Change 2013: The Physical Science Basis. Contribution of Working Group I to the Fifth Assessment Report of the Intergovernmental Panel on Climate Change*, pages 1138–1191. Cambridge University Press, Cambridge, 2013.

E. Rignot and R. H. Thomas. Mass balance of polar ice sheets. *Science*, 297(5586):1502–1506, 2002. doi: 10.1126/science.1073888.

E. Rignot, G. Casassa, S. Gogineni, P. Kanagaratnam, W. Krabill, H. Pritchard, A. Rivera, R. Thomas, J. Turner, and D. Vaughan. Recent ice loss from the Fleming and other glaciers, Wordie Bay, West Antarctic Peninsula. *Geophysical Research Letters*, 32:L07502, 2005. doi: 10.1029/2004GL021947.

E. Rignot, J. E. Box, E. Burgess, and E. Hanna. Mass balance of the Greenland ice sheet from 1958 to 2007. *Geophysical Research Letters*, 35:L20502, 2008. doi: 10.1029/2008GL035417.

E. Rignot, I. Velicogna, M. R. van den Broeke, A. Monaghan, and J. T. M. Lenaerts. Acceleration of the contribution of the greenland and antarctic ice sheets to sea level rise. *Geophysical Research Letters*, 38(5):n/a–n/a, 2011. doi: 10.1029/2011GL046583.

A. R. Robinson, W. G. Leslie, A. Theocharis, and A. Lascaratos. Mediterranean Sea circulation. *Encyc. of Ocean. Sci.*, pages 1689–1706, 2001.

E. Roeckner, G. Bäuml, L. Bonaventura, R. Brokopf, M. Esch, M. Giorgetta, S. Hagemann, I. Kirchner, L. Kornblueh, E. Manzini, A. Rhodin, U. Schlese, U. Schultzweida, and A. Tompkins. The atmospheric general circulation model ECHAM5. Part I: model description. Technical Report 349, Max Planck Institut für Meteorologie, 2003.

O. Rompelman and H. H. Ros. Coherent averaging technique: A tutorial review part 1: Noise reduction and the equivalent filter. *Journal of biomedical engineering*, 8(1):24–29, 1986.

N. Scafetta. Multi-scale dynamical analysis (MSDA) of sea level records versus PDO, AMO, and NAO indexes. *Climate Dynamics*, pages 1–18, 2013. doi: 10.1007/s00382-013-1771-3.

L. Scarascia and P. Lionello. Global and regional factors contributing to the past and future sea level rise in the Northern Adriatic Sea. *Global and Planetary Change*, 106:51–63, 2013.

M. Schaeffer, W. Hare, S. Rahmstorf, and M. Vermeer. Long-term sea-level rise implied by 1.5 °C and 2 °C warming levels. *Nature Climate Change*, 2(12):867–870, 2012.

M. Scheffer, J. Bascompte, W. A Brock, V. Brovkin, S. R. Carpenter, V. Dakos, H. Held, E. H. Van Nes, M. Rietkerk, and G. Sugihara. Early-warning signals for critical transitions. *Nature*, 461(7260):53–59, 2009.

G. Schubert, D. L. Turcotte, and P. Olson. *Mantle Convection in the Earth and Planets*. Cambridge University Press, 2001.

E. Serpelloni, C. Faccenna, G. Spada, D. Dong, and S. D. P. Williams. Vertical GPS ground motion rates in the Euro–Mediterranean region: New evidence of velocity gradients at different spatial scales along the Nubia–Eurasia plate boundary. *Journal of Geophysical Research: Solid Earth*, 118(11):6003–6024, 2013.

I. Shennan and P.L. Woodworth. A comparison of late Holocene and twentieth-century sea-level trends from the UK and North Sea region. *Geophysical Journal International*, 109(1):96–105, 1992.

A. B. A. Slangen. *Modelling regional sea–level changes in recent past and future*. PhD thesis, Utrecht University, the Netherlands, 2012.

A. B. A. Slangen, C. A. Katsman, R. S. W. Van de Wal, L. L. A. Vermeersen, and R. E. M. Riva. Towards regional projections of twenty-first century sea-level change based on IPCC SRES scenarios. *Climate dynamics*, 38(5-6):1191–1209, 2012.

A. B. A. Slangen, M. Carson, C. A. Katsman, R. S. W. van de Wal, A. Köhl, L. L. A. Vermeersen, and D. Stammer. Projecting twenty–first century regional sea–level changes. *Climatic Change*, 124(1–2):317–332, 2014.

M. Snoussi, T. Ouchani, and S. Niazi. Vulnerability assessment of the impact of sea–level rise and flooding on the Moroccan coast: The case of the Mediterranean eastern zone. *Estuarine, Coastal and Shelf Science*, 77(2):206–213, 2008.

S. Solomon. *The physical science basis: Contribution of Working Group I to the fourth assessment report of the Intergovernmental Panel on Climate Change*. Cambridge University Press, 2007.

L. S. Sørensen, S. B. Simonsen, K. Nielsen, P. Lucas-Picher, G. Spada, G. Adalgeirsdottir, R. Forsberg, and C. S. Hvidberg. Mass balance of the greenland ice sheet (2003-2008) from icesat data - the impact of interpolation, sampling and firn density. *The Cryosphere*, 5(1):173–186, 2011. doi: 10.5194/tc-5-173-2011.

G. Spada and G. Galassi. New estimates of secular sea level rise from tide gauge data and GIA modelling. *Geophysical Journal International*, 191(3):1067–1094, 2012. doi: 10.1111/j.1365-246X.2012.05663.x.

G. Spada and P. Stocchi. *Solving the Sea Level Equation, Part I - Theory*. Samizdat Press, 2005.

G. Spada and P. Stocchi. *The Sea Level Equation, Theory and Numerical Examples*. Aracne (Roma), 2006.

G. Spada and P. Stocchi. SELEN: A Fortran 90 program for solving the Sea–Level Equation. *Computers and Geosciences*, 33(4):538–562, 2007. doi: 10.1016/j.cageo.2006.08.006.

G. Spada, A. Antonioli, S. Cianetti, and C. Giunchi. Glacial isostatic adjustment and relative sea-level changes: the role of lithospheric and upper mantle heterogeneities in a 3-D spherical Earth. *Geophysical Journal International*, 165(2):692–702, 2006.

G. Spada, V. R. Barletta, V. Klemann, R. E. M. Riva, Z. Martinec, P. Gasperini, B. Lund, D. Wolf, L. L. A. Vermeersen, and M. A. King. A benchmark study for glacial isostatic adjustment codes. *Geophysical Journal International*, 185(1):106–132, 2011a.

G. Spada, F. Colleoni, and G. Ruggieri. Shallow upper mantle rheology and secular ice sheet fluctuations. *Tectonophysics*, 511(3):89–98, 2011b.

G. Spada, D. Melini, G. Galassi, and F. Colleoni. Modeling sea level changes and geodetic variations by glacial isostasy: the improved SELEN code. *ArXiv e-prints*, 2012.

G. Spada, G. Ruggieri, L. S. Sørensen, K. Nielsen, D. Melini, and F. Colleoni. Greenland uplift and regional sea level changes from ICESat observations and GIA modelling. *Geophysical Journal International*, 189(3):1457–1474, 2012. doi: 10.1111/j.1365-246X.2012.05443.x.

G. Spada, J. L. Bamber, and R. T. W. L. Hurkmans. The gravitationally consistent sea-level fingerprint of future terrestrial ice loss. *Geophysical Research Letters*, 40(3):482–486, 2013.

G. Spada, G. Galassi, and M. Olivieri. A study of the longest tide gauge sea–level record in Greenland (Nuuk–Godthab, 1958–2002). *Global and Planetary Change*, 118:42–51, 2014a. doi: 10.1016/j.gloplacha.2014.04.001.

G. Spada, M. Olivieri, and G. Galassi. Anomalous secular sea-level acceleration in the Baltic Sea caused by isostatic adjustment. *Annals of Geophysics*, 57(4):S0432, 2014b.

N. E. Spencer and P. L. Woodworth. Data holdings of the permanent service for mean sea level (january 1991). Technical report, Bidston Observatory, Birkenhead, 1991.

E. V. Stanev and E. L. Peneva. Regional sea level response to global climatic change: Black sea examples. *Global and Planetary Change*, 32:33–47, 2002.

H. Steffen and P. Wu. Glacial isostatic adjustment in Fennoscandia - A review of data and modeling. *Journal of Geodynamics*, 52:169–204, 2011.

R. W. Stewart. Sea-level rise or coastal subsidence? *Atmosphere-Ocean*, 27(3):461–477, 1989.

P. Stocchi and G. Spada. Influence of glacial isostatic adjustment upon current sea level variations in the Mediterranean. *Tectonophysics*, 474(1):56–68, 2009.

W. Sturges. Large-scale coherence of sea level at very low frequencies. In Geophysics Study Committee, National Research Council, editor, *Sea-Level Change*, page 63. National Academies Press, 1990.

W. Sturges and B.G. Hong. Decadal variability of sea level. In B. C. Douglas, M. S. Kearney, and S. P. Leatherman, editors, *Sea level rise: history and consequences*, pages 165–180. International Geophysics Series (75), 2001.

M. J. Suarez and P. S. Schopf. A delayed action oscillator for ENSO. *Journal of the Atmospheric Sciences*, 45(21):3283–3287, 1988.

K.R. Subrahmanya. Tectonic, eustatic and isostatic changes along the Indian coast. In *Sea-Level Rise and Coastal Subsidence*, pages 193–203. Springer, 1996.

R. T. Sutton and D. L. R. Hodson. Atlantic Ocean forcing of North American and European summer climate. *Science*, 309(5731):115–118, 2005.

M. E. Tamisiea. Ongoing glacial isostatic contributions to observations of sea level change. *Geophysical Journal International*, 186(3):1036–1044, 2011. doi: 10.1111/j.1365-246X.2011.05116.x.

M. E. Tamisiea, J. X. Mitrovica, G. A. Milne, and J. L. Davis. Global geoid and sea level changes due to present–day ice mass fluctuations. *Journal of Geophysical Research*, 106, B12:30,849–30,863, 2011. doi: 10.1029/2000JB000011.

Y. Tanaka, V. Klemann, Z. Martinec, and R. E. M. Riva. Spectral-finite element approach to viscoelastic relaxation in a spherical compressible Earth: application to GIA modelling. *Geophys. J. Int.*, 184:220–234, 2011. doi: 10.1111/j.1365-246X.2010.04854.x.

J. R. Taylor. *An introduction to error analysis: the study of uncertainties in physical measurements*. University Science Books, 1997.

P. Teatini, M. Ferronato, G. Gambolati, W. Bertoni, and M. Gonella. A century of land subsidence in Ravenna, Italy. *Environmental Geology*, 47(6):831–846, 2005.

M. Tegmark. An icosahedronbased method for pixelizing the celestial sphere? *The Astrophysical Journal*, 470:L81–L84, 1996.

M. E. Torres, M. A. Colominas, G. Schlotthauer, and P. Flandrin. A complete ensemble empirical mode decomposition with adaptive noise. In *Acoustics, Speech and Signal Processing (ICASSP), 2011 IEEE International Conference*, pages 4144–4147. IEEE, 2011.

A. Trupin and J. Wahr. Spectroscopic analysis of global tide gauge sea level data. *Geophysical Journal International*, 100(3):441–453, 1990.

M. Tsimplis, G. Spada, M. Marcos, and N. Flemming. Multi-decadal sea level trends and land movements in the Mediterranean Sea with estimates of factors perturbing tide gauge data and cumulative uncertainties. *Global and Planetary Change*, 76(1):63–76, 2011.

M. N. Tsimplis and T. F. Baker. Sea level drop in the Mediterranean Sea: an indicator of deep water temperature and salinity changes? *Geophysical Research Letters*, 27:1731–1734, 2000.

M. N. Tsimplis and S. A. Josey. Forcing of the Mediterranean Sea by atmospheric oscillations over the North Atlantic. *Geophysical Research Letters*, 28(5):803–806, 2001. doi: 10.1029/2000GL012098.

M. N. Tsimplis and M. Rixen. Sea level in the mediterranean sea: The contribution of temperature and salinity changes. *Geophysical Research Letters*, 29(23):51–1–51–4, 2002. doi: 10.1029/2002GL015870.

M. N. Tsimplis, M. N. Raicich, L. Fenoglio-Marc, A. G. P. Shaw, M. Marcos, S. Somot, and A. Bergamasco. Recent developments in understanding sea level rise at the Adriatic coasts. *Physics and Chemistry of the Earth, Parts A/B/C*, 40-41, 2012. doi: 10.1016/j.pce.2009.11.007.

M. N. Tsimplis, F. Calafat, Marcos M., G. Jordà, D. Gomis, L. Fenoglio-Marc, M. V. Struglia, S. A. Josey, and D. P. Chambers. The effect of the NAO on sea level and on mass changes in the Mediterranean Sea. *Journal of Geophysical Research: Oceans*, 118(2):944–952, 2013.

M.N. Tsimplis, M. Marcos, and S. Somot. 21st century Mediterranean sea level rise: steric and atmospheric pressure contributions from a regional model. *Global and Planetary Change*, 63 (2):105–111, 2008.

D. L. Turcotte and G. Schubert. *Geodynamics*. Cambridge University Press, Cambridge, 2002.

A. M. Tushingham and W. R. Peltier. Ice-3G: A new global model of late Pleistocene deglaciation based upon geophysical predictions of post-glacial relative sea level change. *Journal of Geophysical Research: Solid Earth (1978–2012)*, 96(B3):4497–4523, 1991.

Y. S. Unal and M. Ghil. Interannual and interdecadal oscillation patterns in sea level. *Climate Dynamics*, 11(5):255–278, 1995.

A. S. Unnikrishnan and D. Shankar. Are sea–level–rise trends along the coasts of the north Indian Ocean consistent with global estimates? *Global and Planetary Change*, 57(3):301–307, 2007.

H. Valentin. *Die Küsten der Erde: Beiträge zur allgemeinen und regionalen Küstenmorphologie*. Number 246. JP Gotha, 1952.

I. A. van de Leemput, M. Wichers, A. O. J. Cramer, D. Borsboom, F. Tuerlinckx, P. Kuppens, E. H. van Nes, W. Viechtbauer, E. J. Giltay, S. H. Aggen, C. Derom, N. Jacobs, K. S. Kendler, H. L. J. van der Maas, M. C. Neale, F. Peeters, E. Thiery, P. Zachar, and M. Scheffer. Critical slowing down as early warning for the onset and termination of depression. *Proceedings of the National Academy of Sciences*, 111(1):87–92, 2014. doi: 10.1073/pnas.1312114110.

T. P. Vogl, J. K. Mangis, A. K. Rigler, W. T. Zink, and D. L. Alkon. Accelerating the convergence of the back-propagation method. *Biological cybernetics*, 59(4-5):257–263, 1988.

Y. Wada, L. P. H. Beek, F. C. Sperna Weiland, B. F. Chao, Y. H. Wu, and M. F. P. Bierkens. Past and future contribution of global groundwater depletion to sea–level rise. *Geophysical Research Letters*, 39(9), 2012.

T. Wahl, I. Haigh, P. L. Woodworth, F. Albrecht, D. Dillingh, J. Jensen, R. J. Nicholls, R. Weisse, and G. Woppelmann. Observed mean sea level changes around the North Sea coastline from 1800 to present. *Earth Science Reviews*, 2013. doi: 10.1016/j.earscirev.2013.05.003.

K. Walter and H. F. Graf. On the changing nature of the regional connection between the North Atlantic Oscillation and sea surface temperature. *Journal of Geophysical Research: Atmospheres*, 107(D17):ACL–7, 2002.

B. L. Welch. The generalization of "Student's" problem when several different population variances are involved. *Biometrika*, 34:28–35, 1947.

M. Wenzel and J. Schröter. Reconstruction of regional mean sea level anomalies from tide gauges using neural networks. *Journal of Geophysical Research: Oceans (1978–2012)*, 115(C8), 2010.

P. Whitehouse. *Glacial isostatic adjustment and sea–level change. State of the art report.* Swedish Nuclear Fuel and Waste Management Organization (SKB), 2009. SKB TR–09–11.

J. H. Wilkinson, J. H. Wilkinson, and J. H. Wilkinson. *The algebraic eigenvalue problem*, volume 87. Clarendon Press Oxford, 1965.

J. K. Willis, D. P. Chambers, and R. S. Nerem. Assessing the globally averaged sea level budget on seasonal to interannual timescales. *Journal of Geophysical Research*, 113(C6):C06015, 2008.

K. Wolter and M. S. Timlin. Measuring the strength of ENSO events: how does 1997/98 rank? *Weather*, 53(9):315–324, 1998.

P. L. Woodworth. A search for accelerations in records of European mean sea level. *International Journal of Climatology*, 10(2):129–143, 1990.

P. L. Woodworth and R. Player. The Permanent Service for Mean Sea Level: an update to the 21st century. *Journal of Coastal Research*, 19:287–295, 2003.

P. L. Woodworth, N. J. White, S. Jevrejeva, S. J. Holgate, J. A. Church, and W. R. Gehrels. Evidence for the accelerations of sea level on multi-decade and century timescales. *International Journal of Climatology*, 29(6):777–789, 2009.

G. Wöppelmann, G. Le Cozannet, M. Michele, D. Raucoules, A. Cazenave, M. Garcin, S. Hanson, M. Marcos, and A. Santamaría-Gómez. Is land subsidence increasing the exposure to sea level rise in Alexandria, Egypt? *Geophysical Research Letters*, 40(12):2953–2957, 2013.

Z. Wu and N. E. Huang. Ensemble empirical mode decomposition: a noise-assisted data analysis method. *Advances in Adaptive Data Analysis*, 1(01):1–41, 2009.

T. Yanagi and T. Akaki. Sea level variation in the eastern Asia. *Journal of Oceanography*, 50: 643–651, 1994.

J. H. Zar. *Biostatistical Analysis*. Pearson Prentice-Hall, Upper Saddle River, N.J., 2010. 5th Edition.

S. Zerbini, H.-P. Plag, T. Baker, M. Becker, H. Billiris, B. Bürki, H.-G. Kahle, I. Marson, L. Pezzoli, B. Richter, et al. Sea level in the Mediterranean: a first step towards separating crustal movements and absolute sea-level variations. *Global and Planetary Change*, 14(1):1–48, 1996.

G. Zhang, B. E. Patuwo, and M. Y. Hu. Forecasting with artificial neural networks: The state of the art. *International Journal of Forecasting*, 14(1):35 – 62, 1998. doi: http://dx.doi.org/10.1016/S0169-2070(97)00044-7.

X. Zhang and J. A. Church. Sea level trends, interannual and decadal variability in the Pacific Ocean. *Geophysical Research Letters*, 39(21), 2012.

Y. Zhang, J. M. Wallace, and D.S. Battisti. ENSO-like interdecadal variability: 1900-93. *Journal of climate*, 10(5):1004–1020, 1997.

H. J. Zwally, Mario B. G., J. LI, H. G. Cornejo, M.A. Beckley, A. C. Brenner, J.L. Saba, and Donghui Y. Mass changes of the Greenland and Antarctic ice sheets and shelves and contributions to sea-level rise: 1992–2002. *Journal of Glaciology*, 51(175):509–527, 2005.